Modelling the performance characteristics of a hydraulic load control valve

Weber, Steven Thomas

Award date:
2002

Awarding institution:
University of Bath

MODELLING THE PERFORMANCE CHARACTERISTICS OF A HYDRAULIC LOAD CONTROL VALVE

Submitted by

STEVEN THOMAS WEBER

A thesis submitted in fulfilment of the degree of
Doctor of Philosophy
Centre for Power Transmission and Motion Control
Department of Mechanical Engineering
Faculty of Engineering and Design
University of Bath
May 2002

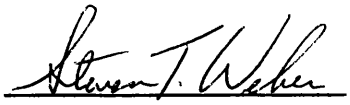

Steven T. Weber

ProQuest LLC
789 East Eisenhower Parkway
P.O. Box 1346
Ann Arbor, MI 48106-1346

ACKNOWLEDGEMENTS

A debt of gratitude is owed to Bob Koski not only for giving me the opportunity of studying for my PhD but also for the many insightful discussions. I also wish to express my appreciation to my supervisors, Kevin Edge and Nigel Johnston. Their guidance and support has been superb.

My thanks and appreciation are due to my many friends and colleagues, past and present, at Sun Hydraulics in Sarasota, Coventry, and Erkelenz. These include Jeff Cooper, Rick Telinger, Rick Grawunde, Jonathan Gamble, John Reckard, and my "accounting team" of Jean Snyder, Debbie Knight, Larisa Baker, and Tricia Fulton. Special thanks are due for Steve Hancox and his wife Lianne for making sure I had plenty of English culture.

The "dream team" of Dave, Joe, and Andy in the hydraulics laboratory at the university are owed my thanks. I am also appreciative of the efforts by the instrumentation group in the mechanical engineering department as well as the other staff members.

I wish to thank Jose Porteiro from the University of South Florida for the many discussions and helpful advice. My thanks also to Bob Pennington of USF for making sure I had buffalo wings and beer when ever I visited Florida and for all of the email jokes.

I wish to thank the friends that I made during my studies especially in the sub-aqua club. I wish to especially thank Nick, Max, Gordon, Emma, Tom, Ian, and Darran.

I wish to express my sincere thanks and appreciation to Bernd Zähe of Sun Hydraulik in Erkelenz, his wife Pat Mahoney, and their children Clara and Marta.

Finally, I wish to express my thanks to my parents, my brothers, and my sister for their support.

DEDICATION

I wish to dedicate my thesis to my parents.

ABSTRACT

A new hydraulic valve designed to provide smooth, positive control of overrunning loads primarily in hydraulic motors was found to be unstable in some field applications. The instability was system dependent and solved with a modification to the original valve design. Unstable operation seems to be related to the tendency of this new load control valve to pressure compensate. Pressure compensation is the tendency for a valve to adjust itself in response to changes in pressure and thus allow a nearly constant rate of flow.

In order to understand the causes of the tendency of the load control valve to pressure compensate, the valve was modelled in the Matlab/Simulink environment. In order to model the valve accurately, both flow visualisation and computational fluid dynamics (CFD) were used to study the effects of hole coverage on both the angle of the jet of oil in each metering hole and the flow coefficient. From these results, a look-up table was created from which the simulation could interpolate values for the jet angle and flow coefficient as a function of valve stroke.

Through experimentation, it was found that friction caused primarily by glyd ring seals produced the significant amount of hysteresis seen in pressure compensation performance curves. Hysteresis manifests itself on the pressure compensation performance curve as a different flow rate for the same pressure. Thus, a friction model was created in order to model effects of the glyd ring seals. The modelled pressure compensation results showed good agreement with the experimentally measured characteristics. The accuracy of the modelled pressure compensation characteristics of the load control valve confirm that neither the exiting jet angle nor flow coefficient are constant with changing hole opening.

The initial stages of work to use the modelling technique to study new hole shapes were undertaken. Jet angles and flow coefficients were estimated from CFD results. Results from this initial study show not only interesting trends for using hole shapes to control the jet angle and flow coefficient, but also demonstrate the potential usefulness of modelling valves prior to manufacturing.

TABLE OF CONTENTS

LIST OF TABLES iv

LIST OF FIGURES v

LIST OF SYMBOLS vii

NOMENCLATURE x

CHAPTER 1 INTRODUCTION

1.1 Background 1

1.2 Problem description and methods and goals of the research 7

1.3 Organisation of the thesis 8

CHAPTER 2 EXPERIMENTAL WORK

2.1 Introduction 9

2.2 Review of past work 9

2.3 Oil hydraulics test stand and test rigs 14

2.4 Flow force measurement apparatus 19

2.5 Valve opening measurement test rig 22

2.6 Interpretation of results 26

2.7 Concluding remarks 31

CHAPTER 3 FLOW VISUALISATION

3.1 Introduction 32

3.2 Review of past work 32

3.3 Design of flow visualisation test rig 37

3.4 Results and discussion 42

3.5 Concluding remarks 48

CHAPTER 4 COMPUTATIONAL FLUID DYNAMICS MODELLING

4.1 Introduction 50

4.2 Review of past work 50

4.2.1 Relevance pf past work to current work Results and discussion 58

4.3 Coanda effect studies 59

4.3.1 Coanda model description 60

4.3.2 Coanda model results and discussion 61

4.4 Load control valve model description 63
4.4.1 Convergence criteria 66
4.4.2 Grid independence study 68
4.5 Results and discussion 70
4.6 Flow force calculation 79
4.7 Concluding remarks 82

CHAPTER 5 MATHEMATICAL MODELLING
5.1 Introduction 83
5.2 Review of past work 83
5.3 Model development 85
5.3.1 Force balance 86
5.4 Simulink model 87
5.4.1 Drive function 89
5.4.2 Pilot pressure 90
5.4.3 Inlet and outlet characteristics 90
5.4.4 Flow force modelling 92
5.4.5 Spring force modelling 93
5.4.6 Friction modelling 94
5.4.7 Integrators 95
5.4.8 Other block functions 96
5.5 Pre-processing and the interpolation block 96
5.6 Results and discussion 101
5.7 Sensitivity studies 107
5.7.1 Jet angle sensitivity analysis 107
5.7.2 Flow coefficient sensitivity analysis 110
5.8 Concluding Remarks 112

CHAPTER 6 EVALUATION OF ALTERNATIVE DESIGNS
6.1 Introduction 114
6.2 Angled holes 114
6.2.1 Results and discussion 115
6.3 Diamond shaped hole 118
6.3.1 Results and discussion 119
6.4 Inverted teardrop shaped hole 122
6.4.1 Results and discussion 123
6.5 Concluding remarks 125

CHAPTER 7 CONCLUSIONS AND RECOMMENDATIONS
7.1 Introduction 127
7.2 Experimental work 127
7.3 Flow visualisation 128
7.4 CFD 128
7.5 Mathematical modelling 129
7.6 Concluding remarks 130

REFERENCES 132

APPENDIX 139
Appendix 1: Matlab M-Files 140
Smooth.m 140
FlowArea.m 141
PressAngle.m 143
PressureMap.m 152
Friction.m 153
Valve.m 154
Interpolate.m 155
FlowCoeff.m 155
Theta.m 160
CQ.m 164

LIST OF TABLES

Table 3.1 Similarity calculations fro inlet flow conditions 41
Table 3.2 Comparison of flow visualisation results 43

Table 4.1 Inlet velocity boundary conditions 66
Table 4.2 Jet angles for the fourth hole series 74
Table 4.3 Comparison of jet angle sensitivity in flow force computation for fourth hole series 76

LIST OF FIGURES

Figure 1.1 Cross-section of the Sun Hydraulics CBEH LJN counterbalance valve 1
Figure 1.2 Hole pattern of load control valve in a 2-D layout 2
Figure 1.3 Cross-section of Sun Hydraulics model MBEM XMN load control valve (shown in open position) 3
Figure 1.4 Pilot modulation performance curves for the MBEM XMN load control valve 4
Figure 1.5 MBEM XMN pressure compensation performance 5

Figure 2.1 Stone (1957) flow force compensated poppet 11
Figure 2.2 Schrenk (1957) flow patterns 12
Figure 2.3 Oil hydraulic test stand schematic 16
Figure 2.4 Pressure compensation performance curves for seven pilot pressures 17
Figure 2.5 Pilot pressure modulation performance curves for three load pressures 18
Figure 2.6 Flow force measurement apparatus 20
Figure 2.7 Sample of force measurements for 200 bar inlet pressure 22
Figure 2.8 LVDT assembled on the load control valve 24
Figure 2.9 Pressure compensation performance for six pilot pressures 25
Figure 2.10 Valve stroke while pressure compensating for six pilot pressures 25
Figure 2.11 Hole segment area 27
Figure 2.12 Full cross-section of the load control valve 28
Figure 2.13 Composite flow coefficient computed for 250 bar inlet 30
Figure 2.14 Composite jet angle calculated for 250 bar inlet 31

Figure 3.1 Schrenk (1957) flow patterns 33
Figure 3.2 Schematic of the electrolysis unit 38
Figure 3.3 Sketch of the flow visualisation test stand 39
Figure 3.4 Plan view of the flow visualisation rig (not to scale) 40
Figure 3.5 Photograph of the flow visualisation test rig 41
Figure 3.6 Photograph of full open exit hole 44
Figure 3.7 Sketch of flow through full open exit hole 44
Figure 3.8 Photograph of ¾ open hole 45
Figure 3.9 Sketch of flow through ¾ open exit hole 45
Figure 3.10 Photograph of ½ open hole 46
Figure 3.11 Sketch of flow through ½ open exit hole 46

Figure 3.12 Exit hole ¼ open 47
Figure 3.13 Sketch of flow through ¼ open exit hole 47

Figure 4.1 Poppet shapes from Vaughan *et al.* (1992) 52
Figure 4.2 Compensation techniques from Sørensen (1999a) 57
Figure 4.3 Valve styles from Sørensen (1999b) 57
Figure 4.4 Cross-section of model geometry to study Coanda effects 60
Figure 4.5 Velocity contour plots from Coanda study [*mm/s*] 62
Figure 4.6 Typical convergence history plot 67
Figure 4.7 Maximum velocity calculated with different node counts 69
Figure 4.8 Jet angle calculated with different node counts 70
Figure 4.9 Idealised valve with exit hole fully open 72
Figure 4.10 Idealised valve with exit hole three-quarters open 72
Figure 4.11 Idealised valve with exit hole half open 73
Figure 4.12 Idealised valve with exit hole quarter open 73
Figure 4.13 Plot of CFD computed jet angles 77
Figure 4.14 Plot of CFD computed flow coefficients 78
Figure 4.15 Trapezoid rule node definition 79
Figure 4.16 Pressure map of piston metering edge 80
Figure 4.17 Comparison of flow forces 81

Figure 5.1 Cross-section of the load control valve showing pressures and diameters 86
Figure 5.2 Free-body diagram of the forces working on the piston 87
Figure 5.3 Simulink diagram of dynamic model 88
Figure 5.4 Driving function for Simulink model 89
Figure 5.5 Inlet pressure-flow characteristic 91
Figure 5.6 Outlet pressure-flow characteristic 91
Figure 5.7 Friction function (viscous friction gradient exaggerated) 94
Figure 5.8 Polynomials for the jet angles 98
Figure 5.9 Polynomials for the flow coefficients 98
Figure 5.10 Single and continuous curve for jet angles 100
Figure 5.11 Single and continuous curve for flow coefficients 100
Figure 5.12 Curve for the total opening area 101
Figure 5.13 Modelled pressure compensation of the load control valve using the Flowcoeff block in the Simulink diagram 102
Figure 5.14 Cumulative jet angle function 104
Figure 5.15 Cumulative flow coefficient function 104
Figure 5.15 Total opening area 105
Figure 5.17 Modelled pressure compensation using smoothed pre-processing 106

Figure 5.18 Experimental results 106
Figure 5.19 'Perfect' pressure compensation for sensitivity study 108
Figure 5.20 Jet angles required to produce 'perfect' pressure compensation 109
Figure 5.21 Valve characteristics using constant jet of 69° 109
Figure 5.22 Flow coefficient calculated to achieve 'perfect' pressure compensation ... 111
Figure 5.23 Pressure compensation with a fixed flow coefficient of 0.65 111

Figure 6.1 Angled cross-hole CFD fluid volume cross-section 115
Figure 6.2 Perpendicular cross-hole 116
Figure 6.3 Drilled hole angled 10° 116
Figure 6.4 Drilled hole angled 20° 116
Figure 6.5 Comparison of exit jet angles for angled exit holes 117
Figure 6.6 Comparison of flow coefficients 118
Figure 6.7 Diamond hole shape 119
Figure 6.8 Diamond shaped hole half covered 120
Figure 6.9 Comparison of jet angles 120
Figure 6.10 Comparison of flow coefficients 121
Figure 6.11 An inverted teardrop design 122
Figure 6.12 Half open inverted teardrop velocity vector plot 123
Figure 6.13 Comparison of jet angles 124
Figure 6.14 Comparison of flow coefficients 125

LIST OF SYMBOLS

A	Area, $[m^2]$
c_d	Discharge coefficient, [-]
c_q	Flow coefficient, [-]
D	Hole diameter, [m]
D_h	Hydraulic diameter [m]
F	Force, [N]
F_{flow}	Flow force [N]
$F_{friction}$	Friction force [N]
F_{spring}	Spring force [N]
F_{total}	Total force [N]
h	Opening height, [m]
k	Spring constant $[N/m]$
m_c	Coulomb friction constant, [N]
m_v	Viscous friction constant, $[Ns/m]$
P	Pressure, [bar]
Q	Flow rate, $[L/min]$
R	Hole radius, [m]
Re	Reynolds number, [-]
v_{inlet}	Inlet volumetric flow rate $[m^3/s]$
v_{outlet}	Outlet volumetric flow rate $[m^3/s]$
γ	Angle of arc of circle, [°]
ΔP	Differential pressure [bar]
θ	Jet angle, [°]

μ	Viscosity, $[Pa \cdot s]$
v	Viscosity, $[m^2/s]$
ρ	Density, $[kg/m^3]$
P	Wetted perimeter, $[m]$

NOMENCLATURE

CFD	Computational Fluid Dynamics
gpm	US gallons per minute [3.785 L/US gallon]
L/min	Litres per minute
PAL	Video format typically where electrical current is supplied at 50 Hz
PIV	Particle Image Velocimetry
RNG	Renormalized Group, a modified k-ε turbulence model
SIMPLE	Semi-Implicit Method for Pressure Linked Equations
tpi	Inverse of thread pitch, threads per inch

CHAPTER 1

INTRODUCTION

1.1 Background

Counterbalance, holding, load control, and over-centre are names given to valves that perform very similar and often the same function. These valves are used in hydraulic systems to permit smooth, positive control of overrunning loads. An overrunning load is one that has the tendency to cause the actuator to move faster than the supply fluid coming from the pump permits. A load control valve acts to restrict the fluid flow from the actuator to prevent cavitation at the inlet of the actuator. An example of a field application where an overrunning load would occur is in the cylinder used to raise and lower the boom of a crane. The weight of the boom would work to increase the speed at which it is being lowered. If the speed were sufficiently large enough to exceed the ability of the pump to keep up with the changing volume of the cylinder, the boom would be "overrunning" the capacity of the pump. The counterbalance valve restricts the flow from the actuator to prevent cavitation at the actuator inlet. Another example of an overrunning load would be the load on the end of a winch cable on a crane. A load control valve would be used to prevent the load from overrunning the supply to the hydraulic motor of the winch during lowering or paying out the cable. A mechanical brake would actually be used to hold the load.

Sun Hydraulics Corporation has a long history and expertise in designing and manufacturing counterbalance valves. Their standard counterbalance design is based upon geometry shown in the cross-section in Figure 1.1. It is essentially a pilot-assisted direct-

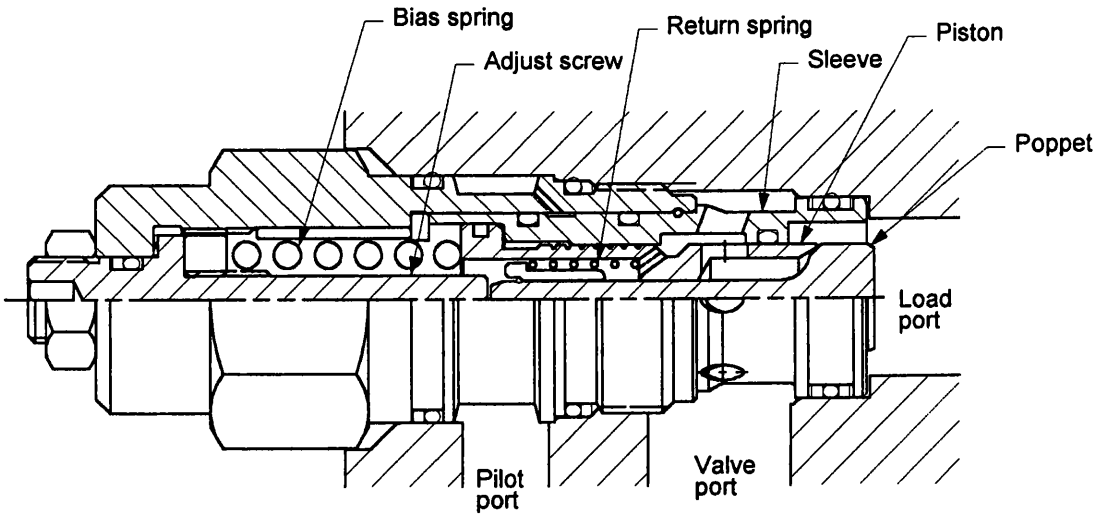

Figure 1.1 Cross-section of the Sun Hydraulics CBEH LJN counterbalance valve

acting relief valve with a free-flow check valve. The pilot-assist feature through external piloting to the *pilot port* effectively reduces the setting of the relief valve to permit smooth, control of overrunning loads. This has proven to be an extremely successful design for Sun Hydraulics. The design does make the valve sensitive to the pressure induced by the load at the *load port*. The result is that the pilot-pressure necessary to assist the opening changes as a function of the load-induced pressure. Whilst this can be beneficial to control stability in cylinder applications, it is often less beneficial in motor applications. In addition, the valve does not have a safe mode of failure in the unlikely event of a failure in the bias spring. The load-induced pressure would force the valve open and the load would fall. This lack of a safe mode of failure is increasingly becoming a selling difficulty in markets with more stringent safety regulations.

In an effort to improve functionality of counterbalance valves, a new load control valve was designed. The new load control valve was designed to be insensitive to load induced pressure. The insensitivity to load induced pressure makes the load control valve ideally suited for motor applications but not as well suited for cylinder applications. Cylinder applications typically require the feedback that the sensitivity to load induced pressure provides for system stability. This is typically not the case with motor applications.

Because the load control valve was designed primarily for motor applications and because it does not work as a relief valve, the manufacturer has avoided calling it a counterbalance valve. Sun Hydraulics has preferred to differentiate the new valve from its line of counterbalance valves by calling it a *load control valve*.

The load control valve has the added benefit of the flexibility to tailor the 'flow-gain' to specific applications by changing the hole pattern in the metering sleeve. The series of cross-holes, arranged in a helical pattern, were designed to limit flow forces acting upon the piston. If the helical pattern on the cylindrical sleeve were mapped onto a flat sheet, the holes would appear like the pattern in Figure 1.2. The top, horizontal line in Figure 1.2 represents the extreme, full open position for the piston while the bottom, horizontal line represents the closed position.

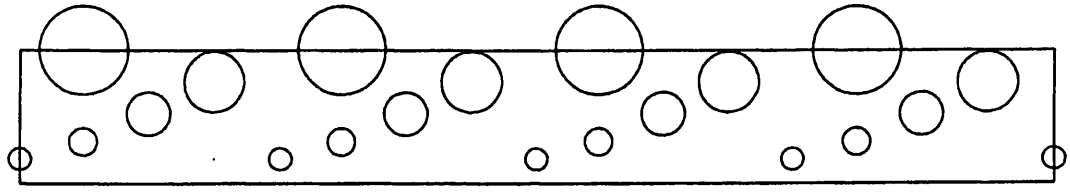

Figure 1.2 Hole pattern of load control valve in a 2-D layout

Excavators are an example of a specific market where the flexibility in flow gain has been applied. These machines often see extra duty beyond their original earth moving design intent. They are often used as small, mobile cranes. Safety legislation now often mandates that equipment that has this dual use must have the appropriate safe modes of failure. For excavators used as cranes, hose break protection must be included. The flexibility of being

able to tailor the flow gain of the valve allows the addition of a load holding valve but without having to redesign the control strategy of the machine. The flow gain on the load control valve can be tailored to avoid conflict with the operator's controls whilst providing the safety protection. If the pilot signal is lost because of a hose break for example, the valve will close to prevent a load from falling.

The new design, shown in cross-section in Figure 1.3, was also produced to have a safe mode of failure in the unlikely event that the *bias springs* break. This is accomplished by sensing the load-induced pressure in the spring chamber where the differential area of the *piston* is slightly larger than the differential area at the *seat*. A small axial drilling through the length of the piston connects the spring chamber hydraulically to the load port. The result is that in the event of a bias spring failure, the load-induced pressure would cause the piston to move to a closed position instead of an open position as in the traditional design.

Just as with the traditional counterbalance valve, the load control valve has two distinct modes of operation. The *poppet* acts as a free-flow check valve between the *valve port* and *load port*. When extending an actuator for example, flow would pass from the directional control valve to the valve port and through the larger holes near the o-ring gland. Once the pressure force in the valve port is sufficient to overcome the spring force that keeps

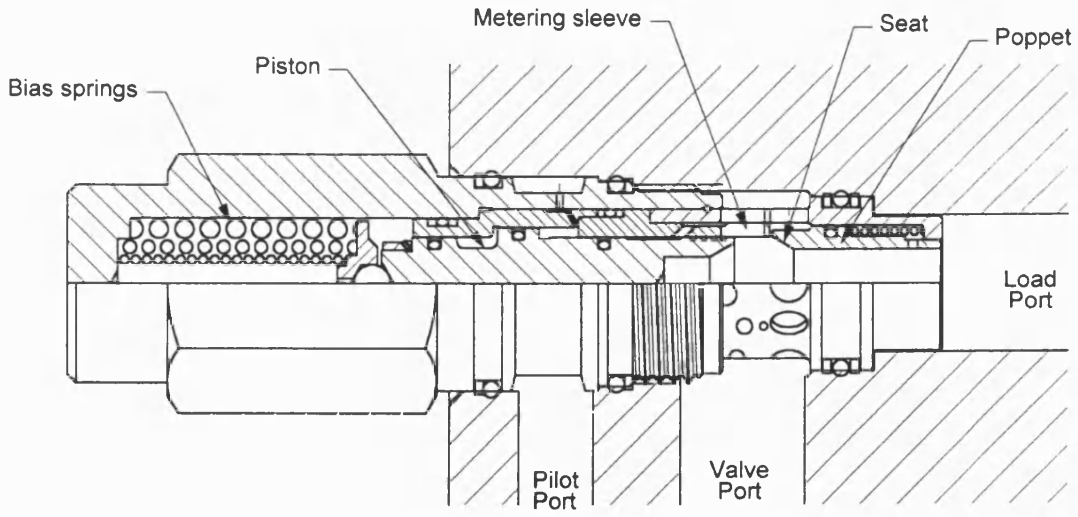

Figure 1.3 Cross-section of Sun Hydraulics model MBEM XMN load control valve (shown in the open position)

the poppet closed against the piston, the poppet would move toward the load port, further compressing the spring. This opens a path for oil to flow from the valve port to the load port and on to the actuator. This is the 'free-flow' operation of the check valve. Once the directional control valve is switched to discontinue the extension of the actuator, for example, the pressure in the valve port would be less than the pressure in the load port. The poppet would move to close the valve because of the spring force and the pressure force in the load port. This is the 'check valve' operation.

The second mode of operation for the load control valve is the 'metering' mode. This mode would occur when retracting an actuator, for example. The metering mode allows for the smooth, positive control of overrunning load that would be for example the boom on a crane or the load at the end of the winch cable. Unlike the traditional counterbalance valve, the load control does use pilot-assist but not the load-induced pressure to open the valve to meter flow from an actuator. The load control valve only works in the metering mode when a pilot signal is applied. To meter flow through the load control valve from the load port to the valve port, pilot pressure is applied to the *pilot port*. When the pressure force of the pilot signal is sufficient to overcome the spring force of the *bias springs*, the *piston* will move toward the spring chamber, further compressing the pre-compressed springs and opening the valve. As the piston moves, it uncovers multiple series of drilled cross-holes in the *metering sleeve*. By increasing the pilot-pressure, the flow rate through the valve increases and conversely, reducing the pilot-pressure reduces the flow rate through the valve.

As was mentioned in the brief description of the traditional counterbalance valve, as the load induced pressure changes, the pilot pressure required to open the valve changes. Conversely, as mentioned in the description for the load control valve, the pilot pressure is independent of the load-induced pressure and is determined by the force of the pre-compressed springs. This is shown graphically in the 'pilot-modulation' performance curves in Figure 1.4. The performance curves show that with 69, 138, and 207 bar (1000, 2000, and

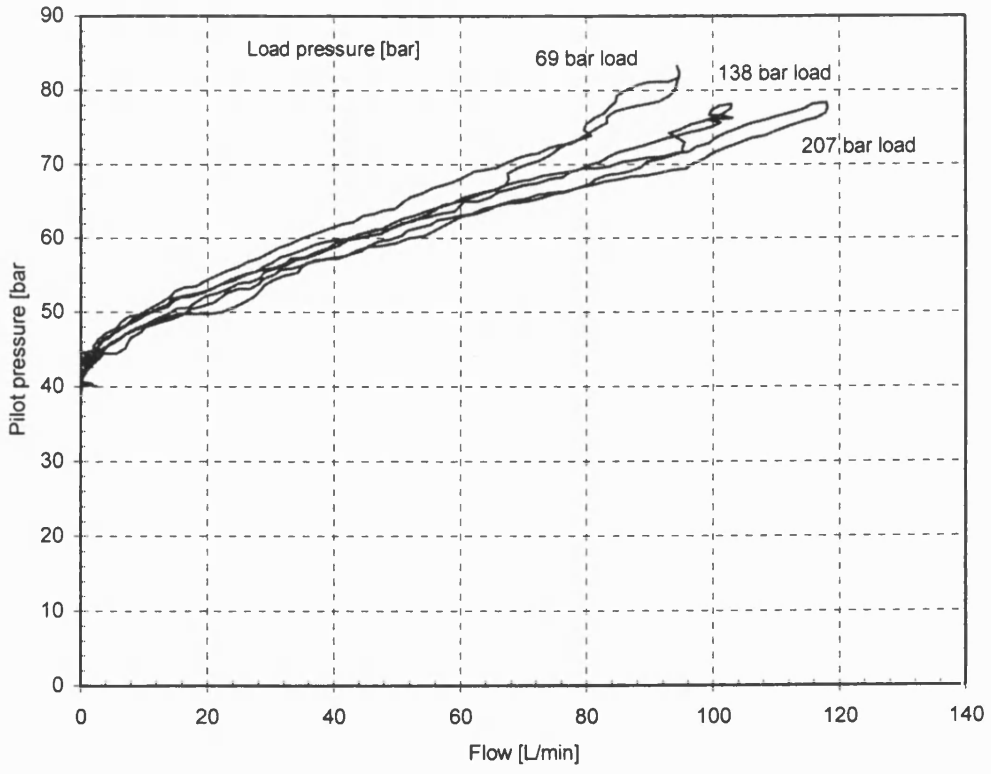

Figure 1.4 Pilot modulation performance curves for the MBEM XMN load control valve

3000 psi) load pressure, the pilot pressure required to open the valve remains constant.

When field trials of the new load control valve were conducted, the results were mixed. In some applications, the valve improved system stability while in others it contributed to system instability. System stability seems to be related to the tendency of the load control valve to 'pressure compensate'. When the pilot pressure is fixed and the load-induced pressure varies, the load control valve demonstrates the tendency to pressure compensate. This mode of operation would occur in field applications when changing the angle of a crane boom or when retrieving fishing nets with a winch on a commercial fishing boat, for example. Pressure compensation is shown graphically in the performance curves in Figure 1.5.

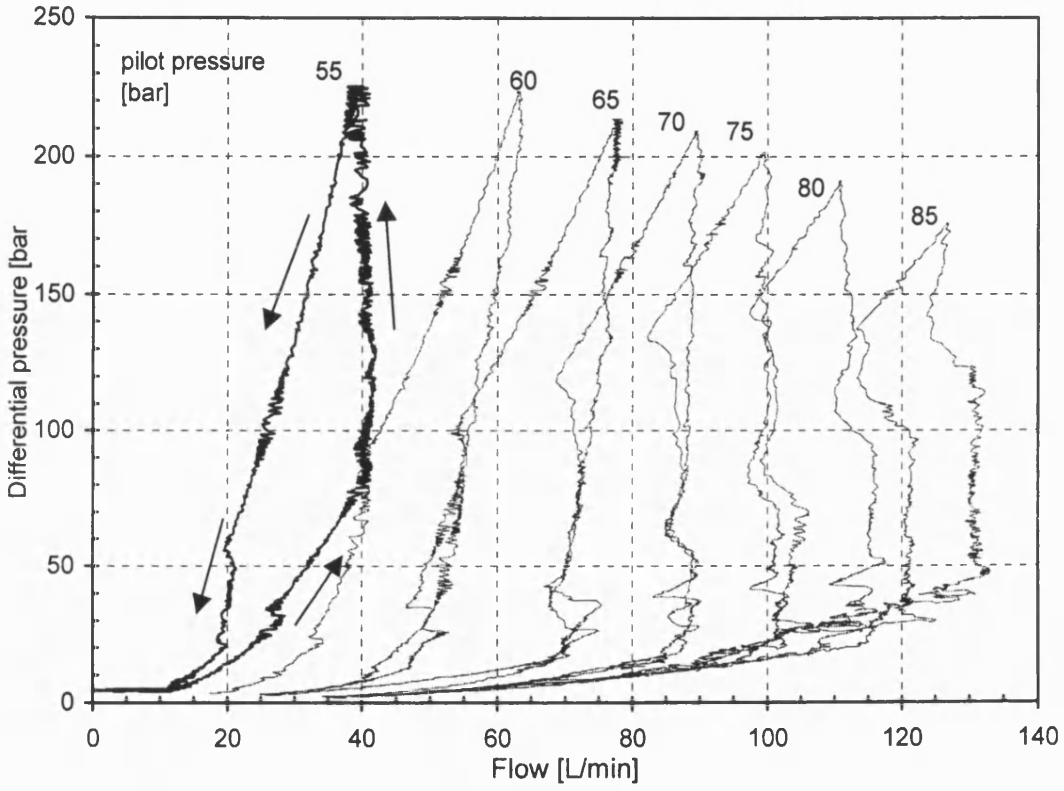

Figure 1.5 MBEM XMN pressure compensation performance

The curve highlighted and annotated with arrows, 55 bar pilot pressure, shows that the hysteresis loop was created in a counter-clockwise fashion. This is true for all of the curves on the graph for the different pilot pressures. Using the annotated curve as a guide, the piston is initially moved, and the valve performs with a fixed orifice pressure-flow characteristic. The region of the curve from 0 to 80 bar pressure and 0 to 40 L/min flow shows this. As the load pressure continues to increase, the flow forces overcome the friction present within the valve and cause the piston to move, partially closing the valve. This is pressure compensation and can be seen as the nearly vertical line at 40 L/min on the graph. The load pressure is reduced as a part of the experimental procedure once the maximum pressure has been reached. Again, the valve exhibits a fixed orifice pressure-flow

characteristic. The region of the curve from 40 L/min flow and 225 bar pressure to 20 L/min and 60 bar pressure shows this. Friction has again prevented the piston from moving. As the flow reduces, the flow forces also decrease to a point when the piston is able to move to open because of the pilot pressure force. The piston moves to open the valve again exhibiting pressure compensation characteristics. This is the nearly vertical line at 20 L/min on the graph. At about 20 bar, the piston stops moving and again displays fixed orifice pressure-flow characteristics.

As a result of the studies described later in this thesis, friction in the range of 20 to 25 N was found to be the primary contributor to the large hysteresis loops present in the curves in Figure 1.5. The three o-ring energised glyd rings on the piston are the primary source of friction. Friction would also be caused if the piston became eccentric to the three guiding diameters. Piston movement with steel-on-steel contact would result.

As the results from the field trials suggest, pressure compensation in some systems aids system instability while it contributes to instability in other systems. Instability is believed to be primarily the result of hysteresis in the pressure compensation performance. Instability is typically seen in systems where the load changes during equipment operation. An example where this has occurred in a field trial of the load control valve is in the winch control circuit for spooling out and retrieving the nets on a fishing boat. As the net is being spooled out or hauled into the boat, the winch motor was observed to be 'surging'. That is to say that the motor speed would increase and then decrease repeatedly during the operation to retrieve the nets. The load control valve was blamed for this instability. When a counterbalance valve was substituted for the load control valve, the instability problem was solved.

A possible explanation to the cause of the instability encountered in the fishing boat application of the load control valve can be deduced from the symptoms of the instability described by the application engineer **(Hydropower A/S 1999)**. As the winch is turning to either spool out or retrieve the net, the load on the winch increases with the drag of the net moving through the water. As the load increases, the load-induced pressure would increase. This is comparable with the differential pressure seen on ordinate of the graph of performance curves in Figure 1.5. As the pressure increases, the flow rate from the pump decreases. As the flow rate decreases, the hysteresis band in the performance graph of the load control valve would develop and the winch speed may decrease. If the winch speed decreased, the load-induced pressure would drop and then the flow rate would increase. This not only would close the hysteresis loop in the performance of the load control valve, but also would allow the winch speed to increase. The cycle would repeat and it would be observed as surging in the winch.

A 'load reactive' or relieving model of the load control valve was designed to overcome system stability problems reported in some field applications. This model is very similar to the original design of the load control valve, but without the seals. Sealing between the different areas of the piston is accomplished through a close, ground and honed fit (less than 1.3 μm or 0.000050 inch) between the piston and sleeves. Hence, the load reactive

model of the load control valve has much less friction affecting the movement of the piston. Therefore, the hysteresis observed in the valve is significantly reduced. This alternative design has been successfully applied to previously unstable systems. It can be surmised that because the difference in flow rate between the up-stroke and down-stroke of the performance curve (see Figure 1.5) has been reduced to approximately zero, a stable operating point is reached that the pump is capable of producing and the winch, for example, is capable of moving the load.

1.2 Problem description and methods and goals of the research

Even with a design alternative that exhibits less tendency to pressure compensate, the desire to understand why the load control valve pressure compensates still exists. Therefore, a programme of research was devised using four different investigative methods. Goals were set for each method used.

The first goal was to assess the working hypothesis that the jet angle and flow coefficient of the oil exiting the metering hole are not constant, but change as the hole coverage changes. **McCloy and Martin (1980)** stated in their book that as a circular hole is initially uncovered, the jet angle is 69°, but as the opening increases to the full opening the angle increases to 90°. Further, they exhibited two graphs that show that the discharge coefficient changes as the exit hole coverage changes. However, it is still commonplace to see fixed values for both the jet angle and flow coefficient quoted in literature. It is believed that the nature of the pressure compensation that the load control valve exhibits is due to changing flow forces which is due to changes in the jet angle and flow coefficient. In order to test this hypothesis, it was decided to use both flow visualisation and computational fluid dynamics (CFD). Defining how the jet angle and flow coefficient changed between the initial opening and full opening of the circular exit hole should enhance the work of McCloy and Martin. It was intended to use the CFD to quantify the jet angles and flow coefficient as hole opening changes. Flow visualisation was used to qualitatively verify the CFD results.

In order to quantify the performance characteristics of the load control valve as shown in Figures 1.4 and 1.5, a programme of laboratory experimentation was designed. The experimental programme was also used to measure the flow forces not only to demonstrate that they are changing but also to provide a basis for verification for mathematical modelling.

The ultimate goal of the research was to develop a thorough understanding of why the load control valve pressure compensates and to suggest methods to control it in order to improve it if possible. One method commonly used to demonstrate a proficient understanding of a dynamic system is mathematical modelling. Modelling permits simulations of a dynamic system to be conducted to predict performance. The dynamic system in the case of this research was the load control valve. Modelling can be especially useful when developing new designs. The design can be modelled and the results evaluated before machining of valve parts takes place.

Mathematical modelling was used in the current research to bring together the knowledge gained from the other research methods. Functions describing the changing jet angle and flow coefficient will be used to develop accurate, modelled performance curves that demonstrate pressure compensation within an acceptable level of error.

1.3 Organisation of the thesis

The thesis is organized into seven chapters. The subject of each chapter is discussed briefly below.

Chapter 2 is titled *Experimental work* and deals with the oil hydraulic experiments. In this chapter, the literature survey concerned with experimental methods and results is discussed. Additionally, two test apparatuses that are used on the test stand are discussed along with the experimental techniques and results.

Flow visualisation is the title for Chapter 3. The chapter begins with a brief literature survey of flow visualisation works that were primarily concerned with valves. The design of the rig that was constructed to conduct the flow visualisation experiments and the experimental technique used are discussed in detail. Results are presented and discussed.

In Chapter 4, titled *Computational fluid dynamics modelling*, the CFD modelling is discussed in detail. The chapter begins with a brief literature survey of CFD works primarily concerned with valves. As part of the discussion of the results of the CFD modelling, comparisons between the CFD results and flow visualisation results are made.

Chapter 5 is titled *Mathematical modelling* and also begins with a brief literature survey. In this chapter, the results from the flow visualisation experiments and CFD modelling are used in a Simulink model of the load control valve. The results obtained are compared to experimental results.

Evaluation of alternative designs is the title of Chapter 6. This chapter begins to demonstrate how the method used to investigate the performance characteristics of the load control valve can be used to investigate other hole shapes. The results of preliminary evaluation of alternative designs to the simple drilled exit holes used for metering the flow of oil from the load control valve are presented and discussed. The evaluations were limited to CFD modelling only because of time constraints.

In Chapter 7, titled *Conclusions and recommendations*, the author makes concluding remarks and recommendations for future work.

CHAPTER 2

EXPERIMENTAL WORK

2.1 Introduction

As part of developing an understanding of the performance of the load control valve, the performance must be quantified. To achieve this, experiments and experimental apparatuses must be designed to measure valve behaviour. Quantification of performance is the only way to determine if the mathematical model of the load control valve that will be presented in Chapter 5 satisfactorily predicts a correct valve performance.

2.2 Review of past work

Before designing the experimental test rigs, a review of past work was conducted in order to learn what equipment and techniques previous researchers have successfully employed. Of particular interest were papers that studied jet angles, flow coefficients, and performance in general of poppet type valves.

In the 1950's, several papers were published on the subject of flow characteristics of poppet valves. **Tidor (1954)** conducted a series of experiments using half of an axisymmetric, two-dimensional model of a valve that was scaled up twenty times. With this size, the inlet diameter was 22.2 mm (0.875 inch). The model was constructed with glass walls so that the flow patterns could be observed. Along with qualitative flow visualisation, quantitative pressure measurements were made with mercury manometers. Eleven manometers were used, with three along the lapped seat surface and five along the poppet surface. Because of both the use of manometers for pressure measurement and the use of glass for wall material, the maximum working pressure was limited to 3 bar (45 psi). The working fluid in the model was Esso Univis 40 hydraulic oil. Air was injected through a 0.30 mm (0.012 inch) hypodermic needle to seed the flow with bubbles for the flow visualisation. The use of a Polaroid camera to document the flow patterns failed because of lighting problems. Several observations were noted by the author, among them that the pressure distribution in the seat area was sensitive to the exhaust pressure in the downstream area. The author also noted that bubbles possibly from cavitation were observed. No conclusions

were drawn as to the effects on the valve performance. Numerous suggestions were made by the author for future work obviously with the feeling that his work left many unanswered questions. The author even comments that, "The flow in a valve cannot be adequately described without further investigation."

Stone (1954) describes the design, building, and calibration of an apparatus to measure flow forces in poppet valves. Theoretical analysis was also conducted. Through the analysis, a series of complex equations that relied upon conformal mapping and Bessel functions to solve were developed. Conformal mapping is a linear transformation used in solving complex vector equations. The theoretical analysis was based upon the assumptions that the flow was steady and neglecting both viscous friction and gravity. Neither experimental nor theoretical results were presented. Because the viscous friction was ignored in the theoretical analysis, the author stated that the experimental results would not agree well with the theory at low valve openings. This is because the boundary layer is a proportionally larger part of the flow at small valve openings and hence low flow conditions.

Stone (1957) extended his previous work by modifying the test apparatus and measuring the discharge coefficient and flow forces in poppet valves of various shapes. The shapes included a 45° cone, a 45° cone with flow force compensation, a 45° sphere, and a 30° cone. The test fluid was a mixture of Esso Univis 40 and J43 oils. The tests were conducted at pressures ranging from 34.5 bar (500 psi) to 138 bar (2000 psi) and temperatures from 29°C (85°F) at low pressure to 49°C (120°F) at high pressure. The author noted that during some tests when oil was exhausting into oil through the valve, the poppet was unsteady and oscillated at a frequency of 1300 Hz. Also noted was the observation of the release of air bubbles in the low-pressure region beneath the poppet. Finally, the observation of the Coanda effect at small openings and with low fluid momentum was noted. Theoretical analysis was conducted on a control volume around the poppet and seat. The analysis assumed an "ideal poppet valve" where the fluid was incompressible, inviscid, and irrotational. Three of the scenarios considered were for the fluid exhausting into air, exhausting into a finite chamber, and exhausting into a real fluid. The flow force predictions were 20% below the measured values when using the theoretical values for the discharge coefficient, c_d, but only 10% below when using the experimentally determined values for c_d. This was attributed to the viscous effects. The author noted that a better understanding of the discharge coefficient is needed to understand the scatter in the results and why the results differed from other researchers. The author did not explain this, but one could surmise that viscous effects would be one cause particularly with the changes in viscosity with temperature. From the analysis, a flow force compensated poppet was developed and tested in the experimental portion of the work and is shown in Figure 2.1. The poppet design was based upon force working upon equal areas. This proved to be relatively successful. **Stone (1960)** is a journal article based upon the author's 1957 thesis.

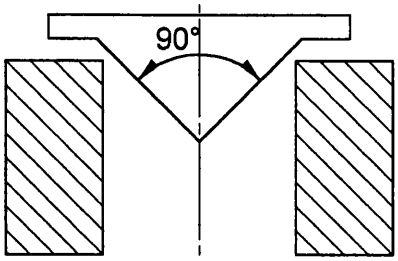

Figure 2.1 Stone (1957) flow force compensated poppet

The work by **Stone (1954, 1957,** and **1960)** demonstrated not only the difficulties in measuring flow forces, but also the difficulties in measuring discharge coefficients. However, even with the difficulties encountered, a flow force compensated design was developed. Hence, the articles are useful references for developing a flow force measurement tool and in trying to understand the effects that discharge coefficients have on flow forces.

Several more papers were prepared in the 1960's from various authors looking at spool, poppet, and disc valves. **Oki (1961)** and **Oki and Kawakami (1961)** are two papers in a series of articles dating back to 1921 that presented the results of research on disc valves. In Oki (1961), results from experiments conducted using water under a constant head of 1.9 m (74.8 in) discharging through a disc valve into air were analysed. The same apparatus was used in Oki and Kawakami (1961) but the diameter ratio between the disc and the valve throat was larger. A variety of valves with different diameter ratios were tested. One of the important conclusions of this work was that flow separation adds hysteresis and uncertainty to the measurements of flow with respect to valve opening. The work in these two papers did reinforce some of the conclusions of Schrenk (1957) (ff. Section 3.2). There was no mention of cavitation but then considering that the work was conducted with a relatively low head, cavitation could not have been much of an issue. Usefulness of this work is questionable when applied to valves in hydraulic systems because of the experimental apparatus and technique of discharging the water test fluid into air.

McCloy and McGuigan (1964) used the results of Schrenk (1957), von Mises (1917), Tidor (1954), Stone (1954, 1957, and 1960), and Tuffias (1957) primarily to develop an understanding of how flow forces, discharge coefficient, Reynolds number, seat geometry, valve height (lift), pressure drop, and flow rate all interact and indicate valve performance under both steady and non-steady flow conditions. One test rig was a two-dimensional, low-pressure valve that had twelve pressure taps strategically located on the poppet along the controlling surface and immediately downstream of the controlling surface. These taps were plumbed to manometers for pressure measurement. Flow forces were calculated by integrating the measured pressures over the surface area of the poppet. The downstream cavity was adjustable in volume, but the exit port remained the same for all experiments. A second, three dimensional, high-pressure, test rig was constructed to

determine if the results observed at low pressures would be the same at high pressure. This rig was later modified to oscillate the poppet to simulate the effects of non-steady flow. Tests were conducted at frequencies of 20 to 120 Hz at 20 Hz increments. Frequencies lower than 20 Hz were not experimented with because of limitations in the rig. From the experimental and analytical work, the authors found that different flow patterns exist in the valves that can affect the flow forces. They were only able to reproduce three of the five distinctive patterns of a previous researcher (ff. Schrenk 1957, section 3.2). Schrenk produced flow patterns A through E, as shown in Figure 2.2 below, but McCloy and McGuigan were only able to reproduce patterns A, B, and E which they called types I, II, and III, respectively. This was attributed to the different experimental techniques employed. Schrenk conducted his experiments with water discharging into air while McCloy and McGuigan conducted their experiments with water discharging into a down stream chamber. They conducted experiments with different size down stream chambers that were either full of air or full of water. Additionally, it was found that different seat geometries have a profound effect on flow characteristics by creating a great deal more scatter in the results. Four different geometries, sharp, radiused, and two different chamfered seats were used in the experiments.

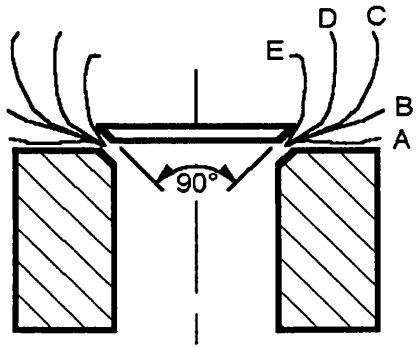

Figure 2.2 Schrenk (1957) flow patterns

There were several important conclusions from McCloy and McGuigan (1964). The first was that the flow was not fully turbulent in the valve of this design until the Reynolds number was greater than 10^4. Secondly the existence of different flow patterns such as those demonstrated by Schrenk (1957) was verified and it was found that type I (Schrenk's type A) flow induced the strongest flow forces. It was demonstrated that flow forces are strongly dependent upon the down stream chamber size. As the chamber decreases, the flow forces decrease because of recirculating flow. Thirdly, the authors developed the empirical conclusion that there was an optimum seat shape and geometry. Discharge coefficient is very sensitive to seat geometry and hence prediction of valve performance for different geometries is very difficult. Finally, it was demonstrated that changes in pressure rate (oscillations) causes changes in discharge coefficient. Negative rates decrease the

discharge coefficient and conversely positive rates increase the discharge coefficient. Although cavitation was mentioned in the introduction of the paper as an area that affects valve performance, none of the work included cavitation. Overall, this is a sound and fundamental paper.

Takenaka *et al.* (1964) analysed disc valves theoretically and experimentally. In the theoretical analysis, the authors made a number of assumptions. They assumed the flow was parabolic in shape at the seat. Since most hydraulic systems operate in a turbulent flow regime particularly in the seat areas of valves, a parabolic shape typical of laminar flow would be very unusual. As **Johnston *et al.* (1991)** (ff. Section 3.2) comments, **Takenaka *et al.* (1964)** ignored the effect of separation of the jet from the seat. This may have been justified with the geometry studied but this made the research less general in its application. However, considering the difficulties associated with modelling such phenomenon mathematically at the time, the current modern analysis tools may eliminate this deficiency. Water under a constant head was the working fluid for the experimental work. The experimental and analytical results did not agree very well. The thrust was over-predicted for smaller openings but was much closer for larger openings for the valve with the disc diameter to throat diameter ratio of 1.5. For the diameter ratio of 2.5, the calculated thrust was again over-predicted. The calculated results for the diameter ratio of 3.0 were much worse when compared to the experimental results. The values for thrust were over-predicted and in the wrong direction. There was no mention of cavitation or its effects.

Urata (1969) is a paper often cited in other works dealing with flow forces in poppet style valves. It is a comprehensive paper covering the thrust of conical valves with both sharp and lapped seats. The study first analysed theoretically and then experimentally the flow through poppet valves. The study dealt with both laminar and turbulent flow. The Reynolds numbers cited for the case of laminar flow was 1010 and the Reynolds number cited for the turbulent flow cases was 5880. Flow visualisation using dye injection was used to develop a qualitative understanding of how the flow behaves going through the valve opening. A two dimensional model was used which had an inlet diameter of 30 mm (1.18 in). The author stated that the validity of the results from the two dimensional model was limited. Thrust or lift forces were quantitatively measured using a cantilevered beam and strain gauges. Both oil and water were used in the experiments. There was an interesting note in the discussion of the flow visualisation results. It was noted that at high Reynolds number, the flow was often pressed against the wall of the valve seat. This was attributed to a Coanda effect. The geometry of the downstream chamber and the port of efflux influence the Coanda effect. The theoretical analysis was conducted by applying boundary layer theory on a fluid that was assumed incompressible and without cavitation. Separate derivations were carried out for the laminar and turbulent flow regimes. The theoretical and experimental results agreed well in the laminar and turbulent flow regimes with small deviations. Where the most error can be observed would be in a transitional flow regime between laminar and turbulent flows. This would not be unexpected since the theoretical

analysis was conducted in laminar and turbulent flow regimes. In addition, the transitional flow regime is a generally accepted area of little knowledge in fluid dynamics.

2.3 Oil hydraulics test stand and test rigs

Review of previous published work showed that often the experimental work was carried out on scaled-up valves, which were often just two-dimensional models. Generally, the working fluid was relatively low-pressure oil but water at low pressure was also used. Studies involving discharge coefficient often cite valve seat and poppet geometry sensitivity in order to explain discrepancies between experimental and theoretical results. Using a true production valve in the current project avoided this problem. The experimental programme was developed around the use of production valves and making measurements of pressures and flows through the valve as well as forces on the piston. Although a scaled-up version of the load control valve may have made it possible to instrument the metering edge of the valve piston to measure local pressure distributions, the scaled-up flow rates to maintain similarity were not possible from the ring main system that was used for the source of high-pressure oil.

The oil hydraulics test stand including the pressure transducers and flow meter was designed around the use of production valves for the experimental programme. Two separate measurement tools were developed for use on the oil hydraulics stand. The first was a flow force measurement apparatus and the second was a LVDT installed on the valve to measure valve opening. The design of the oil hydraulics stand, the experimental procedures used, the flow force measurement apparatus, and the LVDT assembly will be discussed in the following sections

The testing relied upon high-pressure hydraulic oil provided by a positive displacement pump that provided fluid to the laboratory ring main system. A hydraulic circuit upstream from the test specimen controlled the pressure and flow. Figure 2.3 shows the hydraulic schematic of the test circuit adopted including transducer locations. The ring main system is constructed almost entirely of pipe, but the test stand was plumbed with hoses. Beyond the *ball valve* and connections to the ring main system, the circuit was constructed entirely of cartridge valves in line mount bodies. The oil that branches off the main flow in the tee (***A***) forms the pilot pressure. This oil is first directed to the *needle valve* (***B***) and then a *pressure-reducing valve* (***C***). The needle valve was used to turn the pilot signal on or off depending upon the test. The pressure-reducing valve controls the pilot pressure. After the pressure-reducing valve, the oil goes to the pilot port of the valve undergoing test (***D***). The oil flowing through the tee (***A***) forms the main branch. This oil flow is directed to a *pressure-reducing valve* (***E***). From there, the oil goes to a *flow control valve* (***F***). These two valves allow the inlet pressure and flow to the test valve to be controlled. The oil then flows through the valve being tested (***D***). A *pressure relief valve* (***G***) controls the outlet pressure of this valve. This is used to emulate the backpressure arising from the

long lengths of plumbing that would normally be found on actual equipment. The valve can be adjusted over a large range of pressures to simulate a variety of backpressures. After passing through a *flow meter* (*H*), the oil flows back to the system reservoir via the ring main system plumbing. *Pressure transducers* (*PT*) are located at the inlet and outlet of the test specimen. Quick release couplings were used to make the connections to the circuit so that the pressure transducers could be moved to different locations depending upon requirements. A coupling was located at the pilot pressure inlet port on the test specimen so that pilot pressures could be measured when needed.

A National Instruments (Austin, Texas, USA) analogue to digital converter card model DAQCARD-AI-16E-4 was used to sample the transducer signals. Proprietary data acquisition software developed at Sun Hydraulics Corporation using National Instruments *Lab View* software was used to control the data acquisition card. The card was a PCMCIA style and was installed in a Dell Inspiron lap top computer. The computer had an Intel Pentium II 366 MHz processor and 256 megabytes of RAM. Transducers were wired and sampled in a differential mode to minimise the effects of electromagnetic noise. The card has eight channels for input when used in a differential mode or sixteen channels in a single end (referenced or non-referenced) mode. Special care was taken in wiring the data acquisition terminal board because of the floating electrical ground that the laptop computer uses. The maximum theoretical sampling rate for multiple channels is 250 kHz but the rate used was 100 kHz. This rate allowed for very fine resolution in data point sampling but still allowed for very nearly real time display of the data on the video display. Decimation is a technique employed within the data acquisition system to limit file size. This technique compares adjacent data points after sampling is complete and if their values are within the specified range, it strips out the superfluous data points. The range or decimation factor used was 0.8%.

The experimental procedure employed for pressure-compensation performance testing first required that the pilot-pressure be set. This was accomplished by opening the ball valve and needle valve. The pressure-reducing valve downstream of the needle valve was then adjusted to the desired pressure. The experiments were carried out with pilot pressures in the range of 45 to 85 bar with five bar increments between successive tests. With the pilot pressure set, the ball valve closed, and the main pressure-reducing valve at its lowest setting, the data acquisition system was set to simultaneously record the signals from the inlet and outlet pressure transducers and the signal from the flow meter. The ball valve was then opened and the pressure-reducing valve adjust screw was slowly turned clockwise. Once either the full travel of the adjust screw was reached or the maximum flow and inlet pressure were achieved for the pilot-pressure selected, the direction of the adjust screw was reversed by turning it counter clockwise. The time to cycle through the entire range for an individual test was approximately one and a half to two minutes. The maximum adjustment for the adjust screw in one direction is 5.5 turns and the maximum stroke is 5.5 mm (0.216 in).

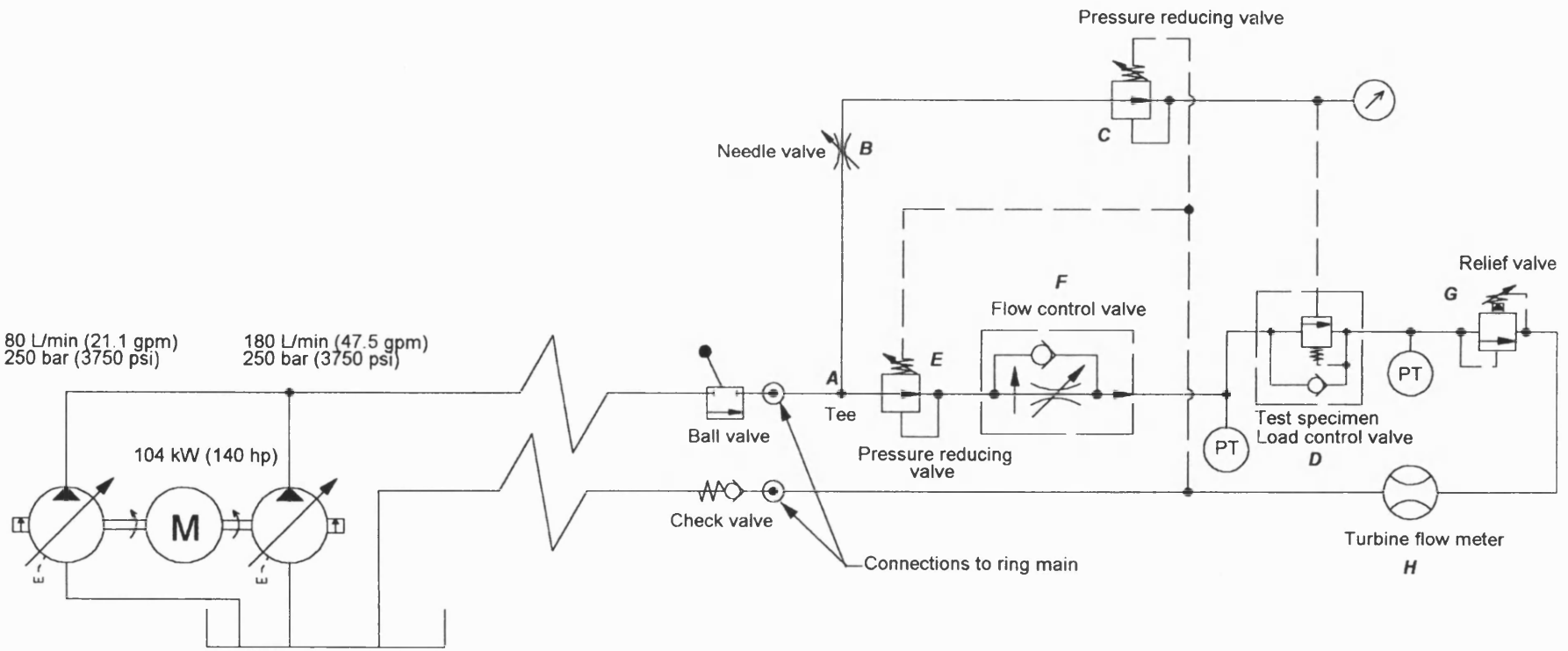

Figure 2.3 Oil hydraulic test stand schematic

A sample of typical results is shown below in Figure 2.4, which is a reproduction of Figure 1.5. As previously explained in Chapter 1, considering the annotated 55 bar pilot pressure curve, the piston is stroked to an initial opening by the pilot pressure action on the area of the pilot section. The initial performance is a fixed-orifice pressure-flow characteristic curve. As the load pressure increases, the flow forces cause the piston to move, partially closing the valve. This is pressure compensation, as will be recalled from the explanation in Chapter 1. After reaching the maximum load pressure, the load pressure is decreased but again the valve exhibits a fixed-orifice pressure-flow characteristic. Once the flow forces have reduced enough, the piston moves to open the valve in a pressure-compensating manner. The final portion of the curves is again fixed-orifice pressure-flow curves. Reviewing the remaining six curves on the graph shows that similar effects are apparent for the higher pilot pressures.

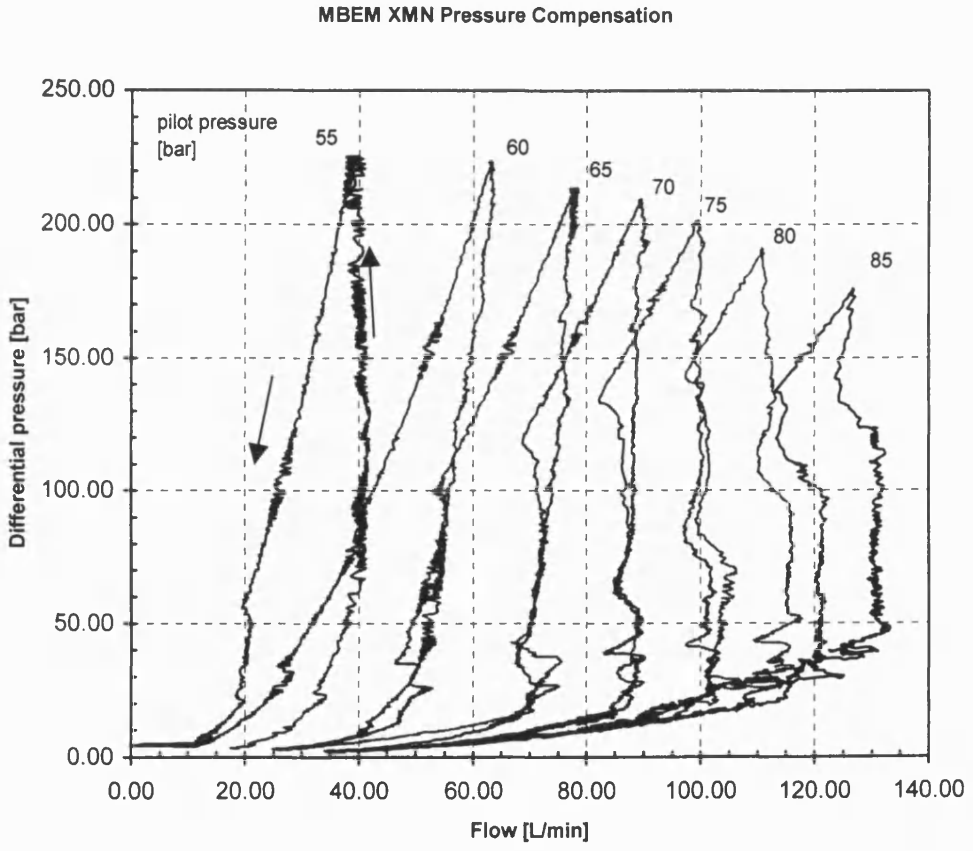

Figure 2.4 Pressure compensation performance curves for seven pilot pressures

Pilot modulation performance measurements results are shown in Figure 2.5. Pilot modulation was measured by first setting the main pressure-reducing valve to a predetermined value. The values used for the experiments were 50, 75, and 100 bar (725, 1088, and 1450 psi). With the load pressure set, the ball valve closed, the needle valve open, and the pilot pressure reducing valve at a minimum setting, the data acquisition system was

set to record the flow rate and pilot pressure. With the ball valve open, the pilot pressure-reducing valve was slowly adjusted to increase pressure. This was accomplished by slowly turning the adjust screw clockwise. The maximum number of turns was 5.5. Once the limit of the adjustment was reached or the limit of pressure and flow for the test stand with the set load pressure were reached, the adjustment on the pilot pressure-reducing valve was reversed. The pressure was lowered by slowly turning the adjust screw counter clockwise. Cycle time for the test was approximately one minute. The experiment was repeated for the successive load pressures.

While pilot modulation was not the area of emphasis of the research, these tests give a more complete picture of the valve performance and provide a measure of the performance, as it would be used in a field application. It clearly demonstrates one of the primary design specifications of an opening pressure independent of the load pressure. The opening pressure is determined by the pre-compression of the primary springs. The nearly linear performance that is similar between the three performance curves is due to the compression of the bias springs and pressures acting on fixed areas. This was also part of the design specification. Hysteresis, the difference between the increasing and decreasing pressure for

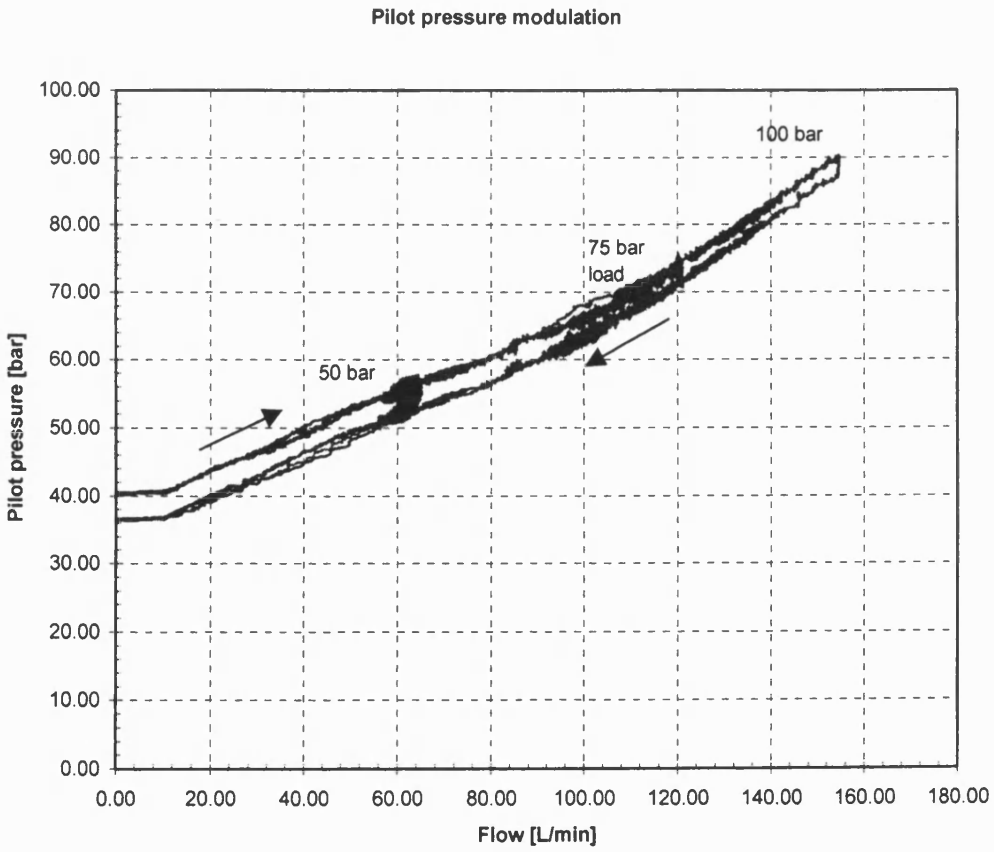

Figure 2.5 Pilot pressure modulation performance curves for three load pressures

the same flow rate, is apparent on the graph. Friction due to the three o-ring energised glyd rings was found to be the primary cause of the hysteresis that is shown in the performance curves. However, as **Oki (1961)** and **Oki and Kawakami (1961)** noted that flow separation adds hysteresis. Flow separation is occurring at the edge of the piston as it uncovers the metering holes. This will be shown in Chapters 3 and 4. Thus, a portion of the hysteresis that is evident in the performance curves is probably a result of flow separation.

2.4 Flow force measurement apparatus

The flow force measurement apparatus described below was adapted from a design by Dr. Jonathan Gamble, formerly of Sun Hydraulics Corporation. It was designed for use in the development of a valve unrelated to the load control valve. Similar designs have been presented in literature **(Nakano *et al.* 1992)**. As stated earlier, one aspect of the experimental work was to measure flow forces in order to make comparisons with the mathematically modelled valve.

A drawing of the flow force test rig is shown in Figure 2.6. The main part is the *pressure tube*. This has an *adapter* at one end that is threaded to match the cartridge valve interface. The other end is plugged. The bore is honed to allow a close fitting *spool* to slide freely. There is an axial slot through the pressure tube that allows access to the outside of the spool. A length of 2 mm diameter threaded rod connects the spool to the valve components under test. A drilling in the end of the spool communicates pressure from the adapter end of the tube to the closed end. Thus, the spool is pressure balanced. The adapter end of the tube has a larger outside diameter and is threaded with a 10-tpi acme thread. A bearing surface for the sleeve was created by grinding the outside diameter of the tube. A key prevents rotation of the sleeve relative to the tube. The front end of the sleeve is threaded with a 16-tpi acme thread. A *collar*, which has two internal acme threads; one 16-tpi and the other 10-tpi, connect the tube and sleeve. Rotating the collar by means of the *handles* will cause the sleeve to slide relative to the tube, with an effective pitch of 26.7-tpi (the reciprocal of the difference of the pitches). The large diameter end of the sleeve is closed using an *end plate* to which is attached one end of the *load cell*. The other end of the load cell is attached to a cross member which in turn is linked via two *tie rods*. The other ends of the tie rods pass through two axial slots in the sleeve and are attached to the two halves of a *split ring* which clamps around the small outside diameter of the spool. There is clearance between the outside of the sleeve and the inside of the split ring. The two halves of the ring each have a finger, which extends inwards to locate into a groove on the outside of the spool. The split ring, connecting rods and *cross member* form a load frame which transfers axial force from the spool to the load cell without touching either the pressure tube or the sleeve. This and the absence of any elastomeric seals help to reduce friction and hysteresis. There is a Linear Variable Differential Transformer (LVDT) (not shown), which is

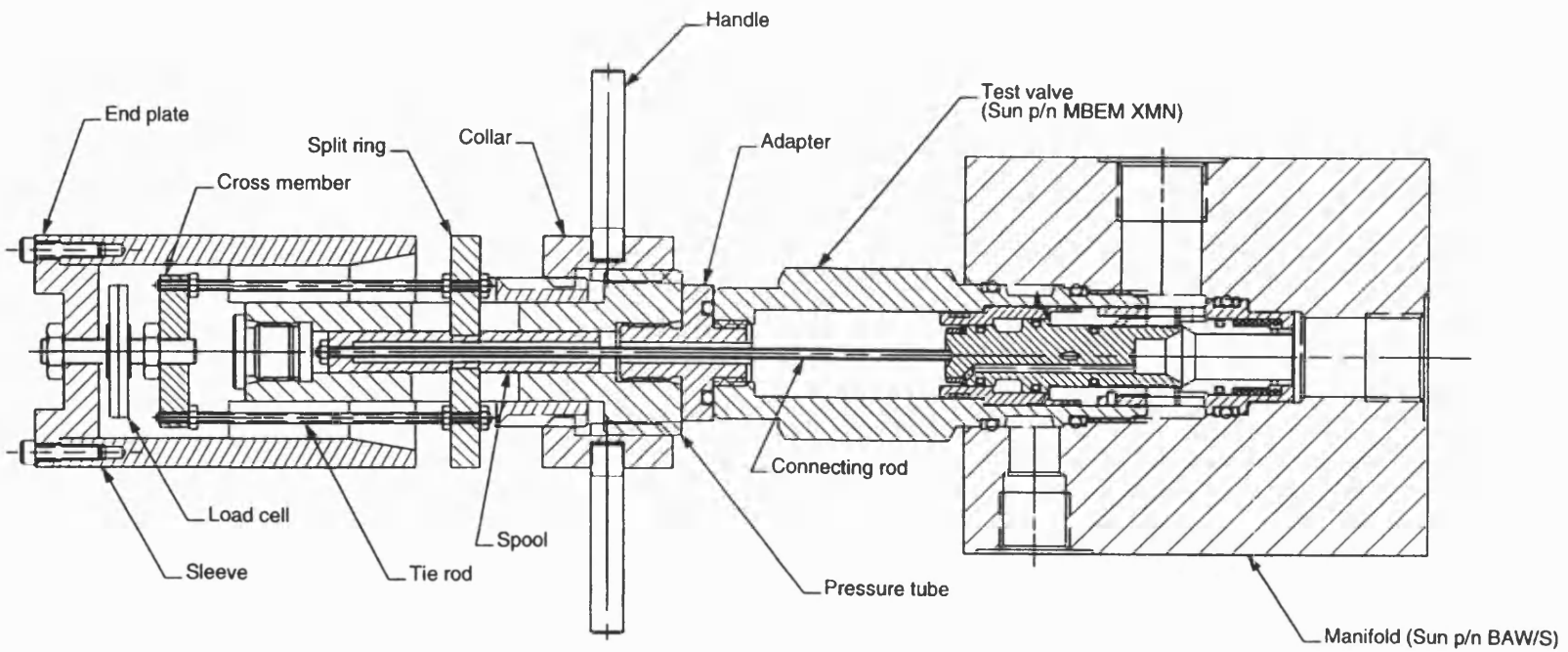

Figure 2.6 Flow force measurement apparatus

attached to the end plate. The LVDT rod extends towards the handle, and contacts a bracket (also not shown) that passes through a slot in the sleeve to attach to the pressure tube. The bracket actually forms the key preventing relative rotation of the sleeve and pressure tube. The LVDT thus measures relative movement between the sleeve and tube. Unfortunately, any compliance in the load cell causes an error in the measurement, but the Entran piezo resistive sensor is very stiff so these errors should be very small. The catalogue-listed deflection at full scale is less than 0.013 mm (0.0005 in). The accuracy of the load cell is defined by the manufacturer as the combined non-linearity hysteresis of the device. When plotted as voltage output against load, a composite error band is formed. The difference between the error band and a theoretical straight line is defined as the maximum error.

With the design of the flow force measurement apparatus, it was not possible to make dynamic measurements. The valve was actuated (opened and closed) by turning the collar with the handles. While this could be done "quasi-dynamically," this mode of operation does not represent the true dynamic performance of the valve. The experimental procedure employed consisted of first setting the inlet pressure by adjusting the pressure-reducing valve immediately downstream of the ball valve. The needle valve was closed, as pilot pressure was not needed. With the test specimen starting from a closed position, the data acquisition system was set to record inlet and outlet pressure, flow rate, and valve opening data while the collar on the flow force measurement apparatus was slowly turned counter clockwise to open the MBEM valve. Once the full stroke of the valve had been reached, the collar was turned in the opposite direction (clockwise) to close the valve. An entire valve opening and closing cycle took approximately two minutes. The procedure was then repeated for a range of inlet pressures (100, 150, 200, and 250 bar). A sample of the results is shown in the graph in Figure 2.7.

The results in Figure 2.7 show that as the flow rate increases, the measured force also increases. This trend is consistent for the different inlet pressures used in the experiments. Considerable hysteresis is present in the measurements, which is primarily caused by friction. The combined effects of friction, pressure force, and flow force are measured by the flow force measurement apparatus; therefore, the force measured is not labelled flow force. The three different pressures act upon the surfaces areas of the valve piston are known as pressure force. Flow force is calculated by subtracting the pressure forces from the measured forces; however, this still leaves friction in the results. This will be discussed further in Section 2.6.

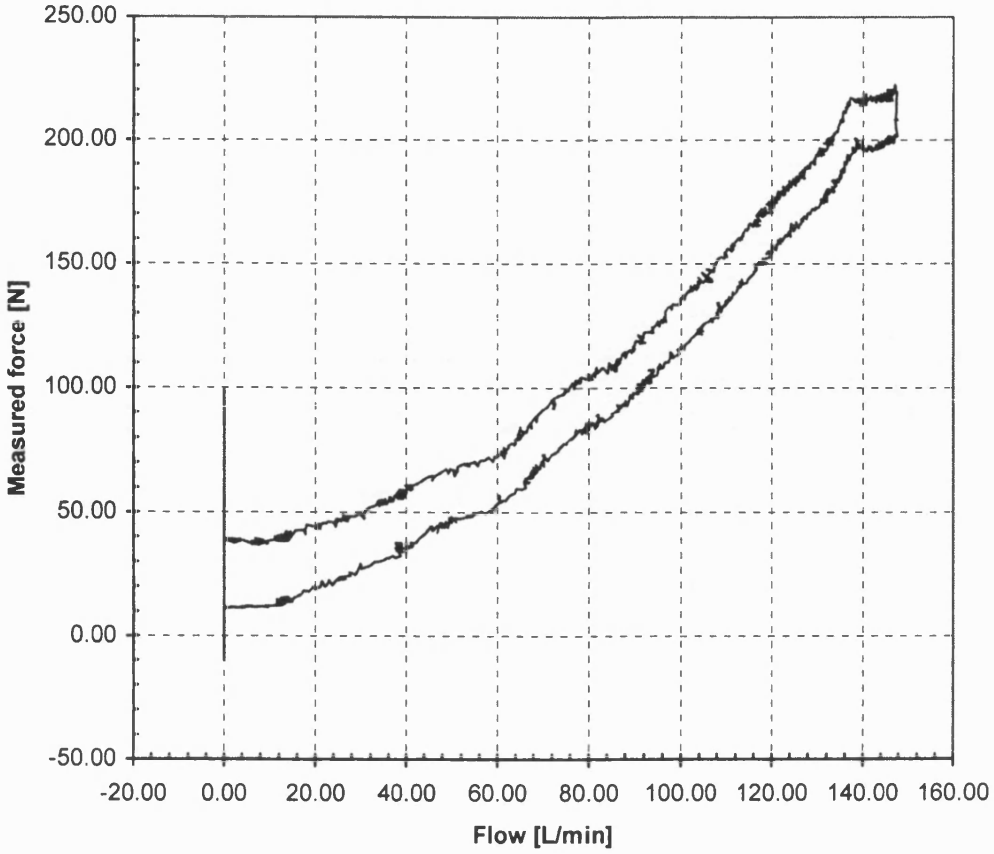

Figure 2.7 Sample of force measurements for 200 bar inlet pressure

2.5 Valve opening measurement test rig

A separate test apparatus was constructed for use on the oil hydraulics test bench to measure valve opening dynamically while the experimental procedure to measure pressure compensation is conducted. Although the flow force measurement apparatus had an LVDT attached, the apparatus was not capable of making measurements dynamically or while employing the procedure to measure pressure compensation performance. The new test rig was constructed by attaching a LVDT to the ball holder spring end of the valve as shown in the drawing in Figure 2.8. The valve was further slightly modified by removing the inner most spring of the nest of springs to allow for clearance for the *threaded rod*. Two springs is a valve option offered by the manufacturer to lower the pilot pressure needed to open the valve. With the *LVDT core* attached to the spring end with the threaded rod, the valve opening was measured during valve operation. This information coupled with pressure and flow proved very useful in designing the CFD simulations discussed in Chapter 4. Because the spring chamber of the valve is at the same high pressure as the inlet port, the LVDT selected had to be capable of withstanding high pressure. The catalogue stated that the LVDT was capable of 200 bar (3000 psi) but the manufacturer (Schaevitz Slough, Berkshire, UK), approved it for

use at 250 bar (3750 psi). This is the maximum pressure that the ring main system can generate, but due to losses in the piping, it is unlikely that this high level of pressure will actually ever be present at the test stand inlet.

The experimental procedure used with the LVDT was the same as for the experiments to measure the pressure compensation performance. The LVDT signal was recorded along with the inlet and outlet pressures and the flow rate. The tests performed with the LVDT attached to the valve were dynamic; therefore, the valve openings measured were representative of true valve operation unlike the valve opening measurements made with the flow force apparatus. Pressure compensation performance curves for the load control valve model MBEM XKN that does not have the inner-most nested main spring is shown in Figure 2.9. As in Figure 2.4, the 55 bar pilot pressure curve is annotated with arrows showing the direction the curve was created. The description of the piston movement for Figure 2.4 is also valid for the curves shown in Figure 2.9. Piston movement during pressure compensation was measured and plotted as the curves in Figure 2.10. The 55 bar pilot pressure curve is annotated with arrows indicating the direction that the curve was created. As can be seen, the valve is initially opened to approximately 3.5 mm. A fixed orifice pressure-flow curve can be seen in the pressure compensation curve for the 55 bar pilot pressure in Figure 2.9 from approximately 10 bar and 15 L/min to approximately 60 bar and 50 L/min. As the load pressure increases, the flow also increases but the piston remains stationary until approximately 50 L/min. Using this flow rate on the 55 bar pilot pressure on the pressure compensation curve in Figure 2.9, it can be seen that the valve is starting to pressure compensate and the flow rate does not increase at the same rate with the increase of load pressure as previously. As the load pressure continues to increase, the valve piston moves to close. This can be seen on the 55 bar pilot pressure curve in Figure 2.10 from approximately 3.5 mm and 55 L/min flow to 2.9 mm and 62 L/min flow. This is the peak flow rate and load pressure on the graph of the 55 bar pilot pressure in Figure 2.9. As part of the experimental procedure, the load pressure is reduced as can be seen on the 55 bar pilot pressure curve in Figure 2.9, but the piston remains nearly stationary as can be seen on the 55 bar pilot pressure curve in Figure 2.10 from approximately 2.9 mm and 62 L/min to 2.9 mm and 28 L/min. As the load pressure continues to be decreased as part of the experimental procedure, the valve again begins to pressure compensate and the piston moves to reopen the valve. This can be seen on the 55 bar pilot pressure curve in Figure 2.10 from 2.9 mm and 28 L/min to approximately 3.4 mm and 30 L/min. At this point, the valve again exhibits a fixed orifice pressure-flow curve as can be seen on the 55 bar pilot pressure curve in Figure 2.9 from approximately 30 bar and 30 L/min to the end of the curve at approximately 10 bar and 15 L/min. On Figure 2.10, 55 bar pilot pressure curve, this is shown as the stationary piston at approximately 3.4 mm and 30 L/min to 3.4 mm and 15 L/min. The same trends are seen in the graphs of the other pilot pressures in Figure 2.9 and Figure 2.10.

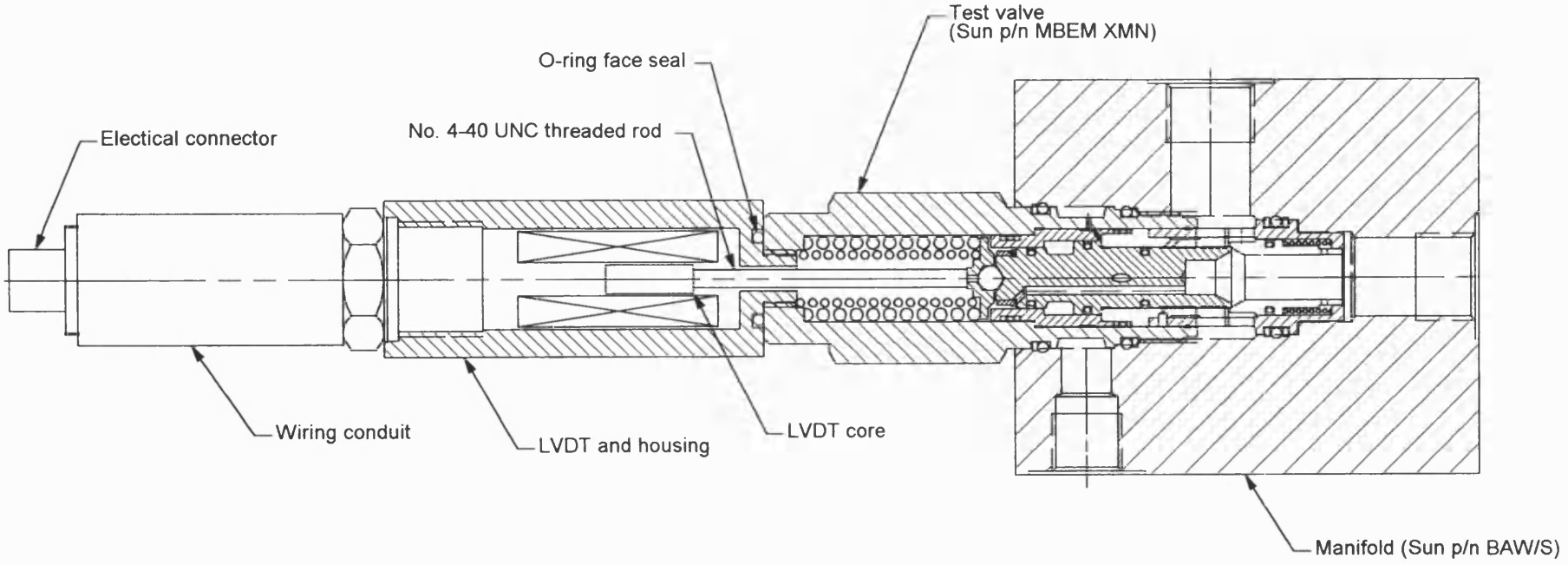

Figure 2.8 LVDT assembled on the load control valve

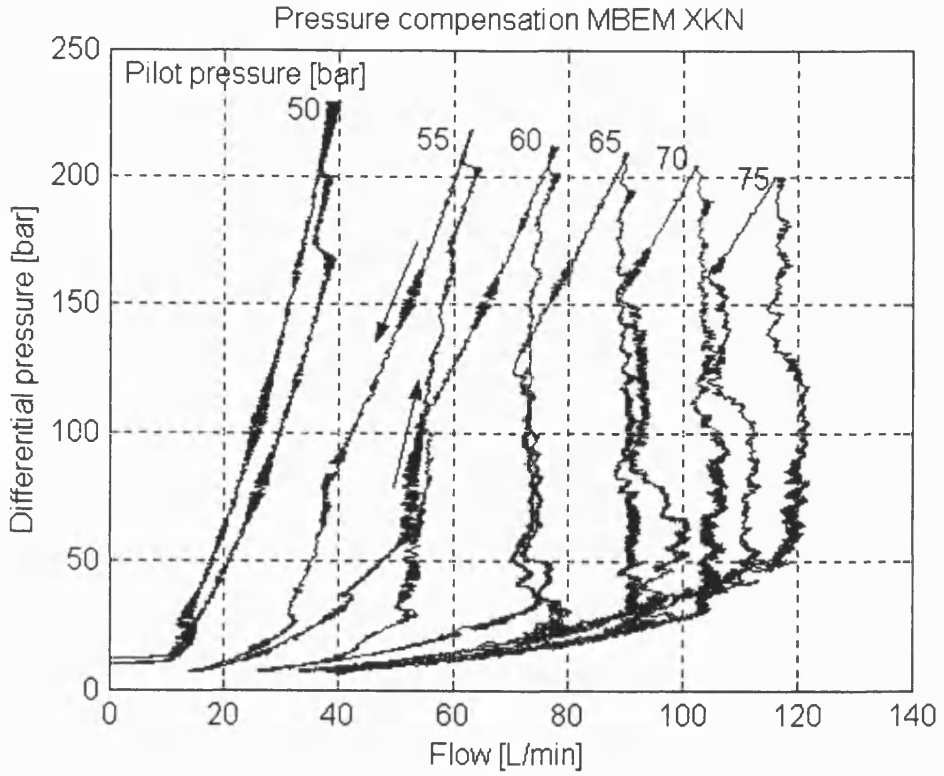

Figure 2.9 Pressure compensation performance for six pilot pressures

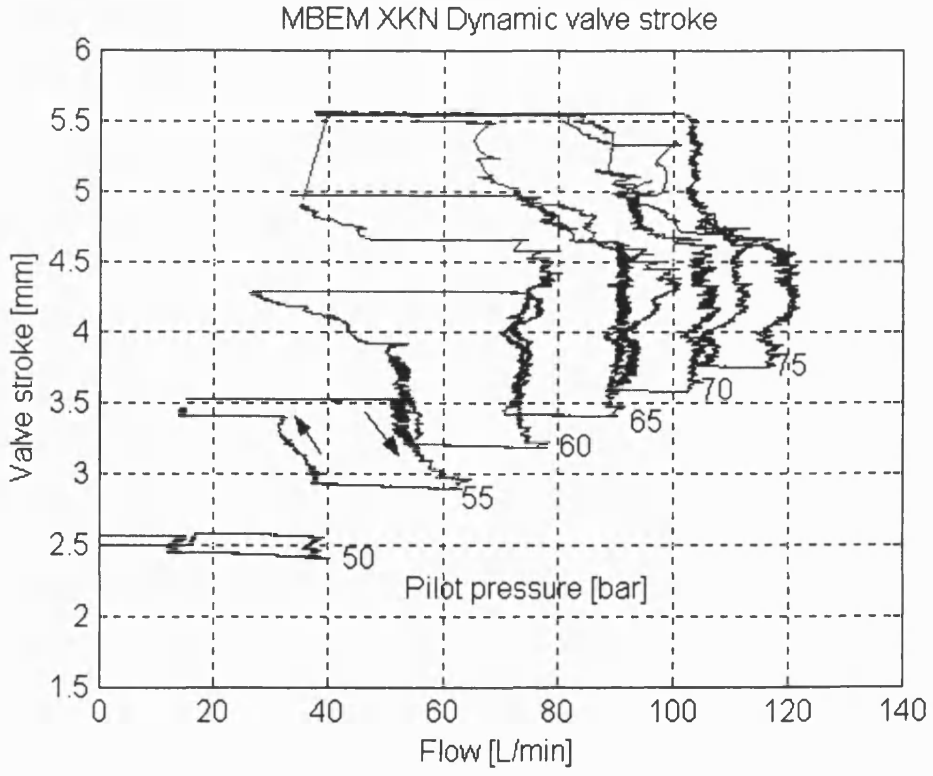

Figure 2.10 Valve stroke while pressure compensating for six pilot pressures

The graph of valve strokes for six different pilot pressures in Figure 2.10 when viewed with the corresponding pressure compensation curves (Figure 2.9) clearly demonstrate that when the load control valve is pressure compensating, the piston is moving to close the valve when the load pressure is increasing and the piston moves to open the valve when the load pressure is decreasing. The valve stroke and flow data used to create Figure 2.10 will be used in creating the CFD models described in Chapter 4.

2.6 Interpretation of results

Interpretation of the experimental results is necessary to make comparisons with data that will be generated through flow visualisation, CFD studies, and mathematical modelling of the load control valve.

As part of the interpretation process, the raw data that was collected was numerically 'smoothed' with the custom written Matlab function *Smooth*. A copy of *Smooth* is provided in Appendix 1. This function, based upon the smoothing technique employed by **Johnston and Drew (1996)**, uses a weighted linear regression technique to fit a function to the measured data over a localized flow rate. All subsequent interpretation of the experimental data was performed on the smoothed data. Using the smoothed data the following parameters were calculated: the pressure drop through the valve, the opening area as a function of valve stroke, flow force, composite jet angles, and composite flow coefficients. In order to calculate the individual values for jet angle and flow coefficient for each hole, knowledge of the flow rate through each hole would have been required and this was not available. The jet angles and flow coefficients computed were thus composite functions because they are values that describe the 'equivalent' jet angles and flow coefficients of multiple holes being uncovered simultaneously.

The differential pressure was calculated from the difference between the measured inlet and outlet pressures as shown in Equation 2.1.

$$\Delta P_{1-2} = P_{inlet} - P_{outlet} \qquad \textbf{(2.1)}$$

Open hole area is the segment area of the circular hole uncovered by the moving piston. Figure 2.11 below shows the case of a hole partially open. Equation 2.2 **(CRC 1996)** given below was used in the custom written Matlab function *Flowarea* to calculate the flow area for a partially open hole from a known valve stroke. The function summed the open hole areas into a total flow area. Total flow area was composed of the open area of all fully and partially uncovered holes. A copy of the function *Flowarea* is provided in Appendix 1.

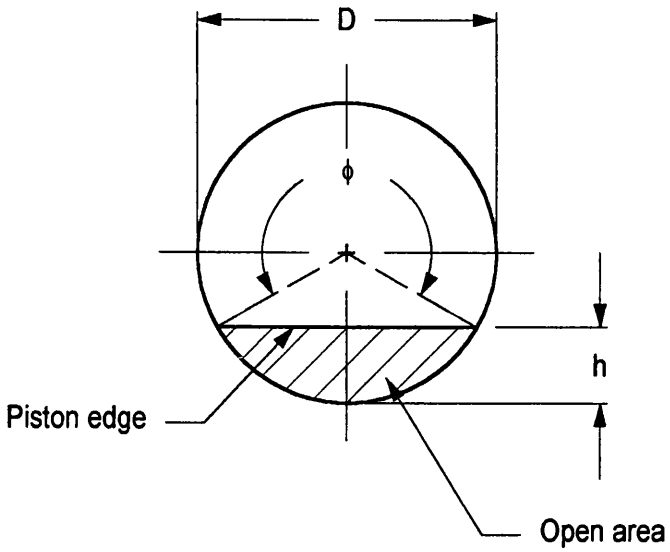

Figure 2.11 Hole segment area

$$A = \frac{D^2}{4}\arccos\left(\frac{\frac{D}{2}-h}{\frac{D}{2}}\right) - h\left(\frac{D}{2}-h\right)\sqrt{2\frac{D}{2}-h^2} \qquad \textbf{(2.2)}$$

Data obtained from using the flow force measurement apparatus was post-processed using the Matlab M-file *PressAngle*. This script file is included in Appendix 1. After first reading the pressure data file generated from the data acquisition software, the script file splits each pressure into two separate data vectors. One vector is created for the increasing flow rate for each pressure and a second vector is created for the decreasing flow rate, again for each pressure. This is done in order to avoid programming difficulties when the curves 'turn' from increasing flow to decreasing flow and to facilitate the removal of hysteresis that might be present in the measurements. Each data vector is smoothed using the *Smooth* function. A mean force is computed from each pressure-flow data vector to remove any hysteresis that might be present. The pressure forces acting on the valve piston as shown in the cross-section in Figure 2.12 are the load pressure and valve port pressure acting upon differential areas. These forces are computed using Equation 2.3 that makes use of Equations 2.4 and 2.5.

$$F_p = \overline{P_1}A_1 + \overline{P_2}A_2 \qquad \textbf{(2.3)}$$

where

$$A_1 = \frac{\pi}{4}\left(D_3^2 - D_1^2\right) \qquad \textbf{(2.4)}$$

$$A_2 = \frac{\pi}{4}\left(D_2^2 - D_3^2\right) \qquad \textbf{(2.5)}$$

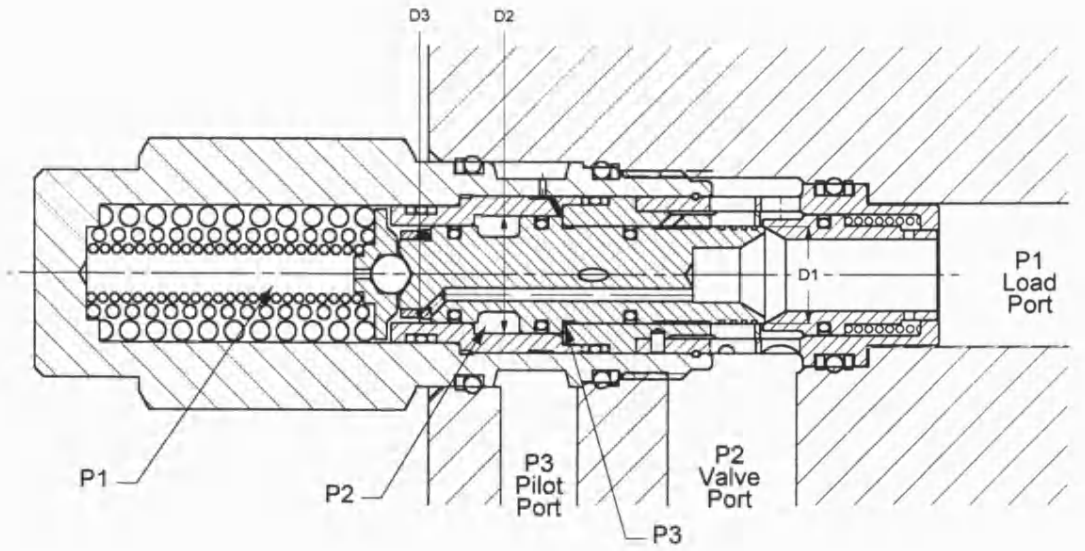

Figure 2.12 Full cross-section of the load control valve

The *PressAngle* script next reads the measured force data typical of the data previously shown in Figure 2.7. The data is again split into two separate data vectors as described previously and smoothed using the *Smooth* function. A mean force data vector (F_{net}) between the force data vector for increasing flow and the force data vector for decreasing flow is calculated to remove hysteresis. This calculation removes the friction force that is present in the measured force. This requires the assumption that friction is constant. The flow force is computed by subtracting the pressure force from the measured force as shown in Equation 2.6.

$$F_{flow} = F_{net} - F_p \tag{2.6}$$

The next set of calculations made in the *PressAngle* script is to smooth the stroke data obtained from the LVDT that was attached to the flow force measurement. The stroke data vector was also split into two separate stroke data vectors and a mean between the two computed to remove hysteresis that might be present as previously described. Stroke data was used to calculate the valve total opening area using equation 2.2 in the Matlab M-file *Flowarea*.

An unquantified degree of uncertainty exists in the calculation of valve opening area due to the uncertainty of knowing when the first hole series began to open. The LVDT on the flow force measurement apparatus could not be zeroed when the piston was against the valve seat because the minimal force needed to distort the *connecting rod* (see Figure 2.6) made it difficult to know when the piston was seated. Instead, the LVDT was zeroed when there was no flow through the valve. This was uncertain because the flow meter used on the oil hydraulic test stand was not capable of measuring flow below approximately 10 L/min. Therefore, a combination of no flow being registered by the flow meter and a lack of the

sounds normally associated with oil flowing through hoses was used to determine when the valves were covered. This was the point that the LVDT was zeroed.

The momentum of a fluid passing through an orifice that does not have a smooth, gradual transition causes a jet to continue to contract after it has passed through the orifice. The vena contracta is the section of smallest cross-sectional area. The contraction coefficient, c_c, is the ratio of the area of the vena contracta to the orifice area. The discharge coefficient, c_d, is the product of the contraction coefficient and the velocity coefficient, c_v. By assuming the velocity coefficient is unity, the contraction coefficient can be approximated as the discharge coefficient. A more convenient term used in hydraulic valves is the flow coefficient, c_q. It differs from the discharge coefficient from the point that downstream pressure is measured. For the flow coefficient, the downstream pressure is measured after the vena contracta where pressure recovery has occurred. For the discharge coefficient, the pressure is measured at the vena contracta. The composite flow coefficient was computed from the flow rate, differential pressure, and opening area using the measured data. This computation was made using Equation 2.7. The flow coefficient computed is a composite flow coefficient because more than one exit hole is open. This calculation requires the assumption that the flow coefficient is the same for each of the four holes in the series. Thus, the effects of the pressure differential throughout the annular area in the cavity that the valve was installed were neglected.

$$c_q = \frac{Q}{A\sqrt{\frac{2\Delta P_{1-2}}{\rho}}} \tag{2.7}$$

Using the *PressAngle* script file to post-process the data obtained from an experiment using the flow force measurement apparatus while the supply pressure was set at 250 bar, Figure 2.13 was created that shows how the composite flow coefficient changes with valve stroke. The composite flow coefficient was computed as previously described. The elliptical shapes plotted on the graph show the location, size, and overlap of the five hole series in the load control valve. Similar variation in the composite computed flow coefficient was observed for the lower inlet pressures used in the experiments with the flow force measurement device.

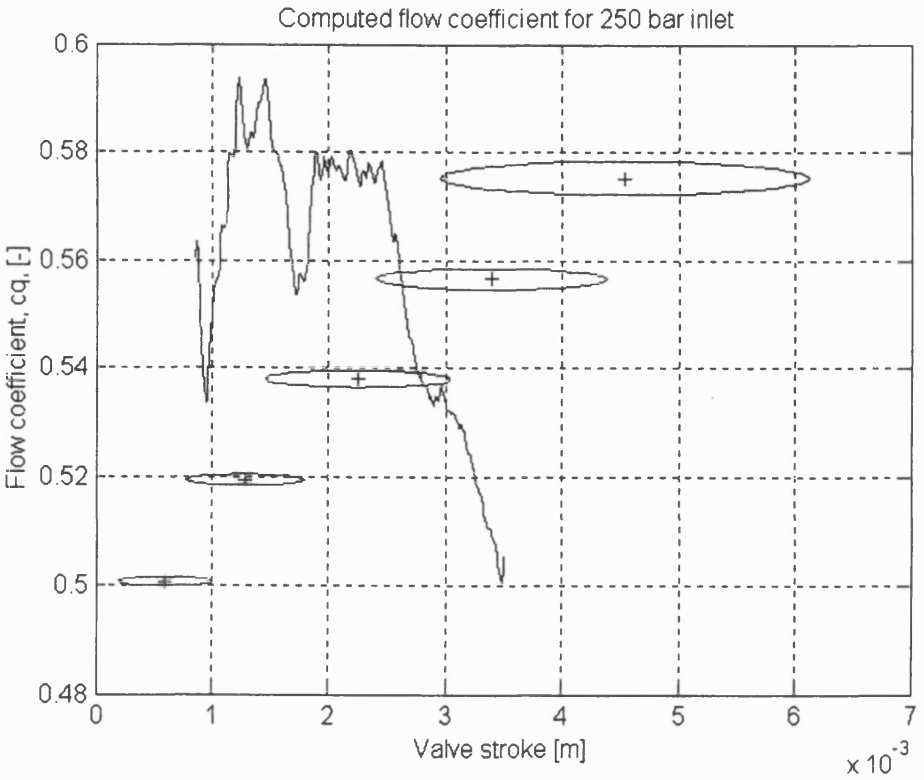

Figure 2.13 Composite flow coefficient computed for 250 bar inlet

The classic equation used to calculate flow force, Equation 2.8, was used to derive an equation for the jet angle with variables that were measured and computed. Composite angles were calculated because each exit hole series would have jet angles that corresponded to opening of the hole and the flow rate through it. As previously discussed, the necessary assumption was made that the exiting jet angles through each hole in a hole series were the same. In effect, the assumption was made that the flow rate through each hole in a hole series was the same. With pressure terms substituted for the velocity and flow rate terms, Equation 2.9 was derived, which neglects inlet velocity. It was used in the *PressAngle* script file to calculate the composite jet angles while post-processing experimental data from using the flow force measurement apparatus.

$$F_{flow} = \rho Q v_{outlet} \cos\theta - \rho Q v_{inlet} \tag{2.8}$$

$$\theta = \arccos\left[\frac{F_{flow}}{2A\Delta P_{1-2} c_q}\right] \tag{2.9}$$

Composite jet angles calculated while post-processing experimental results, when a 250 bar inlet pressure was used, are plotted in Figure 2.14. These results were calculated by using the composite flow coefficients shown in Figure 2.13. Horizontal lines with a centre,

vertical lines indicate the position of the five series of exit holes. It is readily apparent from Figure 2.13 that the jet angle changes significantly as the valve opens and the hole coverage changes. Similar variations in the calculated, composite jet angles were observed in the results post-processed from the experiments that used lower inlet pressures.

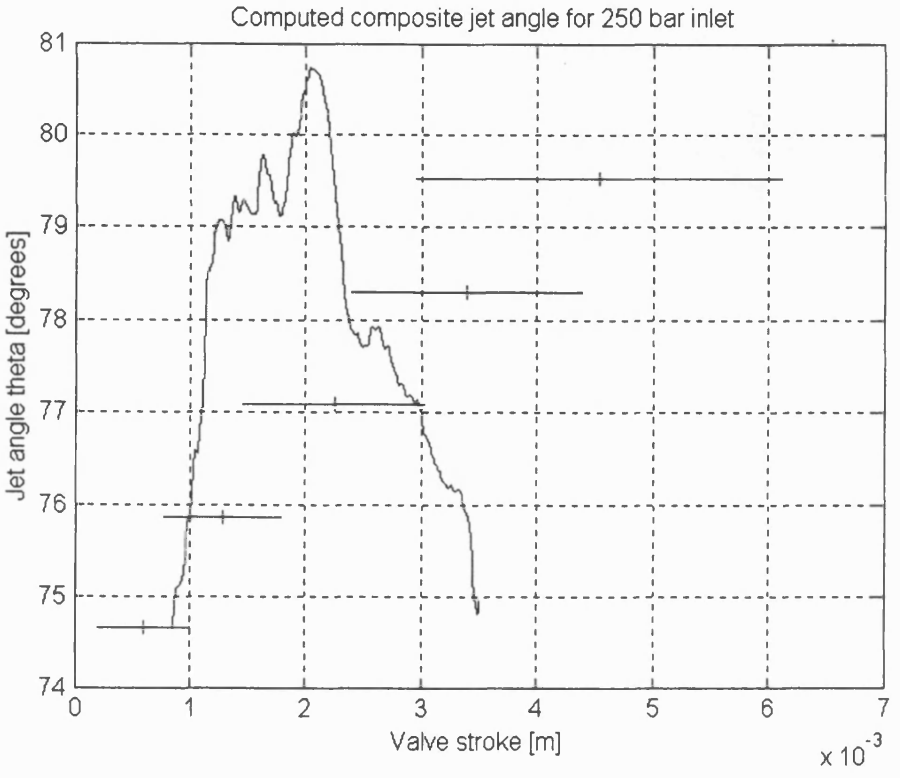

Figure 2.14 Composite jet angle calculated for 250 bar inlet

2.7 Concluding remarks

In this chapter, the necessary data was collected to provide experimental verification for the mathematical model that will be discussed in Chapter 5. Parameters such as flow coefficient, flow force, and jet angle will be shown in later chapters to have a significant effect on the valve performance. The experiments were designed to measure some of these parameters and enable calculations of the remainder. The experiments have been successful in these goals.

While there is always some degree of uncertainty when making measurements in experimental work, the uncertainty introduced into the valve stroke measurement because of the difficulty in establishing the closed position of the valve was more than anticipated. The experimental data from the use of the flow force measurement apparatus will not be directly comparable to the mathematical modelled results that will be presented in Chapter 5 because the device does not allow the valve to operate in its true dynamic mode. However, the values obtained for flow force, jet angle, and flow coefficient will still be useful for model verification.

CHAPTER 3

FLOW VISUALISATION

3.1 Introduction

The hypothesis that the changing flow forces as a result of changing jet angles and flow coefficients are responsible for the pressure compensation characteristics of the load control valve was introduced in Chapter 1. In order to help verify this hypothesis, flow visualisation experiments were conducted. Flow visualisation is an extremely useful tool used to develop an understanding of flow behaviour in complex geometries. It is also very useful in verifying computational fluid dynamics (CFD) results. Qualitative verification is possible by comparing the trends present in the results of the flow visualisation experiments with the results of the CFD simulations. These would include streamline curvatures, areas of recirculating flow, and separation and reattachment. Quantitative verification is possible using techniques of varying degrees of sophistication and accuracy. Using sophisticated techniques, velocities at specific locations can be measured for direct comparison to CFD results. Other techniques allow jet angles to be quantified. This also provides useful comparison to CFD results.

The flow visualisation experiments for the load control valve were designed to help in developing an understanding of the flow behaviour, in particular how the jet angle changes as the piston moves to uncover and cover the exit hole. The primary goal of the flow visualisation experiments was to provide qualitative verification of the CFD results that will be presented in Chapter 4.

3.2 Review of past work

Before starting to design the experimental valve model, a review of past work was conducted. There is limited literature published on the use of flow visualisation for understanding valve flows compared to other research areas. One of the earliest works was that of **Schrenk (1957)**. An extensive and remarkable work, the paper was originally written in German. The English translation prepared in 1957 was a condensed version of the original paper from 1925. In this version, the results of experiments using water at a constant flow rate were presented. The building water main was the source for the water but was fed through an apparatus to provide a constant head. The main objective of these experiments was to investigate valve losses with a view to finding methods of reducing

them. Flow visualisation was conducted utilising a tufts method. Silk threads or tufts were affixed to strategic locations on and immediately downstream of the controlling surfaces to understand the flow patterns through disc valves. This provided Schrenk with the idea of different exiting flow patterns depending upon the flow rate and valve opening, as shown in Figure 3.1. Part of the work was used to experimentally determine the contraction coefficient for the exiting jet. This was done for three different valve/seat arrangements. The contraction coefficient was found to vary with jet angle and the ratio of jet thickness and valve lift ratio. The contraction coefficient along with a pressure drop coefficient was used in a Bernoulli type equation to predict the total pressure drop through the valve. The pressure drop coefficient was determined experimentally as the pressure drop through the throat of valve alone. Schrenk found that a nozzle type design in the seat with a recessed area around the exit of the seat was a simple means to decrease flow resistance.

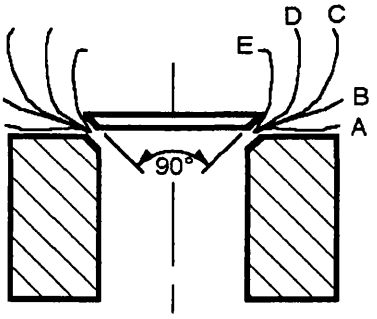

Figure 3.1 Schrenk (1957) flow patterns

In **Green (1970b)**, flow visualisation was used to attempt to verify analysis. The flow visualisation experiments were conducted using a half section of a thin two-dimensional model of a scaled up valve. Water was the working fluid. The experiments were conducted with a range of Reynolds number of 8,000 to 55,000. This thin section may have been the source of errors in the trends of the flow patterns since wall effects may have been more influential than in a full three-dimensional valve. By the author's own statements, the qualitative results were not very reliable, but the observations and deductions about the general trends do seem to support the conclusions drawn from the testing of actual valves. The analysis conducted was based upon the discharge coefficients for both the poppet and seat and the exit holes. Considering both areas of restriction is uncommon and is often overlooked. However, the discharge coefficients were assumed constant and hence showed little effect on calculations. As McCloy and McGuigan (1964) demonstrated, the discharge coefficient is variable and changes with the flow conditions. The author did note that a cavitation bubble was present during the experiments on the poppet surface immediately downstream of the seat, but no assessment of its effect was offered.

Kitamura *et al.* (1985) examined the flow through a butterfly valve. This qualitative visualisation was accomplished using bubbles and polystyrene particles as tracers. Bubbles

occurred naturally as part of cavitation in the closed test loop using a centrifugal pump to circulate water. The polystyrene particles were introduced to the flow as tracers. The particles started out with a diameter of 0.3 mm (0.012 in) and a specific gravity of 1.05. However, the pump impeller sliced many of the particles. Many details were given in the paper about the construction of the test rig and the photographic techniques. A key point was that the clear, acrylic pipe was submerged in a rectangular water tank to reduce optical distortion. This enabled three-dimensional visualisation. Additionally, details of the lighting system, viewing angles, width of light slit, and camera and film details were provided.

Tsukiji *et al.* (1989) also used a tufts method to develop a qualitative understanding of the flow through spool type valves. The aim of the study was to investigate the effects on flow forces by the jet exiting the metering orifice created by the spool and valve. The goal was to use this knowledge to design a new spool valve with smaller flow forces. A three-dimensional, transparent model was constructed of the spool valve to visualise the flow near the metering orifice. Silk thread were used as tufts and attached near the orifice (spool land) edge. Sixteen tufts were used. They were spaced at 22.5° increments around the diameter. A manometer measured the pressure distributions on the spool land. Reynolds number influence, valve opening, and valve chamber depth on the flow direction and the jet angle were investigated. Flow direction was monitored with the tufts using a digital camera with a sampling time of 1/30 second. The resulting design of a flow force compensated spool valve was compared to the non-compensated design. The experimental results showed that overall, the net force had not changed. However, the direction of the force vector had been reversed in some cases depending upon the Reynolds number. Thus, further work would be required to obtain an optimal solution. The flow force compensated spool valve induced a swirl in the flow that reduced or changed the direction of the flow force vector. It appears this was accomplished by relocating the exit port from an axisymmetric location to an off-centre location. The work was carried out at moderately low Reynolds numbers in the range of 1600 to 6000. The major conclusion of the work was that swirling flow might potentially induce smaller magnitude flow forces than non-swirling flow.

Feigel (1990) used qualitative flow visualisation to understand the flow patterns in spool valves. From the developed understanding, simple modifications to compensate for the flow forces were made to the spool geometry that reduced the required operating force of switching solenoids. A directly actuated ISO 07 (CETOP 07) proportional valve was designed using linear motors and solenoids. The aim of the research was to demonstrate that even in complex flows, flow force compensation could be applied. The study was qualitative and used an iterative process to develop an understanding of the flow patterns through spool valves. However, quantitative flow force measurements were taken. The study did not address poppet or disc valves, but did briefly discuss three-dimensional effects in flow patterns, hence the conclusion that flow force compensation can be applied to complex flows. No details of the flow visualisation method were given. Water was the

working fluid in the valve that was seven times scale model. It is interesting to note that a water bath with flat faces was used to house the cylindrical model to aid in photography.

Johnston *et al.* (1991) and the companion paper Vaughan *et al.* (1992) (ff. Section 4.2) presented the results of both experimental and numerical work on poppet and disc valves. In the present article, a theoretical analysis was performed and compared to the experimental results. Although the qualitative trends of the experimental results agreed well with theory, the experimental values were higher than theory. This was explained by the authors as most probably attributable to pressure recovery after the vena contracta. In comparing their results to that of Stone (1957) (c.f. Section 2.2) for the 45° flow force compensated poppet, Figure 2.1, a negative flow force was observed. This occurred for lift/inlet diameter ratio greater than 0.1, $(z/d_o) > 0.1$. It was also at this point a discontinuity was observed in a plot of the results for the flow coefficient, c_q, and flow force coefficient, c_f. The authors surmised that this was the result of jet detaching from the valve seat and attaching to the sidewall. Stone did not note these observations because of the concentration on smaller valve openings. This discontinuity is of importance because in practice valve instability might be induced when operating in the region of discontinuity.

A portion of the experimental work of Johnston et al. (1991) was carried out as flow visualisation. Water was the working fluid for all of the experimental work. Hydrogen bubbles were generated in water through electrolysis and used to seed the flow. The movement of the seed bubbles was captured photographically. A fully axisymmetric valve model was used in the study. Previous work has primary been on partial valve models such as parallel sided slices. The axisymmetric model eliminated the effects of a flat face or the introduction of boundary layers in a sectioned model. Although this portion of the experiments was qualitative in nature, the results are none the less impressive. No details of the photographic techniques nor lighting were provided in the paper, but discussions with the authors revealed that the light sheet was created through slit illumination. Furthermore, a viewing angle between 90° and 120° with respect to the light sheet produced the best results.

Ishii *et al.* (1994) used experimental flow visualisation to study flow in a poppet valve. A fully three-dimensional, steel valve with oil as the working fluid was constructed as part of the experimental apparatus. Two industrial fibre optic scopes were attached to two high-speed video cameras. The sample rate of the cameras was 1/500 second. The fibre scopes included xenon lights to illuminate the flow. Acrylic portholes were mounted in the test valve at 90° to each other for three-dimensional viewing. It was unclear from the article whether the test valve was full scale or scaled up to make visualisation easier. The oil flow was not seeded but relied upon the air bubbles that naturally came out of solution and the bubbles formed from cavitation. The valve was a simple conical poppet that formed a relief valve. The working pressures were between 0.25 MPa (2.5 bar or 36 psi) and 0.78 MPa (7.8 bar or 113 psi). Flow rates were not discussed in the paper.

The study examined the flow under steady and cavitating conditions. A conical, "dart" style poppet valve, which is only controlled by inlet pressure and spring force was studied. This configuration will naturally go unstable at low flow rates. Details were provided on spring rates and mass of the poppets, but were not used. There was mention of digital processing of the photographs taken to yield quantitative flow field information, but no discussion of the technique nor results were presented.

Reduction of the noise cause by cavitation in poppet relief valves was the goal of the work described in **Ueno *et al.* (1994)**. This paper appears to be a continuation of a previous paper written in Japanese. Although six different valve configurations were apparently tested, only three of the six were described in limited detail. Photographs were published in the paper that was part of a flow visualisation experiment, but very few details were given. It appears that oil was the working fluid in the experimentation. Numerical simulation of the valve configurations was carried out using a finite control volume technique. A Reynolds number of 10^3 was cited for the inlet condition in the simulation. No comparisons were apparently made between the simulation results and the experimental results.

An investigation of cavitation in counterbalance valves using flow visualisation was described in **Tsukiji *et al.* (1996a and b)**. ISO 32 oil was the fluid used in the work. The oil was kept at a constant temperature of 40° ± 1°C for the testing. The model was constructed from acrylic by sectioning a full valve and installing a window in the area of interest. Geometry modifications were made which reduced cavitation and hence the noise. The modifications were not described. A brief mention of the observance of the blue light of sonoluminescence was made. More details of the study are given in this second paper that when combined with the first help to clarify the work. It was still unclear from both papers whether the model was full scale or enlarged. The experiments were conducted at Reynolds numbers of 2772, 2847, 3594, and 3478. The flow was photographed with a 35 mm camera using the naturally occurring bubbles of cavitation to seed the flow.

Both of the papers by Tsukiji *et al.* (1996 a and b) were interesting, but do not give enough detail to be useful. Some very good photographs of flow visualisation through the valve model were presented, but again not enough detail was given.

Xiaodong *et al.* (1997) was one of the first to use of particle image velocimetry (PIV) in a hydraulic valve. The authors used PIV on a two-dimensional, acrylic, spool-valve model. The working fluid for the experiments had a viscosity of 0.03 Pa-s and was seeded by trace particles with a diameter of 300 μm and density of 1.01 kg/m^3. The experiments were conducted at a Reynolds number of 50. A 4 mW He-Ne laser that produced a 2 mm thick light sheet was used for illumination. The authors discuss binary-image cross-correlation (BICC) but do not discuss how it was applied to this work. They demonstrated how to calculate the pressure field and vorticity field from the velocity vectors.

The purpose of the work by Xianodong *et al.* (1997) seems to have been the application of a new experimental technique to study the flow through oil-hydraulic spool

valves. The authors commented that the actual flow through the valve is more complex than the two-dimensional model and further work is needed on a three-dimensional model. The paper lacked depth in the detail of the experimental set-up or procedure.

Jankowski and Plutecki (1998) made quantitative measurements of "momentary velocities" in the flow of water through a straight pipe at the rotor inlet of a pump. With the term "momentary velocities," the authors have tried to coin a term to describe the procedure they employed. Images were captured after a predetermined time after seeding the flow. The flow was seeded with hydrogen bubbles produced by electrolysis. The time between seeding the flow and starting to capture the image of the flow is where "momentary velocities" originates. Using a (PAL) video camcorder coupled to a stroboscope for illumination, they introduced the images into computer memory through a frame grabber computer card. The computer processed the images digitally. The borders of the recorded streaklines of the image were determined. From the measurement of the borders, "movement" vectors were determined. These calculations were performed for each streak. The measurements were processed statistically to calculate average values, "nonstationarity of flow", and measurement error. The results were plotted on a velocity distribution diagram. The authors calculated errors between four and seven percent, depending upon flow conditions.

It seems that the procedure implemented by Jankowski and Plutecki (1998) would be limited to relatively slow, laminar flows. The system as implemented is limited to twenty-five frames per second. In addition, this system does not provide real time information. The largest limitation of this novel combination of old techniques and modern equipment is that it is limited to two-dimensional flows.

3.3 Design of flow visualisation test rig

From reviewing past work, it can be seen that bubble generation through electrolysis is one of the simplest methods for seeding the flow for visualisation. The experimental set-up is flexible, less problematic, and relatively inexpensive compared to the other techniques used in past work. Therefore, the experimental model was designed around using this technique to seed the flow and conduct the flow visualisation experiments. In addition, the review of past work demonstrated that the use of a three-dimensional model was an important criterion to avoid wall effects in a two-dimensional model.

In order to enhance flow visualisation, the valve model was scaled up from its true size. Before deciding on a scale factor, several limits had to be investigated. The limiting factors included the flow rate limit for the source of the working fluid; the availability of material from which to machine the model; and the size limitations for the work piece in the equipment that would be used for machining the model.

Water was chosen as the working fluid because a method of generating tracers in the flow was readily available. Electrolysis was used to produce bubbles of oxygen and hydrogen. A schematic of the electrolysis unit is shown in Figure 3.2. The unit is an AC to

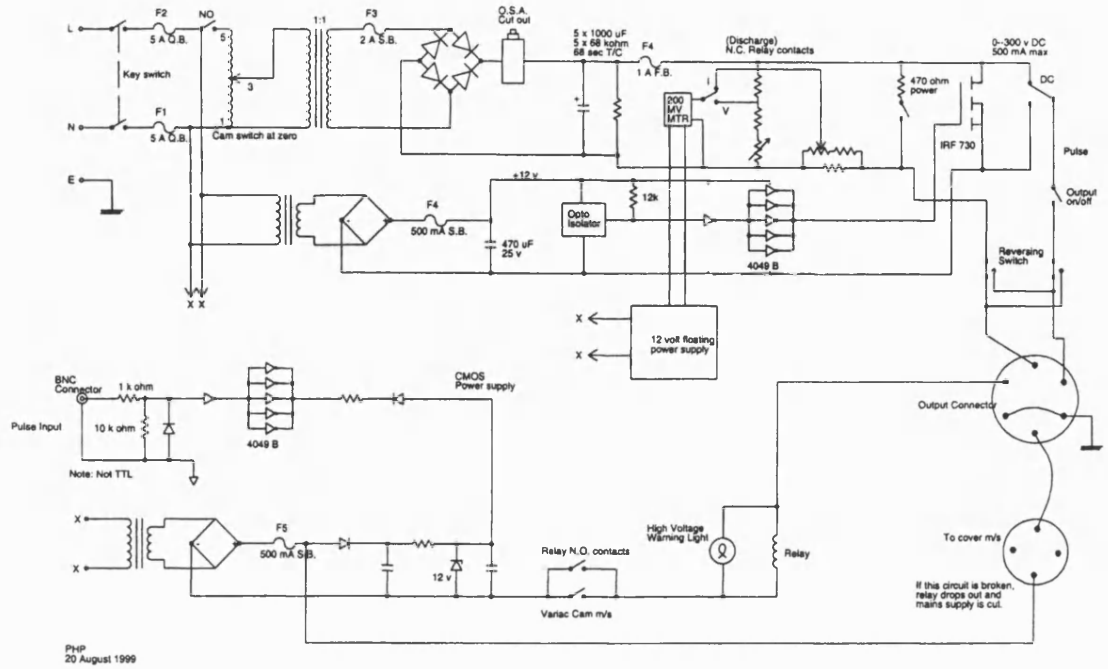

Figure 3.2 Schematic of the electrolysis unit

DC rectifier with capacitors that act as filters and a variable transformer to vary the output voltage. The current level never exceeded 100 mA. Typical voltages used in the experiments were between 50 V and 100 V. A switch to reverse the polarity of the voltage was built into the unit. This is helpful to clear the accumulation of bubbles from the anode and cathode. The anode and cathode for the electrolysis unit were platinum wires 0.125 mm (0.005 inch) in diameter, the smallest size readily available. Literature on flow visualisation recommends the use of stainless steel or platinum wire to avoid corrosion. The wire size to a large extent determines the bubble size **(Merzkirch 1987)**. The laboratory mains water supply was chosen as the source of water. In order to avoid recirculating water that had tracer bubbles suspended in the flow, water draining from the test rig was plumbed to the waste water lines in the laboratory. With the working fluid known and with a general idea of the maximum flow rate that was possible, the model could be scaled to ensure dynamic flow similarity. For identical Reynolds numbers it was found that a four-fold size increase was required. A maximum oil flow of 160 L/min through the full-scale valve then corresponds to a maximum water flow of 17.4 L/min through the water model. The size of the work piece was found to be machinable with available machine tools.

The model was designed as a three-dimensional scaled version of the full-scale valve rather than a two-dimensional flow table model. Scaling based upon Reynolds number will be discussed below. Therefore, the model components were cylindrical in

shape. This presented the problem that the cylindrical shape would distort the view of the area of interest, the metering edge. To limit distortion, the valve model was submerged in a bath with flat walls **(Kitamura *et al.* 1985, Merzkirch 1987, and Tsukiji *et al.* 1989)**. Plexiglas-G acrylic was selected as the material from which to manufacture the scaled model because its index of refraction is reasonably similar to that of water **(Merzkirch 1987)**. The index of refraction for Plexiglas-G provided by the manufacturer is 1.49. The index of refraction of water is 1.33. Plexiglas-G was found to be available in the sizes needed from which to manufacture the valve model. A drawing of the flow visualisation test rig is shown in Figure 3.3. To measure the water flow rate, a rotameter was installed upstream of the model inlet.

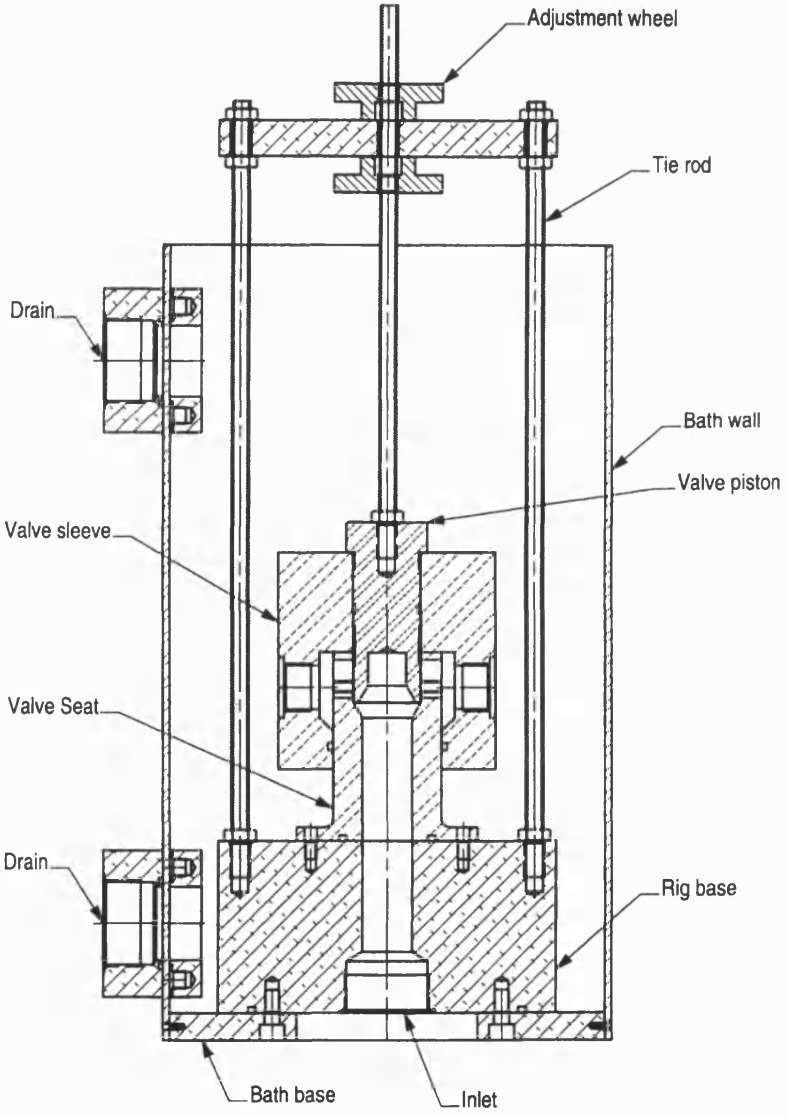

Figure 3.3 Sketch of the flow visualisation test stand

A light source was the final key component for the flow visualisation experiments. To create the light sheet, necessary to create a cross-section of viewable flow, a slide projector was modified for slit illumination. A slide was manufactured with a single, centred

slit 0.75 mm (0.030 in) wide. This produced a light sheet with a focal length determined by the projector's lens. At the metering edge of the valve, the light sheet was approximately 2 mm to 6 mm (0.079 in to 0.236 in) wide, which represents the width of the narrow, focused light sheet to the width of the fringe, unfocused light. The best results with photographs were achieved when the light sheet bisected the exit hole along the centre line thus illuminating the entire cross-sectional diameter. Maximum bubble brightness was obtained with the camera aimed at an angle between 90° and 120° with respect to the light source. A simple plan view drawing showing the layout of the viewing angle with respect to the light source is shown in Figure 3.4. As can be seen in the drawing, the light source was approximately 305 mm (12 in) from the test fixture. This was found to be the optimum distance for a focused light sheet. Photographs were taken with the camera abutting the wall of the water bath. The photograph in Figure 3.5 shows the flow visualisation test stand with the rotameter, electrolysis unit, and slide projector.

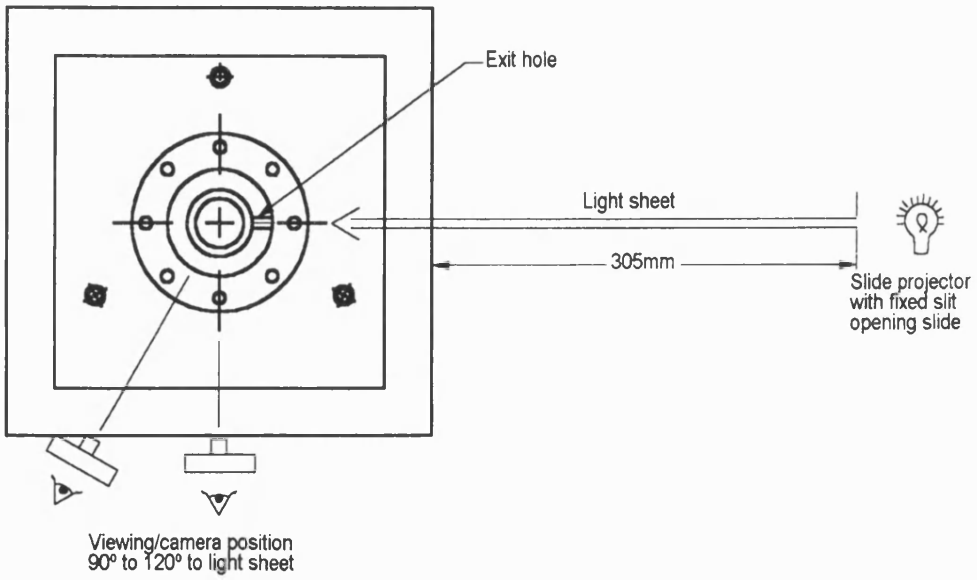

Figure 3.4 Plan view of the flow visualisation rig (not to scale)

Both a digital camera and a 35 mm SLR camera were used for the photography. The quality of photographs taken with the 35 mm SLR camera were considered better because there was more control over shutter speed, aperture, and printing. The 35 mm SLR was used with a total of 21 mm of extension tubes installed between the camera body and the 50 mm lens in order to decrease the focal length. The aperture was typically set for *f*1.8 or *f*2.8 with shutter speeds of ¼ second to ½ second. The film used was 125 ASA but the camera was set for 200 ASA. This allowed more contrast to be instilled into the photographs during the developing and printing.

A single exit hole was drilled into the modelled metering sleeve that is part of the *valve seat* shown in the drawing in Figure 3.4. This prevented the view from being obscured by the geometry of the other drilled holes. Since one of the main goals of the flow

Figure 3.5 Photograph of the flow visualisation test rig

visualisation experiments was to document the change in jet angle at the exit hole, this was a reasonable compromise to make. Additionally, as part of the dynamic similarity calculations, the oil flow rate that corresponded to the fourth hole series, which corresponded to the single drilled hole in the model, was divided by four, because there are four holes in each of the five series of drilled holes. The corresponding reduced flow rate was then used to determine the inlet flow rate of water into the model valve to obtain identical Reynolds numbers. Table 3.1 shows the results of the similarity calculations on the inlet flow conditions. These were based upon an inlet diameter of 8.74 mm (0.344 in) on the full-scale valve and 34.92 mm (1.375 in) on the scaled model. The value of viscosity used for oil was $3.71\times10^{-5}\,m^2/s$ and the value used for water was $1.01\times10^{-6}\,m^2/s$.

Table 3.1 Similarity calculations for inlet flow conditions

Oil flow rate [L/min]	*Reynolds number*	*Water flow rate [L/min]*	*Hole opening*
38.7	2539	4.2	Fully open
32.5	2129	3.5	¾ open
27.5	1802	3.0	½ open
21.2	1392	2.3	¼ open

A further simplification to the flow visualisation rig shown in Figure 3.4 was useful in aiding the photography to document the changing jet angle. The removal of the *valve sleeve* helped reduce the light distortion. This part represents the cavity annulus in which a cartridge valve would normally be installed. Its removal affects the flow through the valve by reducing the downstream pressure. However, no changes in the jet angle were observed

when further experiments were conducted with a flat sheet of Plexiglas installed at the location of the annulus wall. Therefore, conducting the experiments without the valve sleeve was another reasonable compromise to make in order to facilitate the flow visualisation. A comparison of the flow visualisation results for walls at varying distances from the exit hole and for different hole openings will be presented below. In the scaled model, the cavity annulus would be at a distance of 9.5 mm (0.375 in).

3.4 Results and discussion

The photographs that were taken for the valve openings and flow conditions are listed in Table 3.1. Along with each photograph is an accompanying sketch made from observation of the flow. The sketches were drawn to help emphasise the features in the photographs.

As stated previously, the primary goal of the flow visualisation experiments was to provide qualitative verification for the CFD simulations. However, when the photographs produced were better than anticipated, quantitative measurements were made on the exiting jet angle. Measurements were made by first scanning the photographic negative and then printing it scaled to cover a full sheet of A4 paper. Lines were drawn on the printed image overtop of streak lines created by the tracer bubbles. This line was drawn to extend into the main valve chamber where the angle vertex was created by drawing a line parallel to the exit hole. A protractor was used to measure the angle. Due to the glare in the photographs obscuring the streak lines at the metering edge, the measurement of the jet angle was based upon the streak lines within the exit hole. As will be seen in Chapter 4, the measured jet angles compare well with those calculated from the CFD simulations. The maximum variation in measured jet angles between the four different cases for wall distance for a single hole opening was 4°. The typical variation for a single hole opening and the four different wall cases was 1° to 2°. An estimate of measurement error using the unsophisticated method described was ± 5°. The jet angles measured for the four hole opening cases and the four cases of different wall spacing are given in Table 3.2. The last column in this table is for the case without a wall.

The photograph in Figure 3.6 is for the condition of a fully open hole and without a wall downstream of the exit hole. The inlet flow rate was 4.2 L/min. As can be seen in the photograph and the accompanying sketch in Figure 3.7, a small area of recirculation exists near the end of the exit hole. This was a common feature among the four wall cases for the fully open hole. Qualitatively, the jet angle appears to be very close to 90°. Measurements demonstrated this with an average jet angle value of 88° with a maximum variation of 2°.

The photograph in Figure 3.8 shows the flow conditions when only three-quarters of the exit hole is uncovered and without a downstream wall. Two recirculation bubbles are clearly present in the photograph as also shown in the accompanying sketch in Figure 3.9. The first recirculation bubble develops immediately downstream of the metering edge which acts as the jet separation point. The second recirculation bubble forms under the upward

sloped jet near the end of the exit hole. These were common features seen in the four wall cases for the case of a three-quarter open hole. Jet reattachment is starting to occur at the end of the exit hole. The jet flow is clearly present in the photograph. The inlet flow rate was 3.5 L/min. The average of the measurements made on the jet showed that the angle was 78° with a maximum variation of 4°.

The half open condition without a downstream wall is shown in the photograph in Figure 3.10. The accompanying sketch is shown in Figure 3.11. In the photograph, the exiting jet is clearly present as are two recirculation bubbles. Again, the first recirculation bubble develops immediately downstream from where the jet separates from the metering edge of the piston. The second recirculation bubble is near the end of the exit hole, under the upward sloped jet. These features were common in the four wall cases for the case of the half open hole. Jet reattachment is primarily occurring within the exit hole. The inlet flow rate for the half-open hole condition was 3.0 L/min. The average measure of jet angle was 74° with a maximum variation of 2°.

The photograph in Figure 3.12 and the sketch in Figure 3.13 show the condition of an exit hole open by a quarter without a downstream wall. As can be seen in the photograph, the jet is clearly visible as are two recirculation bubbles. The recirculation bubbles are present in the same locations as in the other flow conditions but are much larger than in the previous flow conditions. This was common among the four wall cases for the case of a quarter open hole. Jet reattachment is taking place well within the exit hole. The inlet flow rate for this hole covering was 2.3 L/min. The average jet angle measured was 67° with a maximum variation of 1°.

Table 3.2 Comparison of flow visualisation results

Opening	Jet angle [degrees] for wall distance of 4.3 mm	Jet angle [degrees] for wall distance of 9.5 mm (standard)	Jet angle [degrees] for wall distance of 17 mm	Jet angle [degrees] for no wall
Fully open	89°	86°	89°	86°
¾ open	80°	80°	76°	78°
½ open	74°	74°	76°	74°
¼ open	68°	67°	67°	67°

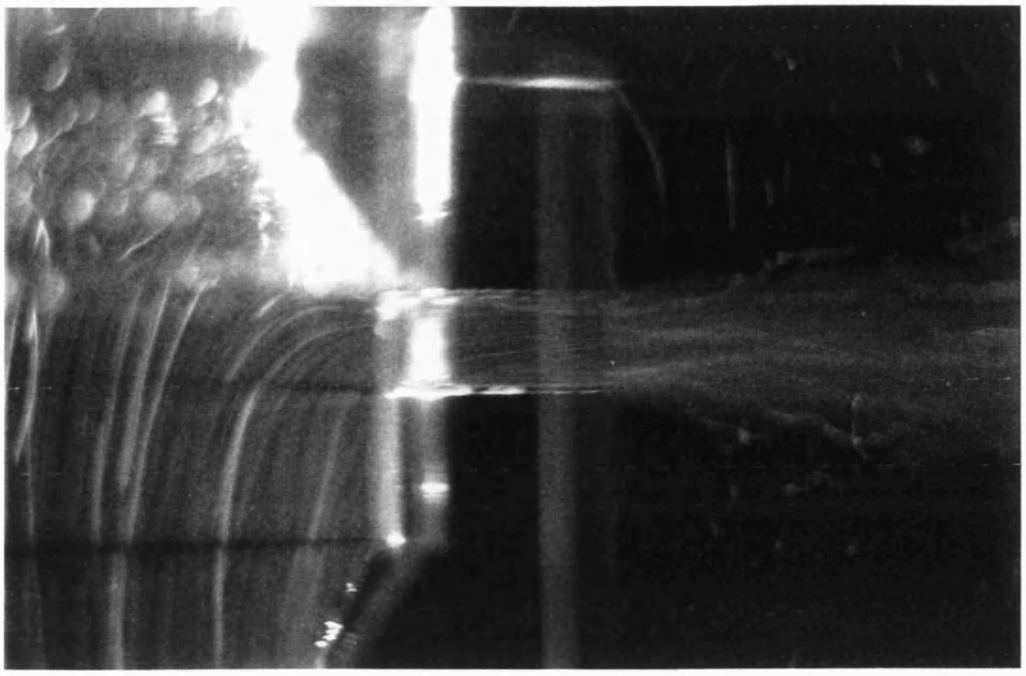

Figure 3.6 Photograph of full open exit hole

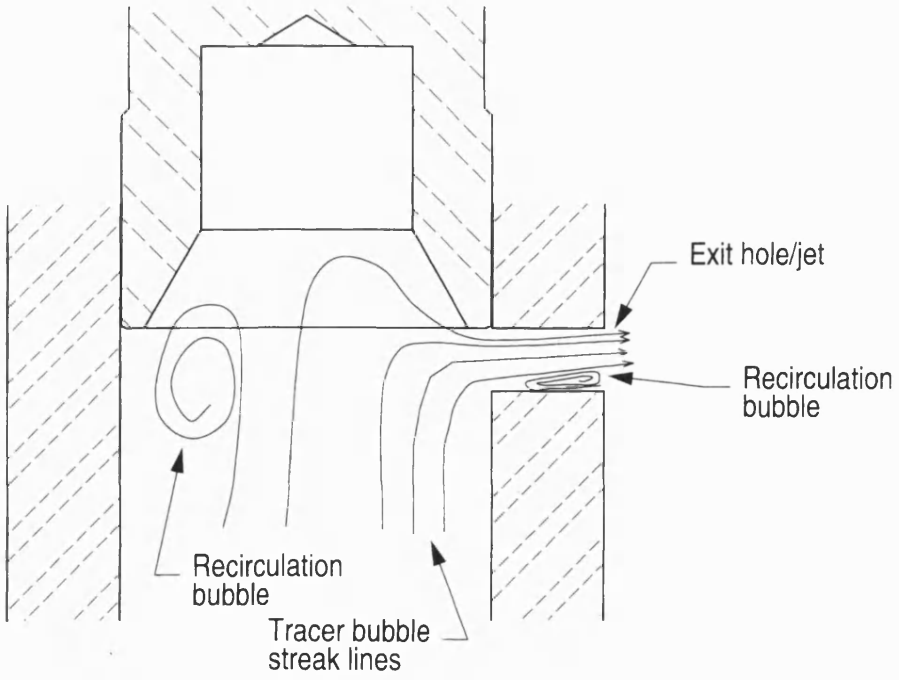

Figure 3.7 Sketch of flow through full open exit hole

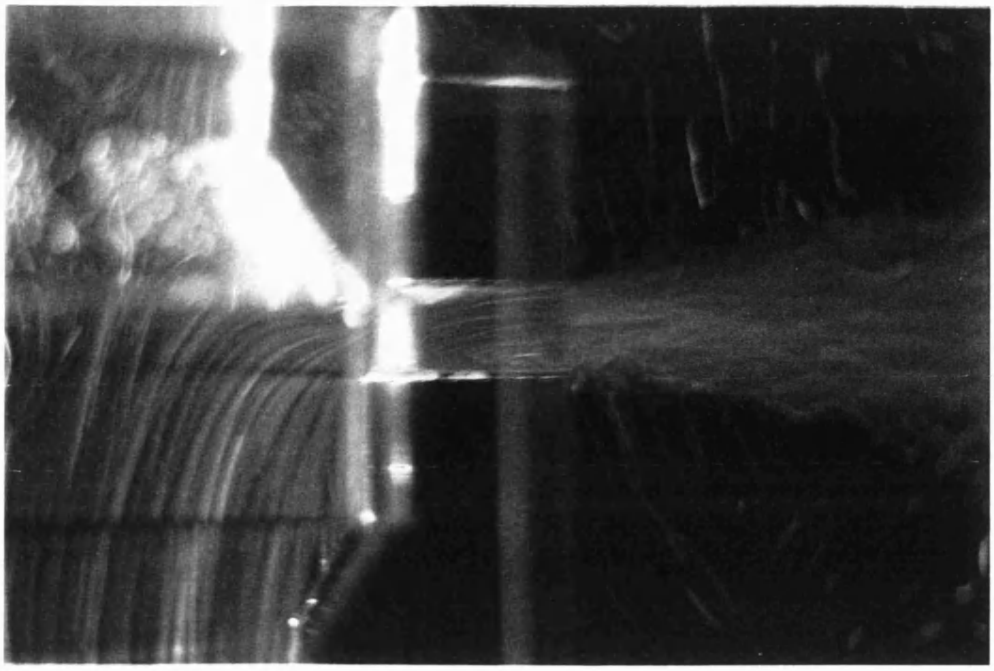

Figure 3.8 Photograph of ¾ open hole

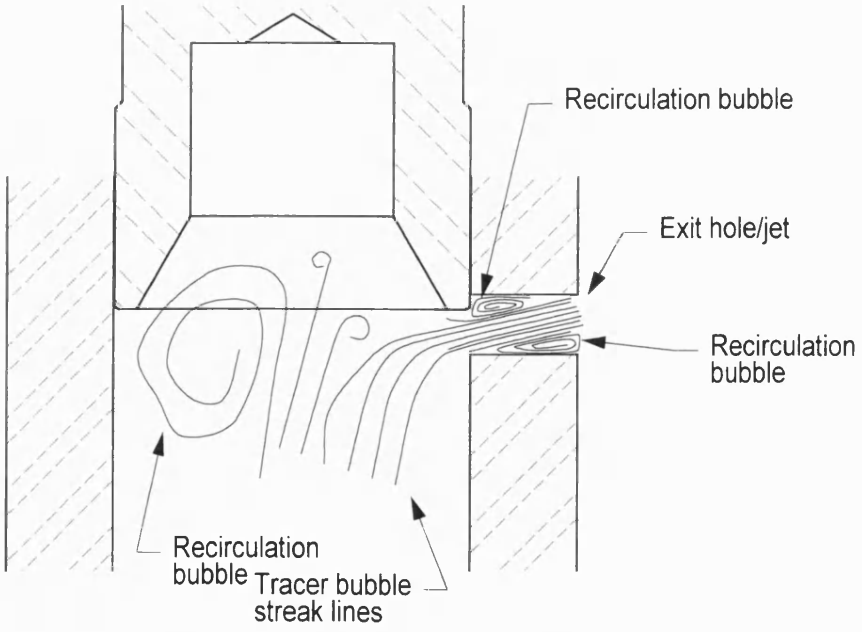

Figure 3.9 Sketch of flow through ¾ open exit hole

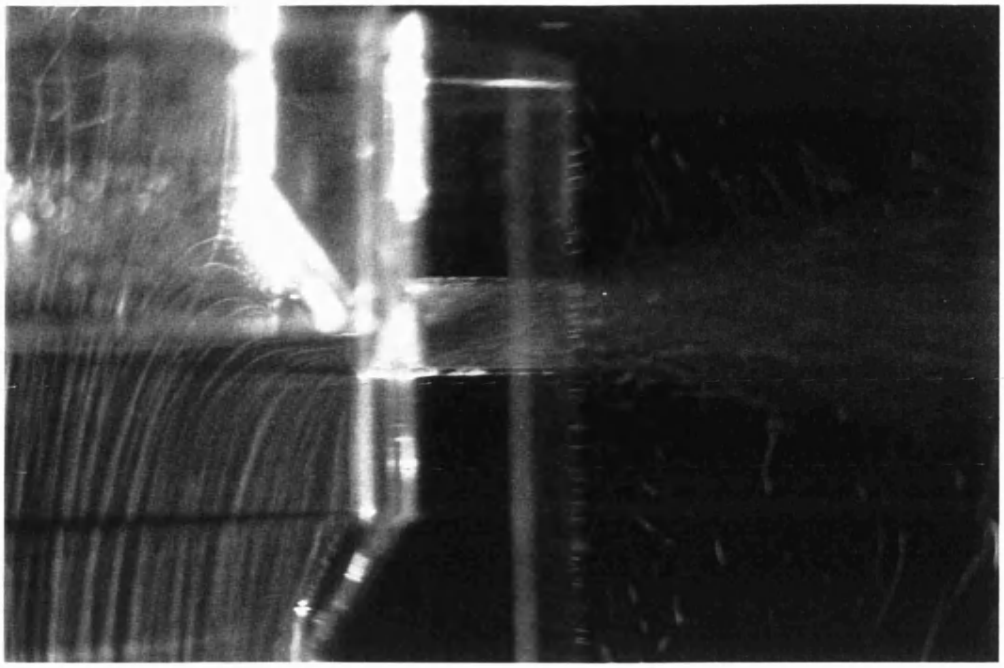

Figure 3.10 Photograph of ½ open hole

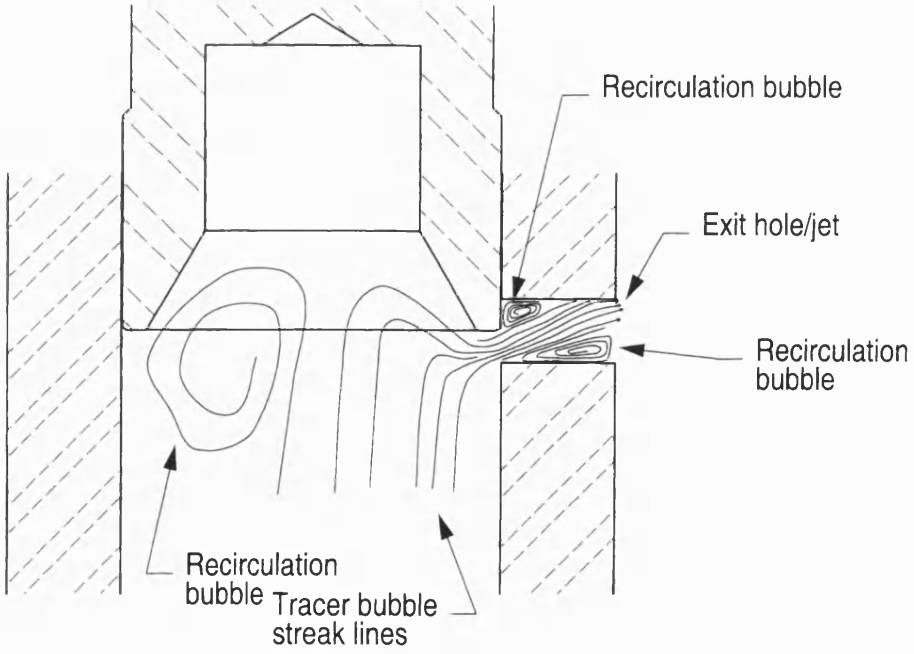

Figure 3.11 Sketch of flow through ½ open exit hole

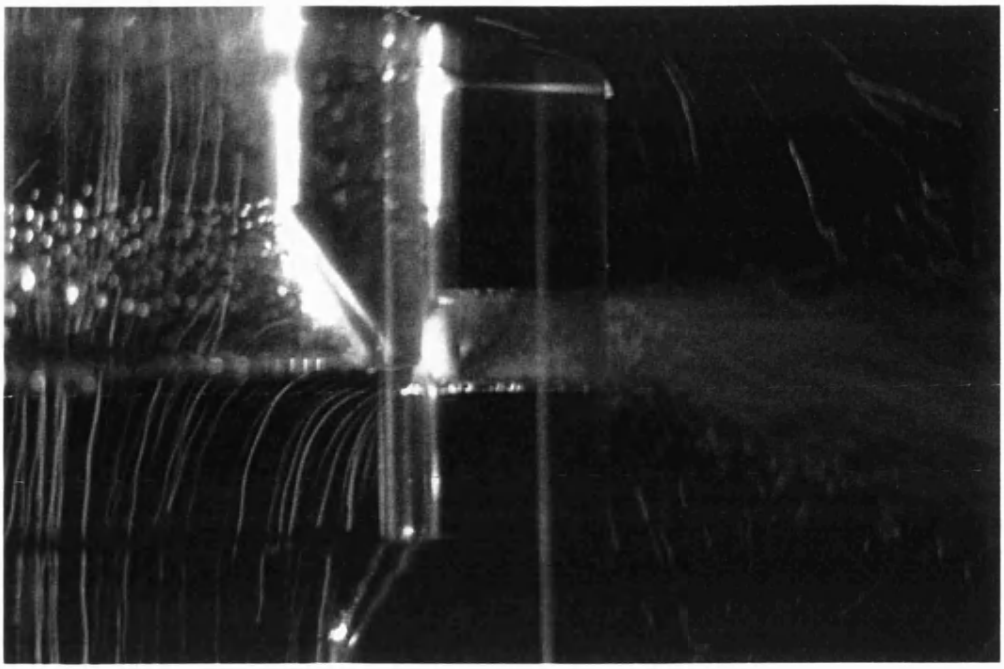

Figure 3.12 Exit hole ¼ open

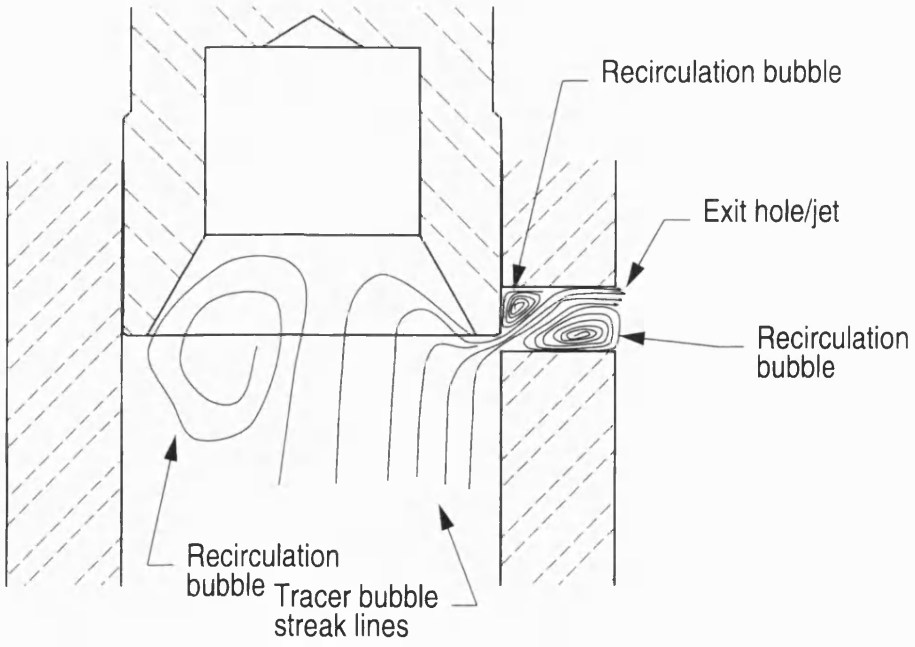

Figure 3.13 Sketch of flow through ¼ open exit hole

In the photographs taken of the flow visualisation experiments, the recirculation bubble in the main valve chamber is partially visible at the left edge of the photo. This results from the asymmetric design of the flow visualisation model and would not be present in the actual valve or a more faithful model of the valve. However, because the recirculation bubble is present in an area of lower velocity compared to the exit hole, it is believed that this recirculation bubble has little influence upon the exiting jet angle.

Another feature visible in the photographs is the countersink region in the end of the valve piston. Streak lines can be seen entering and leaving this region. The influence of the countersink and resulting annular area of the piston edge adjacent to the metering hole was not investigated because of time constraints. Results from a valve developed by the manufacturer in the past that used a similar design suggest that the countersink and annular area of the edge of the piston are relatively unimportant design considerations related to valve performance.

An important observation made during the experiments was that the recirculation bubbles in the exit hole appeared to be unsteady. Recirculation bubbles formed and collapsed multiple times a second in a cyclical pattern. Time constraint prevented investigation into this phenomenon. The implication of the unsteady recirculation bubbles is that the jet angle is not steady for a particular hole opening and flow conditions. This would also be true for the flow coefficient. The result would be that the flow force would also be unsteady since the flow force is linearly related to the cosine of the jet angle as shown in Equation 2.8

The flow visualisation experiments have clearly demonstrated that the jet angle is not constant but changing. **McCloy and Martin (1980)** state in their book that as a circular hole coverage changes from it initial opening to the full opening, the jet angle increases from 69° to 90°. However, it is left to the reader to determine how the jet angle increases as a hole opening changes. A jet angle of 69° is still commonly used in Equation 2.8 to calculate flow force.

3.5 Concluding remarks

Flow visualisation has proven to be a powerful and useful tool to aid in the understanding of the nature of the flow through the load control valve in particular how the jet angle changes with changes to the exit hole opening. The primary goal of qualitatively proving that the jet angles change with hole opening has been met. The results from the flow visualisation experiments were better than expected and led to quantitative measurements on the jet angles. This will prove useful when comparisons are made with CFD results in Chapter 4. Measurements of how the jet angle changed as the hole coverage changed not only reinforces the views of **McCloy and Martin (1980)** but also demonstrates the nature of the changes occurring. Demonstrating that the jet angles change with hole opening lends support to the hypothesis that the tendency of the load

control valve to pressure compensate is related to changing flow forces which are related to changes in the jet angle and flow coefficient.

CHAPTER 4

COMPUTATIONAL FLUID DYNAMICS MODELLING

4.1 Introduction

Computational fluid dynamics (CFD) is the use of numerical methods to solve the governing equations of a discretized flow domain. Governing equations would maintain conservation of mass, momentum, and energy. The most common numerical methods used in commercial CFD software packages are the finite difference, the finite volume, and the finite element methods. The finite volume method seems to be the most popular in current use. This is most likely due to the computational expense of using the higher order accuracy finite element method.

CFD is a powerful analysis tool used to develop an understanding of the nature of fluid flow. CFD was used to simulate the flow through the load control valve. Qualitative results such as streamline curvature, jet separation and reattachment, and areas of recirculation provide insight into the nature of the flow to better understand valve performance. Quantitative measurements made on the results such as jet angles, velocities, and pressures provides more insight into the nature of the flow that is not only useful in developing an understanding of valve performance, but also can be used to predict valve performance when included in a mathematical model of the valve.

4.2 Review of past work

The number of articles published on the use of CFD to study hydraulic valves is limited compared to the amount of literature available on the use of CFD to research other areas such as airfoils or tube banks for example. The majority of the works on hydraulic valves study the flow through spool valves; therefore, in comparison very few articles are published on CFD studies in poppet valves. The majority of the past work attempts to quantify flow forces and to an extent understand the nature of flow forces. One paper in particular studies discharge coefficients in detail. A few papers look at poppet geometry to control flow forces.

Fleming *et al.* (1988) used a commercially available computational fluid dynamics code based upon the finite volume method to examine gas flow through a disc valve. The emphasis of the work was to observe how changing the values of the eddy kinematic viscosity in the turbulence model changed the computed value of the gas force. The work

ended up emphasising computational techniques with turbulence models instead of investigating flows through different valves.

Guo and Nakano (1989) used a boundary element method to study axial flow force compensation in spool valves. The majority of the paper discussed the boundary element method in general terms. The authors also discussed a linear smoothing technique to solve the problem of "zigzag" pressure distributions. Prior to implementing the linear smoothing technique, adjacent boundary elements had pressure values of opposite signs. That was why the pressure distribution was referred to as "zigzag". A "recirculation bucket" on the spool was modelled in two-dimensions. The fluid used in the simulation was viscous and incompressible and the flow was steady. The Reynolds number of the flow in the simulation was 280. Comparison to experimental results from a previous paper did not agree well. The ratio of the flow force caused by the momentum change in the jet flow through the metering orifice to the force in the axial direction generated by the compensation bucket showed a tendency to increase with increasing Reynolds number. The boundary element method simulation did not show this. The authors attributed this to the problems of simulating three-dimensional flows in two-dimensional models.

Ito *et al.* (1992) used a unique combination of numerical techniques to model the flow through a poppet valve. Using the stream and vorticity function combined with the finite-difference method, the steady, axisymmetric, laminar flow was simulated. The flows simulated through a 45° conical poppet valve were of very low Reynolds numbers. The two cited in the paper were 200 and 300. The simulation results showed as would be expected, flow separation at the seat and reattachment to the sidewall of the valve. Comparison of the simulated pressure field in the valve showed less than 10% difference to experimentally measured pressures for flow with a Reynolds number of 200. However, this error was much larger for a Reynolds number of 300. The authors attributed the large error to errors in the stream function and vorticity function calculations. These were prone to error because of the steep pressure gradient through the valve and the convex corner of the poppet. There were no details given on the experimental work. The authors felt that flow forces and pressure distributions would not be significantly affected by turbulent flow and thus the work was just as valid for higher Reynolds number flows. This assumption was left unsupported by the authors. Although the paper was intended to investigate the pressure distributions in poppet valves, the majority of the paper dealt with the unique simulation method developed. When the simulation results did not agree well with the experimental results, the application of the simulation method to the difficult problem was blamed.

Vaughan *et al.* (1992) was a follow up to Johnston *et al.* 1991 (c.f. Section 3.2). The authors demonstrated through the comparison of experimental and CFD results of four different poppet and seat configurations the profound effect that jet separation and reattachment have on the flow, pressure, force characteristics, and susceptibility to cavitation. They pointed out that that the contraction coefficients predicted by von Mises (1917) were developed using potential flow theory assuming inviscid flow. Jet reattachment

and pressure recovery occurring down stream of the vena contracta were also not considered by von Mises.

Vaughan *et al.* found that with a sharp edge seat and conical poppet *valve A* in Figure 4.1, that the jet separation point was fixed by the sharp edged seat. The jet direction was fixed by the poppet angle and reattachment did not occur except where the jet strikes the chamber wall. The CFD simulations for this valve configuration compared well with the experimental results. For the flow force compensated poppet, *valve B* in Figure 4.1, the jet reattached to the seat for a seat diameter to inlet diameter—poppet lift ratio, $Z = L/D$, less than 0.1. For Z greater than 0.1, the jet travelled in a radial direction until it struck the sidewall. This value of Z represented a discontinuity of the plots of valve flow coefficient, c_q, and flow force coefficient, c_f. The resultant values from simulation for c_q were in good agreement with those found experimentally. However, the values of c_f showed some deviation although similar trends were found. These simulations were performed with Reynolds numbers in the range of 10^4 to 10^5 and the simulations used the k-ε turbulence model. For the simulations with the chamfered and chamfered-and-radiused seat, the Reynolds number was 10^4 and the simulation was performed as laminar flow. As with the flow force compensated poppet, the chamfered seat, *valve C* in Figure 4.1, showed a discontinuity in the plot of the results of c_q and c_f. This occurred for Z at 0.04 to 0.05. The jet was attached to the seat for Z less than 0.04 and reattached to the chamber wall for Z greater than 0.05. For the chamfered-and-radiused seat, *valve D* in Figure 4.1, this discontinuity occurred at Z value of 0.1. The simulated results for *valves C* and *D* showed increasing scatter for increasing Z.

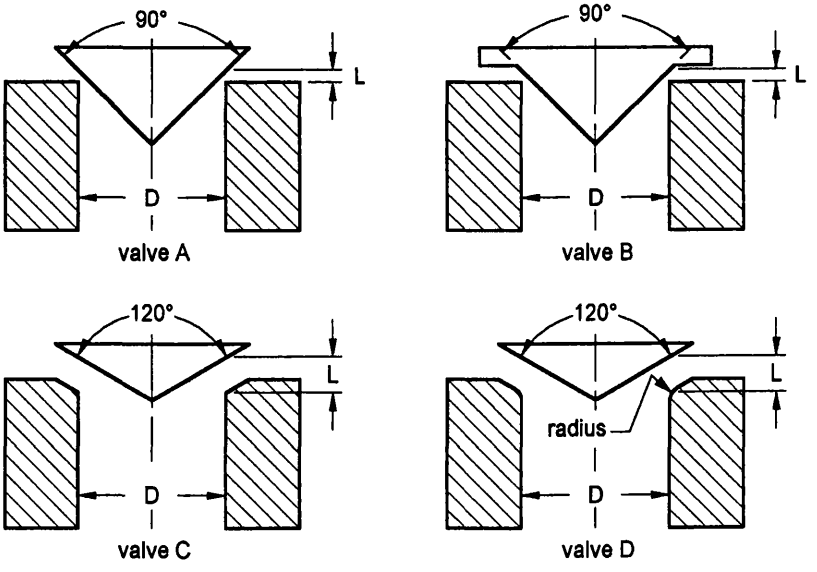

Figure 4.1 Poppet shapes from Vaughan *et al.* (1992)

To understand the source of scatter between the simulation results and experimental results **Vaughan *et al.*** looked at two major areas. Shortcomings in turbulence modelling were one of the reasons for poor correlation of simulation results to experimental results. The k-ε turbulence model does not handle jet separation and reattachment well. The authors also surmised that the pressure and flow characteristics were less sensitive to large-scale downstream recirculation than to the intense small-scale recirculation that occurred in the orifice region. In this region, the high velocities and streamline curvatures caused high body forces in the fluid.

Burnell (1992) conducted a series of simulations and experiments on a pressure drop regulator (PDR) valve used in aviation fuel systems. The objective of the work was to minimise steady state flow forces in the spool valve. Several flow force compensations schemes were investigated. Both two and three-dimensional CFD modelling were used with experimental comparisons made. Of particular interest of the flow force compensations schemes studied was that of the drilled radial holes in a spiral pattern. The limited valve gain and pressure sensitivity of this method were two of the reasons that this study was undertaken. It was found that the flow forces were directly proportional to the pressure drop across the metering holes. The same size and limited number of radial holes used can explain the limited valve gain. However, this provided a linear flow force characteristic. It was found through the research that a further reduction in the flow-force magnitude could be realised in the meter-in configuration if the first hole in the series was angled. This caused the efflux jets to impinge upon the spool land, which generates an opening reaction force.

The CFD analysis was performed using a commercially available code based upon the finite-volume method; the turbulent flow was simulated using the k-ε model. The author acknowledged the limitations of this turbulence model when simulating complex flows involving recirculation, separation, and reattachment. Comparison to experimental results showed that the two-dimensional, axisymmetric model agreed better than the three-dimensional model. Presumably, because of the experimental test limitations, only qualitative comparison of trends was completed. The fluid used was a 95/5 water/oil emulsion. **Vaughan *et al.* (1993)** was a conference paper based upon Burnell's thesis (Burnell 1992).

Several seat configurations were studied for flow force compensation by **Latour (1995)**. The seat of a relief valve was modelled using the finite-element base CFD code FiDAP. The original geometry was not designed to compensate for flow forces. Several edge conditions were modelled. These included chamfer at 45° with various widths as well as different radii. Simulation results were not experimentally verified. A flow force compensating design was modelled and then verified with flow visualisation. The author provided some details of the experimental set-up. Similarity laws used in the scaling of the flow visualisation model were derived in the paper. Flow visualisation was accomplished by injecting particles for tracking in a light sheet that was photographed. Qualitative results seemed to agree well with the simulation results. Although the goal of the research was to

design a flow force compensated relief valve, the resulting valve performance is questionable. The flat and sometimes negative slope on the pressure versus flow performance curve appears to indicate more potential for instability for this valve than the uncompensated valve.

Huang and Kim (1996) modelled flow through a butterfly valve in three dimensions using the commercial finite volume computational fluid dynamics code Fluent. Fluent is based upon Semi-Implicit Method for Pressure Linked Equations (SIMPLE). Only a half model of the valve was modelled due to symmetry. High Reynolds number (greater than 20,000) water flows were modelled. The standard k-ε turbulence model was utilised. The pipe diameter was 25.4 mm and the flap was thin at 1.6 mm. Significant detail on the model building was provided as well as a thorough discussion of the results. Grid independence was verified. The authors demonstrated that reasonable agreement was obtained from calculated pressure loss coefficients when their results were compared to earlier experimental work. Accuracy was sacrificed for reduced solution time. The motivation for the work was apparently to provide a three-dimensional flow visualisation of the incompressible, steady flow through a butterfly valve.

Palumbo *et al.* (1996) compared the results of two different finite element method based CFD programs to theoretical flow force calculations on the spool of a four-position three-way directional valve. A two-dimensional, axisymmetric model was constructed with a structured mesh. Oil was the working fluid. The model was nondimensionalized with reference to the valve opening. Simulations were pressure driven with the inlet boundary pressure condition being specified. No-slip boundary conditions were specified for the walls. The corresponding Reynolds number at the valve opening was 1920 (inlet Reynolds number was 293). Simulations were carried out in the turbulent flow regime with the standard k-ε turbulence model being utilised. While the methods for setting-up the problem differed between the two codes, the results were very similar with only slight differences. The CFD predicted closing force was 258.7 N (58.1 lb_f) for a valve opening of 0.6 mm (0.0236 in). A flow rate was not provided but the maximum rate flow for the valve was 100 L/min (26 US gpm). Theoretical force calculations predicted a force of 212.5 N (47.8 lb_f), a difference of 18%. The authors briefly discussed the experimental validation that was under way at the time, but no results were provided.

Borghi *et al.* (1997) stated the goal of their paper was to find a way to minimise time and effort needed for CFD analysis when applied to hydraulic valves. The study was based upon the analysis of a four-position three way directional valve. The stated maximum flow rate and pressure for the valve was 100 L/min (26 US gpm) and 320 bar (4641 psi). However, the experimental results presented in the paper exceeded this flow rate by more than double. Results for the experimental work showed that the discharge coefficient, c_d, asymptotically approaching a value of 0.6. No comparison of this result to previous research was made. The authors compared their experimental results to their CFD simulation results. The simulations were conducted in the finite-element method based

CFD software FiDAP. A two-dimensional, axisymmetric model was constructed using both structured and unstructured meshes. Each simulation was conducted as both laminar and turbulent. Turbulent simulations utilised the standard k-ε turbulence model. The inlet velocity was the specified boundary condition with no-slip conditions at the walls. The simulations were conducted in a nondimensional form with respect to the valve opening. A non-linear, redimensionalization procedure was implemented to save time in conducting multiple simulations with different inlet velocities for a specified valve opening. With this redimensionalizing procedure developed by the authors, they felt that one simulation only was necessary per valve opening to establish the valve characteristics. This was based upon using the simulation results to calculate the discharge coefficient, c_d, and a regression technique. No details on the regression technique were provided. The laminar simulation results showed considerable disagreement with both the experimental and turbulent simulation results. The turbulent simulation results showed relatively good agreement for larger openings but not as good for smaller openings. The authors went into some detail discussing how they found the true opening position of the valve that had chamfered spool and land edges. This may explain some of the sources for error with the smaller valve openings. In an earlier part of the discussion, the authors stated that they would not be using these results in their analysis, but in the discussion of the analysis, it seems that they did use these results. The authors hypothesised their sources for errors as being both the experimental measure of flow forces and the significant three-dimensional effects of both the computed axial forces on the spool and the computed value for pressure drop. Some of the results showed good agreement while others did not. They did not seem to consider their redimensionalizing scheme as a potential source of error.

The stated topic of the paper by **Borghi *et al.* (1998)** was characterising hydraulic component performance with CFD. The characterisation would make use of the recommendations of previous researchers that experimented with stationary to transitory flow force ratios. The transitory or dynamic flow force was defined as $F_d = \rho L \frac{dQ}{dt}$, where L is the axial length between incoming and outgoing flows. The steady flow force was defined as $F_s = -\rho Q v \cos\theta$, the well known flow force equation. The current work was centred on the pilot stage of a poppet-type relief valve. A two dimensional, axisymmetric model was constructed in the finite-element method based CFD code FiDAP. The standard assumptions of fully developed turbulent field in the restriction, incompressible fluid, Newtonian behaviour, isothermal flow, and constant properties were made. The assumption of incompressible flow was based upon the Mach number being less than 0.2. This standard assumption proves satisfactory, unless extremely fast transients, where the time lag caused by fluid compressibility may affect valve performance, need to be modelled. In this case, a compressible Navier-Stokes formulation would be required. A parabolic velocity distribution was used as the inlet boundary condition. A flow rate of 20 L/min corresponds to a mean velocity of 10.3 mm/s at the inlet. Viscosity of the working fluid was

$28.7x10^{-6}\ m^2/s$. The standard k-ε turbulence model was used. Results for the four valve openings simulated (0.4, 0.7, 1.0, and 1.2 mm) showed a jet form and for all of the openings other than 0.4 mm, the jet reattached to the valve seat down stream of an area of recirculation. The jet in the case of the valve opening of 0.4 mm impacted on a portion of the valve poppet. From the analysis of results, the authors created performance curves for flow and pressure and flow and flow force. The authors through a thorough dimensional analysis briefly discussed in Borghi *et al.* (1997) were able to construct these curves with a single data point. There was no mention of either experimental or theoretical validation of these results. A three-dimensional performance curve was also constructed to demonstrate the relationship between the rate of flow change, dynamic flow forces, and valve opening. The authors stated that from observation of this curve, that it can be noticed that the transient effects rapidly become more relevant than the stationary ones. Again, neither experimental nor theoretical validation was provided. Additional discussion of the transient to stationary flow force ratio suggested that the dynamic flow force reduces the steady flow force by 2.5%. Not enough explanation was given to this suggestion, nor how a single data point can be used to predict valve performance.

Sørensen (1999a) investigated two different flow force compensation techniques for conical poppet valves using both CFD and experimentation. Shell Tellus 32 Oil was the working fluid for both the experimental and simulation. Experimental work was conducted on a test stand capable of 200 L/min (53 US gpm) and 200 bar (2900 psi). Downstream or exit conditions were not specifically discussed but from the sketch of the valve, it appears that the annulus surrounding the poppet is of a volume larger than the poppet itself and has one exit port. Figure 4.2 shows the two different flow force compensation techniques used. The first technique involved changing the angle of the conical poppet, valve, α. Three different values for the angle, α, were tried, 20°, 30°, and 45°. For diverging flow, the valve operated as a direct acting valve. The largest flow force was found with the 20° angle. The relative flow force was found to be nearly linear with respect to the relative valve opening. Because the valve opening area increases with the angle, the relative flow force also increased with decreasing angle, α. The CFD model was a two dimensional, axisymmetric model and created in the software package Star-CD. The RNG k-ε Turbulence model was used. Renormalized group theory (RNG), applied to the k-ε turbulence model and used to simulate flows involving recirculation, produces results that are less diffuse than the standard k-ε model. Both experimental and simulation work was carried out in the range of Reynolds number of 500 to 4600. The sharp seat edge was modelled as a 20-μm chamfer. The simulation results for the 20° and 45° flow coefficients were slightly higher than the experimental results. Speculation on the source of errors included the sensitivity to the chamfer angle and three-dimensional flow effects not simulated in the two-dimensional model. For converging flow in *valve A*, the valve operated as a differential area valve. In this case, the flow forces increased with increasing angle, α. The second flow force

compensation technique included a lip as shown on *valve B* in Figure 4.2. It was found that flow force reduction was dependent on the distance between the valve orifice and the lip, *d* and *h*. The discharge coefficient was not adversely affected by including the lip, but the flow force became sensitive to the kinematic viscosity of the working fluid particularly at small openings.

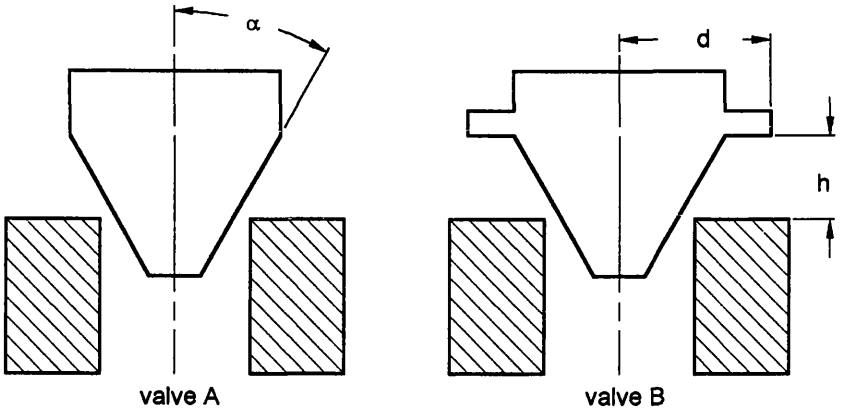

Figure 4.2 Compensation techniques from Sørensen (1999a)

Sørensen (1999b) investigated three poppet styles. As shown in Figure 4.3, the poppet styles were a poppet with a conical seat (*valve A*), a ball shaped poppet with a square seat (*valve B*), and a conical poppet with a square seat (*valve C*). Experimental work was conducted with the same conditions described in **Sørensen (1999a)**. Experimental and simulation work was conducted in the range of Reynolds numbers of between 300 and 5000. Star-CD was the CFD code used for the simulation work. The valves were modelled as two-dimensional, axisymmetric. The RNG-k-ε turbulence model was used for simulating turbulence.

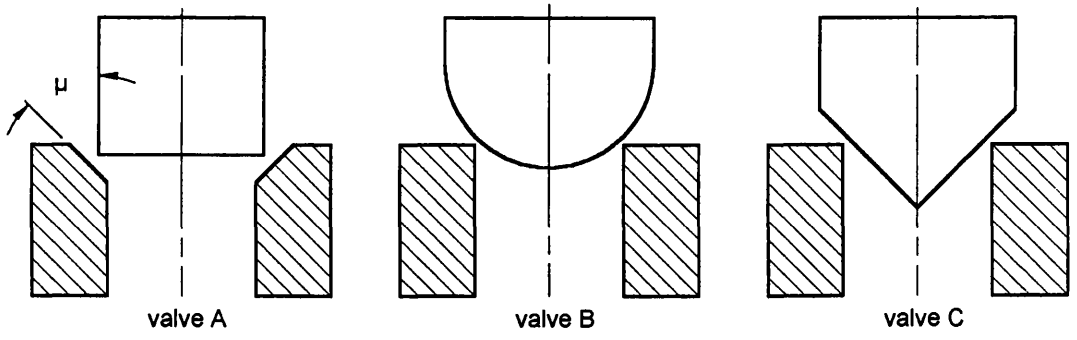

Figure 4.3 Valve styles from Sørensen (1999b)

Simulations of *valve A* demonstrated that decreasing the seat angle decreases the flow forces. Decreasing the seat angle results in a decrease in the angle, μ. Both experimental and simulation results showed a linear relationship between the flow forces and the pressure drop for Reynolds number greater than 600. The author concluded that

the flow force was solely a function of the valve opening. This indicated to the author that turbulent flow prevailed in the examined operating range. The flow coefficient was found to be nearly independent of valve position and dependent on the valve angle, μ.

Simulations for the ball shaped poppet, *valve B*, were conducted at a Reynolds number of 4200. The diameter ratio between the ball and inlet correspond to a 45° angle between the poppet axis and the flow jet. Pressure distributions indicated that the flow force on the high-pressure side of the valve orifice would have increased by decreasing the angle between the flow jet and the poppet axis. On the low-pressure side of the valve orifice, the flow forces increased with increasing flow jet angle simply due to the increasing size of the ball surface. The flow jet followed the shape of the poppet. High velocity along the surface resulted in a decrease in local pressure. A decrease in local pressure increased the flow forces.

For *valve B*, the flow coefficient was found to be independent of the flow jet angle but slightly dependent on the Reynolds number due to the small chamfer at the valve seat. The flow force coefficient was found to be nearly independent of Reynolds number and independent of jet angle. However, at low Reynolds numbers, the flow forces increased with increasing jet angle mainly due to the difference in ball size.

The conical poppet, *valve C*, was investigated with simulations at Reynolds number of 3600. Results were similar to the ball shaped poppet with the highest flow force predicted on the high-pressure side of the valve orifice or upstream of the orifice caused by the restriction. Increasing the poppet angle with respect to the poppet axis decreased the flow forces. The low-pressure side has less effect on the flow forces. For this valve, the results showed a flow force characteristic that varies with the poppet angle.

From the experimental and simulation work, the author concluded that the largest flow forces were obtained with a seat valve with a ball shaped poppet, *valve B*, and the smallest flow forces in the valve with a conical seat, *valve A*. In comparing some of the results for the flow coefficient, the author found good agreement with most of the previous results of Johnston *et al.* (1991), Vaughan *et al.* (1992), and McCloy and McGuigan (1965). The author mentioned that the flow force coefficient was characterised by the influence of the valve geometry on flow force behaviour and therefore depends on the internal flow patterns and pressure distributions in the valve orifices.

4.2.1 Relevance of past work to current work

The articles by Fleming *et al.* (1988), Vaughan *et al.* (1992),and Burnell (1992) acknowledged the limitations of turbulence modelling and the k-ε model in particular. The papers by Sørenson (1999a and 1999b) indirectly acknowledge the limitations and attempt to work around them by using the RNG k-ε turbulence model. Conversely, the articles by Haung and Kim (1996), Palumbo *et al.* (1996), and Borghi *et al.* (1997) used the k-ε turbulence model without recognising the limitations of the model. Careful selection of a

turbulence model is crucial when modelling complex flows involving recirculation, separation, and reattachment (Burnell *et al.* 1992). Turbulence modelling will be necessary in the model of the load control valve. The flow visualisation experiments demonstrated that the flow has strong streamline curvatures and several recirculation bubbles present. Therefore, a turbulence model that avoids isotropic or diffuse results will be necessary.

Ito *et al.* (1992), Vaughan *et al.* (1992), Burnell (1992), Latour (1995), and Sørenson (1999a and 1999b) are all examples of research using CFD to study the effects of flow forces, flow force compensation through geometry modifications. These dealt with poppet type valves except Burnell (1992), which examined a spool type valve. The load control valve is a poppet valve until it works in a metering mode. In a metering mode, it is essentially a spool valve.

Burnell (1992) is an example of three-dimensional CFD modelling. Ito *et al.* (1992) is an example of CFD modelling which produced poor results and hence the two-dimensional model was blamed with suggestions that a three-dimensional model would produce better results. Ideally, a three-dimensional model of the load control valve will be used for the analysis. This will avoid problems of simulating three-dimensional flows in two dimensions.

Borghi *et al.* (1998) is a basic example of using CFD work combined with some basic modelling to predict valve performance. The method discussed for modelling the valve suggests poor results would be obtained; although, no comparison to experimental nor theoretical results were presented. Results from modelling the load control valve will be used to construct an accurate dynamic model.

Vaughan *et al.* (1992) and Sørenson (1999b) included results of variations of flow coefficients among the results presented. Interestingly, Vaughan *et al.* demonstrated that the flow coefficient varies with valve lift while Sørenson (1999b) presented conflicting results that varied with valve geometry. This will be a key issue to be studied with the CFD simulations of the load control valve.

The papers reviewed offer insight into past work that has both produced good results and poor results. When using commercial CFD packages as most of the past work has done, the choices of turbulence models and the number of dimensions to create a model are limited. An important part of using numerical methods to simulate fluid flow is to understand and acknowledge the accuracy and shortcomings of the method used. Commercial packages capabilities are typically in a constant state of improvement. Therefore, limitations seen in past research may no longer be present.

4.3 Coanda effect studies

The flow visualisation experiments demonstrated that jet separation occurs at the metering edge and reattachment occurs or starts to occur within the exit hole. Reattachment and adherence of the jet over wide distances along the wall in the flow direction is known as the Coanda effect, also known as the "tea-pot" effect. Two-

dimensional jets on highly convex, curved walls exhibit this well known effect **(Schlichting, 1979)**. The drilled exit hole has convex walls. The ability of CFD software to adequately resolve jet reattachment related to Coanda effects was a concern early in the research programme. Before developing a model for the load control valve, a model was developed to ascertain the ability of a general CFD code to simulate Coanda effects.

4.3.1 Coanda model description

Matunaga and Hirose (1977) conducted flow visualisation experiments with annular jets that were bi-stable and **Johnston *et al.* (1991)** and **Vaughan *et al.* (1992)** conducted research on poppet valves that exhibited bi-stable jets. Flow visualisation was used in all three studies and CFD was also used in Vaughan *et al.* (1992) to study the flow both qualitatively and quantitatively. The jets studied were bi-stable because of Coanda effects. The jets described by Matunaga and Hirose (1977) switched reattachment points between walls of the outlet tube. Johnston *et al.* (1991) and Vaughan *et al.* (1992) described jets that reattached to the valve seat and then the wall of the outlet as the valve opening increased.

The model created to study the ability of CFD software to capture Coanda effects on separated jets was a two-dimensional, half-section based upon the geometry described in Johnston *et al.* (1991) and Vaughan *et al.* (1992). Figure 4.4 shows the cross-section of the poppet valve that formed the model geometry. The line at the bottom of the drawing is the centre line through the valve. A turning vane similar to that described by Stone (1960) to control flow forces was included on the poppet. FiDAP, a commercially available finite-element base CFD software, was used to create the model. The model was meshed with approximately 7500 quadrilateral elements and 7800 nodes in a structured pattern.

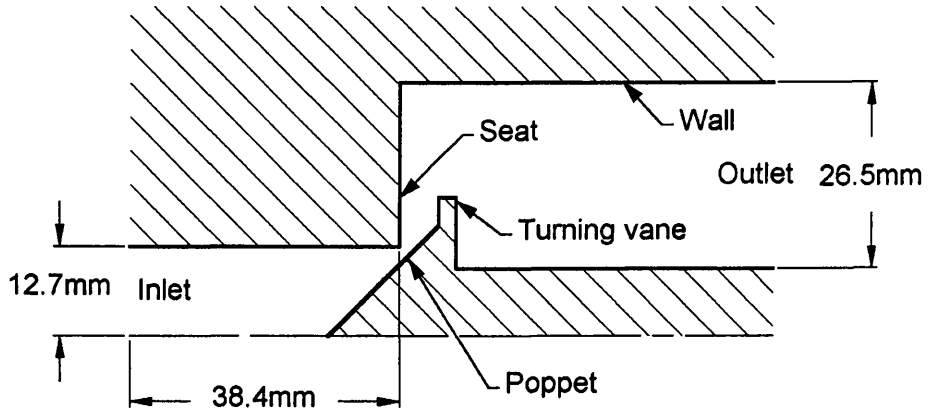

Figure 4.4 Cross-section of model geometry to study Coanda effects

Boundary conditions for the walls were the generally used no-slip conditions. Atmospheric pressure was the outlet boundary condition. A uniform velocity boundary

condition was used at the inlet. The velocity at the inlet corresponded to Reynolds numbers between 1000 and 2000 with the height of the inlet as the length scale. The inlet length was designed to be long enough to allow a velocity profile to develop.

Simulations started with a valve opening that corresponded to the non-dimensional opening of Z=0.10 that exhibited a bi-stable jet in Vaughan *et al.* (1992). The procedure employed was to begin the simulation series at each opening with a velocity corresponding to a Reynolds number of 1000. Subsequent simulations were conducted with the increased velocities corresponding to increments of 100 in Reynolds number. Previous nodal velocities and pressure results were used as initial conditions for the subsequent simulations. The simulations were conducted as steady-state. The fluid properties used in the model were for water. The value for viscosity used was $0.001752 kg/m \cdot s$ and the value used for density was $999.9 kg/m^3$.

The current model did not produce a bi-stable jet for the non-dimensional opening of Z=0.10. After simulating many different openings, results demonstrating a bi-stable jet were produced when the non-dimensional opening of Z=0.15 was modelled.

In spite of the relatively low Reynolds numbers, a turbulence model was used in simulating the fluid flow through the valve model. The use of a turbulence model is justified when considering that the Reynolds numbers calculated were at the inlet and not at the seat where the velocities are significantly higher. Additionally, a critical Reynolds number for pipe flow for example is not applicable for valve flows where the flow path is much less smooth than pipe flow. **Palumbo *et al.* (1996)** also used a turbulence model when simulating relatively low Reynolds number flows through a directional control valve. The RNG k-ε turbulence model was chosen for use in simulating flows through the poppet valve shown in Figure 4.4. As described previously, RNG k-ε turbulence models produce less diffuse solutions than the standard k-ε turbulence model.

4.3.2 Coanda model results and discussion

Results from eight of the twenty simulations are shown in Figure 4.5 as velocity contours. The results show that initially the jet reattaches to the seat although there is a small recirculation bubble present. As the velocity increases with the fixed opening, the Reynolds number increases and the jet reattachment lifts from the seat edge to the wall. As the velocity continues to increase, the jet reattachment moves further up the surface of the wall. As the jet reattachment point moves from the seat edge and up the wall, the recirculation bubble increases in size.

As part of the simulation procedure devised, once the maximum velocity was reach that corresponded to a Reynolds number of 2000, the velocity was incrementally decreased in steps corresponding to decreases in Reynolds numbers of 100. However, unlike when the velocities were increasing, the jet reattachment did not move. The jet reattachment remained at its full extent along the wall.

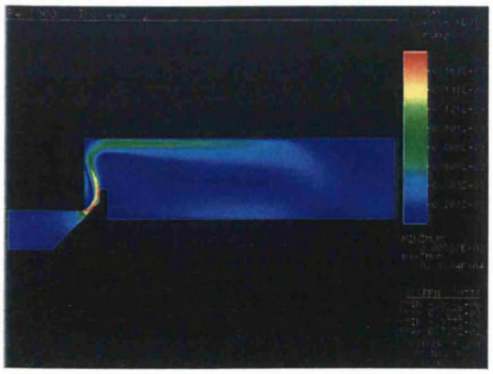

(a) Re=1000

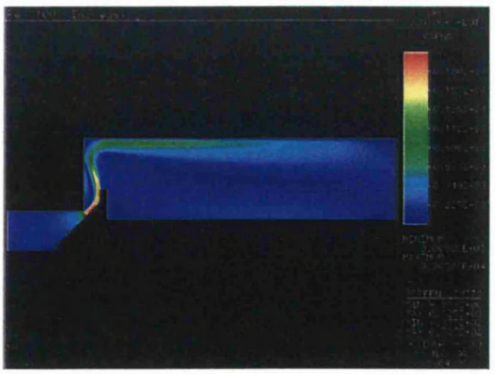

(b) Re=1100

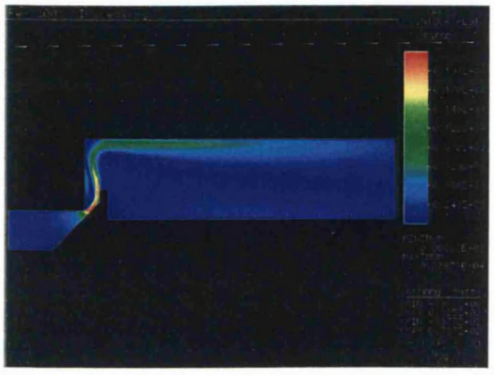

(c) Re=1200

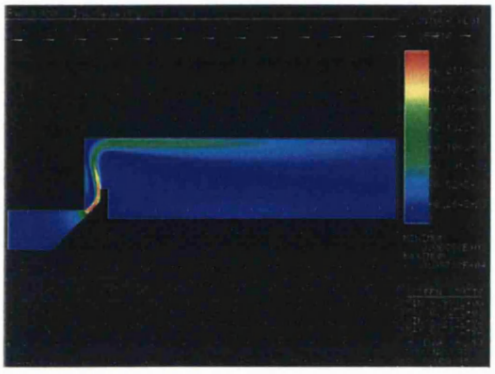

(d) Re=1300

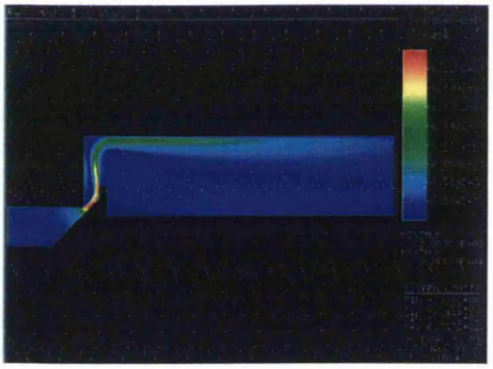

(e) Re=1400

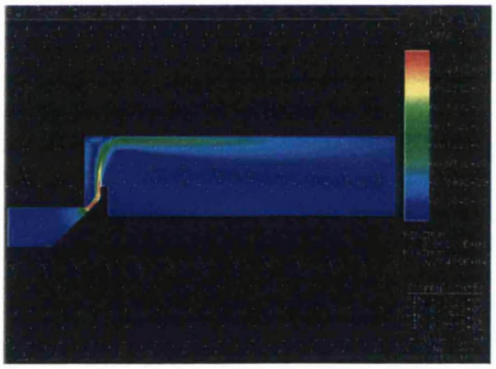

(f) Re=1500

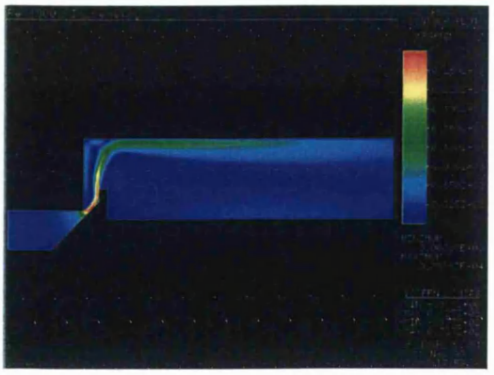

(g) Re=1600

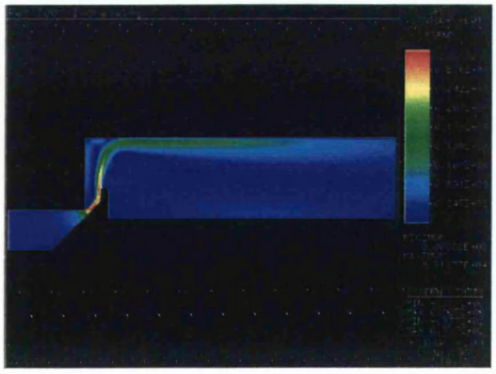

(h) Re=1700

Figure 4.5(a-h) Velocity contour plots from Coanda study [*mm/s*]

The results of the simulations demonstrate that, CFD is capable of modelling Coanda effects. The regions of jet reattachment agree well qualitatively with the results reported in Johnston *et al.* (1991) and Vaughan *et al.* (1992). As reported, it was found that the point of jet reattachment is sensitive to the valve opening; but, unlike the results reported, the jet also demonstrated sensitivity to Reynolds number when the opening is fixed.

4.4 Load control valve model description

The review of past work demonstrated the importance of modelling the valve flow in three dimensions when the valve is not axisymmetric. Generally, earlier works conducted simulations in two-dimensions or two-dimensional-axisymmetric, but works that are more recent have progressed to three-dimensions. This eliminates the concern of getting a true understanding of the three-dimensional flow from a two-dimensional simplification. Thus, CFD software capable of modelling in three dimensions was a very important criterion considered when selecting software for the current research. The commercial CFD package CFX-5 from AEA Technology Engineering Software (Harwell Laboratories, Oxfordshire, UK) was selected because of the relative ease in which a three dimensional model can be created and meshed. Other packages evaluated required a multi-block approach. This type of approach requires that the model be broken into multiple blocks and meshed independently. Although the blocks are meshed independently, the nodes from adjacent blocks must be coincident. This proved to be problematic for the complex geometry of the MBEM valve.

Even though CFX models three-dimensional flows easily compared to other packages, it proved to have shortcomings that forced the valve model to be simplified. It was found that the code had difficulty when trying to mesh the geometry around compound curves. Compound curves were generated from the intersection of the cylindrical outlet hole with the cylindrical flow path within the valve body. The meshing problem stemmed from the global tolerance that was necessary for the entire valve model. To overcome this problem, a simplified valve model was developed. The simplified valve model geometry was built using square cross-sections of the same width as the circular cross-sectional diameters of the main chambers of an actual valve.

Another valve model simplification was the use of a single exit hole for most investigations. As has been discussed previously, the production valve has five series of four holes. In the previous chapter on flow visualisation, it was argued that a faithful scaled model of the production valve with all twenty cross-holes would have obscured the view in an exit hole and made it impossible to study the changing jet angles. While this would not have been the case with the CFD model, to keep the CFD studies more generic, simpler, and more comparable to the flow visualisation studies, a single exit hole was used. For consistency with the experimental work, each of the five hole sizes were modelled as quarter, half, three-quarters, and as fully open.

A cartridge valve such as the MBEM when installed in the cavity machined for it in a manifold has an annular exit area. The chapter on flow visualisation discussed omitting the sleeve that formed the annular exit area for the acrylic model to prevent distorting the view. In the CFD modelling, the full annular area was omitted partly to simplify the modelling, partly to avoid further problems with meshing, and partly to keep the solution times relatively small. Therefore, only a partial annular area was included in the model.

While the simplifications used to generate the CFD model are not realistic, it is believed that the effects of the squared geometry and single exit hole are minimal when the results are analysed for the parameters used in calculating flow forces. The squared geometry would introduce areas of recirculation in the corners that would not be present in the true circular geometry. However, since the corners are a significant distance from the exit hole, the local velocities in the recirculation bubbles would be relatively low. Hence, the calculation of jet angles, presented in the following pages, would show little difference if a more realistic geometry could have been used. The use of the single exit hole and partial annular exit area introduce a significant difference in pressure difference through the valve when compared to an actual valve. To compensate for this difference, the boundary conditions were adjusted as discussed in the following below.

The typical solution times for the model were approximately thirteen to fifteen hours on average. The software was run on a dual Pentium II-400 Xeon parallel processors PC with one gigabyte of RAM.

An automatic meshing algorithm in CFX was used to generate the meshes. Mesh control parameters are used to specify localised mesh densities. The mesh was graded more densely in regions of greater interest such as around the metering edge and in the exit hole. A structured, hexahedral mesh is generated for regions near walls to accurately capture wall effects. The mesh is constructed from what the CFX software calls inflated cells. These inflated cells are also user controlled with inflation control parameters. Typical mesh densities used were of the order of 850,000 elements.

The purpose of meshing the continuum of the valve flow path is to discretize it so that the governing equations for the flow can be solved at discrete points. That is the essence of the finite-difference method. Closely related to the finite-difference method is the method employed by CFX, the finite-volume method. In the finite-volume method, the equations are solved for the discrete volumes instead of discrete points. As **Anderson (1995)** states, the finite-volume method is a discretization of the integral form of the governing equations (also see CFX Users Guide). The equations are solved using a coupled solver in CFX. A segregated solver is commonly used in other CFD codes. With a coupled solver, the governing equations are solved as a single system instead of solving them individually in a 'guess-and-correct' manner.

The flow through the MBEM valve model is in the turbulent regime. Depending upon the inlet velocity (an inlet boundary condition) of the oil entering the valve model, the Reynolds number at the inlet varies between approximately 825 and 2004. However, at the

outlet, the velocity is much higher and therefore the Reynolds number is much higher even with the smaller diameter. Reynolds number is proportional to the length scale or diameter and is defined by equation 4.1.

$$Re = \frac{\rho v D}{\mu} = \frac{vD}{\nu} \tag{4.1}$$

At the outlet, the Reynolds number varies from about 6500 to 18000. The peak Reynolds number is at the metering edge. Reynolds numbers in this region are of the order of 200000 with the diameter or length scale defined by a hydraulic diameter as shown in equation 4.2.

$$D_h = \frac{4A}{\mathrm{P}} = \frac{4 \times area}{wetted \cdot perimeter} \tag{4.2}$$

Unlike flow in pipes, the critical Reynolds number for flow in valves is undefined. Classifying flow as turbulent when the inlet boundary condition is below the critical Reynolds number for pipe flows of 2300 **(White 1986)** has been documented previously **Palumbo *et al.* (1996)**. One rationale behind the use of turbulence models is that valve flows are naturally chaotic because of changing directions and strong streamline curvatures.

Numerical simulation of turbulent fluid flow requires the use of turbulence models to accurately and efficiently model turbulent flow behaviour. While specialists using specialist codes can accomplish direct numerical simulation, the general purpose CFD codes all still use some sort of turbulence modelling. CFX has several options available for turbulence modelling. The option used for the current CFD studies was the differential (or simplified) Reynolds-Stress-Model (RSM) with the Speziale-Sarkar-Gatski (SSG) pressure-strain correlation **(CFX Users Guide 2001 and Wilcox 1994)**.

Simulations of the valve flow were conducted as velocity driven flows. In other words, an inlet velocity condition was specified, but no inlet pressure boundary condition was specified. The alternative to a velocity driven flow is a pressure driven flow. Specifying inlet velocity boundary conditions would seem to be a better practice, as velocity is a conserved term through the conservation of momentum equations. Pressure is a calculated term and not conserved directly. A uniform velocity distribution was specified with an inlet length long enough to allow a velocity distribution to develop. The chaotic nature of the flow in hydraulic valves makes specifying a particular inlet velocity profile guesswork. The values specified could not be determined experimentally since a valve such as the one modelled with a single exit hole and a partial annular area does not actually exist. Therefore, the values for the inlet velocity had to be calculated. Initially, the inlet velocity boundary condition was calculated by dividing the total flow rate when a series of holes was completely uncovered by four. When flow rate for the larger hole series was being computed in this manner, the total flow rate was assumed to flow through the hole series for which the flow rate was being calculated and with no flow through the smaller holes. The consequence of this was that the pressure difference between the inlet and outlet became unrealistically high. The approach that proved to be successful was to calculate the inlet velocity based upon a prescribed pressure difference using equation 4.3 below. The

standard orifice equation, equation 4.4, and equation 4.5 are used to derive equation 4.3. Equation 4.5 shows that the mean local velocity is calculated as the quotient of the flow rate and local flow area.

$$\Delta P_{inlet-outlet} = \frac{\overline{\rho v^2}}{2c_q^2} \tag{4.3}$$

$$Q = c_q A \sqrt{\frac{2\Delta P_{inlet-outlet}}{\rho}} \tag{4.4}$$

$$\bar{v} \equiv \frac{Q}{A} \tag{4.5}$$

An approximate 250 bar (3675 psi) pressure difference was used as a guide to specify the inlet flow rate and hence inlet velocity. Table 1 lists the inlet velocity boundary conditions for the fourth hole series. This fourth hole series was scaled for the flow visualisation experiments. The outlet boundary condition was specified as atmospheric pressure for most cases. However, when unrealistically low minimum pressures were calculated indicating cavitation was likely to be occurring, the outlet pressure boundary condition was changed. "Backpressure" was added. Typically, this was in the range of 10 to 20 bar (147 to 294 psi). This range of backpressure could realistically be encountered in typical field applications. A no-slip condition was specified as the boundary condition for all of the walls. While CFX has the ability to specify the surface roughness of walls, this facility was not used. It was found that when the surface roughness was specified, solution convergence became much more problematic to the point that solutions often diverged. On non-metering surfaces, the maximum surface roughness is specified on part drawings as 3.18 microns (125 micro inches). On metering edges, the maximum surface roughness specified was no greater than 0.406 microns (16 micro inches).

Table 4.1 Inlet velocity boundary conditions

Opening	Quarter	Half	Three-quarter	Full
Velocity [m/s]	1.5	3.8	6.2	7.6

4.4.1 Convergence criteria

Convergence is the tendency of a solution to move toward uniformity and is the goal of all non-linear analysis. Convergence is a relative measure of solution residuals from iterative computations. A simplified and generalised set of equations to describe the calculation of residuals is shown as equations 4.6 through 4.9 were provided in the **CFX Users Guide (2001)**. In equation 4.6, $[A]$ is the coefficient matrix, $[\phi]$ is the solution or variable vector, and $[b]$ is the constant or right-hand-side matrix or vector.

$$[A][\phi] = [b] \tag{4.6}$$

Starting with an approximate solution, ϕ^n, a correction factor, ϕ', is applied and a better solution ϕ^{n+1}, is calculated as shown in equation 4.7. This is an iterative process.

$$\phi^{n+1} = \phi^n + \phi' \tag{4.7}$$

The correction factor, ϕ', is calculated through the time rate of change of the coefficient matrix as shown in equation 4.8.

$$\dot{A}\phi' = r^n \tag{4.8}$$

The residual is calculated from equation 4.9 for each degree of freedom such as velocities, conservation of mass, and the turbulence terms.

$$r^n = b - A\phi^n \tag{4.9}$$

The default convergence criterion employed in CFX is 0.0001 normalised by Log_{10} of the root mean square of the residuals. The RMS of the residuals is found by squaring all the residuals, taking the mean, and then taking the square root **(CFX Users Guide 2001)**. Generally, the maximum residuals would be expected to be one order of magnitude greater than the RMS residuals or 0.001. However, this was not the case for the models of the load control valve. The typical level of convergence achievable was with RMS residuals of 0.0005. With this level of convergence, the maximum residuals were two orders of magnitude higher. With a well-behaved solution, convergence to a maximum residual of 0.001 was possible. At this level, the RMS residuals were typically in the range of 1×10^{-5} or lower. Convergence can be limited by the problem specified, the mesh density, the turbulence model, and the type of processor in the computer used.

In addition to the quantitative measure of convergence, a qualitative one was employed. The normalised residuals were plotted during the solution phase. A solution that met the quantitative measure of convergence although the residuals showed oscillations in the solution were not accepted. A sample of a convergence plot for the governing equations is shown in Figure 4.6. The turbulence equations have separate convergence plots.

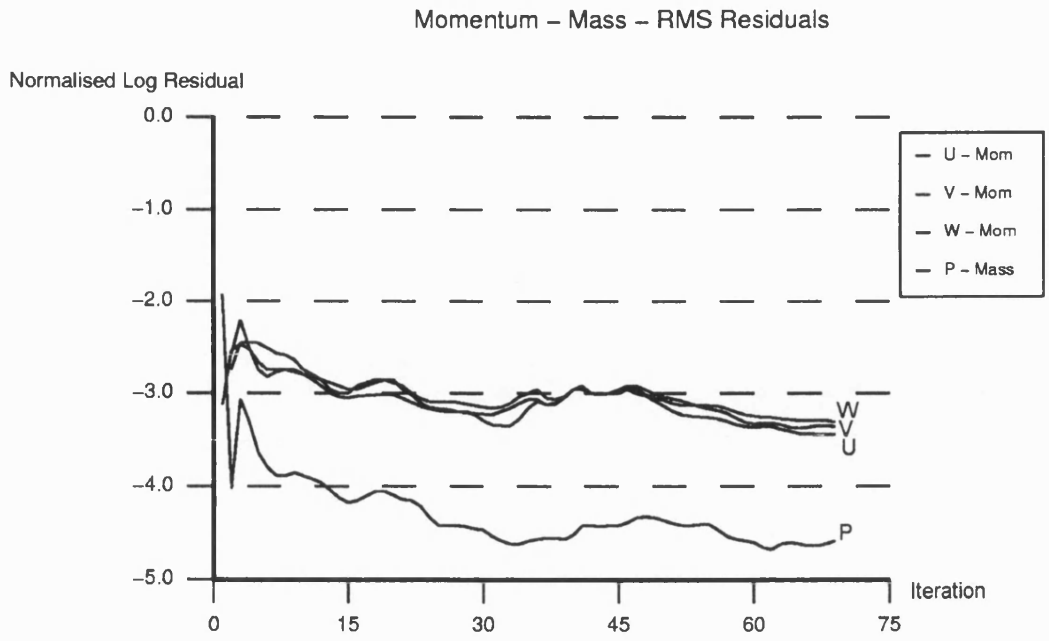

Figure 4.6 Typical convergence history plot

4.4.2 Grid independence study

Prior to discussing the results of the CFD modelling of the load control valve, a brief discussion on grid independence is in order. Applying numerical methods to physical problems always involves a certain amount of uncertainty. In order to limit the uncertainty and develop a level of confidence in the accuracy of the solution, a grid independence study is conducted. This demonstrates that the solution obtained from the CFD simulation does not change with mesh density.

A single valve geometry was meshed with different mesh densities as the procedure employed to conduct the grid independence study. The geometry used consistently throughout the grid independence study was that for the case of the single, fourth exit hole being half open. The hole diameter was 1.98 mm (0.078 inch). The maximum number of nodes represented the practical machine limitations of running the solution entirely in the physical memory of the PC as opposed to disk swapping to the virtual memory. A node count of 7619 represented 36524 elements and was the smallest mesh simulated. A node count of 383945 represented 2057023 elements and was the maximum simulated. Simulations were run until the convergence criterion discussed in section 4.4.1 was reached.

Velocity was chosen as the variable to focus on for the grid independence study because of its importance when calculating jet angles. As previously mentioned, velocity is conserved through the conservation of momentum equation. Results for the maximum velocity calculated during each simulation are shown in Figure 4.7. This demonstrates in a

general sense the dependence of the solution on the grid density. As can be seen, the maximum velocity appears to be approaching 250 m/s asymptotically.

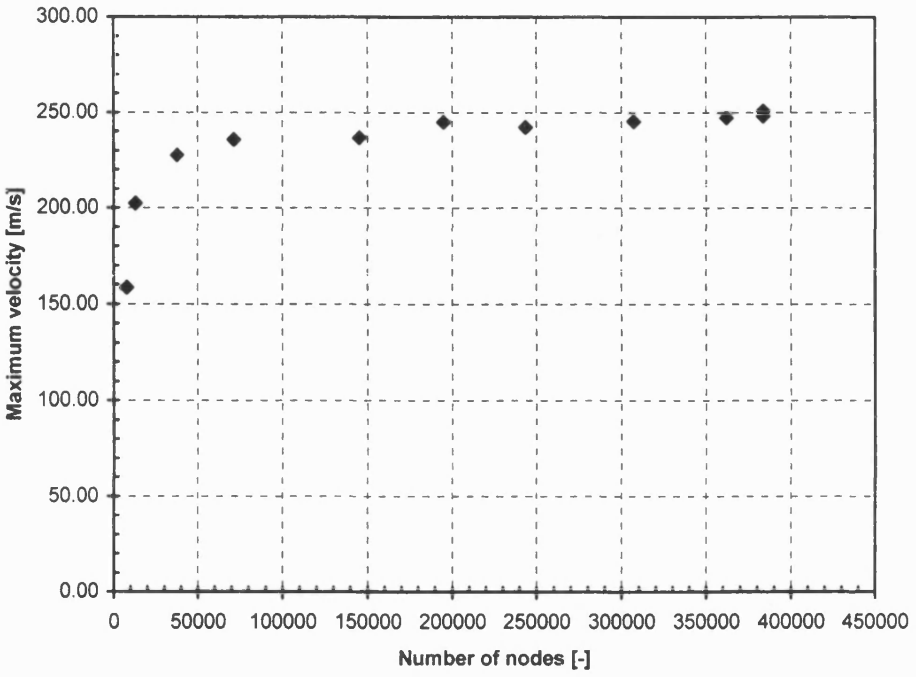

Figure 4.7 Maximum velocity calculated with different node counts

In addition to examining the maximum velocity as part of the grid independence study, the components of velocity used to calculate the exiting jet angle at the metering edge were examined. The individual velocity components were obtained directly from the results of the simulations while the jet angles were calculated from the components using equation 4.10. More in depth discussion on jet angles and their importance follow in Section

$$\theta = \arctan\frac{v_y}{v_z} \qquad \textbf{(4.10)}$$

4.5. Results are plotted in Figure 4.8. The data appears to asymptotically approach a maximum value of approximately 68°. It would appear that more nodes would be necessary to demonstrate this trend conclusively. However, the trends in the velocity components show more conclusively that a maximum has been reached. The jet angle function in equation 4.10 exaggerates the difference by combining the two differences into a single variable. Besides, the maximum number of nodes shown, 383945, is the practical limit of the maximum size mesh possible for the PC used.

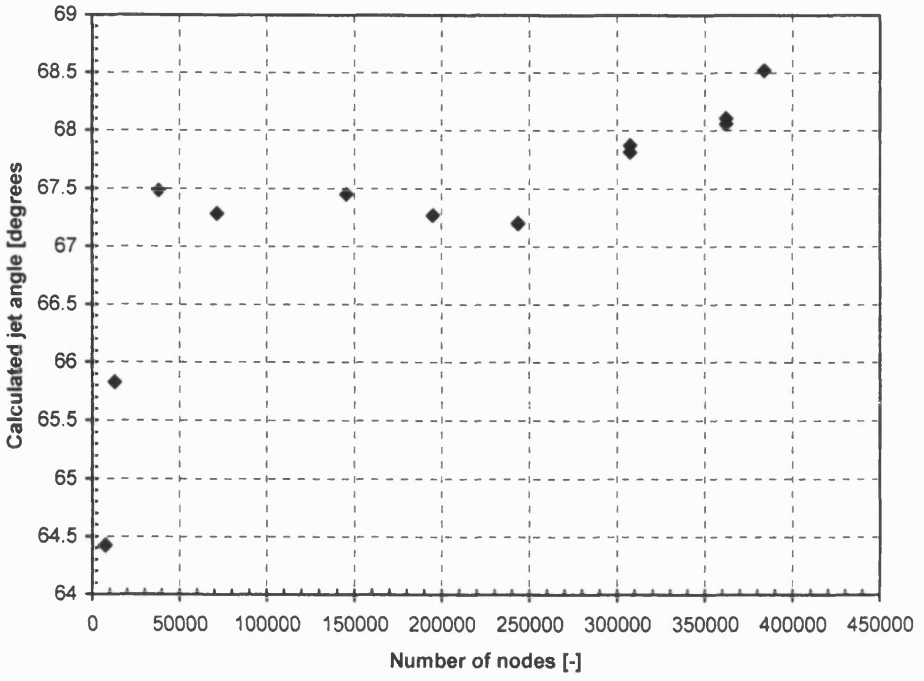

Figure 4.8 Jet angle calculated with different node counts

Based upon the results of the grid independence study, the use of approximately 760000 to 1200000 elements and 245000 to 362000 nodes produce results with reasonable independence of the mesh density. The modelled flow domain increased with decreasing exit hole coverage and increasing exit hole size. With the increasing flow domain, the number of elements and nodes increased. While more elements and nodes could have been used, the numbers used were a balance between reasonable grid independence and cost in terms of time for computation. Typical solution times ranged from six up to twenty-four hours for the PC used. Furthermore, turbulence models that use wall functions have the shortcoming that refining the mesh does not necessarily give a unique solution of increasing accuracy **(Grotjans and Menter 1998)**.

4.5 Results and discussion

The geometry used in the CFD model as previously described in section 4.4 was a simplification of the actual valve geometry. Model geometry of the simplified valve was built using square cross-sections of the same widths as the circular cross-sectional diameters of the main chambers of the actual valve. The inlets for the valve models shown in Figures 4.8 through 4.12 are not shown, but the inlets would be at the bottom of the model if it were shown in smaller scale. The single outlet hole shown in the valve models was the other simplification made in modelling the simplified valve. A section of the annular area of the valve cavity acts as the outlet for the model.

Figures 4.9 through 4.12 show vector plots of an simplified valve model that corresponds to the real valve for the inlet velocities listed in Table 4.1 above. It is immediately evident that the qualitative agreement between the CFD results and the flow visualisation photographs in Figures 3.6, 3.8, 3.10, and 3.12 of Chapter 3 is good. This is particularly evident in the simulations with the partially open holes. The results for these simulation shows the recirculation bubbles in the exit hole as can be seen in the flow visualisation photographs.

By conducting quantitative analysis on the CFD results, the average jet angles were computed from the ratio of the mean radial and axial components of the velocity through the plane of the metering orifice. The results for the fourth hole series are tabulated in Table 4.2, column 2. Also listed in Table 4.2, column 4 are the values of the jet angle measured from the flow visualisation photographs. Unfortunately, because of glare caused by the cylindrical geometry, it was not possible from the flow visualisation photographs to measure the jet angle directly at the metering orifice, and instead the jet angle was measured slightly further downstream within the circular exit hole. To allow a direct comparison between CFD and flow visualisation results, the jet angles were also calculated from CFD results at a similar location within the exit hole, and these are also listed in Table 4.2, column 3. It should be noted, however, that the jet angle at the plane of the metering orifice (column 2 for CFD results) is the relevant one to use in calculating the flow force using equation 4.10 and this angle cannot be obtained from the flow visualisation photographs.

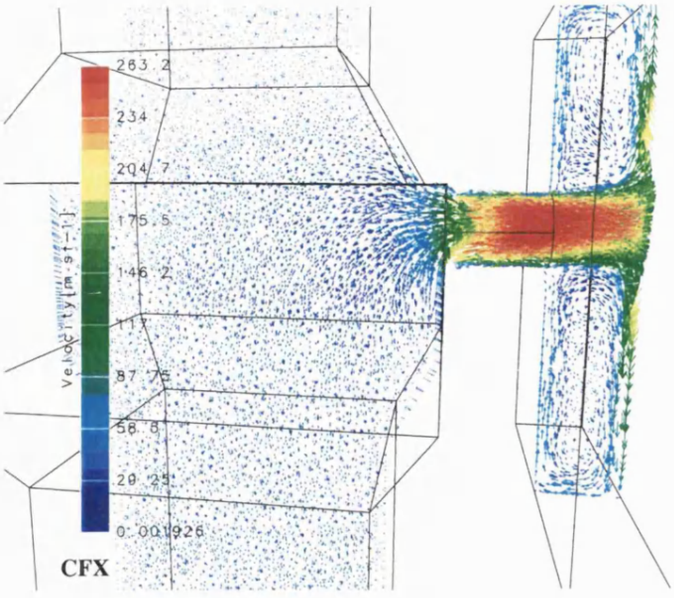

Figure 4.9 Simplified valve with exit hole fully open

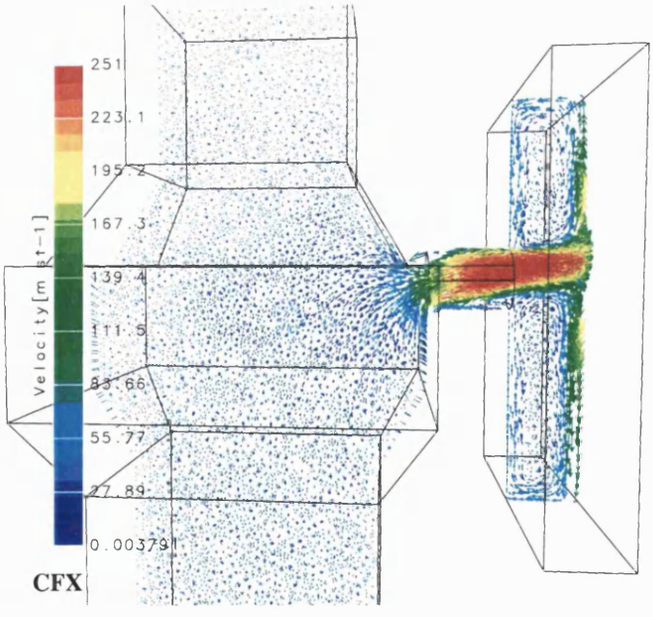

Figure 4.10 Simplified valve with exit hole three-quarters open

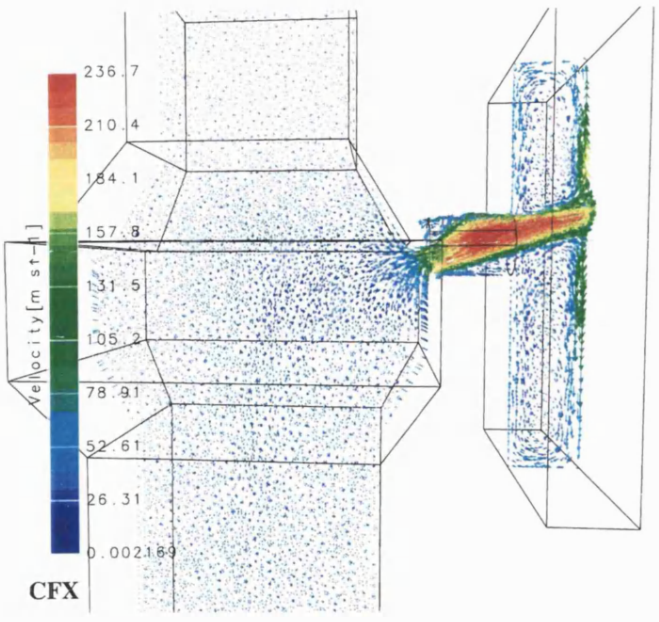

Figure 4.11 Simplified valve with exit hole half open

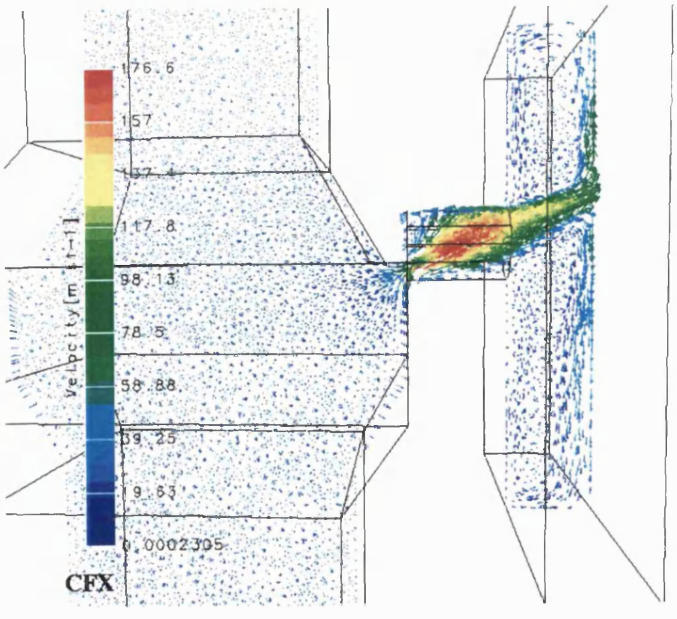

Figure 4.12 Simplified valve with exit hole quarter open

Table 4.2 Jet angles for the fourth hole series

Hole opening	*Jet angle [degrees] at metering edge from CFD*	*Jet angle [degrees] within exit hole from CFD*	*Jet angle [degrees] within exit hole from flow visualisation*
Full	84°	89°	86°
¾	71°	78°	78°
½	67°	71°	74°
¼	61°	66°	67°

The two series of values for jet angle within the exit hole (third and fourth columns of Table 4.2) compare well, especially when considering the potential error introduced in measuring the jet angles from the photographs and from the CFD results. An estimate of measurement error is ± 5°, and the difference between CFD and flow visualisation results is within this error band. This instils confidence in the CFD results. It should be noted that there is some difference between the jet angles obtained from CFD at the metering edge and within the exit hole, the angles being somewhat greater within the exit hole as might be expected with the jet turning toward the direction of the exit hole.

Anderson (1995) suggests that rigorous error analysis of numerical methods is the purview of applied mathematics as opposed to the field of mechanical engineering, but the source of errors must be appreciated by the user of CFD codes. Error in numerical methods such as the finite volume method used within the CFX code are subject to both discretization error and round off error. Discretization error is the difference between an exact analytical solution to the governing equations and an exact solution to the corresponding finite volume equations. Round off error is the numerical error introduced by repetitive calculations in which a computer rounds numbers to some significant figures. As Anderson demonstrates, round off error is related to mesh spacing through a wave number. However, even with a very fine mesh or a 'perfect' computer with no round off error, the error is in actuality related to the time wise behaviour of the solution itself (Anderson 1995). For further reference, consult the **CFX Users Guide (2001)** and **Anderson (1995)**.

The jet angle changes with the valve opening. McCloy and Martin **(1980, p. 184)** briefly noted that as a radial exit hole is first uncovered the jet angle is 69°, but increases to 90° as the hole is uncovered completely. There was no quantification for the jet angle between 69°and 90° as the hole is progressively uncovered. The importance of quantifying the jet angle from when a hole is first partially uncovered until it is completely uncovered can be demonstrated by computing the flow force. By considering the momentum of fluid passing in and out of a control volume between the valve inlet and the metering orifice, the following well-known equation (4.11) can be obtained for the flow force when certain assumptions have been made. These assumptions include that the fluid is nonviscous and incompressible, the diameter of the orifice is large compared to its length so that the flow

can be considered two-dimensional, and that the flow is quasi-irrotational immediately upstream of the orifice which allows for the application of classic hydrodynamics theory **(Blackburn *et al.* 1960)**.

$$F = \rho Q v_{out} \cos\theta - \rho Q v_{in} . \quad \textbf{(4.11)}$$

As an example of computed flow forces and to demonstrate the sensitivity to the jet angle, Table 4.3 was constructed for a single hole from the fourth series of holes (1.98 mm diameter or 0.078 inch diameter) half open. The flow force equation took the form shown in equation 4.12 in computing the values in Table 4.3. The jet angle, θ, was computed from the CFD results using equation 4.10 and was measured from the flow visualisation photos as described in Chapter 3. The velocity, v_{out}, used in equations 4.11 and 4.12 is the maximum velocity.

$$F = \rho A_{out} c_q v_{out}^2 \cos\theta - \rho A_{in} v_{in}^2 \quad \textbf{(4.12)}$$

The outlet area is the opening area of the hole being uncovered and is calculated from equation 4.13 also given in a similar form as equation 2.2 **(CRC 1996)**. In equation 4.13, R is the hole radius and h is the segment height.

$$A_{out} = R^2 \cos^{-1}\frac{R-h}{R} - (R-h)\sqrt{2Rh-h^2} \quad \textbf{(4.13)}$$

The values of theta used were those in Table 4.2, column 2 for the CFD computed value of theta and Table 4.2, column 4 for the flow visualisation measured value of theta. As can be seen by comparing the values for the computed value of flow force, a relatively small change in jet angle has a drastic effect on the computed flow force. Hence, the sensitivity of the flow force equation to the jet angle is demonstrated.

The flow coefficient, c_q, was also computed from quantitative analysis of the CFD results. The flow coefficient differs from the discharge coefficient; with the discharge coefficient, the outlet pressure is measured at the vena contracta of the jet. For the calculation of the flow coefficient, the outlet pressure after pressure recovery has taken place, downstream of the vena contracta, is used. The flow coefficient was calculated from equation 4.14.

$$c_q = \frac{Q\sqrt{\rho}}{A_{outlet}\sqrt{2\Delta P_{inlet-outlet}}} \quad \textbf{(4.14)}$$

Table 4.3, column 4 lists the values of c_q calculated. The variation in values, from 1.02 to 0.77, would have an indirect effect on the calculation of flow forces that is potentially significant. Values for the flow coefficient greater than 1.00 for small openings have been previously reported **(Johnston *et al.* 1991)**. Values greater than 1.00 are generally indicative of pressure recovery due to jet reattachment.

Table 4.3 Comparison of jet angle sensitivity in flow force computation for fourth hole series

Hole opening	*Inlet flow rate [L/min]*	*Inlet velocity [m/s]*	*Flow coefficient [-] from CFD*	*Computed flow force [N] using CFD jet angle at metering edge*	*Computed flow force [N] using jet angle from flow visualisation*
Full	35.0	7.6	0.77	7.5	5.0
¾	38.2	6.2	0.79	19.4	12.4
½	17.5	3.8	0.83	15.2	10.7
¼	6.8	1.5	1.02	9.0	7.3

For comparison of force levels, the initial pre-compression of the three nested springs results in a force of about *40 N* and at the maximum stroke, the force from the springs is about 320 *N*. Table 4.3 shows the flow forces for the single, half open hole from the fourth series. Accounting for all of the holes in each of the five series, the flow force is of the same order as the spring force. In contrast, the pressure-force acting upon the differential area of the piston between the load port and the end in the spring chamber with the maximum rated pressure of 350 bar is just over 3 *N*. This should demonstrate the relative importance of flow forces to the valve performance.

In addition to the valve modelling with the hole size corresponding to the fourth series of holes which is also the hole size modelled in the flow visualisation experiments, the remaining four hole sizes were also modelled. As done with the fourth hole series, the holes for series 1, 2, and 3 were modelled with four different opening positions. The fifth series of holes was only modelled with a quarter and half openings (a half opening is the largest physical opening possible in the fifth hole in the MBEM valve due to stroke limitations on the moving piston).

In addition to the differences already discussed between the valve model and the actual valve, the model lacks the full annular exit area. A partial annular area was included in the model, but the full area was not included to simplify the model and avoid meshing and solver problems.

To demonstrate the consistency and trends in the jet angles computed, the results from computation of the exit jet angles were plotted as shown in Figure 4.13. In the graph of the results, the fully closed position of each hole was plotted using the value of the quarter open position. These plotted points are circled on the graph. The points were plotted to clearly show the overlap that is present between the five series of holes. The trend that becomes apparent from studying the graph of the results is the rate that the jet angles approach the maximum value of approximately 90° changes with the hole diameter. The slope of the plotted results is much more steep for the smaller diameter holes such as in

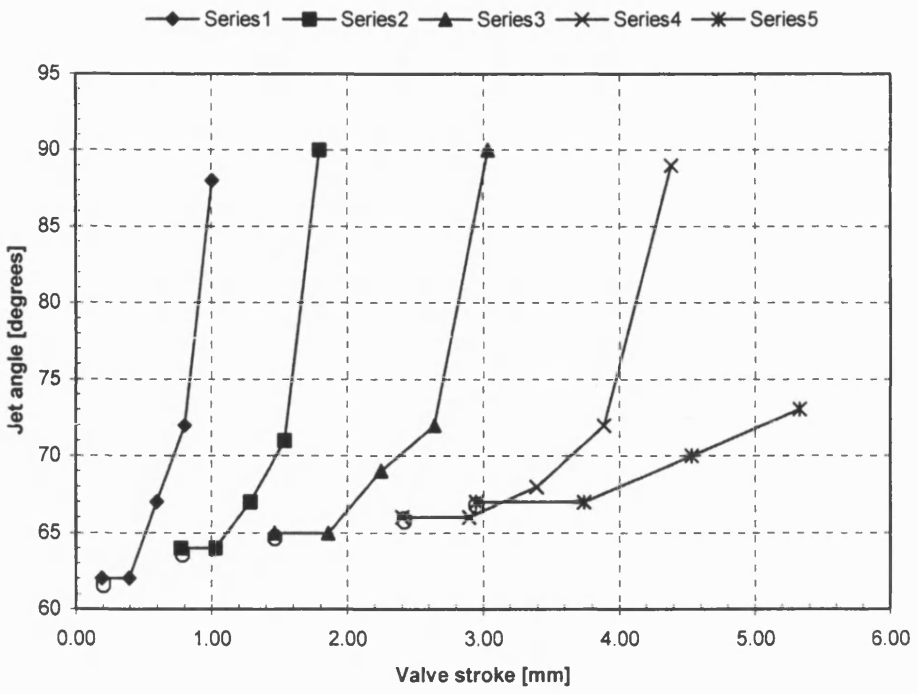

Figure 4.13 Plot of CFD computed jet angle

series 1 (081 mm or 0.032 inch diameter) and series 2 (1.01 mm or 0.040 inch diameter). This is seen in the openings from quarter to three-quarters in particular. As the hole size increases, the slope of the change in jet angles between the quarter to three-quarter openings becomes less steep. This can be seen in the results for series 3 (1.57 mm or 0.062 inch diameter), series 4 (1.98 mm or 0.078 inch diameter), and series 5 (3.18 mm or 0.125 inch diameter).

The flow coefficient results were plotted in Figure 4.14. As was done with the plot of the jet angle results, the value for the computed flow coefficient for the quarter open position was used as the value for the fully closed position. This additional point for each hole series demonstrates the amount of overlap among the hole series. A circle was placed around this data point to indicate that it is for stroke reference only. The graph of the results clearly shows the trend of the flow coefficients increasing with increasing hole opening typically until the hole is approximately three-quarters open. The larger hole series demonstrated a peak value at three-quarters opening but the smaller hole series showed a peak value at approximately half opening. After the peak value was reached, the values for the flow coefficient drops to nearly the value of the flow coefficient for the half open condition.

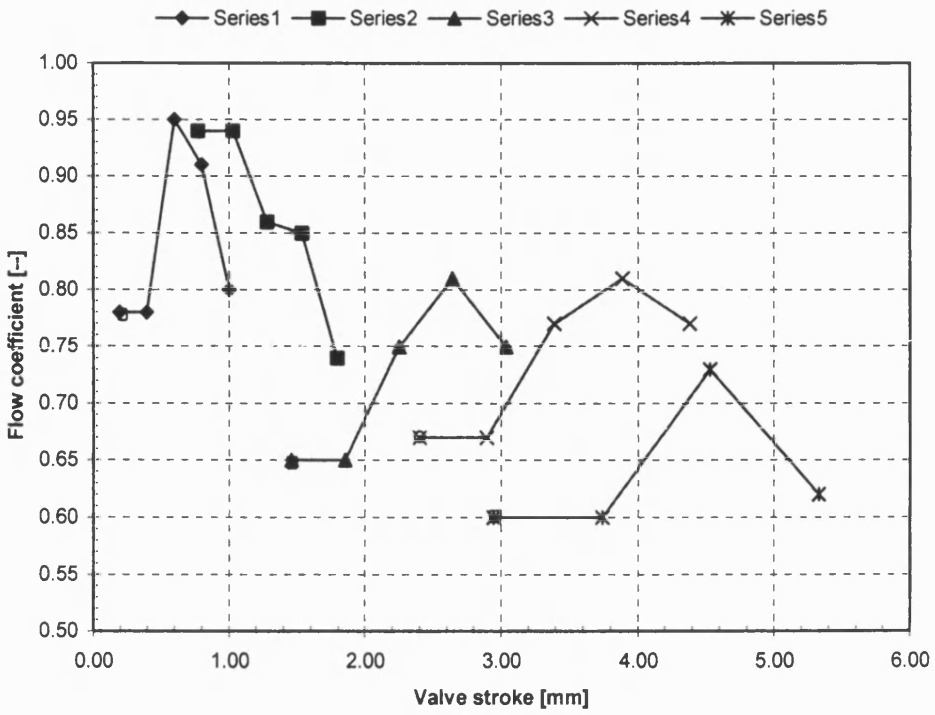

Figure 4.14 Plot of CFD computed flow coefficients

A similar trend in the flow coefficients can be seen in the results reported by **Vaughan *et al.* (1992)**. As the valve experimented and simulated using CFD increases in opening, the flow coefficients increased to a peak value of approximately 1.5 before the values begin falling off to nearly the values for small openings. The authors surmised that the decreasing flow coefficients were the result of jet separation and the reduced pressure recovery. It was implied that CFD poorly predicts flow coefficient. **Menter (1994)** supports this idea by stating that turbulence models based upon the ε-equation predict the onset of separation too late and under predict the amount of separation. It can be surmised that the changing values for the computed flow coefficients from the modelled MBEM valve were also related to jet separation and reattachment and pressure recovery. In the smaller diameter holes, the jet formed by the flow separating from the metering edge of the piston reattaches within the exit hole. In the larger hole sizes, the jet actually impinges on the outer surface of the annular area. Because a fixed length for the exit holes was used for all of the simulations of the different hole sizes, there would appear to be a L/D relationship intertwined with hole opening and jet angle that would at least partially explain the physics of jet reattachment in the MBEM valve and hence the nature of the changing flow coefficients. Time constraints prevented further study into developing an understanding of the nature of the changing flow coefficients.

4.6 Flow force calculation

Calculating flow forces directly from pressure distributions within the CFD software was not easily accomplished. To overcome the deficiency, a method was developed and written as a Matlab M-file called *PressureMap*. A copy is included in Appendix 2. Coordinates and pressure values for the nodes on the metering edge of the valve piston were extracted from the CFD results and loaded into the Matlab environment. The pressure values were sampled from the coordinates that constituted the unstructured mesh. Then, the pressure values were mapped onto a structured mesh. This was because, in order to plot the results, Matlab requires the data to be mapped onto a structured mesh. The final step in calculating the flow force acting on the metering edge of the piston was to integrate the pressure values over the surface area using a trapezoidal rule of the form shown in equation 4.15 for the pressure value at the nodes classified as corner, edge, or internal.

$$F = \frac{h_x h_y}{4} \times \frac{\sum corners + 2 \times \sum edges + 4 \times \sum internals}{A} \qquad \textbf{(4.15)}$$

In equation 4.15, h_x and h_y represent the individual element height and width while A is the surface area of the piston edge that the integration is taking place. Corner, edge, and internal nodes are most easily understood by reviewing Figure 4.15. An example of the resulting pressure contour plot is shown in Figure 4.16. This example is taken from the results of the simulation of fluid flow through a half-open hole of the first hole series that is 0.81 mm (0.032 inch) diameter. The contour plot shows the difference in pressure from the maximum calculated. In the case shown in Figure 4.16, the maximum was 223.1 bar and the largest difference calculated from this maximum was 156.7 bar shown at the bottom of the depression. Plotting the pressure contours on a three-dimensional graph demonstrates how the pressure changes dramatically near the half open hole. This pressure change caused by the change of momentum of the oil flowing through the exit hole is the source of flow forces.

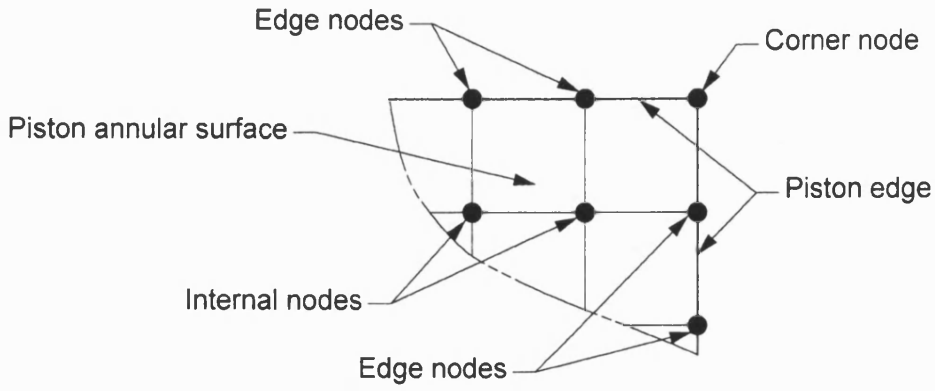

Figure 4.15 Trapezoid rule node definition

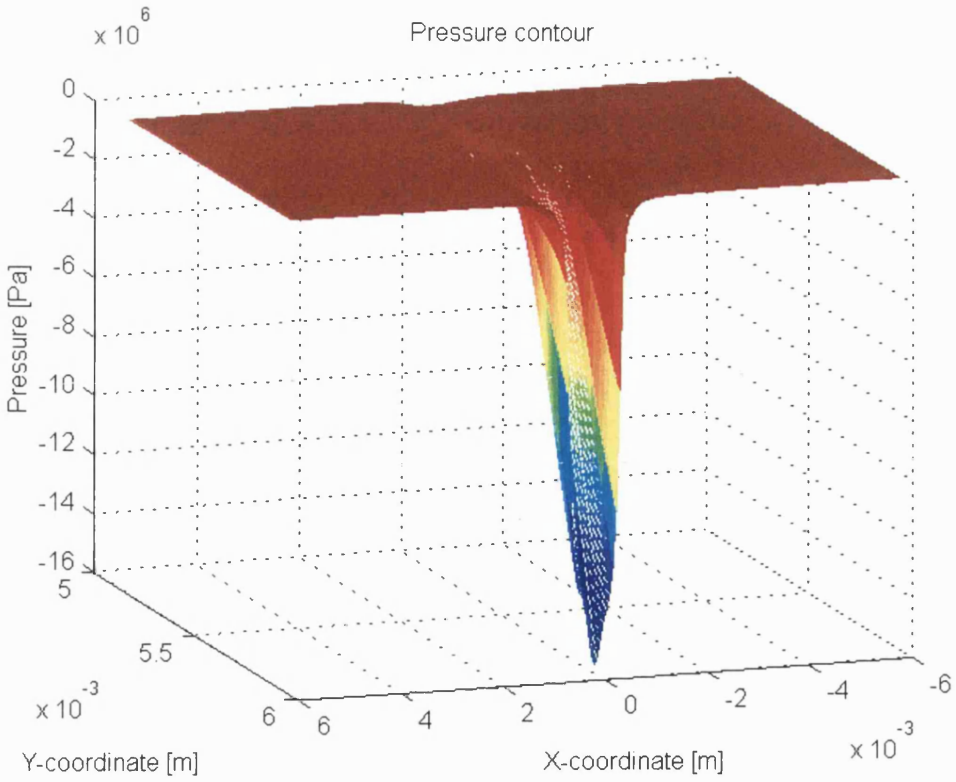

Figure 4.16 Pressure map of piston metering edge

Application of the trapezoidal rule to integrate the pressure over the surface area of the piston edge for the example of the single half open hole from the first series of holes results in a computed flow force of 2.55 N. This value is representative for a single hole from a series of four holes. The product of multiplying this value by four is 10.2 N. The half-open condition of the first series of holes occurs at an approximate stroke of 0.60 mm. Using this stroke and a flow force of 10.2 N, a comparison can be made to the experimental data obtained using the method described in Chapter 2. Experimental results are plotted in Figure 4.17. The first curve of results is the 'uncorrected', raw data. The second curve has been 'pressure corrected'. In other words, the pressure-force caused by pressure acting upon the annular area of the edge of the piston has been subtracted from the measured force. The remainder is the flow force and friction. The next data set shown on Figure 4.17 shows the results of applying the pressure mapping routine to the CFD data. In order to compute the contribution of flow forces between holes at the specific valve openings modelled, linear interpolation was used. Thus, the flow forces computed for the specific hole openings could be used to calculate the flow force for an intermediate opening not modelled. Of course, the use of linear interpolation requires the assumption that the flow force varies linearly between the openings actually modelled. The flow forces through the individual hole series were added to calculate a total flow force. The flow force for when a hole series was uncovered fully was simply added in the calculation of the remaining flow forces.

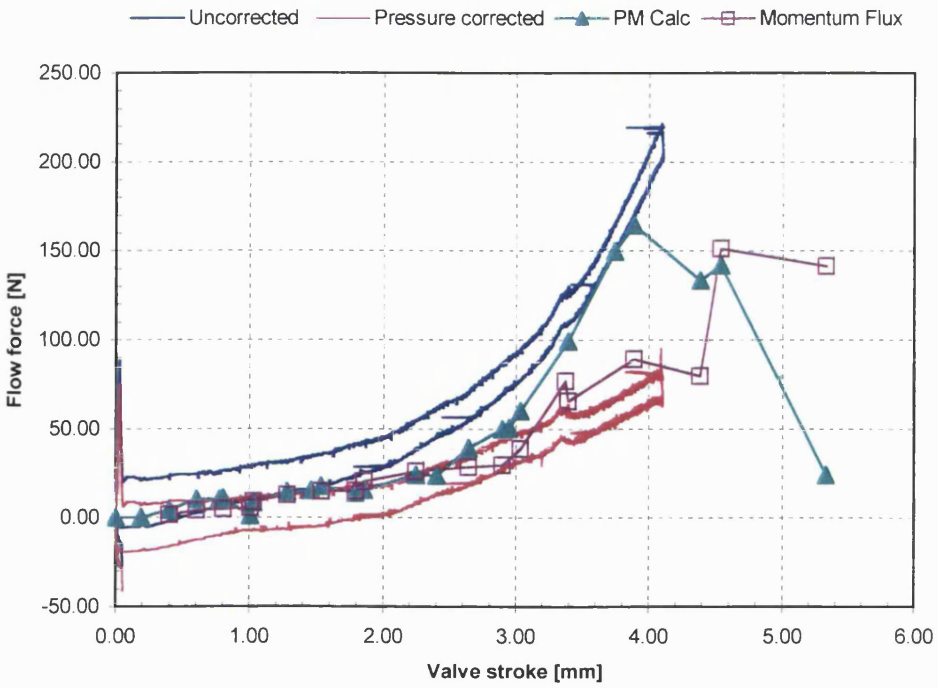

Figure 4.17 Comparison of flow forces

The remaining data set shown on Figure 4.17 is for the flow force calculated from the momentum flux. CFD results for each hole opening were interrogated for the inlet and outlet velocities and inlet and outlet mass flow rates. The product of the velocity and mass flow rate is the momentum flux. The difference between the outlet momentum flux and inlet momentum flux is the flow force. This is shown in equation 4.16, which uses the mass flow-weighted average velocity **(CFX Users Guide, 2001)**. As can be seen in the graph in Figure 4.17, the momentum flux calculated flow force compares well with the pressure corrected data set and the pressure map calculated force well until the approximate valve stroke of 2.24 mm and 25 N force. Beyond this point, the momentum flux calculated flow force has a similar trend as the pressure map calculated flow force.

$$F_{force} = \dot{M}_{out}\left(\frac{1}{\dot{M}}\int \rho v_{yout}\left|u \bullet \hat{n}\right|\right) - \dot{M}_{in}\left(\frac{1}{\dot{M}}\int \rho v_{zin}\left|u \bullet \hat{n}\right|\right) \qquad \textbf{(4.16)}$$

The plot of the data points obtained from the calculation of flow forces using the CFD results shows good agreement with the pressure corrected experimental data up to a stroke of 2.24 mm and 24.2 N force (data points shown as triangles in Figure 4.17). The remainder of data points show much less agreement with the experimental data. This would indicate that the use of linear interpolation as well as simply adding the full open hole flow force to the remaining flow force calculations was overly simplistic. A model with all holes in

the series and even multiple hole series would probably have produced results that agreed better with experimental results.

4.7 Concluding remarks

The CFD simulations and results for the flow through the MBEM valve have been discussed in detail. Comparisons with the flow visualisation showed good agreement to the computed jet angles for the different hole openings for the fourth series of holes. There was good consistency between the specific hole openings among the different hole series for the computed jet angle. A trend for the change in jet angle as the hole coverage changed was clearly evident. Additional computations were made to calculate the flow coefficients for each opening of each hole series that was simulated. The trend for the flow coefficient to increase to a peak value and then decrease as the hole opening increased appears to be related to jet separation and reattachment and the resulting pressure recovery. Previously reported results for computed flow coefficients as valve opening increased demonstrated a similar trend. Time constraints prevented further research into understanding the nature of the changing flow coefficients.

The values calculated for the jet angle and flow coefficient for the different openings and different hole series will be used to create a more accurate mathematical model of the valve operation as will be discussed in detail in Chapter 5. Quantifying the values for jet angle and flow coefficient between a partially open condition and a full open condition will be shown to contribute to making the valve model more accurate.

CHAPTER 5

MATHEMATICAL MODELLING

5.1 Introduction

Mathematical modelling is a useful and powerful tool. It allows for the different parameters that act in a dynamic system to be accounted for in a set of equations. When solved using initial conditions, these equations can accurately predict valve performance. Furthermore, the equations allow sensitivity studies to be easily conducted on the different model parameters.

In the first chapter, a hypothesis was presented that the changing nature of flow forces contributed to create the pressure compensation characteristics of the load control valve. The changing nature of the flow forces is partly a result of the changing jet angles and flow coefficients as the exit hole coverage changes. In subsequent chapters, flow forces, the changing nature of the jet angles, and the changing nature of the flow coefficients were all quantified. Mathematical modelling was employed as the final research tool to use the knowledge gained about the nature of the jet angle and flow coefficients to create an accurate model of the load control valve to prove the hypothesis.

5.2 Review of past work

Unlike CFD modelling or flow visualisation, there is an abundance of literature on modelling of hydraulic valves. There are literally hundreds of papers on the subject of mathematically modelling hydraulic valves and systems dating back to at least 1952. It appears that the use of computers in modelling hydraulics came into use in the late sixties or early seventies. Specialist software packages were developed during the eighties. Literature on their development and use starts appearing in the late eighties onwards. The use of the general-purpose software package Simulink in modelling hydraulic systems and valves started to appear in literature in the early nineties when the software was first released.

Wright *et al.* (1997) show an example of the use of Simulink in modelling a hydraulic valve. The valve modelled in this study was a two-stage servo valve. The analysis was conducted in a classical manner. That is that classical forms of equations such as that for

flow force and pressure drop were used. A nonlinear Simulink model was developed first and later, a linearised model was developed. The analysis investigated the system response while varying the control volume, spring rate, dampening coefficients, spool mass, and the area gradient. The study also investigated effects of fluctuations in the bulk modulus of the oil caused by entrained air. The authors noted that several of these parameters were found to have significant influence on performance characteristics. This article was found to be useful because of the approach taken in developing the model. System dynamics equations were written in terms of force balances. A similar approach was used in developing the model for the load control valve in the present work.

An example of combining the results from CFD analysis with dynamic modelling is provided by **Herr *et al.* (1998)**. The authors used CFD analysis of an automotive shock absorber to develop an equation based upon the classical orifice equation to describe the pressure drop through the control orifices of the shock absorber. This relationship was used in a dynamic simulation conducted in the Easy 5 (Boeing Corporation) modelling environment. The results that were provided showed good agreement between experiment and modelled results. The largest difference noted in the graph of dampening force and displacement is about 300 N at a peak force of 3000 N. The authors were successful in modelling the hysteresis that is present in the system. They identified sources of hysteresis as compliance in the oil and the shock absorber structure even though there was an in-depth discussion about eccentricity of the piston to the cylinder. This would be a possible source of friction and hence, hysteresis. Even though the authors state that the work was still in its early stages, the results were nonetheless impressive. This paper demonstrates a good synergy between CFD and dynamic modelling. Similarly, the dynamic model of the load control valve will rely heavily upon CFD results.

An interesting series of articles that put forth the idea of a non-classical equation to describe the pressure drop through poppet and piston valves started with **Washio *et al.* (1999)**. This was followed up with **Nakamura *et al.* (1999)** and **Washio *et al.* (2001)**. In these articles, the authors assert that the classical orifice equation, $Q = c_q A\sqrt{\frac{2\Delta P}{\rho}}$, is flawed because the flow coefficient is assumed constant when in fact it varies with valve opening. The authors propose a new model, $\frac{\Delta P}{\rho} = \frac{1}{A^2}\left(\alpha Q^2 + \beta \nu l Q\right)$, where α is a nonlinear loss coefficient, β is a linear loss coefficient, and l is a representative length. These loss coefficients are determined empirically by least squares curve fits to experimental data. Comparison of subsequent modelled and experimental results showed very good agreement with little distinguishable differences. In frequency response tests, the agreement was very good up to a frequency of 400 Hz with a maximum difference noted between experiment and modelled results of 5 dB on the gain plot and 20° in the phase plot. This series of papers is an interesting attempt to produce more accurate valve models. The authors state accurate models will contribute significantly in developing and improving oil

hydraulic devices. While the development of a more accurate model is commendable, the dismissal of classical equations and theory deserves more explanation than given. Flow forces are explicitly dismissed as negligible. In one valve experimented with, the maximum flow rate was $80 cm^3/s$ (4.8 L/min) and the maximum pressure was 3.0 MPa (30 bar). In spite of the relatively low flow rates and working pressures, flow forces may contribute significantly to valve performance. Because the new model was only verified for the relatively low working flows and pressures, it was not considered fully verified for use in the current research on the load control valve.

Fairhurst and Watton (2001) used CFD and 'offline computations' to dynamically model the position of the swash plate piston (paw piston) of an axial piston pump. The working fluid was a 95/5 water/oil emulsion. Calculations were conducted outside the CFD software or 'offline' using CFD computed mass flow rates across a pressure boundary to predict the paw position. As part the dynamic model, time was incremented. With the incremented time, the CFD simulation and offline calculations were repeated. In this manner, the dynamic model of the pump pressure compensator was developed. The CFD simulations were primarily conducted in three-dimensions although some two-dimensional, axisymmetric models were used to develop pressure/flow characteristics of the paw piston. The low viscosity fluid required that the leakage past the paw piston be included in the model. A technique was implemented using porous elements in an increased, fictious clearance. Mesh generation problems would have occurred if standard meshing techniques were used in the very fine clearances around the paw piston. Comparison of simulated results and experimental results generally showed good agreement. Typically, the difference between predicted and measured paw piston position was a fraction of a millimetre over a 7 mm stroke. However, the difference approached 1 mm as the simulation time increased. Cavitation was briefly mentioned in the discussion of the results. No discussion was made on how the very low pressures shown may have affected the results.

While the technique developed by Fairhurst and Watton (2001) produced results that demonstrated relatively good agreement with experimental results, the technique is time consuming and computationally heavy.

5.3 Model development

Development of the mathematical model of the load control valve began with writing a force balance after creating a free-body-diagram of the valve piston. A very similar approach was used by Wright *et al.* (1997) as previously discussed. Modelling was conducted within the Matlab-Simulink environment. Simulink is a general-purpose software package developed for modelling, simulating, and analysing dynamical systems. The use of specialist software packages for modelling fluid power components and systems was considered; however, Matlab-Simulink offered more flexibility and ease in creating the load control valve model because of its user interface. Additionally, the use of Simulink in

modelling dynamic systems and components is more common than the use of specialist codes; therefore, the model developed would generally be more readily useable than a model developed in a specialist code.

5.3.1 Force balance

The derivation of the force balance started by first considering the three different pressures present inside the valve and the areas that they work upon as shown in Figure 5.1. As can be seen in the cross-sectional drawing in Figure 5.1, each of the three pressures present in the valve works on two different areas. The load pressure, P_1, works on both the seating diameter, D_1, and the sealing diameter in the sleeve in the spring chamber, D_3. The spring chamber is at the same pressure as the load port because of the axial drilling that communicates this pressure to the spring chamber. Similarly, the pressure at the valve port that is typically referred to as backpressure acts upon two different diameters, D_2 and D_3. An angular drilling connects the vent chamber to the valve port where P_2 is present. The pilot pressure, P_3, also works upon two different diameters, D_1 and D_3.

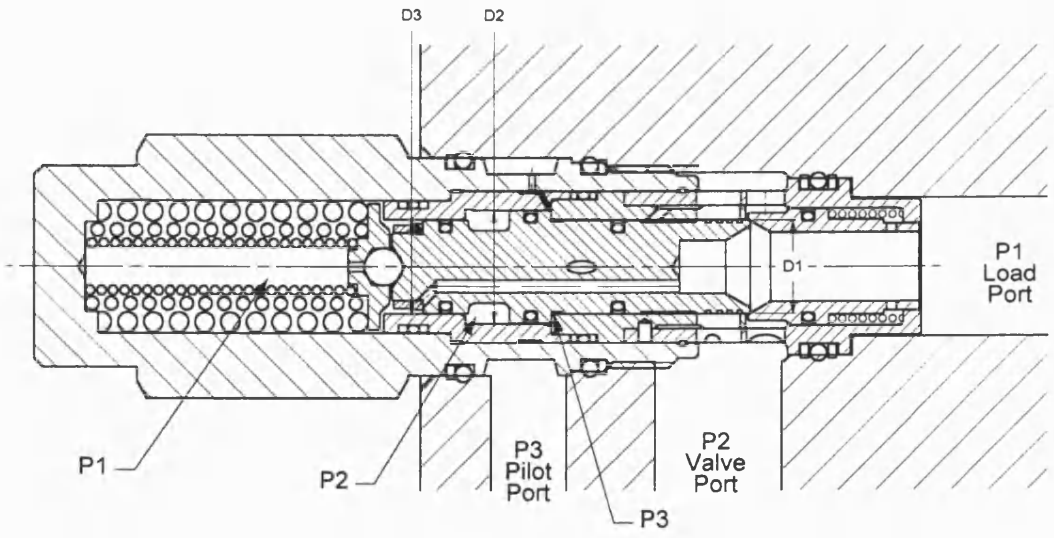

Figure 5.1 Cross-section of the load control valve showing pressures and diameters

Before writing the equations that describe the force balance, a free-body diagram was drawn. The diagram shown in Figure 5.2 shows the spring force, flow force, and pressure forces (pressure multiplied by area) that work upon the piston of the load control valve. The one force that is not shown is the friction force. Friction works in the direction opposite the direction of travel; therefore, it could be shown acting in both directions. Direction of movement that causes the valve to open was assumed as the positive direction as shown in the figure.

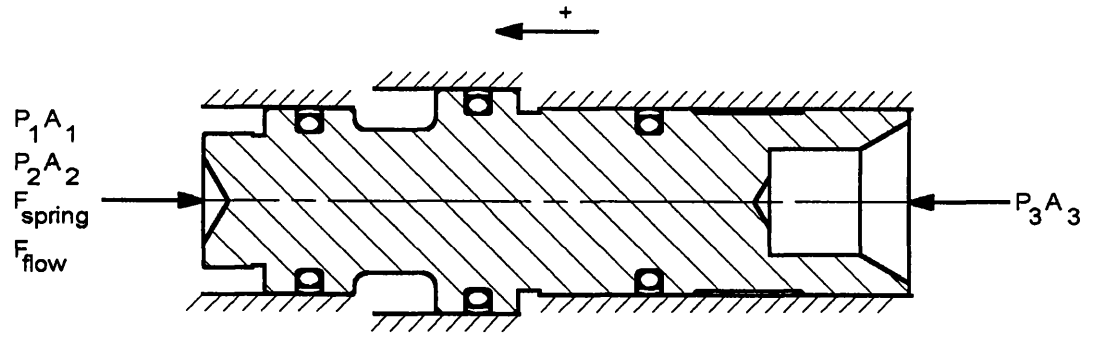

Figure 5.2 Free-body diagram of the forces working on the piston

The first equation, Equation 5.1, is the sum of the pressure forces. Each of the three different pressures present work upon a differential area as described above. In equation form, the differential areas are shown in Equations 5.2 through Equation 5.4.

$$F_p = -P_1A_1 - P_2A_2 + P_3A_3 \tag{5.1}$$

where

$$A_1 = \frac{\pi}{4}\left(D_3^2 - D_1^2\right) \tag{5.2}$$

$$A_2 = \frac{\pi}{4}\left(D_2^2 - D_3^2\right) \tag{5.3}$$

$$A_3 = \frac{\pi}{4}\left(D_2^2 - D_1^2\right) \tag{5.4}$$

Equation 5.5 is a sum of the total forces working upon the valve piston and it is based upon $F_{total} = m\ddot{x}$. This equation includes the pressure force, flow force, spring force, and the friction force. The development of equations 5.6 through 5.7 is explained in detail in the following sections. The computation of the friction force will be explained in detail in section 5.4.6.

$$F_{total} = F_p + F_{flow} + F_{spring} + F_{friction} \tag{5.5}$$

where

$$F_{flow} = 2c_q A_{outlet}\Delta P\cos\theta - \frac{Q^2\rho}{A_{inlet}} \tag{5.6}$$

$$F_{spring} = -k\left(x + x_0\right) \tag{5.7}$$

5.4 Simulink model

The Simulink diagram of the load control valve model is shown in Figure 5.3. A description of the key elements of this model will follow this section. The model was created with standard Simulink blocks along with several blocks that call Matlab functions. Results were plotted to graphs on the screen and written to files for later post-processing. The model was designed to replicate the experimental procedure employed to measure the

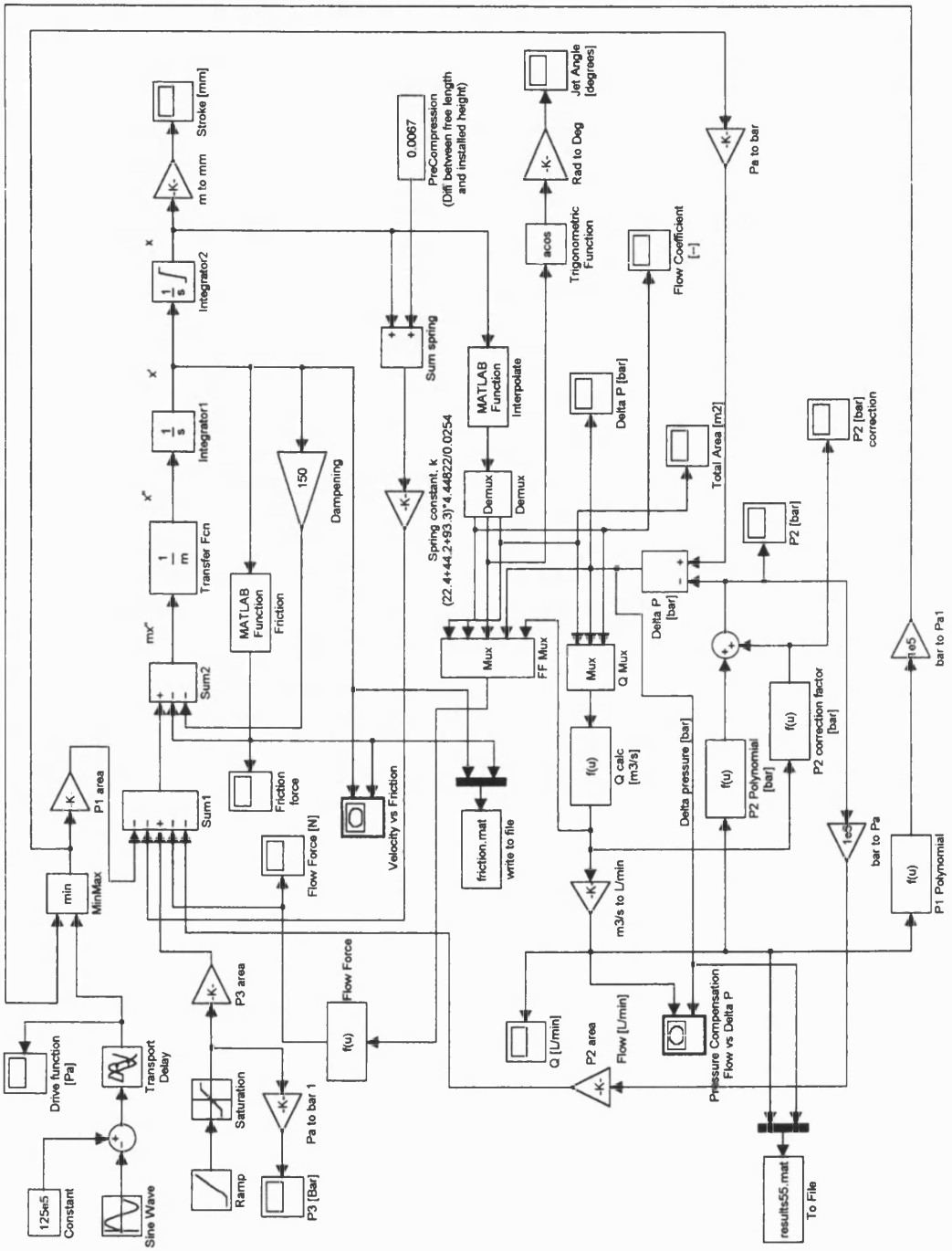

Figure 5.3 Simulink diagram of dynamic model

pressure compensation performance characteristics of the load control valve. Pressure compensation performance curves were the benchmark used for comparison to determine how well the model was approximating experimental results.

5.4.1 Drive function

A driving function was developed to approximate the part of the experimental procedure for measuring pressure compensation that has the load pressure slowly increasing then decreasing by turning the adjust screw on the pressure-reducing valve. The driving function was the sum of a sine wave and a constant 125 bar source as can be seen in the upper left corner of the Simulink diagram. Within the *Sine Wave* block, a phase shift of $\pi/2$ radians was applied. Subtracting this from the constant 125 bar source approximated a cosine curve with a magnitude of 250 bar. A plot of the drive function is shown in Figure 5.4. A cosine curve was approximated with the sine wave and constant source to prevent the modelled load pressure cycling into negative values. Start-up transients were also minimised by starting at a low-pressure value instead of a high value.

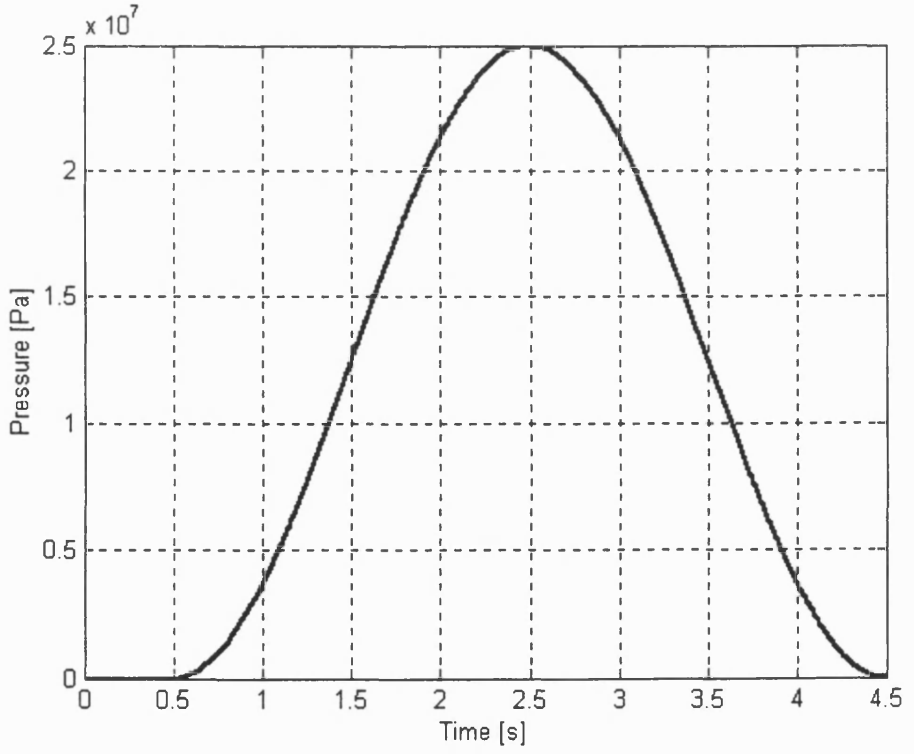

Figure 5.4 Driving function for Simulink model

The sine wave did not start until after a 0.5 second delay as can be seen in Figure 5.4 to ease the problems associated with start-up transients. This was accomplished using the *Transport Delay* block as can be seen in the upper left of the Simulink diagram in Figure

5.3. A 4-second period for the sine wave is also clearly shown in Figure 5.4. As previously mentioned, the driving function modelled the experimental procedure of cycling the load pressure by turning the adjust screw of the pressure-reducing valve on the test stand. In the experiments, this took approximately 90 to 120 seconds. Four seconds was chosen as the period because the relatively slow cycle of pressure minimised transients that would have been present in a smaller period.

5.4.2 Pilot pressure

Pilot pressure was applied and controlled with the *Ramp* and *Saturation* blocks in the upper left side of the diagram. A ramp function was used as opposed to a fixed source in order to limit oscillations that potentially would be caused by a sudden application of high-pressure when the simulation is first started. The saturation block provided the upper limit to the ramp function. A slope of twice the applied pilot pressure worked well since the full-prescribed pilot pressure would be reached in 0.5 second. To fulfil part of the force balance in equation 5.1, the pilot pressure was multiplied by the differential area that it acts with the gain block labelled *P3 area*.

5.4.3 Inlet and outlet characteristics

In order to develop results that more closely matched the experimental results, characteristics of the experimental test stand were included in the model. The characteristic that showed up on the graph of experimental pressure-compensation performance curves was the change in differential pressure with flow rate. This characteristic was for the most part easily measured while using the flow force measurement device described in Chapter 2. While making flow force measurements, inlet, outlet, and flow rate were simultaneously measured. A third order polynomial was fitted to the measured inlet and outlet pressures as a function of the measured flow rate. These are shown in equation 5.9 for the inlet pressure, labelled *P1 Polynomial* on the Simulink diagram, and equation 5.10 for the outlet pressure, labelled *P2 Polynomial* on the Simulink diagram. Equation 5.9 represents what is commonly called the pump curve for the test stand. As the supply pressure increases the pump output is reduced. This is shown in the graph in Figure 5.5 with both the experimental data and the polynomial given in equation 5.9. Conversely, as the supply pressure decreases, the output increases. Equation 5.10 describes how the return line pressure increases with increasing flow rate. It is essentially an orifice equation for the return lines to the oil reservoir for the test stand. This is again shown in the graph in Figure 5.6 with both the experimental data and polynomial given in equation 5.10.

$$P_1 = -0.000014843\left[bar \cdot min^3/L^3\right]Q[L/min]^3 + 0.0015865\left[bar \cdot min^2/L^2\right]Q[L/min]^2 - 0.34478[bar \cdot min/L]Q[L/min] + 244.20[bar] \quad \textbf{(5.9)}$$

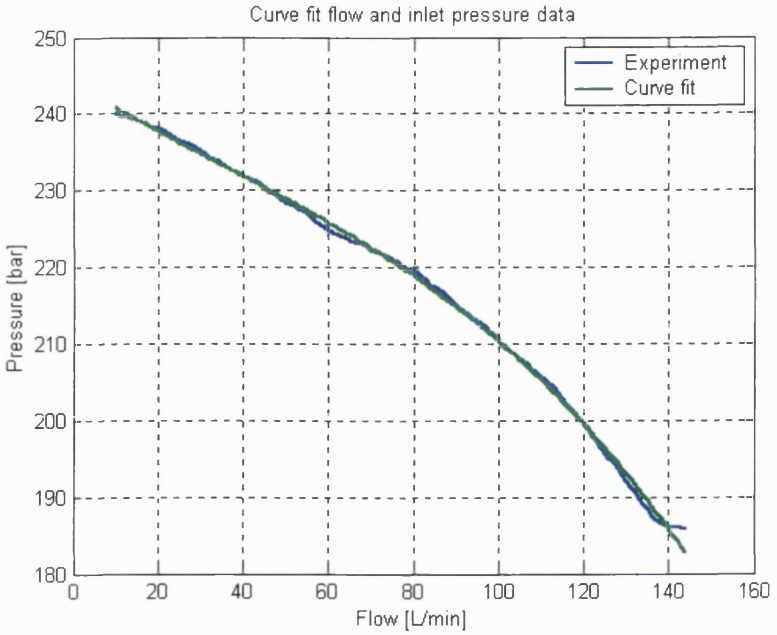

Figure 5.5 Inlet pressure-flow characteristic

$$P_2 = 0.0000043259\left[bar \cdot min^3/L^3\right]Q[L/min]^3 + 0.000037546\left[bar \cdot min^2/L^2\right]Q[L/min]^2 + 0.047497[bar \cdot min/L]Q[L/min] + 2.7941[bar] \quad \textbf{(5.10)}$$

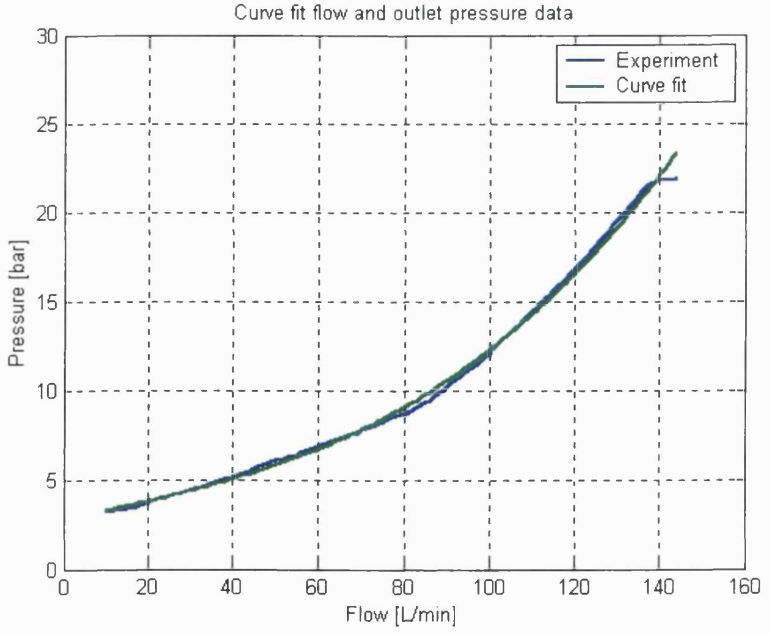

Figure 5.6 Outlet pressure-flow characteristics

The P_1 polynomial was used in the model by limiting the inlet pressure through a *MinMax* block. This block selected the minimum value from a comparison of the value from the driving function and the P_1 polynomial. Maximum load pressures were reduced as flow rates increased with increasing pilot pressure in the pressure-compensation performance curves. The output of the *MinMax* block was multiplied by the differential area that the pressure acts upon as described in the force balance in equation 5.1. This was done with the gain block titled *P1 area*.

The P_2 polynomial was used to calculate the outlet pressure as a function of the flow rate. It was subtracted from the inlet pressure to calculate the differential pressure through the valve that was used to calculate the flow rate. It was also multiplied by the differential area that the outlet pressure acts upon as described in the force balance in equation 5.1. This was accomplished with the gain block labelled *P2 area*.

An addition correction factor was developed to account for the pressure difference between the cavity annulus and the test point downstream of the cavity annulus where the outlet pressure was actually measured. It is shown in equation 5.11. This was labelled *P2 Correction Factor* on the Simulink diagram and was added to the *P2 Polynomial* that is given in equation 5.10. Equation 5.11 comes from the work by Darcy, Hagen, and Poiseuille on laminar flow **(White 1986)**. While a turbulent equation for pressure drop was tried, the laminar equation produced better results and can be justified by calculating a Reynolds number in the hose that returns flow to the reservoir. At a maximum flow rate of $120\,L/\min$, the Reynolds number calculated was 4322. While this value is above the generally accepted critical Reynolds number of 2300, it is below the generally accepted value for turbulent Reynolds number of 10000 **(White 1986)**. In equation 5.11, R_h is a calculated hydraulic radius.

$$P_{2CF}[bar] = \frac{8\mu LQ}{\pi R_h^4} = \frac{8(0.031408Pa\cdot s)(0.0224m)Q[m^3/s]}{\pi(0.0016m)^4 10^5} \qquad \textbf{(5.11)}$$

5.4.4 Flow force modelling

Equation 5.6 above was derived from the classic book equation for computing flow forces shown in equation 5.12. Typically, v_{in} is much smaller in comparison to v_{out}; therefore, $\rho Q v_{in}\cos\theta_{in}$ is rarely shown and hence the *out* subscript is usually omitted. A common assumption is that the $\rho Q v_{in}$ term contributes little to the flow force calculation and therefore is negligible.

$$F_{flow} = \rho Q v_{out-max}\cos\theta_{out} - \rho Q v_{in}\cos\theta_{in} \qquad \textbf{(5.12)}$$

Equation 5.6 was derived by substituting equations 5.13 and 5.15 into equation 5.12. Equation 5.13 is commonly called the orifice equation. Equation 5.14 computes the mean velocity and equation 5.15 computes the approximate velocity at the vena contracta.

$$Q = c_q A \sqrt{\frac{2\Delta P_{inlet-outlet}}{\rho}} \tag{5.13}$$

$$\bar{v} = \frac{Q}{A} \tag{5.14}$$

$$v_{max} = \frac{Q}{c_q A} \tag{5.15}$$

As discussed in section 2.16, the flow coefficient is calculated from the CFD data described in Chapter 4 using equation 5.16.

$$c_q = \frac{Q}{A} \sqrt{\frac{\rho}{2\Delta P_{inlet-outlet}}} \tag{5.16}$$

Jet angles were also computed from the results of the CFD analysis as described in Chapter 4. The average jet angle, θ, was computed from using the mass weighted average of the axial and radial components of the velocity calculated from the CFD software as shown in equation 5.17.

$$\theta = arctan \frac{\overline{v_{radial}}}{\overline{v_{axial}}} \tag{5.17}$$

5.4.5 Spring force modelling

Equation 5.7 is a form of the well known spring equation **(Shigley and Mischke, 1989)**. In Equation 5.7, x is the displacement and x_0 is the initial compression or pre-compression. The spring is initially compressed, also referred to as the installed height. It is simply the height of the spring installed in the valve with the valve closed, in this case. The equation is valid only when the spring is working within its linear range. This was verified experimentally by measuring the force on a materials testing machine as springs from the test valve were compressed.

5.4.6 Friction modelling

The final set of equations that comprise the force balance are the friction force equations. As can be seen from the hysteresis present in the experimental results, frictional forces are present in the load control valve. Sources of friction would be the three o-ring energised glyd-rings and steel-on-steel contact if the piston becomes eccentric with respect to the three bores of the two guiding sleeves within which it moves. After unsuccessfully attempting to implement a variation of the friction model for o-ring sealed pistons proposed by **Miller (1981)** and **Parker (1992)**, a different approach was adopted. Another custom Matlab function was written in order to include frictional forces in the model. *Friction* was written to model stick-slip, Coulomb, and viscous friction. A copy of *Friction* is included in Appendix 1 and the block can be found below the *Sum2* and *Mass* blocks at the centre top of the Simulink diagram. Figure 5.7 shows the friction function developed for the valve model. Note that the scale of the abscissa is of the order of $0.1mm/s$ on the graph. The developed friction function was a smooth function of velocity, such that the force reached the stick-slip value for velocities close to zero and the force reduced to the level of Coulomb and viscous friction for higher velocities.

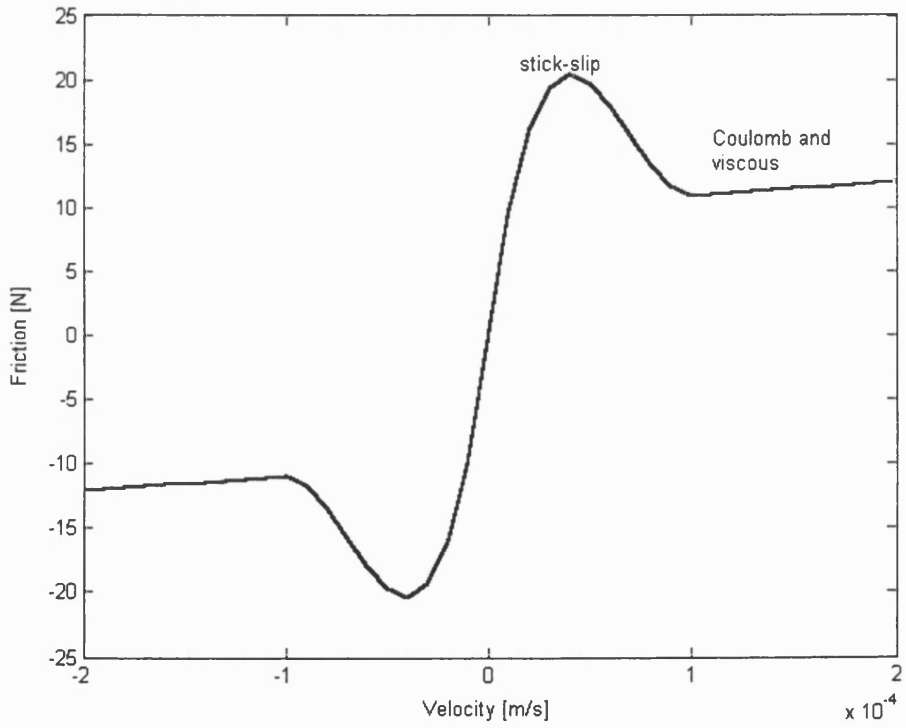

Figure 5.7 Friction function (viscous friction gradient exaggerated)

Values for the Coulomb and viscous friction were determined indirectly from experiments designed to measure flow forces and empirically through trial and error. Using

half of the approximately 30 N hysteresis that was in the measured force data that a typical graph was shown in Figure 2.7 provided the starting point for the empirical trial and error. As can be seen on the graph in Figure 5.7, the value used for stick-slip was 20 N, the value used for the Coulomb friction was 10 N, and the value used for the viscous friction was $5 Ns/m$. The steep, positive sloped portion of the curve passing through zero represents the stick-slip friction. Normally this would be nearly an infinite slope and shown as a vertical line, but having a finite, although very steep slope, makes the programming much simpler. Viscous friction creates the slightly positively sloped portion of the curve after stick-slip portion in the first quadrant of the graph; and in the third quadrant, the slightly positive slope after stick-slip portion represents the viscous friction. The viscous friction gradient was exaggerated for graphing so that it would show up on the large-scale graph. Coulomb friction alone without the added viscous friction would form a horizontal line at the friction force value, 10 N.

Under nominally static conditions, this friction model has the disadvantage that a small degree of 'creep' occurs. With this friction model, it is possible for the valve piston to move very slowly or creep. A very small threshold velocity, v_t in equation 5.8, had to be defined for the transition between stick-slip friction and Coulomb-viscous friction. Excessive 'creep' would have occurred under nominally static conditions where stick-slip friction applied, if the threshold velocity were too large. If it was too small, run-times became excessive. A value of $0.1 mm/s$ was found to be satisfactory and creep was negligible for the conditions studied. The root mean square (RMS) velocity for the case with 85 bar pilot pressure as shown in Figure 5.17 is $0.131 m/s$ (standard deviation $0.131 m/s$) which is three orders of magnitude greater than the threshold velocity of $0.1 mm/s$. This indicates that the majority of time, the piston velocity is much greater than the threshold velocity and hence, the Coulomb and viscous friction terms are the dominant friction terms as opposed to the stick-slip friction.

The velocity of the piston and hence the threshold velocity are functions of the drive signal. With a drive function different than the frequency of 0.25 Hz was used, the threshold velocity would need to be adjusted. A slower drive function would require a slower threshold velocity and conversely, a faster drive function would require a faster threshold velocity.

5.4.7 Integrators

Two integrator blocks were used in the Simulink model. Both are in the upper right portion of the diagram in Figure 5.3. The first was used to integrate acceleration to velocity that was used in both calculating the friction force and the dampening force. The integrator appears as a $1/s$ block. An integral without specified bounds or an indefinite integral was

used and would appear in equation form as shown in equation 5.18. An initial condition of *0 m/s* was used as the system starts at an "at rest" condition.

$$v = \int \frac{dv}{dt} dt + 0 m/s \qquad \textbf{(5.18)}$$

The second integrator used also appears as a $1/s$ block but with the addition of an integral symbol. This indicates that saturation limits were set. The upper saturation limit was the maximum physical stroke of the valve. The lower saturation limit was as close to zero but not zero as that caused a singularity error. Since saturation limits to the integration were specified, an initial condition greater than the lower saturation limit needed to be specified. Within the valve, a dead band exists between the points that the piston contacts the seat and when the first series of cross-holes have started to be uncovered. The length of the dead band, 1.27 mm, was used as the initial condition.

5.4.8 Other block functions

Immediately after the driving function are the blocks *Sum1* and *Sum2*. *Sum1* adds the inlet pressure force, outlet pressure force, pilot pressure force, spring force, and flow force. *Sum2* adds the friction force and a dampening force to the sum of *Sum1*. The sum blocks complete the force balance.

Below the sum blocks and *Friction* block is the *Dampening* block. This block was used in place of calculating the effective dampening caused by the orifices in the piston that communicated oil to the spring chamber and vent chamber. A value of $150 Ns/m$ was empirically determined through simulation trial and error to work best to dampen out without over-dampening oscillations.

The *Q calc* block was used to calculate the flow rate using equation 5.13. The block is near the centre of the diagram. Total open area and flow coefficient were calculated through the *Interpolate* block discussed in section 5.5 and used in calculating the flow rate.

5.5 Pre-processing and the interpolation block

The Simulink model of the load control valve evolved through a series of iterative designs until it reached the final design shown in Figure 5.3. One of the most significant changes made in the development of the model was substituting the custom written Matlab function *Interpolate* for the custom written function *Flowcoeff*. *Interpolate* makes use of the results from a pre-processing M-file that uses the *Flowcoeff* function included in Appendix 1. The significance of this change was to reduce the processing time from several hours to a few minutes.

Originally, the custom written Matlab function *Flowcoeff* used the results from the CFD studies of the simplified valve model to first create a look-up table. Third order polynomials were fitted to the data for each hole series in the look-up tables to describe the jet angle and flow coefficient for each hole series. Figure 5.8 shows the five polynomials that describe the jet angles for the five hole series. The polynomials that describe the flow coefficients for the five hole series are plotted in Figure 5.9. Since the exit holes overlap, the polynomials describing the change in jet angle and flow coefficient for each hole series overlap. In both graphs, the values for the quarter open position for each hole series were also used for the closed position. CFD simulations were not conducted for hole openings less than quarter open, but in order to model the valve opening in the mathematical model, realistic values were needed for openings less than quarter opening. The horizontal lines extending from the full open data points for each series shows that the values for the jet angle and flow coefficient were held constant once the maximum hole opening was reached.

A composite jet angle and composite flow coefficient were computed from the values for jet angle and flow coefficient from the individual hole series. From the results for individual holes, the overall opening area, effective jet angle, and effective flow coefficient were computed. The overall opening area, A, is simply the sum of the uncovered areas for each hole, A_i computed from equation 4.13 shown in Chapter 4. The effective jet angle and flow coefficient are area-weighted averages of the individual values for each hole. Equation 5.15 was used to compute the effective or composite flow coefficient and equation 5.16 was used to calculate the effective or composite jet angle. The individual value for the flow coefficient is c_{qi} and the individual value for the jet angle is θ_i.

$$c_q = \frac{\sum_{i=1}^{5} c_{qi} A_i}{\sum_{i=1}^{5} A_i} \tag{5.15}$$

$$\cos\theta = \frac{\sum_{i=1}^{5} c_{qi} A_i \cos\theta_i}{c_q \sum_{i=1}^{5} A_i} \tag{5.16}$$

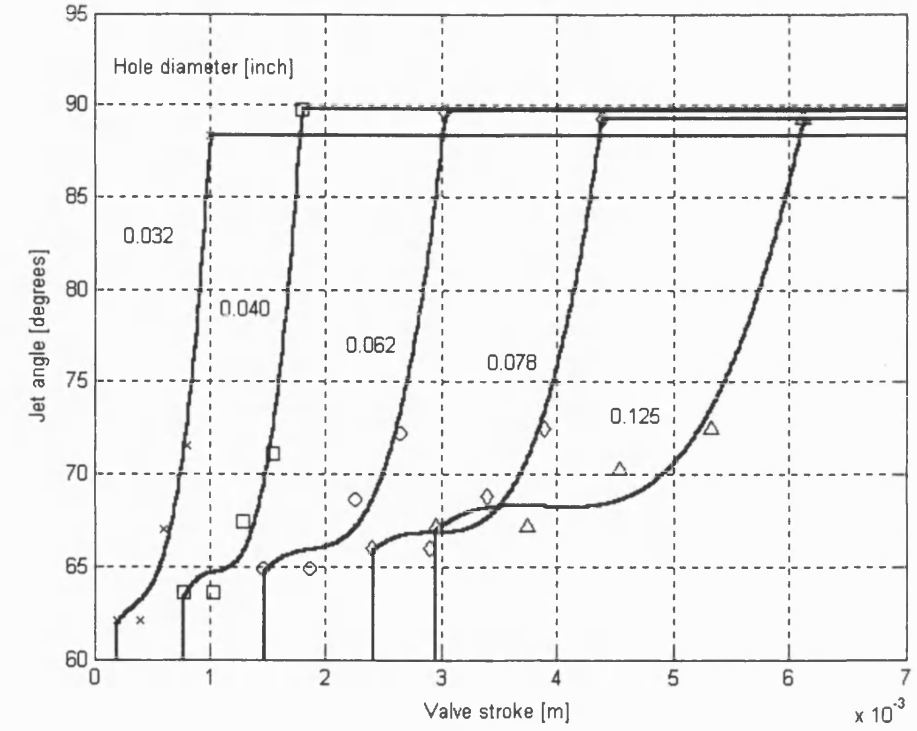

Figure 5.8 Polynomials for the jet angles

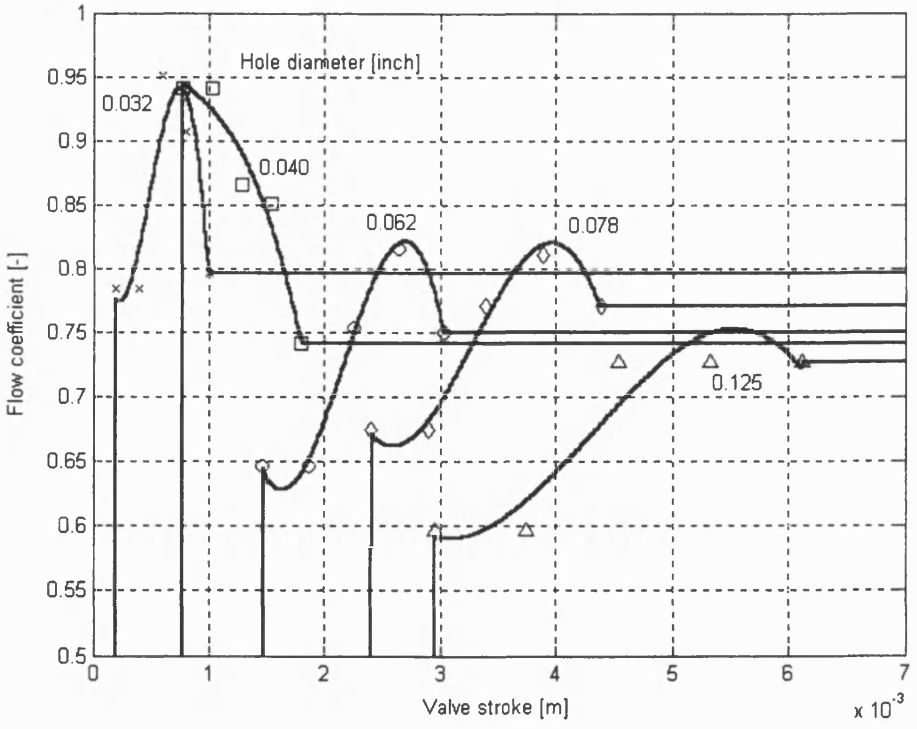

Figure 5.9 Polynomials for the flow coefficients

As the Simulink modelling evolved, the model was revised so that the calculation of the jet angle, flow coefficient, and total opening area was completed as a pre-process (prior to starting the Simulink solver) through an M-file called *Valve* in order to reduce overall processing time. The *Interpolate* function block replaced the *Flowcoeff* block and the Simulink diagram took on the final form shown in Figure 5.3. Through *Valve*, the *Flowcoeff* function was called. As part of *Valve*, an array of values for the valve stroke was created from an initial opening of 0.1 mm to 6.0 mm in 0.01 mm increments. The values for the valve stroke were supplied individually to *Flowcoeff* to compute the jet angle, flow coefficient, and total opening area. The *Interpolate* function block called the Matlab function *Interpolate*. In this function, linear interpolation was used to compute the jet angle, flow coefficient, and total opening area using the valve stroke computed from the dynamic simulation. The use of linear interpolation required the extended range of valve stroke that was created in the *Valve* M-file.

Single curves were created through the *Valve* M-file used in the pre-processing for the jet angle, flow coefficient, and total opening area as functions of valve stroke. Figures 5.10, 5.11, and 5.12 show the single curve for the jet angles, flow coefficients, and total opening area respectively as a function of valve stroke. Included in Figures 5.10 is the curve that demonstrates how the jet angle changes that was calculated from experimental data and shown previously as Figure 2.13. Similarly, Figure 5.11 includes the experimental derived flow coefficient previously shown as Figure 2.13. Comparing the plot of the jet angle in Figure 5.10 to the graph of the polynomials fitted to the CFD calculated jet angles for the individual hole series in Figure 5.8, it is found that the peaks or discontinuities in Figure 5.10 correspond to the full open condition from the individual hole series. Similarly, the full-open condition of the hole series in the graph of the flow coefficient polynomials and data points in Figure 5.9 correspond to subtle, but distinct points in the single curve for the flow coefficient shown in Figure 5.11.

Comparing the single and continuous curves for the jet angles and flow coefficients in Figures 5.10 and 5.11 to the respective curves for jet angles and flow coefficients calculated from experimental data shown alongside that was originally shown in Figures 2.12 and 2.13, a lack of agreement is readily apparent. There are a number of possibilities to explain the cause of the discrepancies. Among these would be the simplifications used to create the valve model such as the lack of a full annular exit area and a single exit hole instead of multiple series of exit holes.

Figure 5.12 is a plot of the total opening area of the valve plotted against the valve stroke. As would be expected, this curve is smooth and continuous. There are no abrupt changes in the opening area with valve stroke indicated in the plot. Part of the design intent of the metering sleeve with the different hole diameters and overlap of the hole series was to permit a smooth, gradual increase in opening area as the valve stroked.

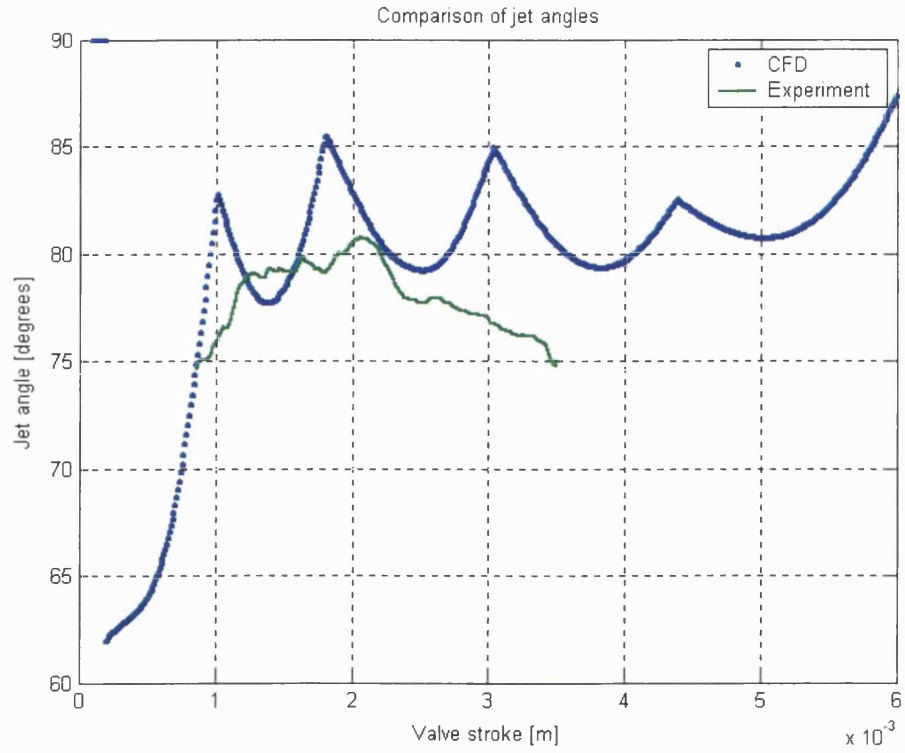

Figure 5.10 Single and continuous curve for jet angles

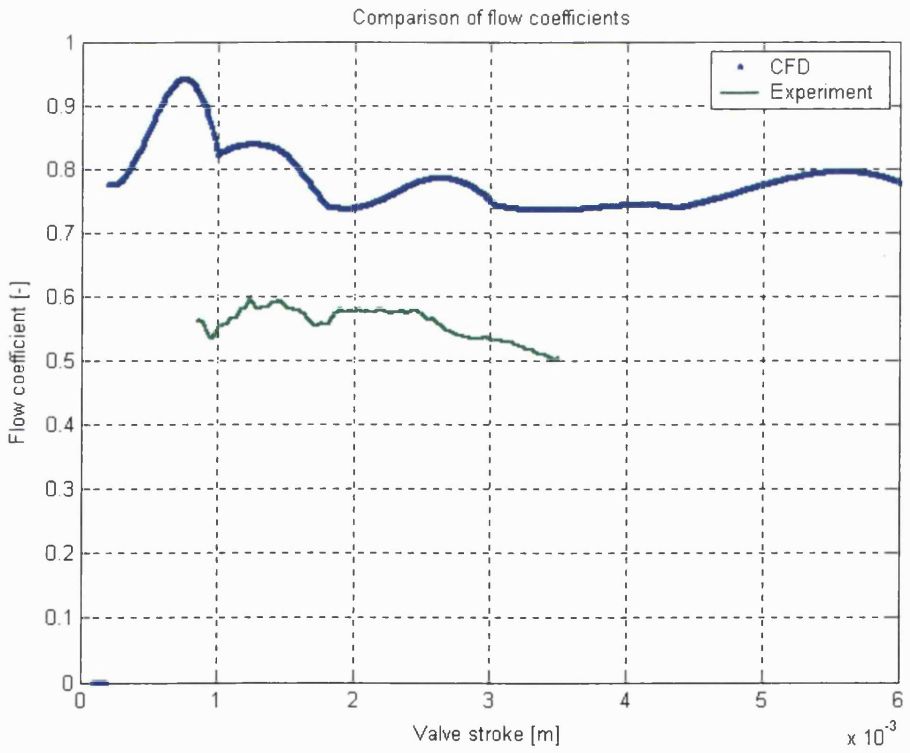

Figure 5.11 Single and continuous curve for flow coefficients

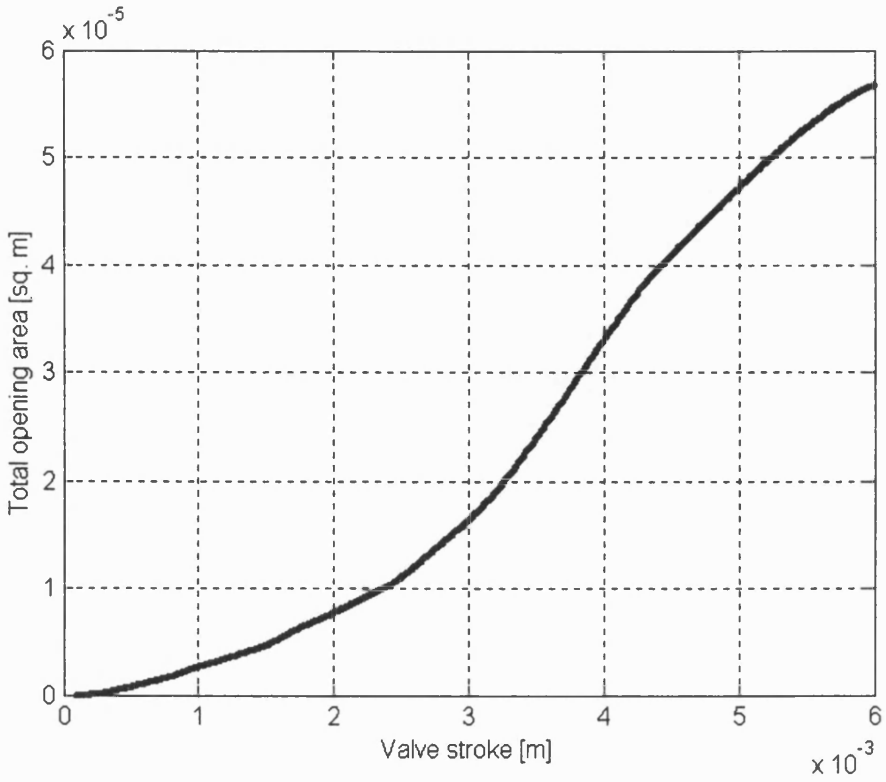

Figure 5.12 Curve for the total opening area

5.6 Results and discussion

The Simulink model pictured in Figure 5.3 was solved using a variable time stepping algorithm 'ode23s' based on a modified Rosenbrock formula of second order **(Matlab 2001)**. The simulation was run for each pilot-pressure with the results plotted to graphs on the screen and with the differential pressure and flow rate written to a data file. The data file for each of the different pilot-pressures was later post processed to produce the performance graph for pressure compensation shown in Figure 5.13.

As a review of what is physically happening within the valve, consider the curve in Figure 5.13 for 55 bar pilot-pressure. When the pilot pressure is applied to the valve, the piston moves to open the valve. A force balance is achieved between the spring force, the pressure force of the pilot signal, flow force, and friction. As the load pressure increases, flow also increases. Initially, the plot of the differential pressure and flow rate are comparable to a fixed orifice pressure-flow curve. This can be seen on the curve for the flow rate from 0 to approximately 41 L/min and the differential pressure from 0 to approximately 48 bar. As the load pressure continues to increase, the valve begins to close due to flow forces working on the piston. This is pressure compensation and can be seen in the performance curves as the near vertical line at 45 L/min from 130 to 245 bar pressure for the case of the 55 bar pilot pressure. When the peak pressure is reached and the load pressure is reduced, the cycle is reversed. The valve again shows the performance of a

fixed area orifice pressure flow with the piston stuck in position because of friction. This is seen as the line from 245 to 48 bar and the flow rate of 40 to 18 L/min. As the flow rate decreases, the forces change and eventually there is enough force to overcome friction and the valve begins to pressure compensate again. However, this time the piston moves to open the valve. This is seen as the portion of the curve from 48 to 0 bar and flow rates from 18 to 0 L/min.

The results from the modelling of the pressure compensating characteristics of the load control valve shown in Figure 5.13 appear to be approaching good qualitative agreement with experimental results reproduced in Figure 5.18. However, it is immediately apparent that the performance curves from the modelled results have more discontinuities present. A discontinuity refers to the abrupt changes in slope of the curves for example at approximately 48 bar and also 125 bar on the 55 bar pilot pressure. Very large discontinuities in the results are present for the curves for the 70 and 75 bar pilot pressures. This trend would have continued with increased pilot pressure, but the inlet characteristics implemented with the *P1 Polynomial* block limited the differential pressure as the flow rate increased. While discontinuities in the curves would be expected because of the nature of the movement of the piston, the large number present in the modelled results is probably due to the discontinuities in the curves that were produced for interpolation of the jet angle and flow coefficients.

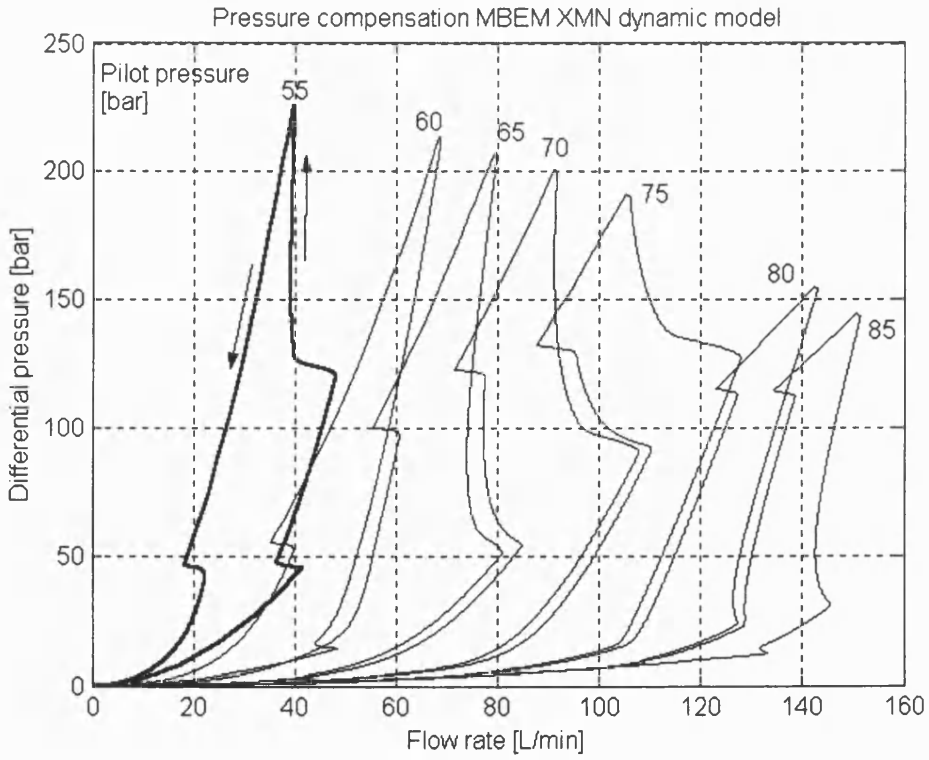

Figure 5.13 Modelled pressure compensation of the load control valve using the Flowcoeff block in the Simulink diagram

Quantitative comparison of modelled results to experimental results demonstrated relatively good agreement. For example, the flow rate at which the valve is pressure compensating with increasing pressure for the 55 bar pilot pressure is approximately 40 L/min in both the modelled results and experimental results. However, with increasing pilot pressure, the modelled results tend to over predict the pressure compensating flow rate. The flow rate at 85 bar pilot pressure is approximately 145 to 150 L/min with the modelled results while it is approximately 133 L/min in the experimental results. This represents an approximate difference of 11%.

Additional pre-processing was found to be necessary in order to improve the correlation between modelled and experimental results. The additional pre-processing was an implementation of the smoothing technique previously discussed in Chapter 2. This technique was based upon the technique devised by **Johnston and Drew (1996)** and it uses weighted linear regression to fit a function to measured data over a localised range of flow rate. The resultant smoothed data for jet angles is plotted in Figure 5.14 and the flow coefficients are plotted in Figure 5.15. They are both annotated as *Smoothed* and the unsmoothed, CFD data is annotated as *CFD*. Similar smoothing was carried out for the total area although no areas of discontinuity existed; hence, the curves are nearly coincident. Both the *CFD* and *Smoothed* data for the total opening area are plotted in Figure 5.16. The smoothing method was found to be sensitive to step size. A step size of 0.25 mm was found through trial and error to produce the best results.

Modelled pressure compensation performance curves from the Simulink model that used the revised pre-processing which included smoothing of the jet angle, flow coefficient, and total opening area are shown in Figure 5.17. The net effect on the valve simulation is that the results are smoother, with fewer abrupt changes and thus better comparable to experimental results. An additional benefit was that the simulation time was significantly reduced with the pre-processing and *Interpolation* block in the Simulink diagram. For convenience for making comparisons, the experimental results are reproduced in Figure 5.18. Immediately evident in the modelled results with smoothed variables is that there are far fewer discontinuities in the curves. A quick comparison to the previous modelled results in Figure 5.13 verifies this. Comparison of the revised model to the experimental results shows that the results compare much more favourably than the previous modelled results. With further analysis, it is evident that the flow rates are still generally 5 to 10 L/min higher in the modelled results when compared to the experimental results with the larger pilot pressures. Comparing the thresholds between the fixed orifice pressure-flow characteristics and the pressure compensation characteristics for the modelled results and the experimental results shows disagreement. For example, on the 55 bar pilot-pressure curve, the threshold on the upward stroke is at about 48 bar with a transition of 5 L/min. The same threshold occurs at about 40 bar in the experimental results and with a transition of about 2 L/min. Similarly, the threshold for the downward stroke for the same 55 bar pilot-pressure curve occurs at about 46 bar with a transition of about 5 L/min for the modelled results;

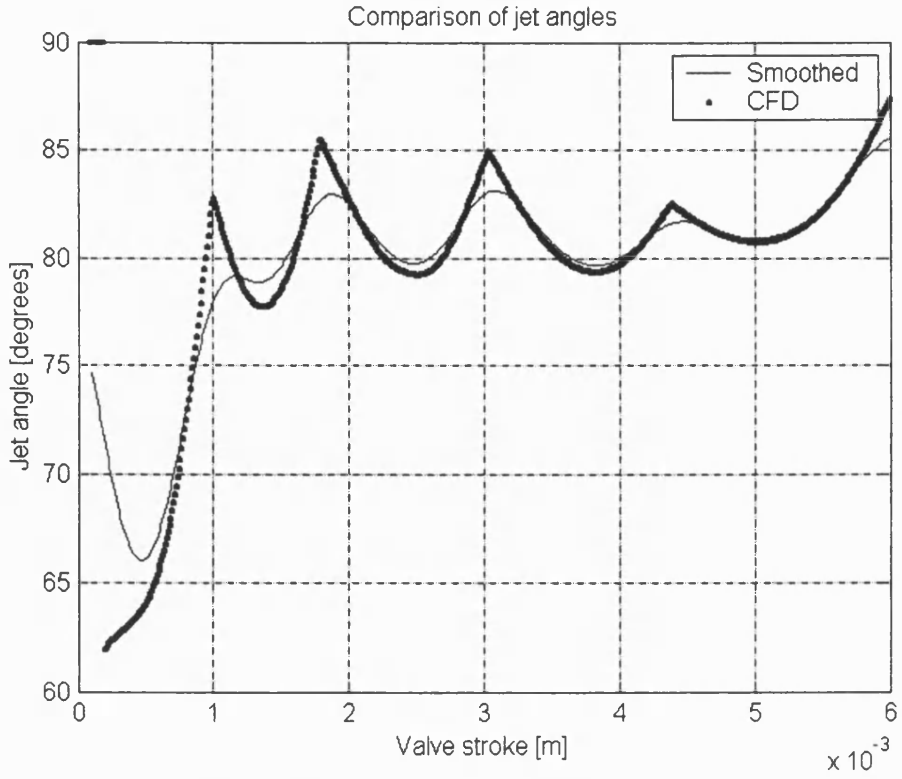

Figure 5.14 Cumulative jet angle function

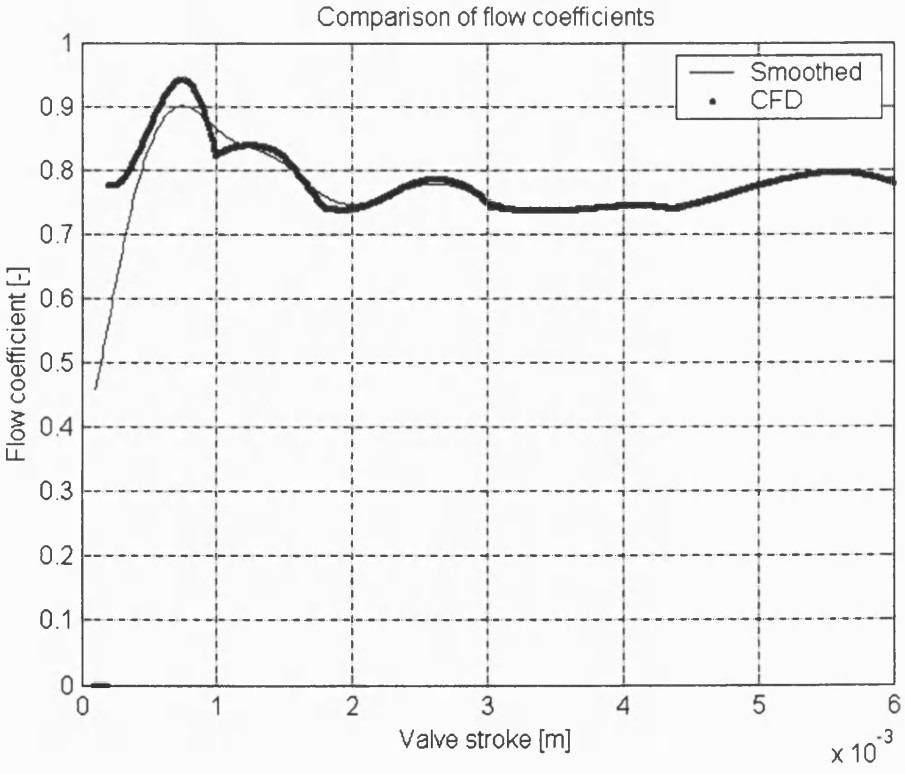

Figure 5.15 Cumulative flow coefficient function

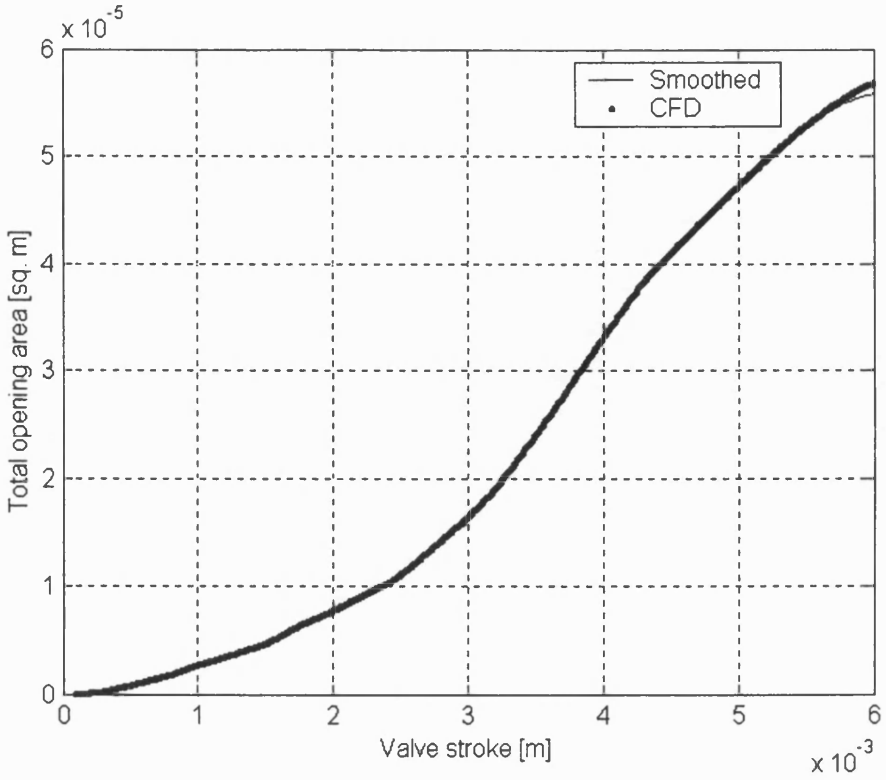

Figure 5.16 Total opening area

however, the transition occurs at about 55 bar with a transition of less than 5 L/min for the experimental results. The thresholds on the downward stroke for all of the curves for the simulated results show similar exaggerated transition regions when compared to the corresponding experimental results. Comparison of the peak differential pressures between the modelled and experimental results shows considerable disagreement as the pilot pressures increase. Time constraints prevented further work on improving this part of the model because modelling the pressure compensation characteristics was deemed more important. A possible explanation for this discrepancy might be the pressure differential across the seals affecting the friction within the valve. The friction function developed did not include a term that was a function of pressure differential across the seal. The curves for the 70 and 75 bar pilot pressures still show the tendency for decreasing flow as the differential pressure increases. This trend was present in the results that did not have smoothing in the pre-process. The current results have the sharp discontinuity smoothed, but the trend is still present. As mentioned previously, this trend would be present for the remaining high pilot pressures if the inlet characteristics had not been implemented with the *P1 Polynomial* block.

Overall, the results show that the pressure compensation characteristics were modelled comparatively well when compared to the experimental results. Comparison of the modelled results and the experimental results justify the use of smoothing.

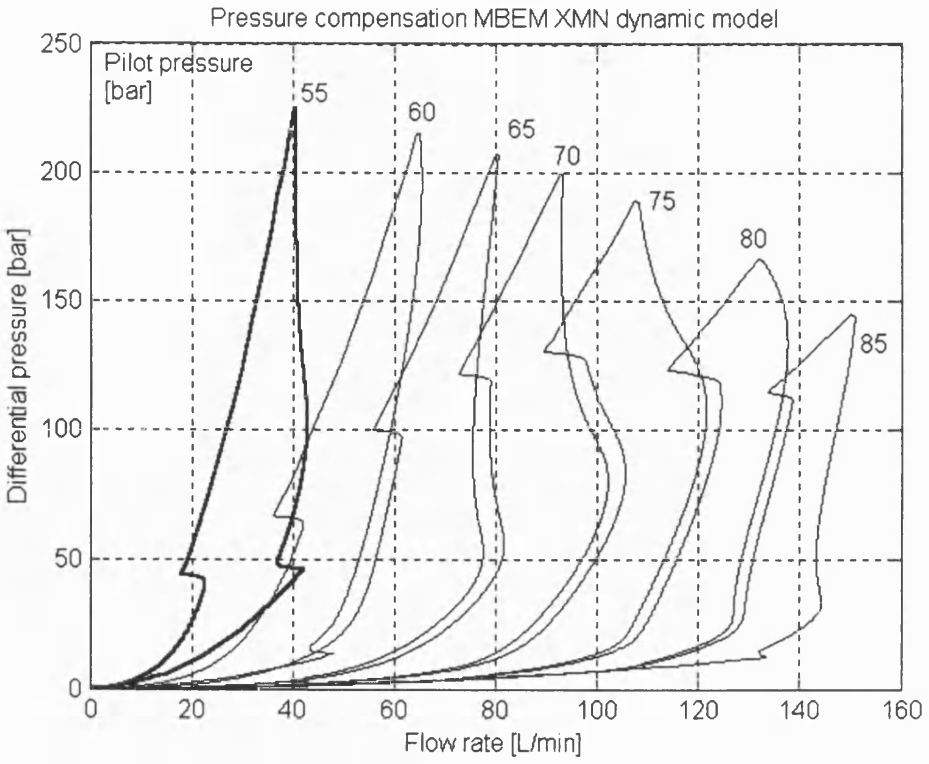

Figure 5.17 Modelled pressure compensation using smoothed pre-processing

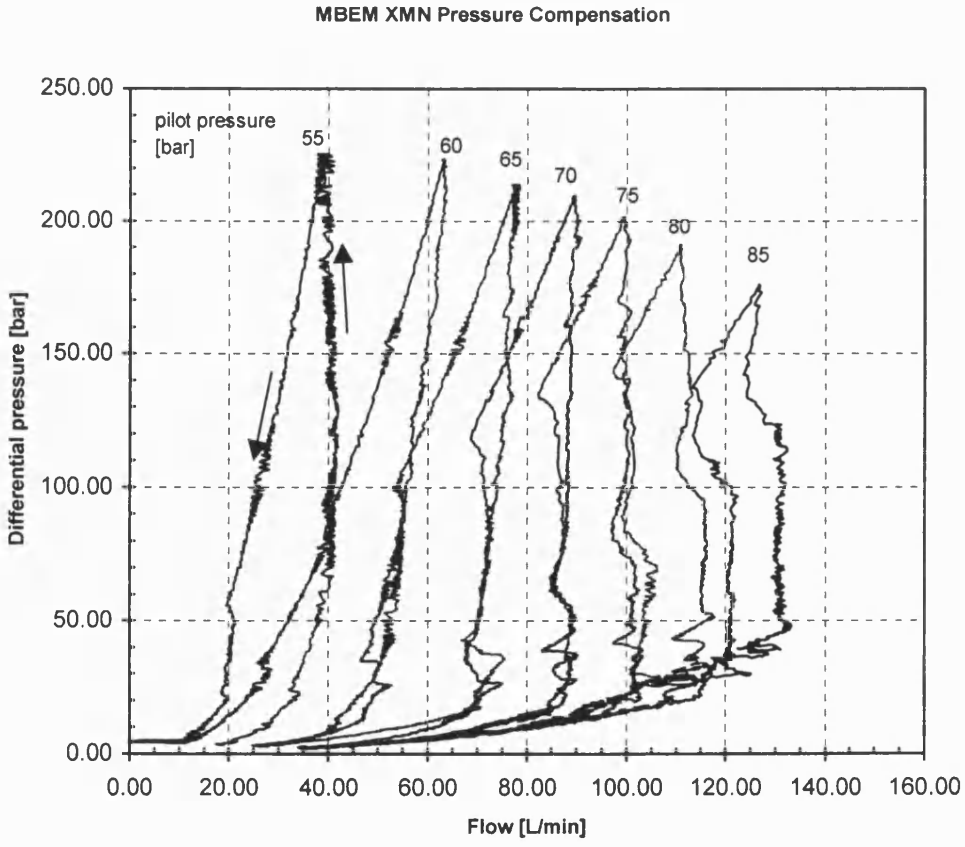

Figure 5.18 Experimental results

5.7 Sensitivity studies

Studies were conducted to determine the sensitivity of the valve modelling to jet angle and flow coefficient. While the modelling results compare well to the experimental work and the modelling makes use of functions to describe the jet angle and flow coefficient as the hole coverage changes, the importance of these functions in improving the simulation results needs further discussion. The studies were undertaken in two distinct manners. Writing separate and independent Matlab script files to simulate a valve that pressure compensates 'perfectly' was the first method. Perfect pressure compensation means that the flow rate is fixed with increasing load pressure and that there is no hysteresis present. The script files were written to calculate the necessary jet angles and flow coefficients for the perfectly pressure compensating valve. The second method was to fix either the jet angle or flow coefficient constant and use this fixed value in the Simulink model.

5.7.1 Jet angle sensitivity analysis

It is common for literature sources to cite a jet angle of approximately 69° **(Merritt, 1967)**. **McCloy and Martin (1980)** describe that the jet angle changes from 69° to 90° in a section on using radial hole orifices as a method of flow force compensation. However, they leave it to the reader to determine how this occurs. Because a change in jet angle as the radial exit hole is uncovered is a fundamental aspect of developing the understanding of the pressure compensation performance of the load control valve, a sensitivity study on the jet angle was conducted.

The study was designed around a load control valve having 'perfect' pressure compensation performance. That is to say, for a given pilot pressure the valve would allow a maximum flow rate that would produce a vertical line on a pressure-flow performance graph. An idealised valve was used with no frictional forces. The Matlab script file *Theta* was written to compute the jet angle necessary to produce perfect pressure compensation performance for a given flow and pilot pressure. Appendix 1 contains a copy of the *Theta* script. A constant flow coefficient of 0.78 was used for the calculations. Figure 5.19 is a graph of the 'perfect' pressure compensation used in calculating jet angles. The values of the flow rates selected correspond to the approximate median value of the flow rates for the experimental results shown in Figure 5.18. The pilot pressures used to achieve the flow rates are shown next to the plotted results. Figure 5.20 shows how the jet angle would have to change as the valve strokes closed in order to achieve perfect pressure compensation. The horizontal lines staggered and overlapping on the graph represent the hole locations. The vertical tick mark represents the centre of the hole. These were added for reference to better understand how the jet angle changes when opening increasingly larger holes that overlap. Again, the pilot pressures used in the calculations are shown next to the plotted

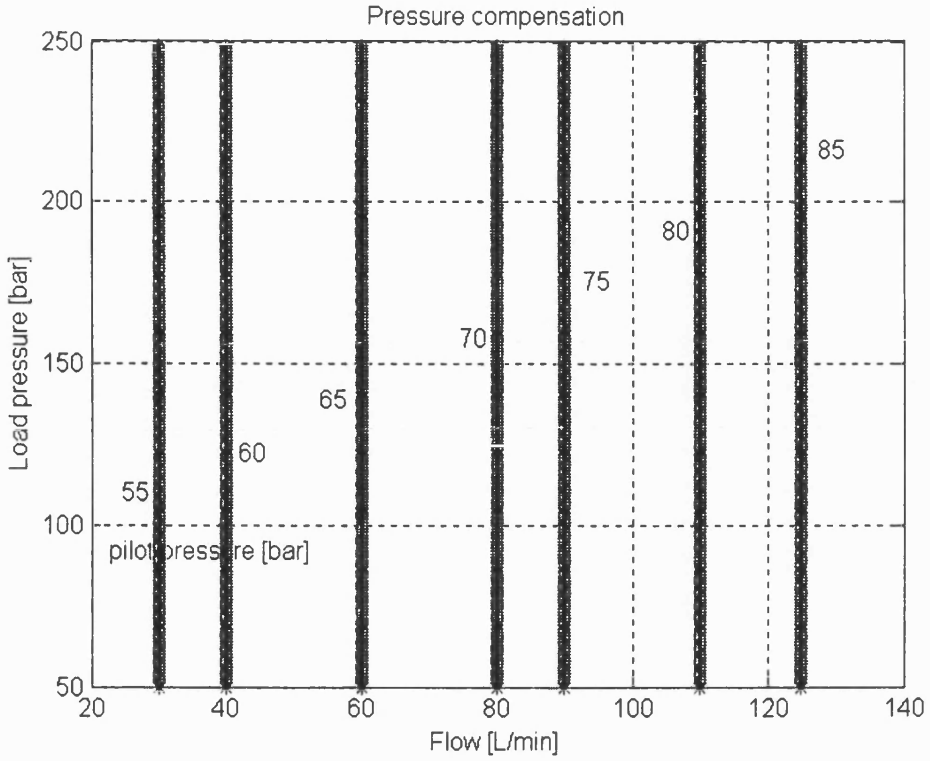

Figure 5.19 'Perfect' pressure compensation for sensitivity study

results. Programming difficulties prevented the simulation from starting at zero load pressure or smaller flow rates. Some vestiges of reality were still necessary in this idealised model.

In practice, achieving small jet angles that the sensitivity study indicates as necessary for perfect pressure compensation would be difficult. A single geometry modification alone would not be enough to alter the jet angle significantly. This will be demonstrated in Chapter 6. Additionally, the sensitivity study on jet angle clearly demonstrates that the angle must change in order to achieve perfect pressure compensation. Therefore, it can be inferred that within the load control valve, the jet angle is changing as the valve pressure compensates for the changes in differential pressure. Hence, in order to better model the valve performance in a pressure-compensating mode, a function that describes how the jet angle changes is necessary.

A second study was conducted to study the jet angle sensitivity using the Simulink valve model shown in Figure 5.3. The jet angle was held to a constant 69° in the *Flowcoeff* function that is part of the pre-processing routine but the flow coefficient was calculated as before. Frictional forces were also calculated as before. As can be seen from the results plotted in Figure 5.21, the pressure compensation curves now slope in the wrong direction compared to the previous simulation results in Figure 5.17 or the experimental results in Figure 5.18. Flow rates are also much reduced compared to the experimental results. The

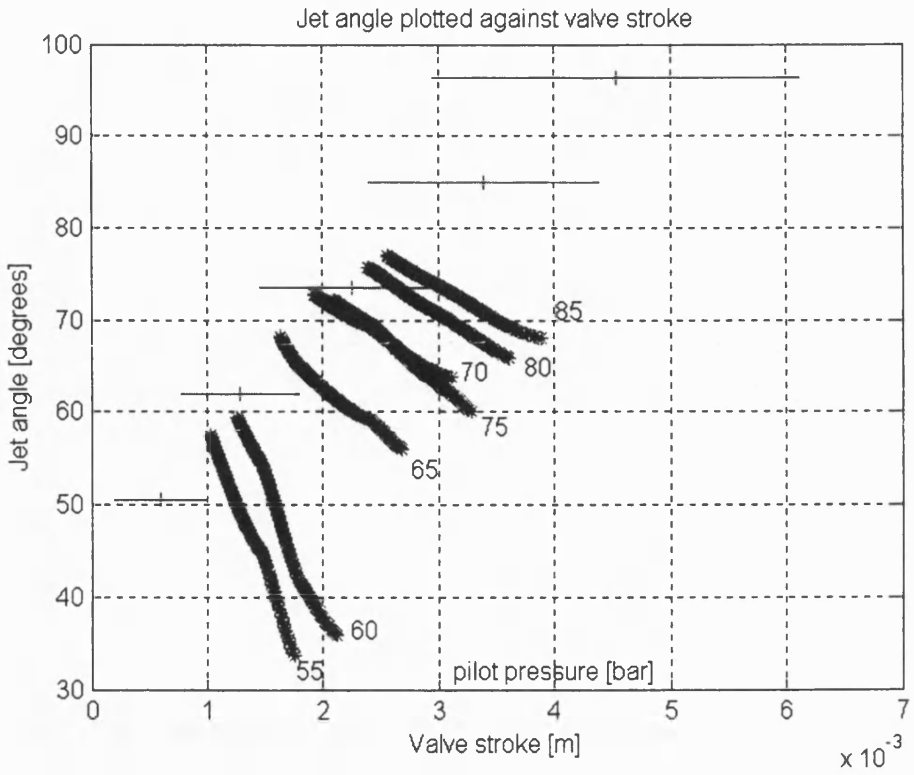

Figure 5.20 Jet angles required to produce 'perfect' pressure compensation

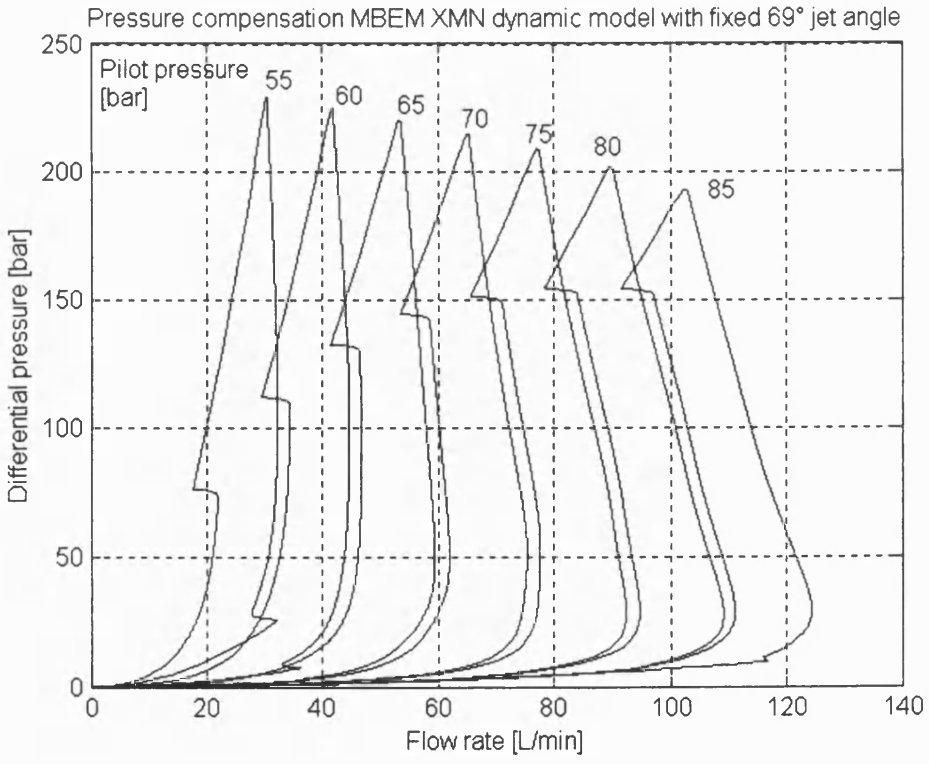

Figure 5.21 Valve characteristics using constant jet angle of 69°

threshold of the discontinuities in the individual curves have been shifted to create larger discrepancies when compared to the experimental results.

Results from the jet angle sensitivity studies provide sufficient basis for the need to include the change in jet angle in the valve model in order to produce more accurate simulation results. While some authors have noted that the jet angle changes as the metering hole coverage changes, literature on modelling valves rarely includes any type of change in the jet angle.

5.7.2 Flow coefficient sensitivity analysis

More attention has been paid in previous research studies to the variation of flow coefficients with both Reynolds number and hole opening than jet angles. Typically, this is done in the form of the discharge coefficient. Often the value of 0.65 is used for the discharge coefficient for flow exiting a sharp edge orifice. This is close to the von Mises asymptote of 0.61 **(McCloy and Martin, 1980)**. McCloy and Martin further this work by providing results of a study on the change of the discharge coefficient with respect to the Reynolds number for several different hole openings. These values for the discharge coefficient approach the approximate value of 0.72 asymptotically.

The first study presented here computes the flow coefficient necessary for 'perfect' pressure compensation if the jet angle is held at a constant value of 69°. This is done with the Matlab script *CQ*. A copy of the script file is included in Appendix 1. An idealised valve is used in the script that assumes no friction. Figure 5.22 shows the results of the calculation of the flow coefficient necessary to achieve perfect pressure compensation. Again, the horizontal lines with a centre tick mark indicate hole location. As with the jet angle study, the values of the flow rates selected correspond to the approximate median value of the flow rates for the experimental results shown in Figure 5.18. The pilot pressures used to achieve the flow rates are shown next to the plotted results. Pressure-flow performance curves are the same as in Figure 5.19. As can be seen in the results in Figure 5.22, a significant and unattainable variation in flow coefficients is necessary to produce perfect pressure compensation. While flow coefficients greater than one have been discussed in Chapter 4 on the CFD work, values for the flow coefficient approaching eight are completely unrealistic and unattainable.

The second part of the flow coefficient study was to use the Simulink model in Figure 5.3 with a fixed value for the flow coefficient in the *Flowcoeff* function that is part of the pre-processing routine. The other parameters of the model were the same as in the simulation discussed above in section 5.5. A value of 0.65 was selected as the constant for the flow coefficient. Figure 5.23 shows the results of the simulation with the fixed value for the flow coefficient. The similar over prediction of the flow rate for modelled results when compared to the experimental results in Figure 5.18 is immediately apparent. Trends are generally the same as the simulation results in Figure 5.17. The hysteresis bands are

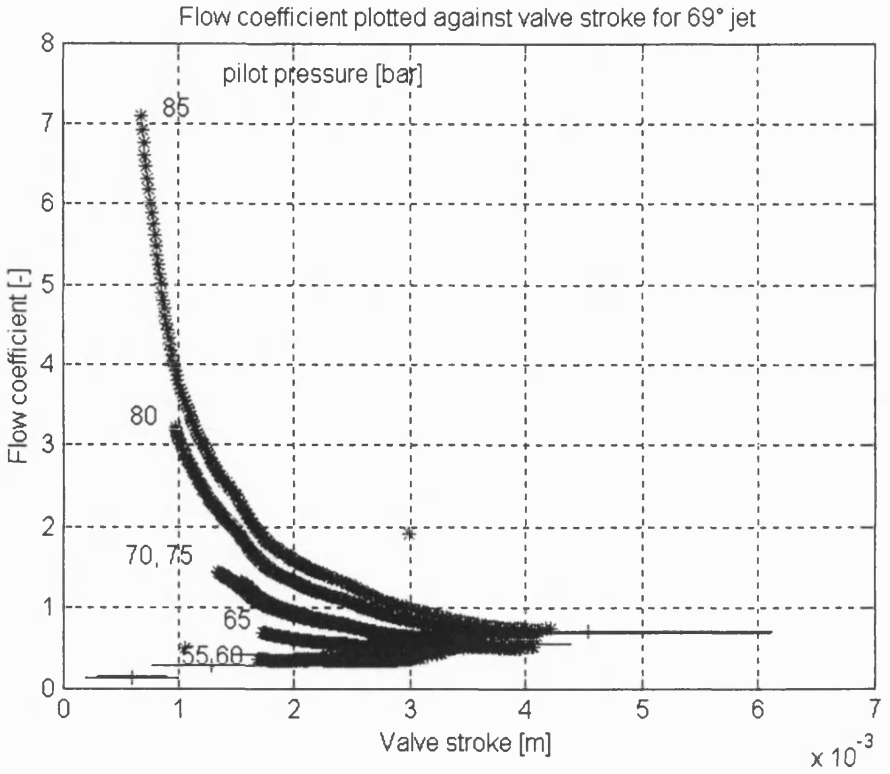

Figure 5.22 Flow coefficient calculated to achieve 'perfect' pressure compensation

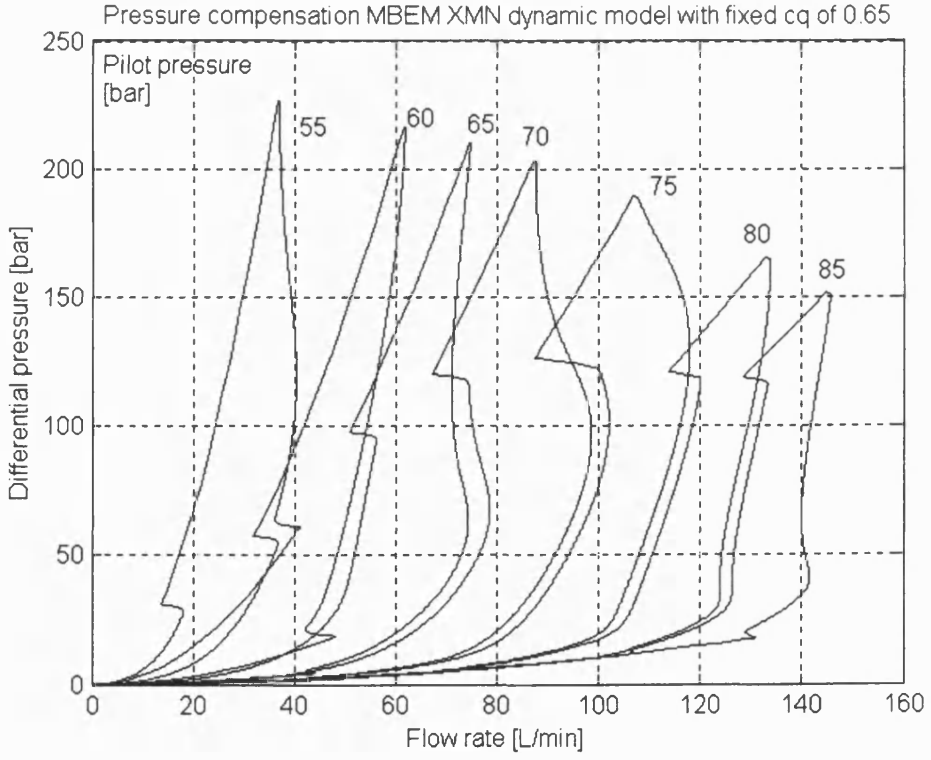

Figure 5.23 Pressure compensation with a fixed flow coefficient of 0.65

narrower for the fixed flow coefficient results compared to the results in Figure 5.17. The discontinuity transitions between fixed-orifice pressure-flow characteristics and the pressure compensation regions for the curves have been shifted higher to higher differential pressures on the upward stroke and to lower differential pressures on the downward stroke.

The sensitivity study on flow coefficients reinforces the need to have a function that describes the changing value as the hole coverage changes. Using this function in the dynamic simulation contributed to producing more accurate simulation results. As with jet angles, other works describing simulations of valves tend to use a constant value for the flow coefficient.

5.8 Concluding remarks

In this chapter, the work described in the previous chapters is used to develop an accurate valve model for the load control valve. The flow visualisation work was used to verify the CFD work. The CFD work was used to develop functions that describe how the jet angle and flow coefficient change as the piston strokes within the valve, covering and uncovering the metering holes. While some literature has made references to the nature of the jet angle and flow coefficient to change with hole coverage change, little work seems to make use of this in valve models. A computationally efficient function for defining both the jet angle and flow coefficient for the load control valve in terms of valve stroke was developed.

The load control valve model was developed in the Matlab-Simulink environment. The model was developed as a dynamic model by making it time based but was not used to produce step response or other dynamic performance predictions. Instead, the modelled results were compared to pressure-flow performance curves from experimental tests. A friction model had to be developed for the valve model. The friction model was based upon a friction-velocity curve. The values used in the friction model were developed empirically predominantly through trial and error but had some basis from the flow force measurements using the technique discussed in Chapter 2. A pre-simulation process computed the jet angle, flow coefficient, and total opening area for the valve in steps of 0.01 mm opening increments. These results were then smoothed with the developed function to enable linear interpolation to be used within the dynamic simulation to compute the needed jet angle, flow coefficient, and total opening area. This method worked well in reducing errors and producing results that compared well with the experimental results. However, the method was sensitive to the smoothing step size. Through trial and error, the step size of 0.25 mm was determined to produce the best results.

The sensitivity studies conducted added proof to the need for functions to describe the jet angle and flow coefficient instead of constant values when building an accurate, dynamic model.

While conducting this work, the lack of literature on fictional forces in hydraulic valves was a difficulty. Although the solution developed seems to work well, reliance on experimental versus empirical data would give more assurance of the results. Experimental as well as modelling work in this area is needed to better the results of the dynamic simulation.

Frictional forces within the load control valve are primarily the result of three o-ring energised glyd rings that provide dynamic sealing of the piston. Some level of friction is necessary to act to dampen motion and the load control valve would not function correctly without some friction. If friction levels could be reduced, hysteresis would be reduced and better pressure compensation performance would be achieved. However, in all likelihood, the near leak free operation of the valve would be lost and hence the valve would no longer be capable of operating as a load holding valve and would then only be capable of load control. This would limit its use in some applications such as in cylinders but the better performance would allow for its use in other applications.

It is envisaged that a 'library' of jet angles for different hole coverage and different hole diameters would be developed. This would speed-up the development of future valve models and hence valve designs.

Mathematical modelling as stated in the introduction was intended to develop a better understanding of the performance of the load control valve. It has been demonstrated that this goal has been achieved.

CHAPTER 6

EVALUATION OF ALTERNATIVE DESIGNS

6.1 Introduction

The ultimate goal of the research was the development of general tools that could be used in future valve design projects to predict performance characteristics prior to machining of parts to construct the valve. Thus, the same procedure used to develop the accurate model of the load control valve can be employed in future designs. Once a concept drawing is produced, CFD models could be constructed to simulate the flow through the valve in order to research the nature of the jet angles and flow coefficients. Using the CFD results, an accurate dynamic model can be constructed that would give the engineer a better idea of the valve performance. This would allow for design changes prior to machining parts for the valve. This would offer a time and material savings in the design process and limit the need for the 'cut-and-try' method of valve design.

In the following sections, the effect of variations in the hole shape and angle are investigated and the analyses of CFD results of design alternatives to the standard drilled hole are presented. These results can be used in the development of an accurate valve model or to design other alternative holes prior to manufacturing a valve. With completed CFD studies, the same procedure employed in Chapter 5 can be used for the alternative designs. This may require rewriting the Matlab function *Flowcoeff* to calculate the opening area based upon the modified design instead of the series of staggered holes that form a helical pattern. Time constraints prohibited completing the CFD studies and subsequent valve modelling for the different hole shapes to be discussed.

6.2 Angled holes

A simple alternative to the cross-holes drilled perpendicular to the surface of the sleeve is to angle the holes. Figure 6.1 shows a cross-section of the fluid volume used in the CFD modelling. This drawing clearly illustrates how the cross-hole could be rotated from perpendicular at some angle. Two variations were simulated with CFD. The first was a rotation of 10° and the second was a rotation of 20°. The hole size selected for these studies was the 1.98 mm (0.078 inch) diameter that was the same size used in the flow

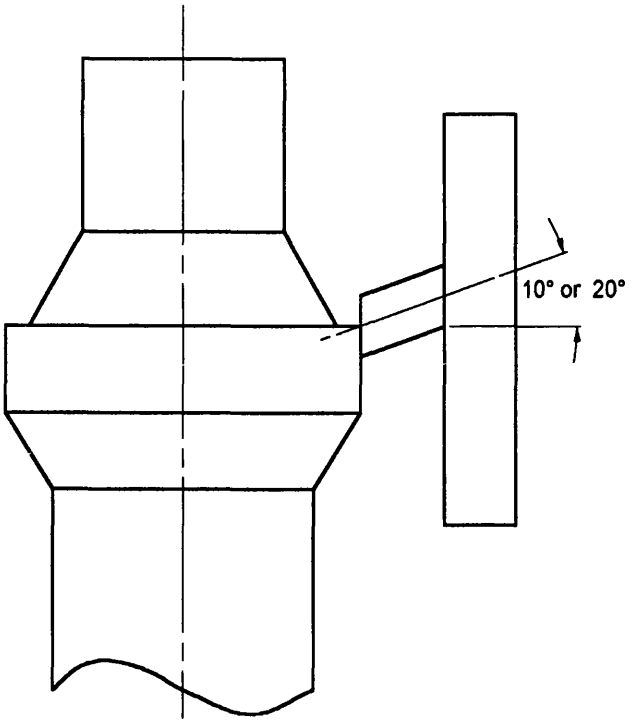

Figure 6.1 Angled cross-hole CFD fluid volume cross-section

visualisation studies. A flow visualisation model could be easily constructed for verification of the CFD results for the jet angle.

The angled cross-holes could be easily machined in production without the need of any special processes or tools. Drilling the cross-hole at an angle would require that either the work piece or the tool to be rotated on its axis by the desired angle. It was hoped that angling the exit hole would act to control the exiting jet angle by acting to channel the flow on the predetermined angle.

6.2.1 Results and discussion

The simplified valve model used in Chapter 4 was used to simulate the fluid flow through the angled hole designs. Figure 4.3 is reproduced as Figure 6.2 to again illustrate the velocity vector results of the diameter cross-hole drilled perpendicular to the surface of the valve sleeve and half open. A velocity vector plot for the 10° angled hole with the exit hole half covered is shown in Figure 6.3. Similarly, Figure 6.4 shows the velocity vector plot for the 20° angled hole that is also half covered. From comparison of the three velocity vector plots, differences are immediately evident. In the case of the perpendicular hole, jet separation and reattachment down stream of the metering edge is clear. For the two cases of the angled holes, jet separation does not seem to be occurring. The jet remains attached to the lower wall of the exit hole. There is a common area of recirculation for all three cases

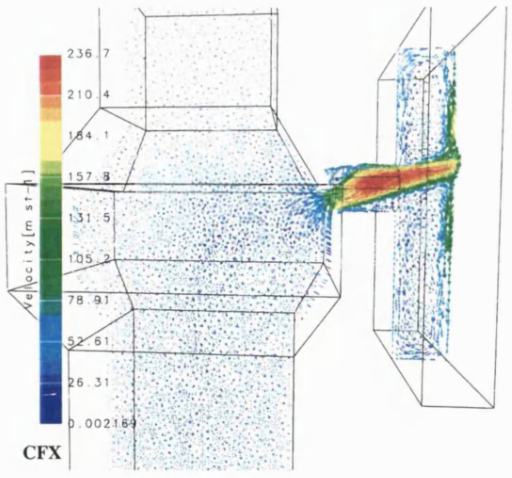

Figure 6.2 Perpendicular cross-hole

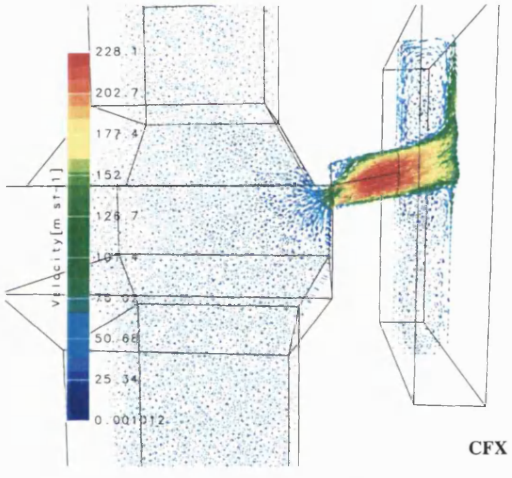

Figure 6.3 Drilled hole angled 10°

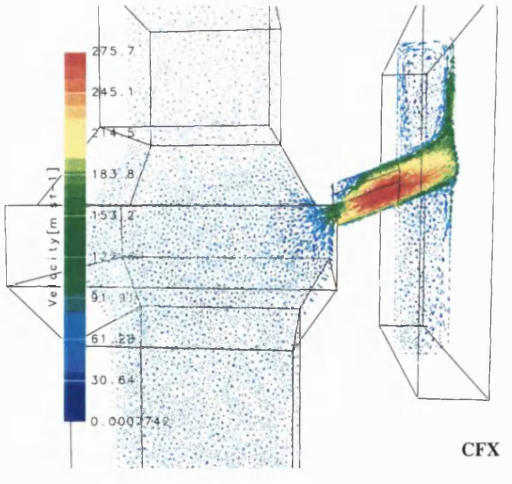

Figure 6.4 Drilled hole angled 20°

above the jet, immediately downstream of the metering edge. However, the recirculation bubble below the jet in the case of the perpendicular cross-hole is not present for the angled holes.

Quantitative analysis of the results from the CFD simulations for the 10° and 20° angled exit holes leads to the graph shown in Figure 6.5 for the jet angles. The results for a standard drilled hole, perpendicular to the sleeve surface is shown for comparison. As can be seen by comparing the jet angles, the largest difference between the angled exit holes is just over 1° for the 10° increase in angle for the exit hole at full opening. The other openings exhibit less than 1° difference. However, the largest difference is found when comparing the 20° angled hole results to the standard drilled hole. Again, the maximum is at the full opening (with 6.9° difference). The minimum difference is at the half open position (with 1.2°difference). It can be concluded from the graph of jet angles in Figure 6.5

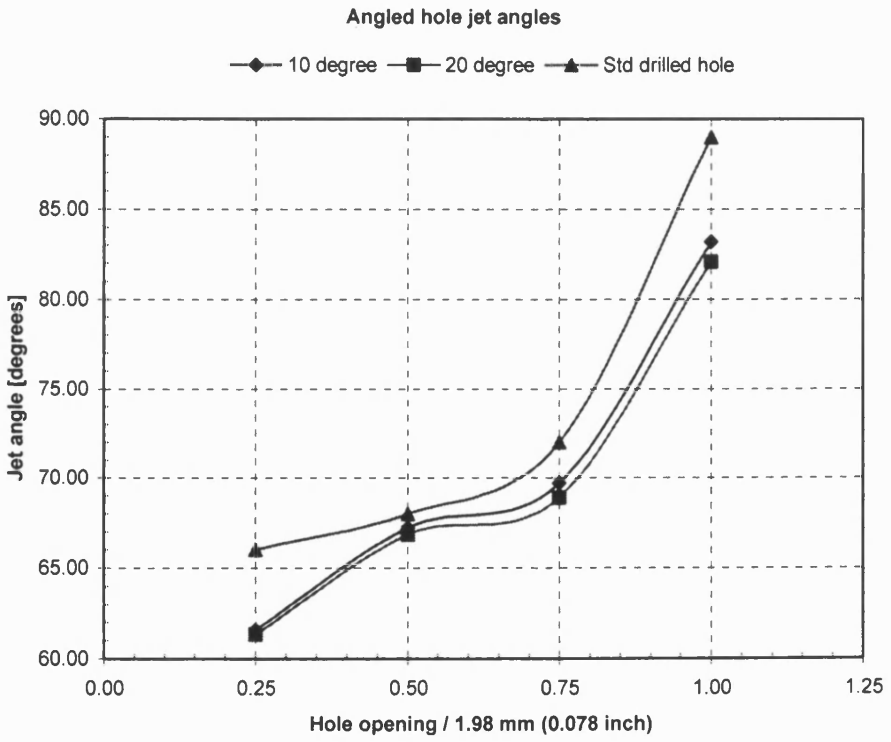

Figure 6.5 Comparison of exit jet angles for angled exit holes

that the jet angle can be modified if only slightly by changing the angle of the exit hole; however, the trends remain the same. The change in the jet angles by changing the angle of the exit hole would affect the flow force as was demonstrated in Figure 6.5.

Quantitative analysis of the flow coefficients also leads to the graph shown in Figure 6.6. The graph shows drastic differences in the flow coefficient compared to the standard drilled hole as a result of rotating the exit hole 10° and 20°. The largest difference of 0.39 can be seen at the quarter opening position. The flow coefficient greater than 1.00 would

indicate pressure recovery taking place as was pointed out in **Johnston *et al.* (1991)**. As was mentioned previously, jet separation and hence reattachment occurs for the case of the perpendicular cross-hole, but jet separation does not occur for the angled holes. It can be surmised that this is why the results for the flow coefficient between the angled and perpendicular holes show such drastically different trends.

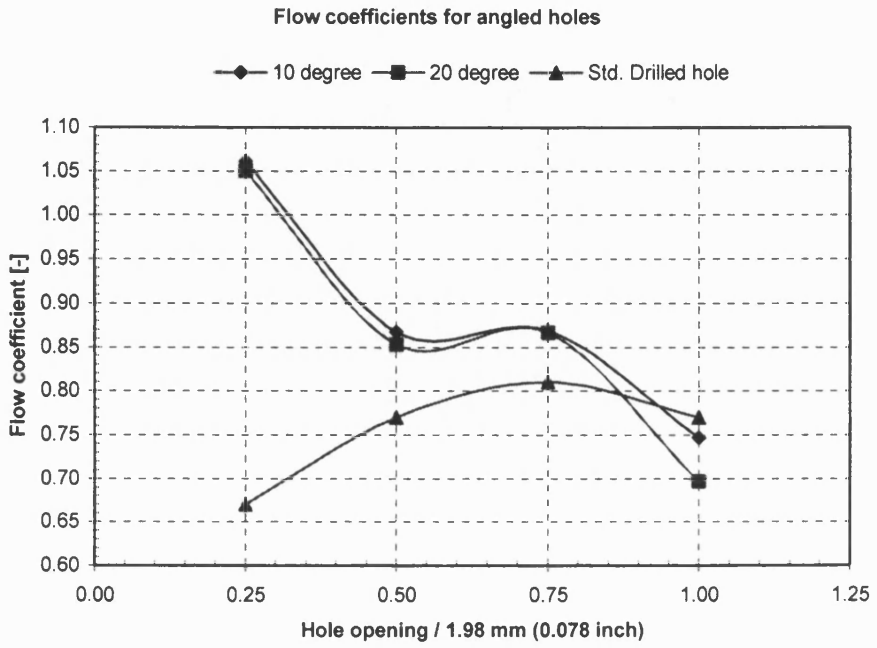

Figure 6.6 Comparison of flow coefficients

Whether change in flow coefficient and jet angle caused by angling the exit holes is good, bad, or unimportant to the performance of a valve would depend upon the performance sought. The trends exhibited, in particular the large change in flow coefficient, by the angled holes would seem to indicate that angled holes would probably not be the ideal exit holes for the load control valve. However, it would be desirable to continue the study further by using the changed flow coefficient and jet angle in the model of the valve in order to get a better idea of how the change to the exit hole effects the valve performance.

6.3 Diamond shaped hole

The second hole shape investigated was a diamond shaped hole. The shape, as shown in Figure 6.7, would require more specialized machining techniques in order to manufacture parts than the simple drilled hole. A diamond shape can be machined into a valve part simply through a process of drilling and milling or by using a comparatively more exotic process such as wire EDM (electric discharge machining). The goal of using a shape such

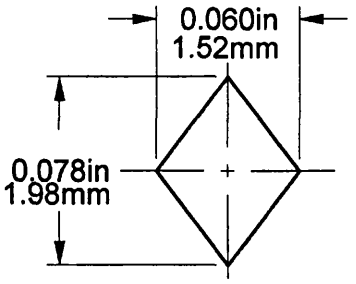

Figure 6.7 Diamond hole shape

as the diamond shape is to provide fine metering of oil as the diamond is initially uncovered but increasing the flow area as the diamond is further uncovered. It was envisioned that a staggered, helical pattern could be created from small diamonds to create the metering sleeve. Alternatively, a single series using multiple, larger diamonds would provide both fine metering to control a load as well as large flow area when that is needed. The aspect ratio could by altered to change the controlling characteristics of the valve as well as to reduce the flow area. Additionally, the diamond shape could be angled as was done in the previous section using drilled holes.

6.3.1 Results and discussion

The CFD studies on the diamond shaped hole again used a simplified valve model as the base. A velocity vector plot for the case of the diamond uncovered by half is shown in Figure 6.8. Comparison of the results of the hole drilled perpendicular to the surface shown in Figure 6.2 demonstrates some differences. The recirculation bubble below the separated jet is larger for the diamond shaped hole than it is for the circular hole. Similarly, the recirculation bubble above the jet is larger as it appears to extend further downstream than the case for the drilled hole. Quantitative analysis of the CFD results for the jet angles leads to the graph in Figure 6.9 to be produced. The largest difference in jet angles occurs at the quarter open position with 5° difference. In addition to the points that the two curves cross, the smallest difference between the curves occurs at the full open position with 2° difference. The diamond shape has the effect on the exiting jet of 'flattening' the curve or making it more linear. It is anticipated that a similar effect would be found on the flow forces.

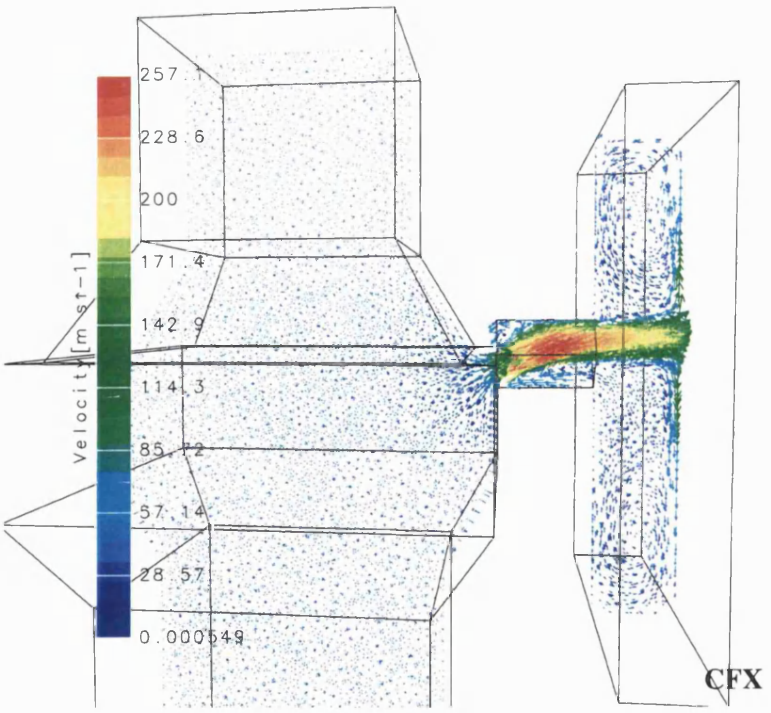

Figure 6.8 Diamond shaped hole half covered

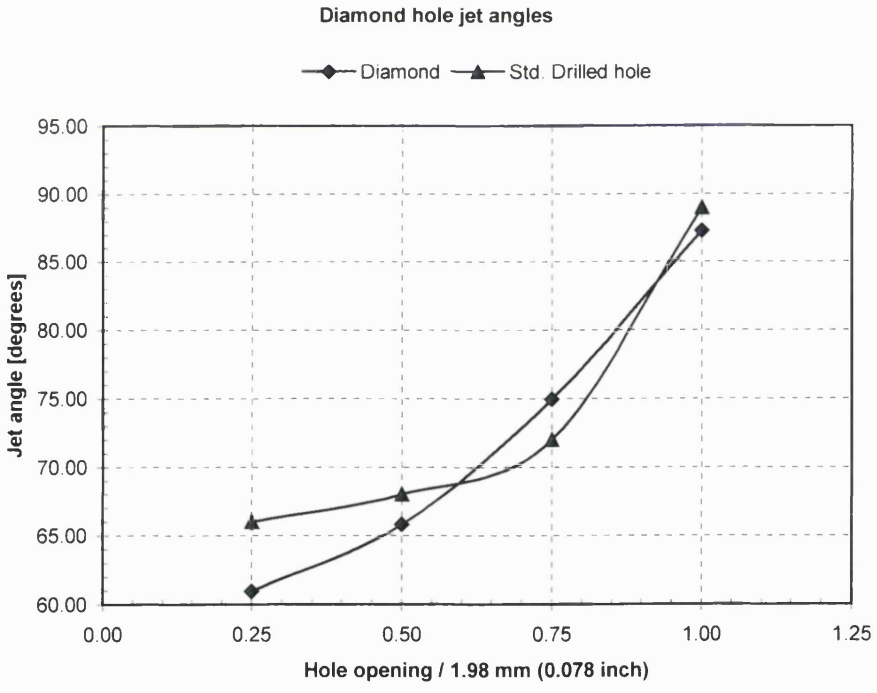

Figure 6.9 Comparison of jet angles

Quantitative analysis of the flow coefficients leads to the graph shown in Figure 6.10. The graph shows dramatic differences in the flow coefficients between the diamond shaped hole and the 1.98 mm (0.078 inch) diameter drilled hole. The dramatic difference is highlighted by the 0.59 difference for the quarter open hole. Besides the point where the two curves cross, the smallest difference occurs when the holes are full open. The difference at this point is 0.03. As has been mentioned previously, flow coefficients greater than 1.00 indicate pressure recovery and this is related to jet reattachment. Jet reattachment is related to jet separation occurring at the exit hole.

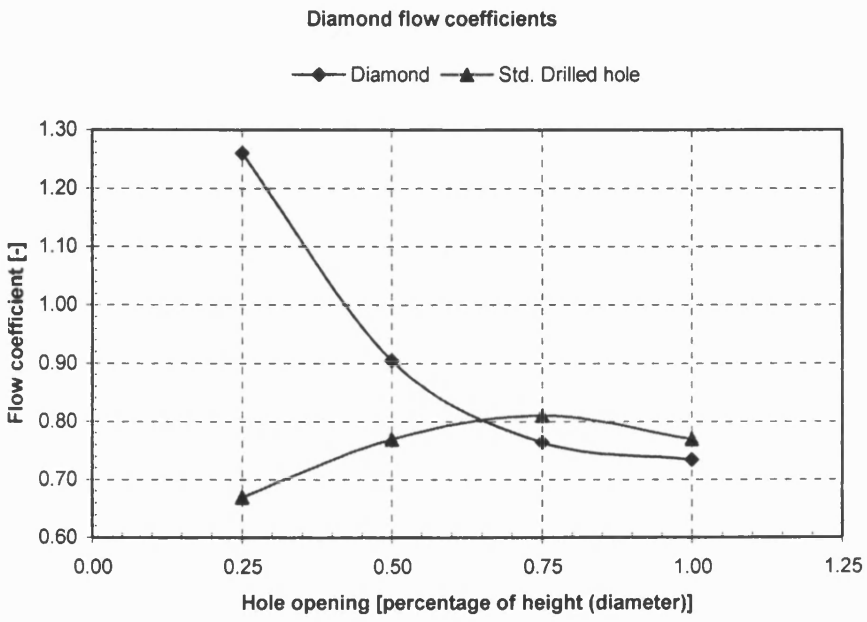

Figure 6.10 Comparison of flow coefficients

As with the angled exit holes examined in the previous section, whether the diamond shaped hole is good, bad, or unimportant to the valve performance depends upon the performance sought. Further study through the implementation of the hole parameters to the developed model would be necessary to make a more conclusive decision on the applicability of the diamond shaped hole performance improvement in the load control valve.

6.4 Inverted teardrop shaped hole

The final hole shape investigated was an inverted teardrop. It is envisioned that this shape, if made sufficiently large, would replace the multiple series of drilled holes with either a single series or at most two staggered series of shaped holes. The intention of the design was to produce a shape that would both give small flow areas with small piston strokes and large flow areas with increased flow area with a smooth gradient with a single shape. There are several manufacturing options to create the shape. The exotic option would be the use of wire EDM machining. Another, less exotic but time consuming and hence expensive method would be to plunge and traverse with mills to create the desired shape. Possibly the simplest method would be to simply drill holes with twist drills while compensating for drill walk while machining.

The design shown in Figure 6.11 was a first attempt at an inverted teardrop design. The starting point of the design in addition to producing a shape that would create a smooth

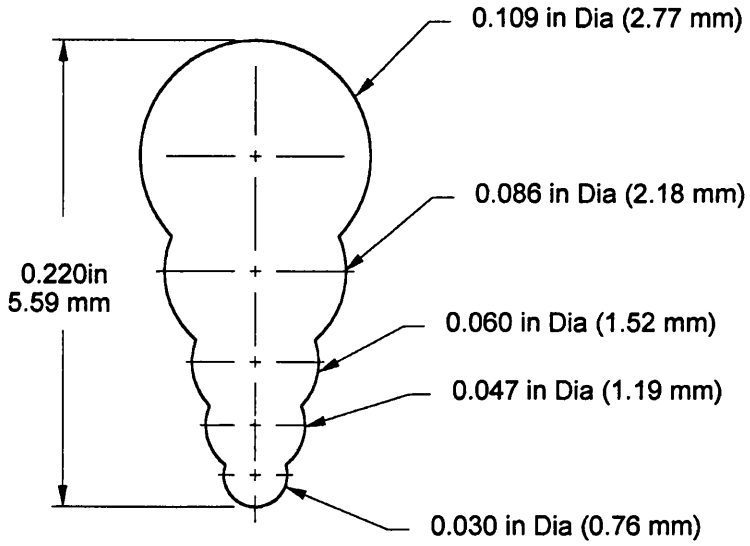

Figure 6.11 An inverted teardrop design

area gradient and the control possibilities describe previously; hence, the first attempt was to duplicate the opening area of the five series of holes. The maximum opening area of the five series of holes is approximately $5.671\times10^{-5}m^2$. The maximum opening area of the inverted teardrop shape designed was $1.026\times10^{-5}m^2$. The shape in Figure 6.5 could be manufactured from drilling five overlapping holes as shown. A single series of four shapes would replace the five series of four drilled holes per series.

6.4.1 Results and discussion

A sample of the CFD simulation results is the velocity vector plot shown in Figure 6.12. The plot is for the case of the inverted teardrop shape being half open. What is immediately evident is that the exiting jet is much larger in size than for the simple drilled hole. This is typical for all four cases of hole opening simulated. The recirculation bubble that is commonly present above the exiting jet is also present for the inverted teardrop shape. Jet separation does not appear to occur. As can be seen, the jet appears to remain attached to the lower edge of the hole.

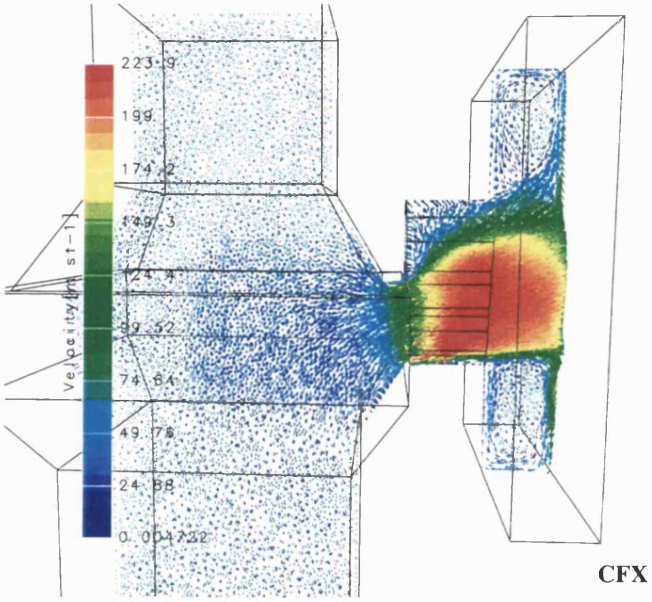

Figure 6.12 Half open inverted teardrop velocity vector plot

Quantitative analysis of the results from the CFD simulations for the inverted teardrop shape leads to the jet angles plotted in Figure 6.13. The jet angle results for the standard drilled hole and the smoothed jet angles obtained from the CFD data for all five series of drilled holes used in the production valve are shown for comparison. The smoothed curve is the same as shown in Figure 5.10. The calculated jet angles for the inverted teardrop shape shown in Figure 6.13 shows a range or variation of 1.3°. This is significantly less than the range for the single, standard drilled hole of 1.98 mm (0.078 inch) diameter. Similarly, the smoothed CFD results for the five hole series also shows significantly more variation.

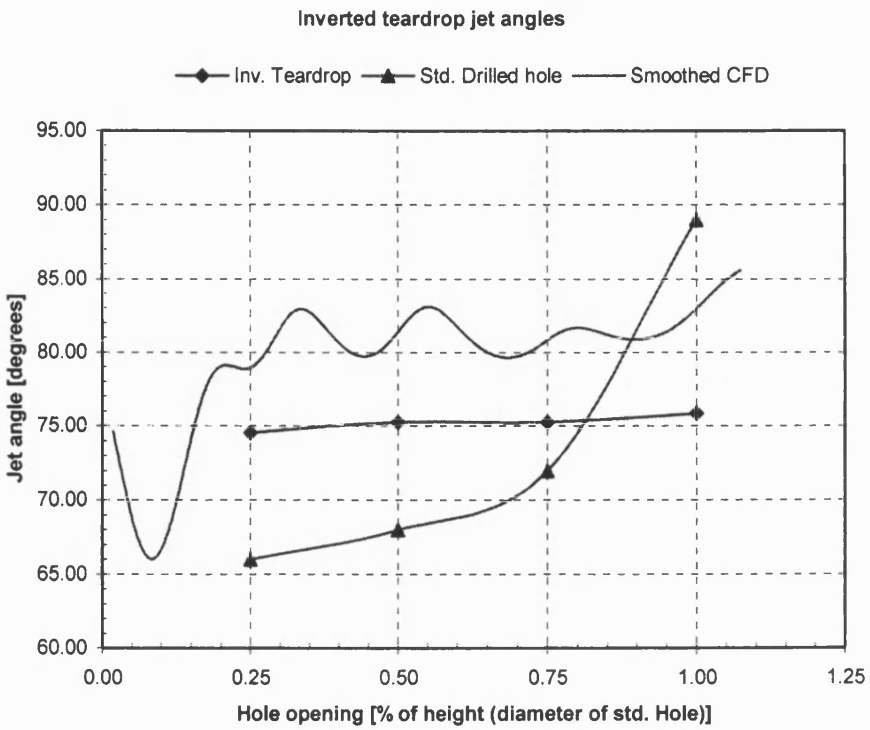

Figure 6.13 Comparison of jet angles

Quantitative analysis of the flow coefficient calculations shows similarly small variation as was seen with the jet angles. The results are shown in the graph in Figure 6.14. Again, the results for the standard, single drilled hole and the smoothed flow coefficients obtained from the CFD data for all five series of drilled holes used in the production valve are shown for comparison. The smoothed curve is the same as shown in Figure 5.12. The range of variation for the flow coefficient for the inverted teardrop was 0.06, which again is significantly less than that for the single drilled hole or that for the smoothed, five series, CFD results. It can be surmised that the small variation in flow coefficient follows from the small variation in jet angle. The typically lower value would be the result of not having jet reattachment in the inverted teardrop design. The trend indicated by the inverted tear drop designed exit hole would seem to indicate that it would probably be an ideal shape to use with the load control valve.

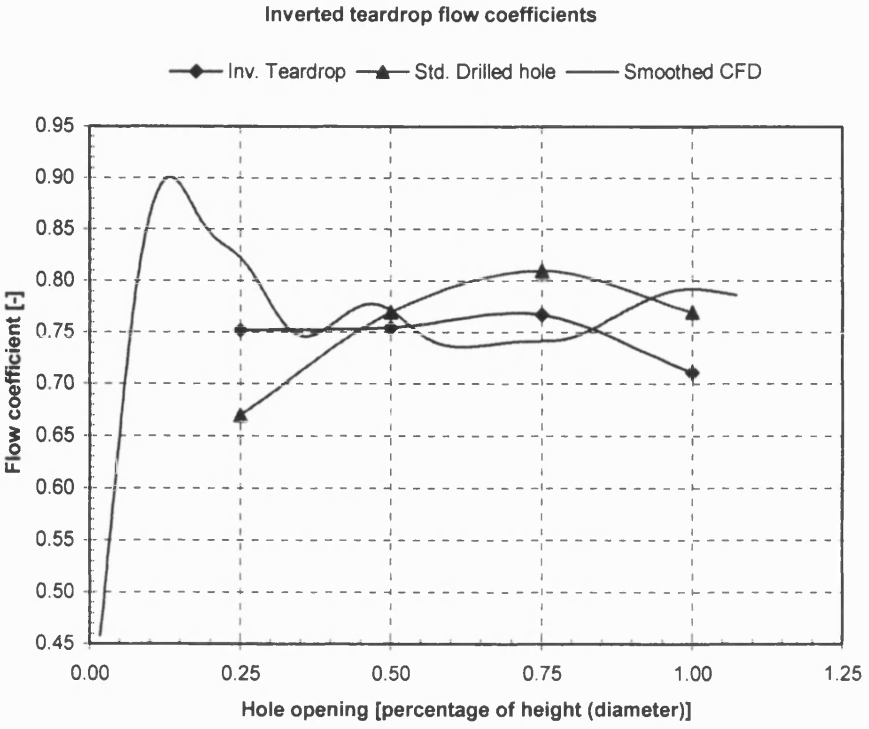

Figure 6.14 Comparison of flow coefficients

The results from the study on the inverted teardrop are the most intriguing of the different shapes briefly investigated. They represent a good attempt at controlling flow forces by controlling the exiting jet angle and flow coefficient. The near constant jet angle and flow coefficient may lead to the flow force varying more directly with flow rate instead of varying as a combination of flow rate and hole opening. Further study through the introduction of the flow coefficients and jet angles into the valve model would be the minimum necessary in order to determine if the valve performance would improve, not change, or not be as good compared to the current design.

6.5 Concluding remarks

The beginning steps for producing an accurate valve model to aid in the design of metering holes were started through the CFD simulations. Following completed CFD studies, the results for the jet angle and flow coefficient would be pre-processed. The custom written Matlab function *Flowcoeff* would need to be modified to correctly calculate opening area as the piston moves for the different shaped holes. This work was not completed for the different shaped holes examined in this chapter because of time constraints.

The three different alternatives to the simple drilled hole offer examples of potential methods to control flow forces by controlling jet angles and flow coefficients. This would be better demonstrated with a completed study. Of the different hole shapes examined, the

inverted teardrop shape is the most intriguing although potentially the most complex and difficult to manufacture. The diamond shaped hole would also be difficult to manufacture. The simplest to manufacture would be the angled cross-holes. However, the minimal change in jet angles compared to the standard drilled holes and the drastic difference in flow coefficients would make it not an attractive alternative. Hence, a compromise would have to be reached between the degree of difficulty and expense to manufacture and the degree of flow force control.

CHAPTER 7

CONCLUSIONS AND RECOMMENDATIONS

7.1 Introduction

A programme of research was conducted to investigate the pressure compensation characteristics of the load control valve designed by Sun Hydraulics. Understanding the cause of the pressure compensation within the valve and attempt to control it in order to improve its characteristics were the goals of the research.

Experimentation was used to measure pressure compensation characteristics, to measure valve flow rates and piston stroke, and to quantify flow forces. Flow visualisation was used not only to aid in developing an understanding of how the jet angles change with piston movement, but also in both qualitative and quantitative verification of the CFD results. CFD was also used to aid in developing an understanding of how the jet angles change with piston movement and also how the flow coefficients changed. These changes were quantified for use in the mathematical modelling. A mathematical model was developed using the Matlab-Simulink environment. The model made use of the functions developed to describe the changes in jet angle and flow coefficient. A friction model was also developed. These "sub-models" were key in modelling the pressure compensation characteristics that closely matched the experimental results.

The results from the mathematical modelling demonstrated that an understanding of the pressure compensation characteristics of the load control valve had been developed. The initial work into design alternatives for the metering holes shows promise in potential methods of controlling pressure compensation characteristics.

7.2 Experimental work

Experimentation was used to measure the valve performance primarily in a pressure compensation mode. Pilot modulation was also measured. These two measures provided a good picture of the performance characteristics of the valve. This was necessary in order to develop the research programme. Quantifying the valve stroke during pressure compensation was a key point of interest. This would verify that the valve piston was moving when the valve was pressure compensating. Measurement was made possible with

an LVDT that could withstand the high pressures in the spring chamber. This worked well for the most part. The only difficulties encountered was that the inner most spring in the nest of springs had to be removed for the connecting rod that connected the valve's piston to the LVDT's moving core. While the use of two of the three nested springs is a valve option to lower the cracking pressure, the majority of measurements made with the valve used all three springs. The use of a smaller diameter connecting rod but of sufficient strength may allow for the use of all three springs.

Quantifying flow forces was also a key measurement to be made with experimentation. A flow force measurement rig was adapted from a design used in research at Sun Hydraulics. The rig worked well in a static or quasi-dynamic mode. It was not designed to work in a dynamic mode. A flow force measurement rig that would work in a dynamic mode would allow direct comparisons to be made between experimental results and modelled results for flow forces.

7.3 Flow visualisation

The flow visualisation work proved to be remarkably successful. The resulting photographs show that the jet angle changes with changing hole opening caused by movement of the valve piston. While originally intended only for qualitative verification of the flow visualisation results, the results were good enough to make some quantitative measurements. Although the photographs produced for the flow visualisation work were of high quality, a glare obscures the metering edge of the piston. This prevented measurements of the jet angle at the point of actual interest. An area of future work would be to attempt to remove this glare. This would probably require the use of a laser and light sheet optics as a light source. This should produce a light sheet confined to a more narrow width than the slide projector and slit illumination used.

Quantitative verification was limited to the unsophisticated, simple measurements of exiting jet angles using a protractor on the photographs. While this method works, more state of the art methods are becoming available and should be considered in future work. Particle Image Velocimetry (PIV), for example, would produce velocity information throughout the flow field that could be compared more directly with the CFD results for quantitative verification.

7.4 CFD

The CFD work produced many useful results in spite of some shortcomings. Model geometry was simplified into a 'simplified' geometry because of severe difficulties encountered when trying to create the intersection between the cylindrical geometry of the valve's main chamber and a circular exit hole. This was related to the global tolerance that

needs to be prescribed when initially building a model. An extremely small tolerance was necessary in order to create the intersection and resulting compound curves without creating gaps. The gaps act as leak paths for the fluid. This is perfectly reasonable and easy to set; however, setting such tight tolerances in the geometry-building module created problems for the automatic meshing module. In order to work around the meshing problems, the global tolerance needed to be increased. This then recreated problems in the geometry-building module. Whether this is a fault of the CFD code or its user was never determined. Overcoming this fault would produce models that more faithfully reproduce the geometry present in the valve. With the software improvements announced at the user's group meeting in November 2001, building a more realistic valve model should be much easier.

Functions were developed in the dynamic modelling of the valve to describe the resulting composite jet angles and flow coefficients. An attempt was made to verify this with CFD results. This would have required a model being produced that would give the flow rates through individual holes with multiple holes being modelled. While the concept seems simple enough, in practice it was found difficult to implement. Surfaces were created in the entrances to the outlet holes. The surfaces were given boundary conditions that would have allowed flow to pass through them in any direction. However, the meshing module did not accept such surfaces being within the flow domain.

Another area that CFD would be useful in investigating further is the annular exit area in the cavity that the valve is mounted. This would require multiple exit cross-holes as well as a single, large exit from the annular area. Creating models to investigate the pressure gradient that is present in the annular region were attempted, but the multiple outlets proved problematic for the meshing module. Hopefully, with further improvement to the meshing module and with more experience, this type of model and research might be possible.

7.5 Mathematical modelling

The mathematical modelling progressed from use of a spreadsheet program to the use of the Matlab-Simulink environment. Matlab functions were developed to predict the jet angle and flow coefficient based upon the CFD results. Composite functions were developed to combine the data from the individual hole series into a single value for jet angle and for the flow coefficient. The use of CFD results to aid in producing models that are more accurate is a hybrid technique of modelling. This technique is relatively new in literature and has only progressed as CFD codes have progressed. It proved to be key to the success in modelling the load control valve. However, the success of the modelling was not entirely due to the use of CFD results. The simple friction model that was developed led to major improvement in the accuracy of the prediction. The friction model remains

unverified in the strictest sense. The improved results offer empirical verification, but an experimental based verification programme is warranted.

The model developed was used in a quasi-dynamic mode and it produced results that closely matched experimental results for pressure compensation. Dynamic responses to a step function or other dynamic input signals were not tested. It is conceivable that the load control valve would be subjected to a step-type pressure input in field applications. This was considered as part of both the experimental testing programme and the modelling programme. Future work on this testing and modelling would be useful.

Dynamic testing might show that the dampening term used in the model would need to be better defined. The manner in which dampening was added to the model was intended as a 'catch-all' for the dampening created by the different orifices present in the valve and for the dampening effect of the oil moving through the piston and the chambers within the valve. Further dynamic testing may show that these would need to be explicitly included in the model.

Future work should also include the modelling of a winch system including the load control valve such as described in Chapter 1 for the fishing boat. The system model could then be used to predict instability as was encountered in the application of the valve.

7.6 Concluding remarks

Among the suggestions for future work, reworking the squared geometry to a more faithful representation of the true valve geometry should be given priority. More faithful valve geometry would improve the overall credibility of the work. Dynamic response testing both experimental and simulated should also be given priority. Further development work on the model developed would add to the confidence in the model and may lead to improved comparison to experimental results. Further verification work through further work on improving flow visualisation results, dynamic measurement of flow forces, experimental verification of the friction model, and including system components in the Simulink model would further the credibility of the work and improve the overall confidence in the results.

A generic design tool was developed as part of the research into understanding the pressure compensation characteristics of the load control valve. The generic design tool is the methodology used to model the load control valve. The Simulink model could be reused to model other valves without modification if the same configuration of areas and pressures are used in the valve. Otherwise, the model could easily be modified. In order to model the metering hole effects, the *Flowcoeff* function would have to be modified. However, using the framework within the function developed for the load control valve, modifying the function for other valves would not be as difficult a task as writing a function from scratch. The friction parameters might need modifying in the *Friction* M-File, but this is easily accomplished because this was anticipated when the script file was written.

Hence, with few modifications, the model of the load control valve can be used to model other valves. Therefore, the model is considered a generic design tool that should be of great use in valve design by limiting the number of iterations of a design that are constructed to reach the final product.

REFERENCES

Anderson, J. D. Jr. (1995). *Computational fluid dynamics:the basics with applications*, McGraw-Hill, New York, New York, USA, pp. 123-128.

Blackburn, J. F., Reethof, G., and Shearer, J. L. editors **(1960).** *Fluid Power Control*, MIT Press, Cambridge, Massachusetts, USA, pp. 297-313.

Borghi, M.; Cantore, G.; Milard, M.; and Paoluzzi, R. (1997). "Experimental and numerical analysis of forces on a hydraulic distributor," *The Fifth Scandinavian International Conference on Fluid Power, SCFP '97*, Linköping, Sweden, May 28-30, pp. 83-98.

Borghi, M.; Milani, M.; and Paoluzzi, R. (1998). "Transient flow force estimation on the pilot stage of a hydraulic valve," *Proceedings 1998 ASME IMECE Fluid Power Systems and Technology*, FPST-Volume 5, pp. 157-162.

Burnell, Lee Robert. (1992) *The Use of Computational Fluid Dynamics to Minimise Flow-Forces in Spool Valves*, Master of Philosophy thesis, Department of Mechanical Engineering, University of Bath.

Carlson, H. (1978) *Spring Designer's Handbook*, Marcel Dekker, Inc., New York, New York, USA, pp. 294-296.

Crawford, R. J. (1985). *Plastics and rubbers engineering design and applications*, Mechanical Engineering Publications, London, p. 22.

CFX Users Guide (2001). AEA Technology Engineering Software, Harwell Laboratories, Oxfordshire.

***CRC Standard Mathematical Tables and Formulae* (1996).** 30th Edition, CRC Press, Boca Raton, FL, USA, pp. 277-278.

Fairhurst, M. and Watton, J. (2001). "CFD analysis of a pump pressure compensator operating with a water-based fluid," *Power Transmission and Motion Control (PTMC 2001)*, Professional Engineering Publishing Ltd, London, pp. 21-32.

Feigel, H. J. (1990). "Strömungskraftkompensation in Hydraulik-Schieberventilen", *9. Aachener Fluidtechnisches Kolloquim 20-22 März*, Band 2, pp. 79-98.

Fleming, J. S.; Tramschek, A. B.; and Abdul-Husain, J. M. H. (1988) "A comparison of flow and pressure distribution in simple valves using different computational methods",*Proceedings 1988 International Compressor Engineering Conference at Purdue July 18-21*, pp. 117-120.

Geißler, G. (1998). "Flow force coefficient—a basis for valve analysis", *Bath Workshop on Power Transmission and Motion Control (PTMC '98)*, Professional Engineering Publishing Ltd, London, pp. 235-250.

Green, W. L. (1970a). "The poppet valve—flow force compensation", *The 1970 Fluid Power International Conference*, pp. S1-S6.

Green, W. L. (1970b). "Designing a flow-compensated poppet valve—analytical", *Hydraulics and Pneumatics*, Volume 23, October, pp. 108-110.

Grotjans, H. and Menter, F. R. (1998). "Wall functions for general application CFD codes," *ECCOMAS 98 Proceedings of Fourth European Computational Fluid Dynamics Conference*, John Wiley, pp. 1112-1117.

Guo, Mao-Ying and Nakano, Kazuo. (1989). "Numerical study for the compensation of axial flow force in a spool valve by boundary element method", *Fluid Power Transmission and Control—Proceedings of the 2nd International Conference March 20-22, Hangzhou, China*, International Academic Publishers, pp. 171-176.

Herr, F., Mallin, T., Lane, J., and Roth, S. (1998). "A shock absorber model using CFD analysis and Easy 5," Fluid *Power Systems and Technology: Collected Papers Proceedings of the 1998 ASME International Mechanical Engineering Congress and Exposition, November, Anaheim, California*, FPST-Vol. 5, ASME, New York, New York, pp. 69-75, [revised edition of the paper bound in the proceedings provided by the authors during the meeting].

Hydropower A/S (1999). Email correspondence, Esbjerg, Denmark.

Huang, Chen Dong and Kim, Rhyn H. (1996). "Three-dimensional analysis of partially open butterfly valve flows", *Transactions of the ASME Journal of Fluids Engineering*, ASME, New York, Volume 118, September, pp. 562-568.

Hutchings, Ian M. (1992). *Tribology Friction and Wear of Engineering Materials*, Edward Arnold, London, pp.65-66.

Ishii, Y.; Yonezawa, Y.; Tsukiji, T.; Suzuki, R.; and Ishii, S. (1994). "Flow visualization in a three-dimensional poppet valve", *Flucome '94 Toulouse (France) 29 August-1 September Fourth Triennial International Symposium on Fluid Control, Fluid Measurement, Fluid Mechanics, Visualization, and Fluidics*, Volume 2, Ensae, Toulouse, France, pp. 1095-1099.

Ito, K.; Takahasi, K.; and Inoue, K. (1992). "Pressure distributions and flow forces on the body of a poppet valve," *Fluid Power Systems Modelling and Control 4th Bath International Fluid Power Workshop 18th-20th September 1991*, Research Studies Press, Somerset, England, pp. 123-138.

Jankowski, Janusz and Plutecki, Janusz (1998). "Measurement of momentary velocity fields in liquid flow with hydrogen bubble method", *8th International Symposium on Flow Visualization Sorrento, Italy, August 29-September 2*, pp. 196.1-196.7.

Johnston, D. N.; Edge, K. A.; and Vaughan, N. D. (1991). "Experimental investigation of flow and force characteristics of hydraulic poppet and disc valves," *Proceedings of the Institution of Mechanical Engineers*, Volume 205, Part A, pp. 161-171.

Johnston, D. N. and Drew, J. E. (1996). "Measurement of positive displacement pump flow ripple and impedance," *Proceedings of the Institution of Mechanical Engineers*, Vol. 210, Part I, pp. 65-74.

Kitamura, Masaaki; Yamazaki, Kazuhiro; Okada, Yoshitugu; and Hasimoto, Kazuji (1985). "Visualizing flows in butterfly valve", *Flow Visualization III, Proceedings of the Third International Symposium on Flow Visualization September 6-9, 1983 Lansing, Michigan*, Hemisphere Publishing, New York, pp. 537-541.

Latour, Christoph. (1995). "Flow force compensation in 2-way cartridge valves—flow visualisation and computational fluid dynamics," *Proceedings of the Fourth Scandinavian International Conference on Fluid Power*, Tampre, Finland, September 26-29, pp. 399-411.

Matlab-Simulink Online Help (2001). *Using Simulink: Coulomb and Viscous Friction*, Matlab version 12.1, Simulink version 4, Mathworks, Cambridge, MA, USA.

McCloy, D. and Martin, H. R. (1980). *Control of Fluid Power Analysis and Design 2nd (Revised) Edition*, Ellis Horwood Ltd, Chichester, pp. 92-95, 184-186.

McCloy, D. and McGuigan, R. H. (1964). "Some static and dynamic characteristics of poppet valves", *Proceedings of the Institution of Mechanical Engineers*, Volume 179, Part 3H, pp. 199-213.

Menter, F. R. (1994). "Two-equation eddy viscosity turbulence models for engineering applications," *AIAA Journal*, Volume 32, Number 8.

Merritt, Herbert E. (1967). *Hydraulic Control Systems*, John Wiley, New York, New York, USA, pp. 101-108.

Merzkirch, Wolfgang. (1987). *Flow Visualization Second Edition*, Academic Press, Boca Raton, Florida, USA, pp. 48-52, 55-56.

Miller, Edward *editor* (1981). *Plastics Products Design Handbook Part A Materials and Components*, Marcel Dekker, New York, pp. 279-346.

Mitunaga, Akiharu and Hirose, Tatuzo. (1977). "An investigation of a coaxial annular jet in a circular tube," *Bulletin of the Japanese Society of Mechanical Engineers*, Vol. 20, No. 146, August, pp. 971-976.

Nakamura, Yoshinari; Washio, Seiichi, and Yu, Youngguang (1999). "Modeling of dynamic behaviors of a poppet valve," *Fluid Power, Proceedings of the Fourth International Symposium on Fluid Power, Tokyo, 15-17 November*, Japan Hydraulics and Pneumatics Society, pp. 315-320.

Nakano, Kazuo; Watanabe, Haruo, and Guo, Mao-ying. (1992). "Experimental study for the compensation of axial flow force in a spool valve", *Journal of Fluid Control*, Volume 21, Nos. 2-3, Delbridge Publishing, Cupertino, California, USA, pp. 7-26.

Oki, Iwao. (1961). "Experimental research on disc valves (7^{th} report, experimental formulae for discharge and lifting-force of flat seated valve)", *Bulletin of JSME*, Volume 4, No. 13, pp 87-93.

Oki, Iwao and Kawakami, Kosaku. (1961). "Characteristics of flat-seated valves with broader seat-face (8^{th} report, experimental research on disc valve)", *Bulletin of JSME*, Volume 4, No 14, pp. 278-286.

Palumbo, A.; Paoluzzi, R.; Borgi, M.; and Milani, M. (1996). "Forces on a hydraulic valve spool," *Fluid Power—Proceedings of the Third JHPS International Symposium on Fluid*

Power, Yokohama, November 4-6, Japan Hydraulics and Pneumatics Society, Tokyo, pp. 543-548.

***Parker O-Ring Handbook (1992)**, ORD5700, Parker Seal Group, Lexington, KY, USA, pp. A6.4-A6.6.*

Parker Seals (1999). *Facsimile copy dated 18 February of material specifications for Polon 132 from the Packing Division, Hampshire, IL, USA to Sun Hydraulics Corp.*

Ueno, Hisanori; Okajima, Assushi; Tanaka, Hiroyoshi; and Hasegawa, Takanori. (1994). "Noise measurement and numerical simulation of oil flow in pressure control valves," *JSME International Journal*, Series B, Volume 37, No. 2, pp. 336-341.

Schlichting, Hermann (1979). *Boundary-Layer Theory*, 7th edition, McGraw-Hill, New York, p. 752.

Schrenk, E. (1957). "Disc valves; flow patterns, resistance and loading", BHRA Report T-547.

Shigley, Joseph Edward and Mischke, Charles R. (1989). *Mechanical Engineering Design, Fifth Edition*, McGraw-Hill, New York, p.92.

Sørensen, H. L. (1999a). "Experimental and numerical analysis of flow force compensation methods for hydraulic seat valve," *Proceedings of The Sixth Scandinavian International Conference on Fluid Power May 26-28, Tampere, Finland*, Volume 1, Tampere University of Technology (TUT) Print, pp. 471-482.

Sørensen, H. L. (1999b). "Numerical and experimental analyses of flow and flow force characteristics for hydraulic seat valves with difference in shape," *Bath Workshop on Power Transmission and Motion Control (PTMC 99)*, Professional Engineering Publishing Ltd, London, pp. 283-295.

Stone, J. A. (1954). *Design and development of an apparatus to study the flow-induced forces in a poppet-type flow valve*, B. S. Thesis, Department of Mechanical Engineering, Massachusetts Institute of Technology (MIT), Cambridge, Massachusetts, USA.

Stone, J. A. (1957). *An investigation of discharge coefficients and steady state flow forces for poppet type valves*, M. S. Thesis, Department of Mechanical Engineering, Massachusetts Institute of Technology (MIT), Cambridge, Massachusetts, USA.

Stone, J. A. (1960). "Discharge coefficients and steady-state flow forces for hydraulic poppet valves", *Transactions of the ASME Journal of Basic Engineering*, ASME, Volume 82, Number 1, March, pp. 144-154.

Takenaka, T. and Urata, E. (1969). "The dynamic characteristics of oil hydraulic control valves", *Bulletin of the JSME*, Volume 12, No. 52, p. 765-773.

Takenaka, Toshio; Yamen, Ryuichiro; and Iwamizo, Tatsuo. (1964). "Thrust of a disc valve", *Bulletin of JSME*, Volume 7, No. 27, pp. 558-566.

Tidor, M. (1954). *A study of* pressure *and flow in a poppet valve model,* B. S. Thesis, Department of Mechanical Engineering, Massachusetts Institute of Technology (MIT), Cambridge, Massachusetts, USA.

Tsukiji, Tetsuhiro; Takahashi, Koji; and Hori, Hiroyuki. (1989). "A study on the axial flow forces in a spool valve using flow visualisation and image processing techniques", *Fluid Power Transmission and Control—Proceedings of the 2nd International Conference, March 20-22, Hangzhou, China*, International Academic Publishers, pp. 177-182.

Tsukiji, Tetsuhiro; Sumikawa, Hiroakazu; Sumita, Takashi; and Sato, Takehio. (1996a). "Cavitation in hydraulic holding valve," *Proceedings of the ASME Fluids Engineering Division Summer Meeting July 7-11, San Diego, California, USA*, Volume 236, Part 1, pp. 373-378.

Tsukiji, Tetsuhiro; Sumikawa, Hiroakazu; Sumita, Takashi; and Sato, Takehio. (1996b). "Flow visualization in hydraulic holding valves", *Fluid Power—Proceedings of the Third JHPS International Symposium on Fluid Power, Yokahma, November 4-6,* Japan Hydraulics and Pneumatics Society, Tokyo, pp. 437-441.

Tuffias, R. H. (1957). *Discharge coefficients for flow through round edged orifices*, M. S. Thesis, Department of Mechanical Engineering, Massachusetts Institute of Technology (MIT), Cambridge, Massachusetts, USA.

Urata, Eizo. (1969). "Thrust of a poppet valve", *Bulletin of JSME*, Volume 12, No. 53, pp. 1099-1199.

Vaughan, N. D.; Johnston, D. N.; and Edge, K. A. (1992). "Numerical simulation of fluid flow in poppet valves," *Proceedings of the Institution of Mechanical Engineers*, Volume 206, Part C, pp. 119-127.

Vaughan, N. D.; Johnston, D. N.; and Burnell, L. R. (1993). "The use of computational fluid dynamics in hydraulic valve design", *Fifth Bath International Fluid Power Workshop on Circuit, Component Design, and System Design, September 16-18, 1992*, Research Studies Press, Somerset, England, pp. 226-244.

von Mises, R. (1917). "The calculation of flow coefficients for nozzles and orifices," *V. D. I.*, Band 61, Nr 21, 22, and 23, May, June, and July.

Washio, S., Nakamura, Y., and Yu, Y. (1999). "Static characteristics of a piston-type relief valve," *Proceedings of the Institution of Mechanical Engineers*, Vol. 213, Part C, pp. 231-239.

Washio, Seiichi; Nakamura, Yoshinari, and Shojino, Kohya (2001). "Measurement of static and dynamic performance of a poppet valve for accurate modelling," *Proceedings of the Seventh Scandinavian International Conference on Fluid Power, SIFP '01, Linköping, Sweden, May 30-June 1*, Vol. 2, pp. 87-98.

White, F. M. (1986). *Fluid mechanics*, McGraw-Hill, New York, New York, USA.

Wilcox, D.C. (1994). *Turbulence modeling for CFD*, DCW Industries, La Cañada, California, USA, pp. 230-232.

Wright, Heather; Alleyne, Andrew, and Liu, Rui (1997). "On the stability and performance of two-stage hydraulic servovalves," Fluid *Power Systems and Technology: Collected Papers Proceedings of the 1997 ASME International Mechanical Engineering Congress and Exposition, November 16-21, Dallas, Texas*, FPST-Vol. 4, ASME, New York, New York, pp. 215-222.

Xiaodong, Ruan; Xiangoqun, Song; and Yamamoto, Fujio (1997). "PIV measurements of flow field in spool valve chamber", *Proceedings of the International Conference on Fluid Power Transmission and Control, September, Hangcow China*, pp. 42-45.

APPENDIX

Appendix 1: Matlab M-files

Smooth.m

```
function zc = smooth (f, fband, fz, z, n_rows);
%
% function zc = smooth (f, fband, fz, z, n_rows);
% Matlab function based upon D.N. Johnston and J. Drew's C++ Smoothing program
% Translated to Matlab by STW, 7 July 2000
%
% Apply smoothing to experimental data.
%
% f =
% fband = band width frequency
% fz = first column of data
% z = second column of data
% n_rows = number of rows of data
% n_cols = number of columns of data
%
 %disp ('***In function smooth***');
  nband = 0;  %number of points in band--counter
  s=0;
  t=0;

  for i=1:n_rows

    fdiff = (fz(i) - f) / fband;
    if fdiff > -3
      if fdiff <3
        nband = nband + 1;
        w = exp (-abs(fdiff * fdiff));
        t = t + (w * z(i));
        s = w + s;
      end;
    end;
   end;

  if nband < 3

    fprintf ('Error: insufficient data near ');
    fprintf ('%2.0f', f);
    fprintf (' L/min \n');

  end;

 %
```

```
end;


zc = t / s;

% return zc;
```

FlowArea.m

```
function TotalArea = FlowArea(stroke)
%   Calculate the flow area in square meters on a per stroke basis with the hole series,
%   hole Dia(i)meter,
%   nominal hole location, number of holes per series, and stroke known in meters.
%   Option Explicit to require variable declarations.
%   Declare all calc values as Single, dimension all arrays
%   to be 1-based indexes (VB normally uses 0-based indexes).

% NoSeries, i;
% NomLoc(5);
% HolePerSeries(7);
% Dia(7);
% Segment1, Segment2;
% x, y;
% TotalArea, HoleArea;
% Area1, Area2;

%Load variable(s)

NoSeries = 5;
TotalArea =0;
HoleArea = 0;

%Load arrays

NomLoc(1) = 0.0235 * 0.0254         %dims in meters
NomLoc(2) = NomLoc(1) + (0.027 * 0.0254)
NomLoc(3) = NomLoc(1) + (0.065 * 0.0254)
NomLoc(4) = NomLoc(1) + (0.110 * 0.0254)
NomLoc(5) = NomLoc(1) + (0.155 * 0.0254)


Dia(1) = 0.032 * 0.0254                     %dims in meters
Dia(2) = 0.04 * 0.0254
Dia(3) = 0.062 * 0.0254
Dia(4) = 0.078 * 0.0254
Dia(5) = 0.125 * 0.0254

HolePerSeries(1) = 4;                       %number of holes in each series
HolePerSeries(2) = 4;
HolePerSeries(3) = 4;
HolePerSeries(4) = 4;
HolePerSeries(5) = 4;



for i=1:NoSeries

   if(stroke < (NomLoc(i) - Dia(i) / 2))      %hole not open
         %disp('Hole not open');
```

```
    Segment1 = 0;
    Segment2 = Dia(i) / 2;

  else

    if (stroke > NomLoc(i))

      if (stroke > (NomLoc(i) + Dia(i) / 2))        %hole wide open
      %disp('Hole wide open');
      Segment1 = Dia(i) / 2;
      Segment2 = 0;

      else     %lower segment wide open upper segment partially open
      %disp('Lower segment wide open, upper segment partially open');
      Segment1 = Dia(i) / 2;
      Segment2 = (NomLoc(i) + Dia(i) / 2) - stroke;

      end

      else     %lower segment partially open upper segment not open
      %disp('Lower segment partially open, upper segment not open');
      Segment1 = stroke - (NomLoc(i) - Dia(i) / 2);
      Segment2 = Dia(i) / 2;

      end


  end

%First calculate lower hole segment (segment1) area as "area1"

  if (Segment1 > 0)

    if (Segment1 < Dia(i) / 2)

      x = (((Dia(i) / 2) - Segment1) / (Dia(i) / 2));
      Area1 = (Dia(i)*Dia(i) / 4) * acos(x)- ((Dia(i) / 2) - Segment1) * sqrt(2 * (Dia(i) / 2) *
Segment1 - Segment1 * Segment1);


    else

      Area1 = 0.5 * ((pi * Dia(i) * Dia(i)) / 4);

     end

    %Now calculate the upper hole segment (segment2) area as "area2"

    if (Segment2 > 0)

      y = (((Dia(i) / 2) - Segment2) / (Dia(i) / 2));
      Area2 = (0.5 * pi * Dia(i) * Dia(i) / 4) -((Dia(i) * Dia(i) / 4) * acos(y) - ((Dia(i) / 2) -
Segment2) * sqrt(2 * (Dia(i) / 2) * Segment2 - Segment2 * Segment2));

    else

      Area2 = 0.5 * ((pi * Dia(i) * Dia(i)) / 4);
       end;

  else
```

```
    Area1 = 0;
    Area2 = 0;

        end
  %the total area of one hole exposed by the piston stroke

  HoleArea = Area1 + Area2;


  %the total flow area for the series at the nominal location exposed by the piston stroke

  TotalArea = TotalArea + HolePerSeries(i) * HoleArea;

% loop back and start calculations for the next nominal location and hole size


end
```

PressAngle.m

```
% hyd2xl
% Matlab script file to import ascii text file generated by
% the HyDaq data acquisition system, and save it in an excel compatable format
% with the hysteresis removed and resampled to a defined list of ordinate values
%
% Modified for MBEM research---STW 27 July 2000
% First load the data from HyDaq - will be stored in an array of matrices called "data"
%
% Load ascii text file generated by Hydaq. The script reads the ascii text file by starting
% 'hyload'. The experimental data is loaded into an array called data which then is broken
down
% to the matrices x (the x axis of the original plot) and y(:,*) where * is a wild card for each
% of the y-axis data (currently with hydaq, this is limited to either 1 or 2). The script then
% applies the 'smooth' to the data. A smoothing bandwidth, step 'frequency, and truncation
limits
% must be specified. Finally, a polynomial curve fit is applied once an order for the
polynomial
% is specified. The script then asks for the second part of the experimental data. As
written, the
% the script expects the pressure data first and then the flow force/valve stroke data.
Output files
% must be specified for each part of the script. The flow force data is read and again the
smooth
% subroutine is applied with the necessary limits specified. Output curves are produced for
each
% of the data sets.
%
%
%


rho = 870.0;  % density (kg/m3)
Dia1 = 0.01189101;
Dia2 = 0.01427226;
Dia3 = 0.01189609;
Area1 = pi * (Dia3*Dia3-Dia1*Dia1) / 4;
Area2 = pi * (Dia2*Dia2-Dia3*Dia3) / 4;
Area3 = pi * (Dia2*Dia2-Dia1*Dia1) / 4;
```

```
p3=0;  %Applied pilot pressure. Zero since valve stroked manually with FF fixture and port
open to ATM

%Load arrays

NomLoc(1) = 0.0235 * 0.0254;        %dims in meters
NomLoc(2) = NomLoc(1) + (0.027 * 0.0254);
NomLoc(3) = NomLoc(1) + (0.065 * 0.0254);
NomLoc(4) = NomLoc(1) + (0.110 * 0.0254);
NomLoc(5) = NomLoc(1) + (0.155 * 0.0254);


Dia(1) = 0.032 * 0.0254;                    %dims in meters
Dia(2) = 0.04 * 0.0254;
Dia(3) = 0.062 * 0.0254;
Dia(4) = 0.078 * 0.0254;
Dia(5) = 0.125 * 0.0254;


hyload;                                     % Load data using custom script program
%disp('Define plot range:');
%xmin=input('Min x value: ');
%xmax=input('Max x value: ');
%xinc=input('x increment: ');
xtrunc1=input('Xmin truncation: ');                     % Ignore any x < xtrunc1
xtrunc2=input('Xmax truncation: ');                     % Ignore any x > xtrunc
disp(' ');

[name,path]=uiputfile('*.dat','Save Data File');% Get file name & path to save data
f_name=[path,name];                                     % Concatenate name and path
fid=fopen(f_name,'w');                                  % Open output file

n_traces=max(size(data));                               % Deteremine the number of
separate traces

fprintf(fid,'%s\r\n',char(header.cartridge));
fprintf(fid,'%s\r\n',char(header.title));
fprintf(fid,'%s\r\n',char(header.notes));
fprintf(fid,'%s\r\n',char(header.operator));

[n_rows n_cols]=size(transducer);
for i=1:n_cols
  fprintf(fid,'%s,%s\r\n',char(transducer(i).name),char(transducer(i).units));
end

% z_choice=input('Do you want to find the zero point (y/n)?: ','s');
% if z_choice=='y'
%   y_index=input('Transducer number of y data: ');
% end

for i=1:n_traces                            % Consider each trace in turn
  fprintf(fid,'\r\n');
  % Make x & y vectors
  x=data{i}(:,1);                                   % x vector is first column of data
  y=abs(data{i}(:,2:n_cols));                       % y vector is in subsequent columns
  % Split vectors into ascending and descending portions
  max_i=find(x==max(x));                            % Find index of max value
  x1=x([1:max_i]);
  x2=x([length(x):-1:max_i]);                       % Note double up max x data point
```

```
  y1=y([1:max_i],:);
  y2=y([length(x):-1:max_i],:);    %x1, y1 are the increasing vectors while x2 and y2 are the
decreasing
  % Generate new x vector                          % vectors--STW
  %new_x=[xmin:xinc:xmax]';
  % Sort x vectors
  [x1,index]=sort(x1);
  y1=y1(index,:);                          % Shuffle y1 vector so points match x1
  [x2,index]=sort(x2);
  y2=y2(index,:);                          % Shuffle y2 vectors so points match x2
  % Top & tail the data to remove hysteresis "turnaround"
  index_1=find(x1> xtrunc1 & x1<(max(x)-xtrunc2));
  index_2=find(x2> xtrunc1 & x2<(max(x)-xtrunc2));
  %size(index_1)
  %size(index_2)
  if length(index_1)>0 & length(index_2)>0
    x1=x1(index_1);
    x2=x2(index_2);
    y1=y1(index_1,:);
    y2=y2(index_2,:);
    % Interpolate y vectors to fit new x data and take average
    % Take each y column in turn
    % for j=1:n_cols-1
    %   new_y1=linterp(x1,y1(:,j),new_x,'lin');
    %  new_y2=linterp(x2,y2(:,j),new_x,'lin');
    % new_y(:,j)=(new_y1'+new_y2')/2;
    % end
  end;
   display (' ');
   fband = input ('Enter smoothing bandwidth: ');
   fstart = xtrunc1          %input ('Enter starting frequency: ');
   fend = xtrunc2                    %input ('Enter ending frequency: ');
   fstep = input ('Enter step frequency: ');
 %
 %
 [counter1, trash1]=size(x1);
 [counter2, trash2]=size(x2);
 counter3=1;


    dp1=y1(:,1)-y1(:,2);
    dp2=y2(:,1)-y2(:,2);


    for f = fstart:fstep:fend

      z1(counter3) = smooth (f, fband, x1, y1(:,1), counter1);
      z2(counter3) = smooth (f, fband, x2, y2(:,1), counter2);
      z3(counter3) = smooth (f, fband, x1, y1(:,2), counter1);
      z4(counter3) = smooth (f, fband, x2, y2(:,2), counter2);

      avg_z1(counter3)=(z1(counter3)+z2(counter3))/2;
      avg_z2(counter3)=(z3(counter3)+z4(counter3))/2;
      deltaP(counter3)=avg_z1(counter3)-avg_z2(counter3);

      fp(counter3)   =   (-avg_z1(counter3)*Area1-avg_z2(counter3)*Area2+p3*Area3)*1.e5;
%pressure force in Newtons
```

```
    fprintf('%g\t',    f    ,    z1(counter3),    z2(counter3),    z3(counter3),    z4(counter3),
deltaP(counter3));
    fprintf('\r\n' );
    %fprintf (fid,'%\t', f, z);
    fprintf(fid,'%g\t\t\t',f,  x1,  x2,  z1(counter3),  z2(counter3),  z3(counter3),  z4(counter3),
deltaP(counter3));
    fprintf(fid,'\r\n' );

    counter3=counter3+1;
  end;

  q=(fstart:fstep:fend);

  order=input('What order polynominal for curve fit? ');
  pf1=polyfit(q,avg_z1,order);
  pfy1=polyval(pf1,q);
  figure(2);                    % Start a new graph (raw data is plotted
                                % on figure 1 by the routine hyload)

  plot(q,avg_z1,q,pfy1);
  xlabel ('Flow [L/min]');
  ylabel ('Pressure [bar]')
  title ('Curve fit flow and inlet pressure data');
  grid on;

  order=input('What order polynominal for curve fit? ');
  pf2=polyfit(q,avg_z2,order);
  pfy2=polyval(pf2,q);
  figure(3);                            % Start a new graph (raw data is plotted
                                        % on figure 1 by the routine hyload)

  plot(q,avg_z2,q,pfy2);
  xlabel ('Flow [L/min]');
  ylabel ('Pressure [bar]')
  title ('Curve fit flow and outlet pressure data');
  grid on;

  order=input('What order polynominal for curve fit? ');
  pf3=polyfit(q,deltaP,order);
  pfy3=polyval(pf3,q);
  figure(4);                            % Start a new graph (raw data is plotted
                                        % on figure 1 by the routine hyload)

  plot(q,deltaP,q,pfy3);
  xlabel ('Flow [L/min]');
  ylabel ('Pressure [bar]')
  title ('Curve fit flow and calculated pressure difference');
  grid on;



  % if z_choice=='y'
  %   zero(i)=find_zero(new_x,new_y,y_index-1);
  % end
  % Plot data
  %for j=1:n_cols-1
  %  subplot(1,n_cols-1,j);
  % plot(x,y(:,j),new_x, new_y(:,j), new_x, new_y(:,j),'o');
  %hold on              % Keep same graph for all traces
  %grid on;             % Display grid
```

```
    %end
    %for j=1:length(new_x)                    % Write data to disk
    %  fprintf(fid,'%8.3f',new_x(j));
    % for k=1:n_cols-1
    %   fprintf(fid,',%8.3f',new_y(j,k));
    %end
    %fprintf(fid,'\r\n');
    %end
    %end
end
hold off;
fclose(fid);
figure(1);
hold off;

%
%
%
%  Need to load the valve stroke data in order to calculate the flow area.  This is then
%  used to calculate a function that describes the discharge coefficient.  This function
%  can then be used in the valve.m script to better model the valve performance...hopefully!!
%
%
%

disp (' Now load measured flow force, valve stroke, and flow data... ');
figure (5);
hyload;

disp(' ');

[name,path]=uiputfile('*.dat','Save Data File');% Get file name & path to save data
f_name=[path,name];                       % Concatenate name and path
fid=fopen(f_name,'w');                    % Open output file

n_traces=max(size(data));                 % Deteremine the number of separate traces

fprintf(fid,'%s\r\n',char(header.cartridge));
fprintf(fid,'%s\r\n',char(header.title));
fprintf(fid,'%s\r\n',char(header.notes));
fprintf(fid,'%s\r\n',char(header.operator));

[n_rows n_cols]=size(transducer);
for i=1:n_cols
  fprintf(fid,'%s,%s\r\n',char(transducer(i).name),char(transducer(i).units));
end

% z_choice=input('Do you want to find the zero point (y/n)?: ','s');
% if z_choice=='y'
%   y_index=input('Transducer number of y data: ');
% end

for i=1:n_traces                          % Consider each trace in turn
  fprintf(fid,'\r\n');
  % Make x & y vectors
  x=data{i}(:,1);                         % x vector is first column of data
  y=abs(data{i}(:,2:n_cols));             % y vector is in subsequent columns
  % Split vectors into ascending and descending portions
  max_i=find(x==max(x));                  % Find index of max value
  x1=x([1:max_i]);
```

```
  x2=x([length(x):-1:max_i]);          % Note double up max x data point
  y1=y([1:max_i],:);
  y2=y([length(x):-1:max_i],:);        %x1, y1 are the increasing vectors while x2 and y2
are the decreasing
  % Generate new x vector              % vectors--STW
 % new_x=[xmin:xinc:xmax]';
  % Sort x vectors
  [x1,index]=sort(x1);
  y1=y1(index,:);                      % Shuffle y1 vector so points match x1
  [x2,index]=sort(x2);
  y2=y2(index,:);                      % Shuffle y2 vectors so points match x2
  % Top & tail the data to remove hysteresis "turnaround"
  index_1=find(x1>(xtrunc1)& x1<(max(x)-xtrunc2));
  index_2=find(x2>(xtrunc1)& x2<(max(x)-xtrunc2));
  %size(index_1)
  %size(index_2)
  if length(index_1)>0 & length(index_2)>0
    x1=x1(index_1);
    x2=x2(index_2);
    y1=y1(index_1,:);
    y2=y2(index_2,:);
    % Interpolate y vectors to fit new x data and take average
    % Take each y column in turn
    % for j=1:n_cols-1
    %   new_y1=linterp(x1,y1(:,j),new_x,'lin');
    %  new_y2=linterp(x2,y2(:,j),new_x,'lin');
    % new_y(:,j)=(new_y1'+new_y2')/2;
    % end
  end
 end

 [counter1, trash1]=size(x1);
 [counter2, trash2]=size(x2);
 counter4=1;

 disp (' ');
 disp ('Smoothing based upon previously entered limits...');
 disp (' ');


  % Convert stroke measurements from mm to m
  %
  y1(:,2)=y1(:,2)/1000;
  y2(:,2)=y2(:,2)/1000;

  % Apply smoothing to measured force data and stroke data
  %
   for f = fstart:fstep:fend

     ftot1(counter4) = smooth (f, fband, x1, y1(:,1), counter1);
     ftot2(counter4) = smooth (f, fband, x2, y2(:,1), counter2);
     ftot_mean(counter4) = (ftot1(counter4)+ftot2(counter4))*4.448222/2; %convert force
data from lbs to newtons

     fflow(counter4)=ftot_mean(counter4)+ fp(counter4); % >>> Subtract pressure force from
mean force to calc Fflow

     stroke1(counter4) = smooth (f, fband, x1, y1(:,2), counter1);
     stroke2(counter4) = smooth (f, fband, x2, y2(:,2), counter2);
     stroke_mean(counter4)=(stroke1(counter4)+stroke2(counter4))/2;
```

```
    fprintf('%g\t', f , ftot_mean(counter4), stroke_mean(counter4));
    fprintf('\r\n' );
    fprintf(fid,'%g\t\t\t',f, ftot_mean(counter4), stroke_mean(counter4));
    fprintf(fid,'\r\n' );

    counter4=counter4+1;

  end;


% q=(fstart:fstep:fend);

% Curve fit and plot the mean measured force and stroke data

order=input('What order polynominal for curve fit for flow vs. flow force? ');
  pf_force=polyfit(q,fflow,order);
  pfforce=polyval(pf_force,q);
  figure(6);                              % Start a new graph (raw data is plotted
                                          % on figure 1 by the routine hyload)

  plot( q, fflow, q, pfforce);
  xlabel ('Flow [L/min]');
  ylabel ('Flow force [N]')
  title ('Curve fit flow force and flow data');
  grid on;

order=input('What order polynominal for curve fit for flow vs. stroke? ');
  pf_stroke=polyfit(q,stroke_mean,order);
  pfstroke=polyval(pf_stroke,q);
  figure(7);                              % Start a new graph (raw data is plotted
                                          % on figure 1 by the routine hyload)

  plot( q, stroke_mean, q, pfstroke);
  xlabel ('Flow  [L/min]');
  ylabel ('Measure stroke [m]')
  title ('Curve fit measured stroke and flow data');
  grid on;

order=input('What order polynominal for curve fit for stroke vs. flow force? ');
  pf=polyfit(stroke_mean, fflow,order);
  pfcombo=polyval(pf,stroke_mean);
  figure(8);                              % Start a new graph (raw data is plotted
                                          % on figure 1 by the routine hyload)

  plot( stroke_mean, fflow , stroke_mean, pfcombo);
  xlabel ('Stroke  [m]');
  ylabel ('Flow force [N]')
  title ('Curve fit flow force and stroke data');
  axis ([0, 5e-3, 0, 110]);
  grid on;

%
%
% Analysis...
%
% Compute flow coefficient and jet angle using smoothed data
%
%
```

```
  for cc=1:counter4-1

    area(cc) = FlowArea(stroke_mean(cc));

    CoefDis(cc)=(q(cc)/6e4)/(area(cc)*sqrt(2*deltaP(cc)*1e5/rho));
    %Cd=Q/(area*sqrt(2*delta P/rho))

    cos_theta(cc)=(fflow(cc))/(2*deltaP(cc)*1e5*CoefDis(cc)*area(cc));
    theta(cc) = acos(abs(cos_theta(cc)))*180/pi;

    end

  % fband = input ('Enter smoothing bandwidth: ')/1000;
  % fstart = input('Enter starting stroke: ')/1000;
  % fend = input ('Enter ending stroke: ')/1000;
  % fstep = input ('Enter step frequency: ')/1000;



% Plot jet angle and discharge coefficient

figure (9);
plot (stroke_mean,theta(:));
xlabel ('Valve stroke [m]');
ylabel ('Jet angle theta [degrees]');
title (' Jet angle as a function of valve stroke');
grid on;
hold on;

theta_max=max(theta);
theta_min=min(theta);
theta_step=(theta_max-theta_min)/5;


t=0:pi/20:2*pi;

plot(Dia(1)/2*sin(t) + NomLoc(1),Dia(1)/2*2*cos(t) + theta_min)
plot(NomLoc(1),theta_min,'+')
plot(Dia(2)/2*sin(t) + NomLoc(2),Dia(2)/2*2*cos(t) + (theta_min+theta_step))
plot(NomLoc(2),(theta_min + theta_step), '+')
plot(Dia(3)/2*sin(t) + NomLoc(3),Dia(3)/2*2*cos(t) + (theta_min + 2*theta_step))
plot(NomLoc(3),(theta_min + 2*theta_step), '+')
plot(Dia(4)/2*sin(t) + NomLoc(4),Dia(4)/2*2*cos(t) + (theta_min + 3*theta_step))
plot(NomLoc(4),(theta_min + 3*theta_step), '+')
plot(Dia(5)/2*sin(t) + NomLoc(5),Dia(5)/2*2*cos(t) + (theta_min + 4*theta_step))
plot(NomLoc(5), (theta_min + 4*theta_step),'+')


figure(10)
plot (stroke_mean, CoefDis);
xlabel ('Valve stroke [m]');
ylabel ('Flow coefficient, Cq, [1]');
title (' Discharge coefficent as a function of valve stroke');
grid on;
hold on;

Cd_max=max(CoefDis);
Cd_min=min(CoefDis);
Cd_step=(Cd_max-Cd_min)/5;
```

```
plot(Dia(1)/2*sin(t) + NomLoc(1),Dia(1)/2*2*cos(t) + Cd_min)
plot(NomLoc(1),Cd_min,'+')
plot(Dia(2)/2*sin(t) + NomLoc(2),Dia(2)/2*2*cos(t) + (Cd_min+Cd_step))
plot(NomLoc(2),(Cd_min + Cd_step), '+')
plot(Dia(3)/2*sin(t) + NomLoc(3),Dia(3)/2*2*cos(t) + (Cd_min + 2*Cd_step))
plot(NomLoc(3),(Cd_min + 2*Cd_step), '+')
plot(Dia(4)/2*sin(t) + NomLoc(4),Dia(4)/2*2*cos(t) + (Cd_min + 3*Cd_step))
plot(NomLoc(4),(Cd_min + 3*Cd_step), '+')
plot(Dia(5)/2*sin(t) + NomLoc(5),Dia(5)/2*2*cos(t) + (Cd_min + 4*Cd_step))
plot(NomLoc(5), (Cd_min + 4*Cd_step),'+')

hold off;

figure(11)
plot (stroke_mean, area);
xlabel ('Valve stroke [m]');
ylabel ('Opening area [sq. m]');
title('Opening area as a function of valve stroke');
axis ([0, 5e-3, 0, 3.5e-5]);
grid on;
hold on;



hold off;

%tidy up workspace
clear ans;
clear area;
clear cc;
clear f_name;
clear fid;
clear i;
clear index;
%clear index_1;
%clear index_2;
clear j;
clear k
clear max_i;
%clear n_cols;
%clear n_rows;
% clear n_traces;  t_size(1) is the number of rows of data
clear new_x;
clear new_y;
clear new_y1;
clear new_y2;
clear x;
%clear x1;
%clear x2;
clear xinc;
clear xmax;
clear xmin;
clear xtrunc1;
clear xtrunc2;
clear y;
%clear y1;
%clear y2;
clear y_index;
```

```
clear z_choice;
```

PressureMap.m

```
% PressureMap.m        24 September 2001  STW
%
% Script file to compute the flow force from pressure data extracted
% from CFD data.  Uses the pressure data for the piston edge adjacent
% to the exit hole.  Uses a trapezoidal rule for integrating the data
% over the area.
%
% Assumes coordinate and pressure data from CFD analsysis is in workspace
% memory.  Then resamples data to a mapped meshed, using cubic interpolation
% for smoothing to remap the pressure data to the mapped mesh.  Because CFD
% data from a surface that is shapped like trapezoid, the remapping command
% 'griddata' produces NaN in the data vector.  These are replaced with the
% maximum pressure value in the data set to "square" up the data.
%
%

%reset sums
p_corner_sum = 0;
edge1_sum = 0;
edge2_sum = 0;
edge3_sum = 0;
edge4_sum = 0;
edge_sum = 0;
internalnodes_sum = 0;
internal_sum = 0;

% Work with raw data to produce graph

pc = p - max(p);

[xsize,scratch]=size(x);
[ysize,scratch]=size(y);
xm=linspace(min(x),max(x),xsize);
ym=linspace(min(y),max(y),ysize);
[xx,yy]=meshgrid(xm,ym);
pm=griddata(x,y,pc,xx,yy,'cubic');
pm(isnan(pm))=max(max(pm));
mesh(xx,yy,pm)
xlabel('X-coordinate [m]')
ylabel('Y-coordinate [m]')
zlabel('Pressure [Pa]')
title('Pressure contour')

%Size the mesh

[scratch,cx] = size(xm);
[scratch,cy] = size(ym);

xlength = max(max(xm)) - min(min(xm));
ylength = max(max(ym)) - min(min(ym));

hx = xlength / cx;
hy = ylength / cy;

surfacearea = xlength * ylength;
```

```
cellarea = hx * hy;

% Sum the corner node pressures

p_corner_sum = pm(1,1) + pm(cx,cy) + pm(1,cy) + pm(cx,1);

% Sum the edge node pressures

for i=2:(cx-1)
edge1_sum = edge1_sum + pm(i,1);
edge3_sum = edge3_sum + pm(i,cy);
end

for j=2:(cy-1)
edge4_sum = edge4_sum + pm(1,j);
edge2_sum = edge2_sum + pm(cx,j);
end

edge_sum =2*(edge1_sum + edge2_sum + edge3_sum +edge4_sum);

%sum internal nodes

for i=2:(cx-1)
   for j=2:(cy-1)
      internalnodes_sum = internalnodes_sum + pm(i,j);
   end
end

internal_sum = 4 * internalnodes_sum;

% Perform trapezodial integration for 2-D mesh

f_force = (cellarea/4)*(p_corner_sum + edge_sum + internal_sum)
```

Friction.m

```
function u = friction (vel)

%
%
% Matlab function to calculate fricition acting on the piston of the
% MBEM valve.
%
%
% STW 15 May 2001
%
%
% mc coefficient of Coulomb friction (N-s/m)
% mv coefficient of viscous friction (N-s/m)
%
%
frict =0;
velocity = vel;


x1=[0 0.399 0.401 0.999 1.00];
x2=[0 -0.399 -0.401 -0.999 -1.00];

stiction = 2; %height of stiction peak relative to coulomb fricition
```

```
y1=[0 stiction stiction 1 1];
y2=[0 -stiction -stiction -1 -1];

p1 = polyfit(x1,y1,4)
p2 = polyfit(x2,y2,4)

mc = 10; %Coulomb friction
mv = 5;  %Viscous friction slope
%fs = 10; %Stiction value

%threshold =0.0000325; %0.1 mm/s band that falls under the threshold and uses Coulomb
friction
threshold = .0001;   %3.25e-6;        %1.95e-5;

if (velocity >= 0)
  if (velocity <threshold)
    frict = mc*polyval(p1, velocity/threshold);
  else
    frict=mc;
  end

else if (velocity <= 0)
    if (velocity >-threshold)
      frict = mc*polyval(p2, velocity/threshold);
    else
      frict=-mc;
    end
 end
 end


frict=frict+mv*velocity;

u = frict;

%end of function
```

Valve.m

```
% Matlab script to start valve model
%
% Valve openings

global vstroke
global s_theta
global s_cq
global s_theta
global s_area

global u
global cq
global cos_theta
global total_area


freq = 0.00025;

vstroke=0.0001:.00001:0.0060;
```

```
[i,j]=size(vstroke);

for count = 1:j

   u = flowcoeff(vstroke(count));
   cq(count) = u(1);
   cos_theta(count) = u(2);
   total_area(count) = u(3);
   disp (count)
end

for count=1:j
   s_theta(count)=smooth(vstroke(count),freq,vstroke,cos_theta,j);
   s_cq(count)=smooth(vstroke(count),freq,vstroke,cq,j);
   s_area(count)=smooth(vstroke(count),freq,vstroke,total_area,j);
end
```

Interpolate.m

```
function nu = interpolate(stroke)

% Matlab function to interpolate values for Cq, jet angle, and total area
% as calculated from the function flowcoeff and smoothed using the function
% smooth as called in the Matlab script file valve.m
%
% STW 6 September 2001
%
%

global vstroke
global s_theta
global s_area
global s_cq

%disp(size(vstroke))
%disp(size(s_cq))
%disp(size(s_theta))
%disp(size(s_area))
%disp (stroke)

nu(1) = interp1(vstroke, s_cq, stroke,'linear');
nu(2) = interp1(vstroke, s_theta, stroke,'linear');
nu(3) = interp1(vstroke, s_area, stroke,'linear');


% end of function
```

FlowCoeff.m

```
function u = flowcoeff(stroke)
%  Calculate the flow area in square meters on a per stroke basis with the hole series,
%  hole Dia(i)meter,
%  nominal hole location, number of holes per series, and stroke known in meters.
%  Option Explicit to require variable declarations.
%  Declare all calc values as Single, dimension all arrays
%  to be 1-based indexes (VB normally uses 0-based indexes).
```

```
% NoSeries, i;
% NomLoc(5);
% HolePerSeries(7);
% Dia(7);
% Segment1, Segment2;
% x, y;
% TotalArea, HoleArea;
% Area1, Area2;

%Load variable(s)

NoSeries = 5;
TotalArea =0;
HoleArea = 0;
%Load arrays

NomLoc(1) = 0.0235 * 0.0254;        %dims in meters
NomLoc(2) = NomLoc(1) + (0.027 * 0.0254);
NomLoc(3) = NomLoc(1) + (0.065 * 0.0254);
NomLoc(4) = NomLoc(1) + (0.110 * 0.0254);
NomLoc(5) = NomLoc(1) + (0.155 * 0.0254);


Dia(1) = 0.032 * 0.0254;                    %dims in meters
Dia(2) = 0.04 * 0.0254;
Dia(3) = 0.062 * 0.0254;
Dia(4) = 0.078 * 0.0254;
Dia(5) = 0.125 * 0.0254;

a(1)=pi/4*Dia(1)*Dia(1);
a(2)=pi/4*Dia(2)*Dia(2);
a(3)=pi/4*Dia(3)*Dia(3);
a(4)=pi/4*Dia(4)*Dia(4);
a(5)=pi/4*Dia(5)*Dia(5);

HolePerSeries(1) = 4;                       %number of holes in each series
HolePerSeries(2) = 4;
HolePerSeries(3) = 4;
HolePerSeries(4) = 4;
HolePerSeries(5) = 4;

cqfunction(1,1)=0.784;
cqfunction(1,2)=0.784;
cqfunction(1,3)=0.951;
cqfunction(1,4)=0.907;
cqfunction(1,5)=0.796;

cqfunction(2,1)=0.941;
cqfunction(2,2)=0.941;
cqfunction(2,3)=0.866;
cqfunction(2,4)=0.851;
cqfunction(2,5)=0.742;

cqfunction(3,1)=0.646;
cqfunction(3,2)=0.646;
cqfunction(3,3)=0.754;
cqfunction(3,4)=0.816;
cqfunction(3,5)=0.750;

cqfunction(4,1)=0.674;
```

```
cqfunction(4,2)=0.674;
cqfunction(4,3)=0.771;
cqfunction(4,4)=0.811;
cqfunction(4,5)=0.771;

cqfunction(5,1)=0.597;
cqfunction(5,2)=0.597;
cqfunction(5,3)=0.727;
cqfunction(5,4)=0.811;
cqfunction(5,5)=0.771;


theta_ref(1,1)= 62.12;
theta_ref(1,2)= 62.12;
theta_ref(1,3)= 67.02;
theta_ref(1,4)= 71.58;
theta_ref(1,5)= 88.29;

theta_ref(2,1)= 63.59;
theta_ref(2,2)= 63.59;
theta_ref(2,3)= 67.41;
theta_ref(2,4)= 71.10;
theta_ref(2,5)= 89.74;

theta_ref(3,1)= 64.89;
theta_ref(3,2)= 64.89;
theta_ref(3,3)= 68.62;
theta_ref(3,4)= 72.24;
theta_ref(3,5)= 89.72;

theta_ref(4,1)= 66.00;
theta_ref(4,2)= 66.00;
theta_ref(4,3)= 68.85;
theta_ref(4,4)= 72.47;
theta_ref(4,5)= 89.23;

theta_ref(5,1)= 67.21;
theta_ref(5,2)= 67.21;
theta_ref(5,3)= 70.24;
theta_ref(5,4)= 72.47;
theta_ref(5,5)= 89.23;


stroke_ref(1,1)= NomLoc(1)-(Dia(1)/2);
stroke_ref(1,2)= NomLoc(1)-(Dia(1)/4);
stroke_ref(1,3)= NomLoc(1);
stroke_ref(1,4)= NomLoc(1)+(Dia(1)/4);
stroke_ref(1,5)= NomLoc(1)+(Dia(1)/2);

stroke_ref(2,1)= NomLoc(2)-(Dia(2)/2);
stroke_ref(2,2)= NomLoc(2)-(Dia(2)/4);
stroke_ref(2,3)= NomLoc(2);
stroke_ref(2,4)= NomLoc(2)+(Dia(2)/4);
stroke_ref(2,5)= NomLoc(2)+(Dia(2)/2);

stroke_ref(3,1)= NomLoc(3)-(Dia(3)/2);
stroke_ref(3,2)= NomLoc(3)-(Dia(3)/4);
stroke_ref(3,3)= NomLoc(3);
stroke_ref(3,4)= NomLoc(3)+(Dia(3)/4);
stroke_ref(3,5)= NomLoc(3)+(Dia(3)/2);
```

```
stroke_ref(4,1)= NomLoc(4)-(Dia(4)/2);
stroke_ref(4,2)= NomLoc(4)-(Dia(4)/4);
stroke_ref(4,3)= NomLoc(4);
stroke_ref(4,4)= NomLoc(4)+(Dia(4)/4);
stroke_ref(4,5)= NomLoc(4)+(Dia(4)/2);

stroke_ref(5,1)= NomLoc(5)-(Dia(5)/2);
stroke_ref(5,2)= NomLoc(5)-(Dia(5)/4);
stroke_ref(5,3)= NomLoc(5);
stroke_ref(5,4)= NomLoc(5)+(Dia(5)/4);
stroke_ref(5,5)= NomLoc(5)+(Dia(5)/2);


% Create cubic polynomials to describe Cq and theta

cq(1,:) = polyfit(stroke_ref(1,:),cqfunction(1,:),3);
theta(1,:) = polyfit(stroke_ref(1,:),theta_ref(1,:), 3);

cq(2,:) = polyfit(stroke_ref(2,:),cqfunction(2,:),3);
theta(2,:) = polyfit(stroke_ref(2,:),theta_ref(2,:), 3);

cq(3,:) = polyfit(stroke_ref(3,:),cqfunction(3,:),3);
theta(3,:) = polyfit(stroke_ref(3,:),theta_ref(3,:), 3);

cq(4,:) = polyfit(stroke_ref(4,:),cqfunction(4,:),3);
theta(4,:) = polyfit(stroke_ref(4,:),theta_ref(4,:), 3);

cq(5,:) = polyfit(stroke_ref(5,:),cqfunction(5,:),3);
theta(5,:) = polyfit(stroke_ref(5,:),theta_ref(5,:), 3);


cq_area_sum = 0;
scratch_cq = 0;
cq_area_costheta_sum = 0;
holearea_sum = 0;
scratch_chord = 0;
chord = 0;


for i=1:NoSeries

   if(stroke < (NomLoc(i) - Dia(i) / 2))      %hole not open

      Segment1 = 0;
      Segment2 = Dia(i) / 2;
     scratch_cq = cqfunction(i,1);
     scratch_theta = theta_ref(i,1);
     scratch_cosine = cos(pi/180*scratch_theta);
     %scratch_chord = 0;
    else

      if (stroke > NomLoc(i))

          if (stroke > (NomLoc(i) + Dia(i) / 2))        %hole wide open

          Segment1 = Dia(i) / 2;
          Segment2 = 0;
          scratch_cq = cqfunction(i,5);
          scratch_theta = theta_ref(i,5);
```

```
        scratch_cosine = cos(pi/180*scratch_theta);
        %scratch_chord = 0;

        else     %lower segment wide open upper segment partially open

       Segment1 = Dia(i) / 2;
       Segment2 = (NomLoc(i) + Dia(i) / 2) - stroke;
        scratch_cq = polyval(cq(i,:),stroke);
        scratch_theta = polyval(theta(i,:), stroke);
        scratch_cosine = cos(pi/180*scratch_theta);
       %scratch_chord = 2*sqrt(Segment2*(Dia(i)-Segment2));

        end


        else     %lower segment partially open upper segment not open
        %disp('Lower segment partially open, upper segment not open');
        Segment1 = stroke - (NomLoc(i) - Dia(i) / 2);
        Segment2 = Dia(i) / 2;
        scratch_cq = polyval(cq(i,:),stroke);
        scratch_theta = polyval(theta(i,:),stroke);
        scratch_cosine = cos(pi/180*scratch_theta);
     %scratch_chord = 2*sqrt(Segment1*(Dia(i)-Segment1));

     end

  %First calculate lower hole segment (segment1) area as "area1"

  if (Segment1 > 0)

     if (Segment1 < Dia(i) / 2)

        x = (((Dia(i) / 2) - Segment1) / (Dia(i) / 2));
        Area1 = (Dia(i)*Dia(i) / 4) * acos(x)- ((Dia(i) / 2) - Segment1) * sqrt(2 * (Dia(i) / 2) *
Segment1 - Segment1 * Segment1);



     else

        Area1 = 0.5 * ((pi * Dia(i) * Dia(i)) / 4);

     end

     %Now calculate the upper hole segment (segment2) area as "area2"

     if (Segment2 > 0)

        y = (((Dia(i) / 2) - Segment2) / (Dia(i) / 2));
        Area2 = (0.5 * pi * Dia(i) * Dia(i) / 4) -((Dia(i) * Dia(i) / 4) * acos(y) - ((Dia(i) / 2) -
Segment2) * sqrt(2 * (Dia(i) / 2) * Segment2 - Segment2 * Segment2));

     else

        Area2 = 0.5 * ((pi * Dia(i) * Dia(i)) / 4);
     end;

     else

     Area1 = 0;
```

```
    Area2 = 0;

    end
    %the total area of one hole exposed by the piston stroke

  HoleArea = Area1 + Area2;
  scratch_cq = scratch_cq * HoleArea * HolePerSeries(i);

  TotalArea = TotalArea + HolePerSeries(i) * HoleArea;

  cq_area_sum = cq_area_sum + scratch_cq;
  cq_area_costheta = scratch_cq * scratch_cosine;
  cq_area_costheta_sum = cq_area_costheta_sum + cq_area_costheta;

  chord = chord + scratch_chord;

% loop back and start calculations for the next nominal location and hole size


end

if (TotalArea <= 0)
  cq_calc = 0;
  costheta_calc = 0;
else
  cq_calc = cq_area_sum / TotalArea;
  costheta_calc = cq_area_costheta_sum / (cq_calc * TotalArea);
end;
u(1)=cq_calc;
%u(1) = 0.65;
u(2)=costheta_calc;
%u(2)=cos(69*pi/180);
u(3)=TotalArea;
% end of function
end
```

Theta.m

```
% Script theta
%
% Designed to calculate the jet angle necessary to produce
% constant flow rate for a given pilot pressure with changing
% load pressure.
%
% Based upon:
%                 Cos(theta)=(Fp-kx)*(Area_opening)*Cq/(rho*q^2)
%
%
%
%


Dia1 = 0.01189101;
Dia2 = 0.01427226;
Dia3 = 0.01189609;

% Differential areas in square meters
Area1 = pi * (Dia3*Dia3-Dia1*Dia1) / 4;
Area2 = pi * (Dia2*Dia2-Dia3*Dia3) / 4;
```

```
Area3 = pi * (Dia2*Dia2-Dia1*Dia1) / 4;

k =(22.4 + 44.2 + 93.3)*4.448222/0.0254;    %36321.56561 convert lbf/in to Nt/m
% Spring rates from measured data and not from specifications

x0 = 0.005776713; %end of deadband in meters
x = 0;

cq = 0.78;
rho = 870.0;  % density (kg/m3)
%theta = 77.0; % jet angle

c = 0.2; %damping term

%inlet area
Area_inlet = pi/4*(0.344*0.344*0.0254*0.0254);


count=1;

% read file name to save output data
fid=0;

while fid<1
[name,path]=uiputfile('*.dat','File name to save output data? ');
f_name=[path,name];                                    % Concatenate name and path
fid=fopen(f_name,'w');                                 % Open output file

if fid==-1
        disp('Failed to open');
end
end

%Set values for P1, P2, and Q

pfirst=30;
plast=350;
pstep=1;

% polynomial for P2 derived from 100 bar data

pf2=[ 0.00000409601501   0.00011069710797   0.04068847689494   2.89374283165111];


for uu=1:8
p3_array(uu) = 85;
end



qfirst=98/60e3; %q in units of cubic m/second
qlast = 105/60e3;
qstep = 1/60e3;

xi = 0.005; %inital guess at valve stroke
xh = 0.0055; %initial guess at valve stroke xi-1


disp (' ')
disp ('Thinking.....')
```

```
disp (' ')

% Print headers in file
fprintf(fid,'Flow(L/min)    P1(bar)          P2(bar)          P3(bar) Stroke(mm)
        JetAngle(degree)');
fprintf(fid, '\r\n');

p2 = 1;
flow_count = 0;

for flow =qfirst:qstep:qlast
    flow_count = flow_count + 1;
    p3 = p3_array(flow_count)

    for ii = 0:10
    dp2 = (polyval(pf2,flow*60e3) - p2); %caluclate P2 pressure as function of flow rate
    p2 = p2 + dp2 * 0.3; %P2 in bar
    end % ii iteration counter

    for p1 =pfirst:pstep:plast %step through P1 in bar
      delta_p = abs(p1 - p2); %delta p in bar

      opening_area = flow / (cq * sqrt(2*delta_p*1e5/rho)); %pressure converted from bar to
Pa

      % Use the Secant Method (finite divided difference) to calculate the valve stroke
      % that would create the opening area calculated above

      epsilon = 1; %error check flag
      disp (p1)
      while abs(epsilon) > 0.02

        xj = xi - ((flowarea(xi)-opening_area)*(xh-xi))/(flowarea(xh) - flowarea(xi));

        epsilon = (xj - xi) / xj;

        xh = xi;
        xi = xj;

      end


      fp = (-p1*Area1-p2*Area2+p3*Area3)*1.e5;   %pressure force
      fspring = - k * (xi + x0); % Spring force from Hook's Law

      cos_theta = ((fp + fspring)*opening_area*cq) / (rho * flow * flow);

       jangle = acos(cos_theta)*180/pi;

% Lood arrays with calculated data and write to file
      qs(count)=flow*60e3; %save in units of bar
      p1s(count)=p1;
      stroke(count)=xi;
      p2s(count)=p2;
      delta_p(count) = p1 - p2;
      theta(count) = jangle;
      countsave(count)=count;
      count=count+1;

      fprintf(fid,'%4.2f\t\t',flow * 60.e3 , p1, p2, p3, xi * 1000 , jangle);
```

```
    fprintf(fid,'\r\n' );


  end %p1 loop

end %flow loop

% Plot results

    figure (30)
    plot(qs,p1s,'r*')
    xlabel('Flow [L/min]')
    ylabel('Load pressure [bar]')
    title('Pressure compensation')
    grid on



    figure (31)
    plot(qs,stroke,'r*')
    xlabel('Flow [L/min]')
    ylabel('Valve stroke [m]')
    title ('Valve stroke during pressure compensation')
    grid on



    figure (33)
    plot(qs,p2s)
    xlabel ('Flow [L/min]')
    ylabel ('Outlet pressure [bar]')
    title ('Outlet pressure during pressure compensation')
    grid on



    figure (36)
    plot (stroke, theta,'r*')
    xlabel ('Valve stroke [m]')
    ylabel ('Jet angle [degrees]')
    title  ('Jet angle plotted against valve stroke')
    grid on
    hold on

    theta_max=max(stroke)*20000;
    theta_min=min(stroke)*20000;
    theta_step=(theta_max-theta_min)/5;

    NomLoc(1) = 0.0235 * 0.0254;        %dims in meters
    NomLoc(2) = NomLoc(1) + (0.027 * 0.0254);
    NomLoc(3) = NomLoc(1) + (0.065 * 0.0254);
    NomLoc(4) = NomLoc(1) + (0.110 * 0.0254);
    NomLoc(5) = NomLoc(1) + (0.155 * 0.0254);
    Dia(1) = 0.032 * 0.0254;                                %dims in meters
    Dia(2) = 0.04 * 0.0254;
    Dia(3) = 0.062 * 0.0254;
    Dia(4) = 0.078 * 0.0254;
    Dia(5) = 0.125 * 0.0254;
```

```
        t=0:pi/20:2*pi;

        plot(Dia(1)/2*sin(t) + NomLoc(1),Dia(1)/2*2*cos(t) + theta_min+30)
        plot(NomLoc(1),theta_min+30,'+')
        plot(Dia(2)/2*sin(t) + NomLoc(2),Dia(2)/2*2*cos(t) + (theta_min+theta_step)+30)
        plot(NomLoc(2),(theta_min + theta_step)+30, '+')
        plot(Dia(3)/2*sin(t) + NomLoc(3),Dia(3)/2*2*cos(t) + (theta_min + 2*theta_step)+30)
        plot(NomLoc(3),(theta_min + 2*theta_step)+30, '+')
        plot(Dia(4)/2*sin(t) + NomLoc(4),Dia(4)/2*2*cos(t) + (theta_min + 3*theta_step)+30)
        plot(NomLoc(4),(theta_min + 3*theta_step)+30, '+')
        plot(Dia(5)/2*sin(t) + NomLoc(5),Dia(5)/2*2*cos(t) + (theta_min + 4*theta_step)+30)
        plot(NomLoc(5), (theta_min + 4*theta_step)+30,'+')

clear count
clear flow_count

      % ******* END OF SCRIPT  ******
```

CQ.m

```
% Script cq
%
% Designed to calculate the jet angle necessary to produce
% constant flow rate for a given pilot pressure with changing
% load pressure.
%
% Based upon:
%       Cos(theta)=(Fp-kx)*(Area_opening)*Cq/(rho*q^2)
%
%
%       Cq=(rho*q^2)cos(theta)/(Fp-kx)*(Area_opening)
%
%
% Last modified : 2 July 2001

   Dia1 = 0.01189101;
   Dia2 = 0.01427226;
   Dia3 = 0.01189609;

    % Differential areas in square meters
   Area1 = pi * (Dia3*Dia3-Dia1*Dia1) / 4;
   Area2 = pi * (Dia2*Dia2-Dia3*Dia3) / 4;
   Area3 = pi * (Dia2*Dia2-Dia1*Dia1) / 4;

   k =(22.4 + 44.2 + 93.3)*4.448222/0.0254;    %36321.56561 convert lbf/in to Nt/m
   % Spring rates from measured data and not from specifications

   x0 = 0.005776713; %end of deadband in meters
   x = 0;

   cq = 0.72;  % starting value, to kick things off....
   rho = 870.0;  % density (kg/m3)
   %theta = 77.0; % jet angle

          c = 0.2; %damping term

         %inlet area
  Area_inlet = pi/4*(0.344*0.344*0.0254*0.0254);
```

```
count=1;

 % read file name to save output data
fid=0;

while fid<1
        [name,path]=uiputfile('*.dat','File name to save output data? ');
        f_name=[path,name];             % Concatenate name and path
        fid=fopen(f_name,'w');          % Open output file

        if fid==-1
        disp('Failed to open');
        end
 end

%Set values for P1, P2, and Q

pfirst=25;
plast=250;
pstep=1;

% polynomial for P2 derived from 100 bar data

pf2=[ 0.00000409601501   0.00011069710797   0.04068847689494   2.89374283165111];


for uu=1:11
  p3_array(uu) = 65;
end



qfirst=65/60e3; %q in units of cubic m/second
qlast = 75/60e3;
qstep = 1/60e3;

xi = 0.005; %inital guess at valve stroke
xh = 0.0055; %initial guess at valve stroke xi-1


disp (' ')
disp ('Thinking.....')
disp (' ')

% Print headers in file
fprintf(fid,'Flow(L/min) P1(bar)          P2(bar)          P3(bar) Stroke(mm)
        JetAngle(degree)');
fprintf(fid, '\r\n');

p2 = 1;
flow_count = 0;
theta = 77;
cos_theta = cos (theta*pi/180);
m=50;  %slope of the PC curve

for flow_loop =qfirst:qstep:qlast
  flow_count = flow_count + 1;
  p3 = p3_array(flow_count);
```

```
    flow = flow_loop; % something to get things started

    %flow = (flow_loop-0.000005417)/m;


  for ii = 0:10
    dp2 = (polyval(pf2,flow*60e3) - p2); %caluclate P2 pressure as function of flow rate
    p2 = p2 + dp2 * 0.3; %P2 in bar
    end % ii iteration counter

    for p1 =pfirst:pstep:plast %step through P1 in bar
       %disp('Paused...')
       %pause


      delta_p = abs(p1 - p2); %delta p in bar

      %flow = (delta_p + 17.5e7)/1.615e12; % flow in cubic m/s to add a slope to the PC
curve

      opening_area = flow / (cq * sqrt(2*delta_p*1e5/rho)); %pressure converted from bar to
Pa

      % Use the Secant Method (finite divided difference) to calculate the valve stroke
      % that would create the opening area calculated above

      epsilon = 1; %error check flag
      disp (delta_p)
      while abs(epsilon) > 0.001
        %opening_area = flow / (cq * sqrt(2*delta_p*1e5/rho))

        xj = xi - ((flowarea(xi)-opening_area)*(xh-xi))/(flowarea(xh) - flowarea(xi));

        epsilon = (xj - xi) / xj;

        xh = xi;
        xi = xj;

        %display('paused...')
        %pause

        %end


      fp = (-p1*Area1-p2*Area2+p3*Area3)*1.e5;   %pressure force
      fspring = - k * (xi + x0); % Spring force from Hook's Law

      cq = abs((rho * flow * flow * cos_theta)/((fp + fspring)*opening_area));
      %abs used as brute force to prevent negative numbers

      end  %while loop

% jangle = acos(cos_theta)*180/pi;

% Lood arrays with calculated data and write to file
                qs(count)=flow*60e3; %save in units of bar
      p1s(count)=delta_p;
      stroke(count)=xi;
      p2s(count)=p2;
      delta_p(count) = p1 - p2;
```

```
    alpha(count) = cq;
    countsave(count)=count;
    count=count+1;

    fprintf(fid,'%4.2f\t\t',flow * 60.e3 , p1, p2, p3, xi * 1000 , alpha);
    fprintf(fid,'\r\n' );


  end %p1 loop

end %flow loop

% Plot results

    figure (30)
    plot(qs,p1s,'*')
    xlabel('Flow [L/min]')
    ylabel('Load pressure [bar]')
    title('Pressure compensation')
    grid on



    figure (31)
    plot(qs,stroke,'*')
    xlabel('Flow [L/min]')
    ylabel('Valve stroke [m]')
    title ('Valve stroke during pressure compensation')
    grid on




    figure (33)
    plot(qs,p2s,'b*')
    xlabel ('Flow [L/min]')
    ylabel ('Outlet pressure [bar]')
    title ('Outlet pressure during pressure compensation')
    grid on



    figure (36)
    plot (stroke, alpha,'r*')
    xlabel ('Valve stroke [m]')
    ylabel ('Flow coefficient [1]')
    title  ('Flow coefficient plotted against valve stroke for 80 degree jet')
    grid on
    hold on

    theta_max=max(stroke)*200;
    theta_min=min(stroke)*200;
    theta_step=(theta_max-theta_min)/5;

       NomLoc(1) = 0.0235 * 0.0254;         %dims in meters
       NomLoc(2) = NomLoc(1) + (0.027 * 0.0254);
       NomLoc(3) = NomLoc(1) + (0.065 * 0.0254);
       NomLoc(4) = NomLoc(1) + (0.110 * 0.0254);
       NomLoc(5) = NomLoc(1) + (0.155 * 0.0254);
       Dia(1) = 0.032 * 0.0254;                              %dims in meters
```

```
        Dia(2) = 0.04 * 0.0254;
        Dia(3) = 0.062 * 0.0254;
        Dia(4) = 0.078 * 0.0254;
        Dia(5) = 0.125 * 0.0254;

    offset=0;

        t=0:pi/20:2*pi;

        plot(Dia(1)/2*sin(t) + NomLoc(1),Dia(1)/2*2*cos(t) + theta_min+offset)
        plot(NomLoc(1),theta_min+offset,'+')
        plot(Dia(2)/2*sin(t) + NomLoc(2),Dia(2)/2*2*cos(t) + (theta_min+theta_step+offset))
        plot(NomLoc(2),(theta_min + theta_step)+offset, '+')
        plot(Dia(3)/2*sin(t)    +    NomLoc(3),Dia(3)/2*2*cos(t)    +    (theta_min    +
2*theta_step+offset))
        plot(NomLoc(3),(theta_min + 2*theta_step)+offset, '+')
        plot(Dia(4)/2*sin(t)    +    NomLoc(4),Dia(4)/2*2*cos(t)    +    (theta_min    +
3*theta_step)+offset)
        plot(NomLoc(4),(theta_min + 3*theta_step)+offset, '+')
        plot(Dia(5)/2*sin(t)    +    NomLoc(5),Dia(5)/2*2*cos(t)    +    (theta_min    +
4*theta_step)+offset)
        plot(NomLoc(5), (theta_min + 4*theta_step)+offset,'+')


clear count
clear flow_count

    % ******* END OF SCRIPT  ******
```